University of Bath

PHD

Use of V-band geostationary satellites to deliver multimedia services

Page, Andrew

Award date:
2003

Awarding institution:
University of Bath

Link to publication

General rights
Copyright and moral rights for the publications made accessible in the public portal are retained by the authors and/or other copyright owners and it is a condition of accessing publications that users recognise and abide by the legal requirements associated with these rights.

- Users may download and print one copy of any publication from the public portal for the purpose of private study or research.
- You may not further distribute the material or use it for any profit-making activity or commercial gain
- You may freely distribute the URL identifying the publication in the public portal ?

Take down policy
If you believe that this document breaches copyright please contact us providing details, and we will remove access to the work immediately and investigate your claim.

Download date: 13. May. 2019

Use of V-band Geostationary Satellites to Deliver Multimedia Services

submitted by Andrew Page

for the degree of PhD

of the University of Bath

2003

COPYRIGHT

Attention is drawn to the fact that copyright of this thesis rests with its author.

This copy of the thesis has been supplied on condition that anyone who consults it is understood to recognise that its copyright rests with its author and that no quotation from the thesis and no information derived from it may be published without the prior written consent of the author.

This thesis may be made available for consultation within the University Library and may be photocopied or lent to other libraries for the purposes of consultation.

A. Page.

UMI Number: U209982

All rights reserved

INFORMATION TO ALL USERS
The quality of this reproduction is dependent upon the quality of the copy submitted.

In the unlikely event that the author did not send a complete manuscript
and there are missing pages, these will be noted. Also, if material had to be removed,
a note will indicate the deletion.

UMI U209982
Published by ProQuest LLC 2013. Copyright in the Dissertation held by the Author.
Microform Edition © ProQuest LLC.
All rights reserved. This work is protected against
unauthorized copying under Title 17, United States Code.

ProQuest LLC
789 East Eisenhower Parkway
P.O. Box 1346
Ann Arbor, MI 48106-1346

Abstract

This study considers the use of geostationary satellites as a platform for the delivery of multimedia services operating at V-band (40 to 50 GHz). Radio spectrum at V-band has been allocated by the ITU for Broadband Satellite Services (BSS), and several commercial space companies have been licensed to exploit the radio resource. The spectrum allocation provides a massive one Gigahertz of radio spectrum, previously unused by satellite operators. The spectrum available at V-band facilitates the use of greater bandwidths and therefore higher data rates. Also, earth station antennas with beamwidth ~3° (desirable in order to avoid very precise alignment) will be smaller at V-band than at lower frequencies.

The propagation environment at such frequencies is markedly different from that widely experienced at C and Ka-band. In particular, the presence of rain on the radio path, inevitability results in attenuation so great as to cause link outage. Even the presence of gaseous attenuation and heavy cumulus clouds can cause link outage. Consequently the thesis initially presents statistical predictions of annual and monthly link availability for a typical European coverage area , including all causes of path attenuation.

In such an environment fade mitigation techniques (FMT) are essential for improving the Quality of Service to an end user. The recent dramatic changes in the cost and size of computer memory, are particularly useful and enable large amounts of traffic to be cached at remote terminals, in order to provide buffers against fading. In order to assess the effectiveness of such techniques in future systems, a novel method is proposed for the generation of tropospheric attenuation time series.

The time series model is based on assimilated weather forecast data and weather radar images. It provides a tool for generating synthetic time series with a high temporal resolution, for arbitrary locations within the coverage area bounded by the data, while retaining the integrity of the spatial correlation between different points. The model has been validated against empirical beacon measurements recorded from the Italsat propagation experiment.

Finally, the study has integrated the model into a network simulation of a typical multimedia system. The study has immediate application to performance evaluation for fade countermeasures in DVB-S and VSAT systems.

Acknowledgements

I would like to thank Professor Peter Watson for the opportunity of taking part this study and for all of this valuable guidance, enthusiasm and experience over the last few years. Also, Dr Robert Watson for his advice and technical knowledge. Many thanks to all academic and support staff in the Electrical and Electronic Engineering Dept. for all their help. And the staff and students in my research group, for being good friends and sharing the experience over the last few years together.

Finally to my family and friends, in particular Erica for her constant support and encouragement from the beginning.

Table of Contents

Abstract ii
Acknowledgements iii
Table of Contents iv
Table of Figures vii
List of Tables ix
1 Introduction 1
2 Background 4
2.1 European Multimedia Satellite Systems 4
2.1.1 SES Astra 4
2.1.2 EuroSkyWay 5
2.2 High Altitude Platforms 5
2.3 Why Satellite? 6
2.4 V-band Satellite Filings 7
2.5 Multimedia Applications 9
2.5.1 DTH Broadcasting 9
2.5.2 Interactive Video Broadcast 10
2.5.3 Video-on-Demand 10
2.5.4 Internet 11
2.5.5 Web Caching 13
2.5.6 Multicasting 13
2.5.7 Video Conferencing 14
2.5.8 Distance Learning 14
2.6 Fade Mitigation Techniques 14
2.6.1 Power Control 15
2.6.2 Signal Processing 16
2.6.3 Diversity 20
2.7 Satellite Broadcast Technology & Systems 23
2.8 Onboard Processing 23
2.8.1 Regeneration 24
2.8.2 Switching 26
2.9 Satellite Antenna 27
2.9.1 Multi-beam Antenna 27
2.9.2 Shaped Reflector Antenna 28
2.9.3 Active Phased Array Antenna 29
2.10 Power Amplifiers 30
2.11 MF-TDMA 32
2.11.1 Power Requirements 33
2.11.2 Synchronization 34
2.11.3 Intermodulation 34
2.11.4 Medium Access Control 34

2.11.5 Acquisition 35
2.11.6 Allocation 35
2.11.7 Implementation 36
2.12 DVB-S 36
2.12.1 MPEG Multiplex 37
2.12.2 Energy Dispersal 37
2.12.3 Reed-Solomon Coding 37
2.12.4 Interleaving 38
2.12.5 Convolutional Coding 38
2.12.6 Modulation 39
2.12.7 Bit Rate vs. Transponder Bandwidth 39
3 Long Term Propagation Prediction 41
3.1 Introduction 41
3.2 Atmospheric Attenuation 42
3.3 Gaseous Attenuation 43
3.3.1 Absorption 43
3.3.2 Refractivity 44
3.4 Cloud Attenuation 45
3.5 Rain Attenuation 46
3.6 Long Term Propagation Prediction Model 48
3.6.1 Overview 48
3.6.2 Pseudo-Satellite Geometry 51
3.6.3 Long Term Point Predictions 52
3.7 Link Performance Analysis for a European Coverage 57
3.7.1 Conclusions 58
4 System Design 60
4.1 Architecture 60
4.2 Return Channel 60
4.2.1 Transponder Utilisation 62
4.2.2 Number of Users 63
4.3 Outbound Channel 63
4.3.1 Transponder Utilization 64
4.3.2 Link Budgets 65
4.3.3 Test Case Link Analysis 66
4.3.4 Annual European Availability 67
4.3.5 Seasonal Availability 67
4.4 Conclusions 70
5 Approaches to Time Series Generation 72
5.1 Introduction 72
5.2 Statistical Models 73
5.2.1 Maseng-Bakken Model 73
5.2.2 Fractals 77

5.3 Empirical-Statistical Models 79
5.3.1 Matricciani-Riva 79
5.3.2 Fiebig Model 79
5.3.3 Matricciani Model 83
6 Sources of Data for Development of Time Series Generator 85
6.1 Satellite Beacon Data 85
6.2 Hourly Synoptic Data 86
6.3 One Minute Rain Gauge Network 87
6.4 Radiosonde Data 88
6.5 Meteorological Satellites 88
6.6 Unified Model 89
6.6.1 Spatial & Temporal Resolution 90
6.6.2 Mesoscale Model Outputs 91
6.7 Weather Radar 92
7 New Approach to Time Series Generation 94
7.1 Introduction 94
7.1.1 Power Spectrum 95
7.1.2 Cumulative Distribution 96
7.2 Rain Attenuation Time Series Model 97
7.2.1 Low frequency Components 97
7.2.2 High Frequency Components 97
7.3 Gaseous Attenuation 99
7.4 Cloud Attenuation Model 99
7.4.1 Cloud Liquid Water Content 99
7.4.2 Cloud Attenuation 100
7.5 Scintillation 101
7.5.1 Scintillation Power Spectrum 101
7.5.2 Scintillation Intensity 101
7.6 Results 103
7.7 Validation of Time Series Simulator 105
7.7.1 Power Spectrum 105
7.7.2 Comparison with Measured Attenuation Time Series 105
7.8 Conclusions 107
8 System Modelling 108
8.1 Introduction 108
8.2 Modelling Philosophy 108
8.2.1 Software Considerations 109
8.3 Test Case Protocol Stack 115
8.3.1 Outbound Channel 115
8.3.2 Return Channel 116
8.4 Results 117
8.5 Conclusions 119

9 Conclusions 120
9.1 Prediction of Monthly Availabilities 120
9.2 Development of Novel Time Series Generator 120
10 Future Work 122
Appendix A Unified Model Output Fields 123
Appendix B Pressure on UM Levels 125
Appendix C Geopotential Height on UM Model Levels 127
Appendix D Relative Humidity on UM Levels 129
Appendix E Water Vapour Density 130
Appendix F UM Position Grid 131
Appendix G Wind Speed & Direction 134
Appendix H Rain Rate 135
Appendix I Scintillation Variance 136
References 139
List of Publications 153

Table of Figures

Figure 2.2-1 High Altitude Platforms 6
Figure 2.6-1 Effect of Forward Error Correction [Saunders, 1998] 17
Figure 2.6-2 Turbo Encoder block diagram [Sklar, 1997] 19
Figure 2.6-3 Cumulative annual attenuation distributions in the 12-50 GHz frequency bands, earth station at Cambourne (50.13°N, 5.59°W), 13.2°E GEO satellite. 22
Figure 2.8-1 SkyPlex system functional block diagram [Elia and Colzi, 1996] 26
Figure 2.9-1 SECOMS EHF Spot Beam Coverage [Losquadro, 1997, Losquadro and Schena, 1999] 28
Figure 2.9-2 Shaped Reflector Antenna [Saunders, 1998] 29
Figure 2.11-1 MF-TDMA frame structure 33
Figure 2.12-1 DVB-S Channel Coding & Modulation System [ETSI, EN 300 421] 37
Figure 2.12-2 Convolutional Coder of Rate ½ [ETSI, DVB-RCS] 39
Figure 2.12-3 E_b/N_0 degradations due to transponder bandwidth limitations [ETSI, EN300421] 40
Figure 3.2-1 Cumulative Atmospheric Attenuation against Time Exceeded 42
Figure 3.3-1 Total Zenith Attenuation due to Atmospheric Gases from sea level 44
Figure 3.4-1 Height of Cloud and Rain 46
Figure 3.5-1 Specific Attenuation Through Rain as a Function of Frequency (horizontal polarisation) 47
Figure 3.6-1 KWSA Propagation Prediction Model Flowchart 50
Figure 3.6-2 Pseudo Satellite Geometry 52
Figure 3.6-3 Measured cumulative distribution of total attenuation at 39.6 and 49.5 GHz (Spino D'Adda, 1994-1996) [Polonio and Riva, 1998] 55
Figure 3.6-4 Predicted Monthly attenuation statistics at 49.5 GHz for Spino D'Adda 56
Figure 3.7-1 Attenuation due to atmospheric gases and cloud for an availability of 99% 57

Figure 4.2-1 Test Case System Architecture 61
Figure 4.2-2 Single MF-TDMA Data Frame Structure 62
Figure 4.3-1 Annual Availability contours for a threshold of 10dB at 40GHz, 19.2°E (Note : excludes antenna pattern and range loss) 68
Figure 4.3-2 Annual Availability contours for a threshold of 10dB at 50GHz, 19.2°E (Note : excludes antenna pattern and range loss) 68
Figure 4.3-3 Availability contours for January for a threshold of 10dB at 50 GHz, 19.2°E 69
Figure 4.3-4 Availability contours for July for a threshold of 10dB at 50 GHz, 19.2°E 69
Figure 5.2-1 Block diagram of the discrete sampled implementation of the Maseng-Bakken model 75
Figure 5.2-2 Maseng-Bakken rain attenuation time series example 75
Figure 5.2-3 Idealised power spectrum of log rainfall 78
Figure 5.3-1 Fiebig-Schnell Classification of received signal type by segmentation [] 80
Figure 5.3-2 Measured PDF's of $P(y|x)$ for various values of x and $\Delta\tau = 64s$. [14] 81
Figure 5.3-3 Fiebig rain attenuation time-series example [14] 82
Figure 5.3-4 Geometrical structure of rain events 84
Figure 6.1-1 ITALSAT beacon measurement at Spino D'Adda, 07 January 1994 86
Figure 6.6-1 Illustrative left a) Mesoscale Model Output – Specific Humidity grid on pressure level; right b) Network Radar Image 92
Figure 7.1-1 Outline block diagram of the time series generator 95
Figure 7.1-2 Ideal on average power spectral density of slant path attenuation 96
Figure 7.2-1 Comparison of simulated rain attenuation time series for widespread rain 98
Figure 7.2-2 Comparison of simulated rain attenuation time series for showery rain 98
Figure 7.4-1 Example of critical humidity profile using a UM vertical profile 100
Figure 7.5-1 Example refractive index structure parameter C_n^2 using UM profile 103
Figure 7.6-1 Example of Generated Time series from Bath 104
Figure 7.6-2 Example of Generated Time series from Chitterne 104
Figure 7.6-3 Example of Generated Time series from Sparsholt 104
Figure 7.7-1 Power spectral density for the simulated Sparsholt time series shown in Figure 7-9 106
Figure 7.7-2 Comparison between measured Italsat link data and simulated time series 106
Figure 7.7-3 Comparison between measured Italsat link data and simulated time series 107
Figure 8.2-1 COTS software scope 109
Figure 8.2-2 Standard Radio Terminal Node Model 112
Figure 8.2-3 TDMA Process Model 113
Figure 8.2-4 Transceiver Pipeline Stages 114
Figure 8.3-1 Outbound Path Protocol Stack 115
Figure 8.3-2 Return Path Protocol Stack 117
Figure 8.4-1Screenshot of the OPNET User Interface 118
Figure 8.4-2 Example of time-series attenuation integrated into the OPNET physical layer. 118
Figure 9.2-1 Distribution of UM vertical layers 126
Figure 9.2-2 Example UM field on standard & Equatorial Lat-Lon Grids 132

List of Tables

Table 2-1 FCC Filings for V-band Multimedia Satellite Systems 8
Table 2-2 Required E_b/N_0 (dB) for BER of 2×10^{-4} [ETSI, EN 300 421] 17
Table 2-3 TWTA Performance 31
Table 2-4 DVB-S Bit Rates versus Transponder Bandwidth 40
Table 3-1 Comparisons between predicted and measured attenuation for Spino D'Adda 53
Table 4-1 Return channel transponder utilisation 62
Table 4-2 Return channel transponder utilisation 64
Table 4-3 Test Case Link Budget 65
Table 4-4 Test Case Predicted Annual Link Availability 66
Table 6-1 Supplied subset of Mesoscale Model output fields 92
Table 10-1 Unified Model Output Fields 123

1 Introduction

Over the last decade the market in global multimedia communications has evolved at an astonishing rate, driven in part by the proliferation and growth of the internet. More recently, the downturn in world financial markets has slowed growth and lead to a change of fortunes for many telecommunications companies who invested heavily and restructured in anticipation of expected growth. Despite this, the demand for access to broadband services continues to rise, fed by the advent of new broadcasting and data applications (including www, electronic commerce, video-on-demand).

In this financial climate, Service Providers seek to increase market share through the delivery of improved services, with larger bandwidths and the introduction of novel new applications. As a further pressure, any technical solutions must be achieved in the most efficient and cost effective manner possible.

This study investigates the use of geostationary satellite systems to deliver multimedia services to subscribers, direct to the home (DTH). Such systems build on present direct broadcast technology, with the addition of a satellite return path from the subscriber to the Service Provider, in order that they may request supplementary information and services.

Geostationary satellites provide a natural broadcast platform, widely used for the delivery of broadband and broadcast services. They are unique in their intrinsic ability to accommodate a large number of remote terminals with rapid deployment and over large areas. Such systems are ideal to exploit the point-to-multipoint (outbound link) and point-to-point (inbound link) nature of interactive multimedia applications.

Present DTH satellite networks rely on additional terrestrial infrastructure (i.e. telephone lines) to provide interactivity. By removing terrestrial limitations, satellite return channel systems can offer higher data rates, over wider areas not previously serviced by terrestrial networks. These systems will further exploit the highly asymmetric nature of multimedia traffic to allow large numbers of subscribers to access broadband satellite resources.

The majority of existing commercial satellite broadcast systems are operated at Ku-band (11/14 and 12/14 GHz), with a small number of transponders emerging at Ka-band (20-30 GHz). This study considers the merits of a V-band (40-50 GHz) system, taking advantage of the large available bandwidth (~1 GHz) already allocated by the ITU[1] for delivery of broadband satellite services. Nomenclature for the bands is defined in [ITU-R, V431].

Chapter 2 introduces the satellite multimedia market and potential applications which can exploit such systems. Emerging technology such as satellite onboard processing, efficient multiple access schemes and fade mitigation techniques (FMT) are considered appropriate for the system design.

At V-band frequencies, the quality of the radio link is dominated by atmospheric effects, specifically rain, clouds and gaseous attenuation. These propagation factors must be well characterised over the region to enable the full capacity of the satellite to be utilised. Chapter 3 explains the attenuating effects of the atmosphere and validates the use of prediction models for the prediction of annual and monthly service availability in the presence of such effects.

Long term propagation analysis is useful in the design of satellite fixed power budgets, but becomes less significant when operating in the aggressive propagation environment experienced at V-band. At Ku-band and to a lesser extent Ka-band, system power margins can be increased dynamically to maintain a high level of availability (>99.7%) through the majority of strong atmospheric events. Chapter 4 assesses a proposed V-band satellite multimedia system, based on a practical satellite architecture, an emerging satellite technology (MF-TDMA) and open commercial standards (ETSI DVB-S). Long term availability analysis is presented for an end-to-end return channel link. The analysis is extended to illustrate the availability of such a fixed power system across a European coverage area.

[1] International Telecommunications Union, http://www.itu.org

When operating at V-band, even relatively small rain events are beyond the compensation capability of power control alone, so other fade mitigation techniques (FMTs) must be considered. Chapter 5 proposes a novel method of generating time series of short-term atmospheric attenuation based on forecast meteorological inputs. The model avoids the requirement for empirical data such as the accurate measurement of a satellite beacon. The high cost of experimental satellites means appropriate empirical satellite records are rare, and limited to a small number of sites, configurations, frequencies and elevation angles.

Furthermore, the time series model is shown to give a good comparison when validated against empirical satellite data. The utility of the model is to allow the evaluation of dynamic FMTs and real-time system performance using software simulations. Since the model is based on meteorological forecast data, it also provides a method for the optimisation of satellite system resources to pre-empt service outage by minimising service disruption through remote data caching and time diversity.

Chapter 8 proposes a method for simulating the real-time performance of satellite networks in real-time, utilising the synthetic time series generator to represent atmospheric fading across the system. The simulation aims to demonstrate the effectiveness of software tools for evaluating the performance of future V-band satellite systems and the gain of different FMTs on end-user applications.

Finally, Chapter 9 reviews the results of the study presented here, and assesses the future of multimedia satellite systems operating at V-band.

The Appendix contains supplementary information which is necessary to process 'raw' data files, upon which the model is based, into a form suitable for use in the generation of synthetic time series. A list of the author's publications are also included.

2 Background

2.1 European Multimedia Satellite Systems

It is easy to identify the advantages, and hence demand for interactive services in both business and residential markets. Presently, the "mass market" sector, with Direct to Home (DTH) services and broadband Multimedia Satellite Services (MSS) are driving growth in the telecommunications industry. Satellite systems already command a leading position in the distribution of digital broadcasting, spurred by the introduction of free subscriber receiving equipment (antennas & decoders).

2.1.1 SES Astra

With its constellation of Astra spacecraft, Societe Europeene des Satellites[2] (SES) of Luxembourg is Europe's leading broadcast satellite network, serving 83.3% (28.3 million) of the DTH market. The Astra constellation currently consists of 13 Ku-band geostationary satellites broadcasting analogue & digital television, data and radio services across Europe and Asia. In June 1999 Astra 1H was launched carrying 2 Ka-band transparent transponders to introduce the Astra Return Channel System (ARCS). Following in-orbit testing of ARCS technology, and the successful delivery of an in-orbit backup (Astra 1K in the third quarter of 2002), ARCS will become the worlds first commercial Ka-band enabled service.

ARCS provides data rates between 144 kbit/s to 2.048 Mbit/s for 0.6m to 1.2m receive antenna respectively. Bandwidth is allocated efficiently by the hub "on-demand" on a cell by cell basis (each cell supports a data rate of 16 kbit/s). The outbound Ku-band broadcast link is fully DVB-S compliant and provides a maximum downlink data rate of 38 Mbit/s.

[2] http://www.astra.lu

2.1.2 EuroSkyWay

Alenia Spazio are developing the EuroSkyWay[3] system (previously SECOMS) to provide bi-directional broadband communications to small fixed and mobile terminals. Using a constellation of 5 geostationary satellites, digital on-board processing and operating at Ka-band which was planned to be operational by 2003. EuroSkyWay will offer high speed "bandwidth on demand" internet access, video conferencing and home shopping. PC based user terminals will be able to receive up to 32 Mbit/s and transmit up to 2.048 Mbit/s. Two smaller portable terminals will receive 2.048 Mbit/s and transmit up to 512 kbit/s and 64 kbit/s using laptop and palm-top terminals respectively.

2.2 High Altitude Platforms

High Altitude Platforms (HAPs) are being developed which offer an alternative to space based platforms. HAPs float (with the support of propulsion systems) or fly in the stratosphere above metropolitan areas. Since HAPs operate at a lower altitude than space based platforms, they are unable to provide the same coverage area from a single platform, although several HAPs can be interconnected through a satellite or terrestrial backbone.

Sky Station had been developing a helium-filled balloon to fly approximately 22 km above as many as 250 metropolitan areas [Clarke, et al., 1998]. Sky Station had plans to deploy its first system in the year 2002 (although the current status of the programme is unknown) using V-band frequency spectrum approved by the FCC. Each balloon will be as wide as a football pitch and nearly twice as long. They will be powered by solar cells and rely on propulsion systems to maintain a flight path in the strong jet steam. The proposed communication systems will provide 2 Mbit/s uplink and 10 Mbit/s downlink.

A different approach is being taken by Angel technologies for their HALO (High Altitude Long Operation) Network[4], each HALO site is serviced by a fleet of three HALO aircraft which operate in overlapping shifts around-the-clock. The HALO aircraft will operate in a circular orbit of roughly 5 to 8 miles (8 to 12km) in diameter at an altitude ranging from 52,000 to 60,000 feet (16 to 18km), with a footprint 50 to 75 miles (80 to 112km) in diameter.

---

[3] http://www.alespazio.it/program/tlc/eurosk/eurosk.htm

[4] http://www.angelhalo.com

Business users will be offered connection speeds ranging from 5 to 12.5 Mbps. Initial high capacity users can enjoy links at 25 Mbps and higher. Consumers will be able to access video, data, and the Internet at rates ranging from 1 to 5 Mbps. Angel will offer higher data rates as the broadband market matures.

Finally, at least one other high-altitude system is being planned by Japan's PTT. A study has been completed to confirm the feasibility of using 270m solar and fuel powered unmanned airships, capable of carrying a one ton communications payload. This project aims to produce an integrated network of 15 airships to serve most of Japan [Tozer and Grace, 2001].

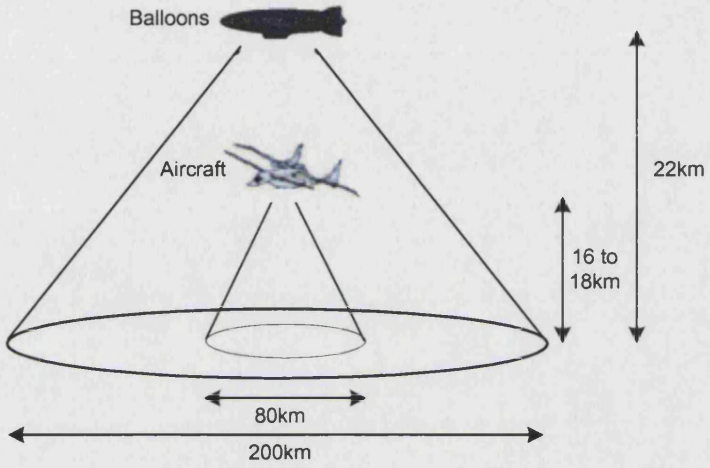

Figure 2.2-1 High Altitude Platforms

2.3 Why Satellite?

Satellites are unmatched in their ability to deliver vast amounts information efficiently, to a large number of distributed users. They can be built and deployed in a relatively short period of time (a minimum construction time of 18 months for a standard commercial payload) and once operational, any site within the satellite footprint can be equipped quickly and cheaply to communicate with it.

For regions where terrestrial infrastructure is limited or non-existent, satellite cover may be the only option. Satellite systems offer an opportunity to bypass congested terrestrial or fibre networks. The service can be simplex, duplex or asymmetric, while remaining insensitive to location and user density.

In the future, it is likely that data services delivered directly to subscribers in the home, will be much enhanced from the simple reception of broadcast media. The increased range of

available media content, particularly through the continued growth of the internet, will change the nature of subscribers from passive to interactive users. Subscribers may become participants in the media they watch, interacting with content providers via narrowband messaging and the internet. In return, multimedia content may become driven by the consumer and distributed to individual subscribers or small groups.

Accordingly, satellite bandwidth will become increasingly occupied by internet traffic, supporting broadband streaming and multicast applications, such as multimedia rich web sites with high quality music and video content. Current terrestrial internet technology is not optimised for this type of multicasting, especially when it comes to broadband multimedia. Furthermore, these services will be provided using 'bandwidth-on-demand', to efficiently allocate resources when required.

Satellite distribution suffers from one major disadvantage, namely the inherent delay between two communicating earth terminals. For geostationary systems, the latency is at least 250 ms on each path between the hub and VSAT. This is approximately 10 times higher than a point-to-point fibre optic link across the Atlantic. Although transmission delay does not affect broadcast (or internet UDP (User Datagram Protocol)) applications, it does reduce the performance of interactive applications which require handshaking between two sites. Unfortunately, internet protocols such as TCP (Transmission Control Protocol) are seriously affected by satellite propagation delay and these protocols must be specifically adapted for use in the satellite environment [Ghani and Dixit, 1999, RFC2488, 1999].

2.4 V-band Satellite Filings

Under the influence of deregulation, broadband satellite networks are becoming increasingly global in order to address world-wide markets. The majority of satellite Ku-band capacity around the world is already in use and is therefore not available for broadband applications. Filings to the FCC (Federal Communications Commission) for Ka-band frequency spectrum started in 1995 and all available US spectrum has already been allocated. As Europe begins to gradually introduce Ka-band services, the US are proposing ambitious global systems and will profit from satellite technology.

Requests for license and spectrum assignments for V-band systems flooded into the FCC in September 1997, when the commission decided to open this part of the bandwidth to commercial satellite systems. To date there have been 16 filings for capacity (given in Table

2-1), although it is likely to be another 5-6 years before any of these systems become operational.

The suggested level of investment in the satellite industry reflects the increased confidence among investors and a continued demand for global connectivity. If all proposed V-band DTH satellite systems were built, over $80 bn in investment would be necessary [Consulting, 2000]. Since 13 Ka-band satellite systems licensed in the US remain unfinanced and unbuilt, there are doubts as to how many of these systems will become reality [Foley, 1998]. However, there are still a number of viable competitors in the broadband satellite market.

Table 2-1 FCC Filings for V-band Multimedia Satellite Systems

Company	System	Service Type	Number & Orbit	Phased Array Antenna	OBP	Cost ($Bn)	Data Rates (Mbit/s)
Cai Satcom		FSS	1 GEO	No	No	0.3	38
Denali	Pentriad	FSS & BSS	9 HEO	Yes	No	1.9	10-3875
GE Americom	GE*StarPlus	FSS	11 GEO	No	Yes	3.4	1.5-155
Globalstar	GS<40	FSS	80 LEO	Yes	No	3.4	2-52
Hughes	Expressway	FSS	14 GEO	No	No	3.9	1.5-155
Hughes	Spacecast	FSS	6 GEO	No	No	1.7	0.4-155
Hughes	StarLynx	MSS	20 GEO 4 MEO	Yes	Yes	2.9	<2portable <8 vehicle
LEO One USA	V-band	MSS	48 LEO	No	Yes	0.3	0.032–0.256
Lockheed Martin	Q/V-band	FSS & BSS	9 GEO	Yes	Yes	4.7	0.384-2488
Loral	CyberPath	FSS	4 GEO	Yes	Yes	1.2	0.4-90
Motorola	M-Star	FSS	72 LEO	Yes	No	6.2	2-52
Orbital Sciences	OrbLink	FSS	7 MEO	No	No	0.9	10-1250
PamAmSat	V-Stream	FSS	12 GEO	No	No	3.5	1.5-155
Spectrum Astro	Aster	FSS	25 GEO	No	No	2.4	2-622
Teledesic	VBS	FSS & BSS	72 LEO	Yes	Yes	1.95	10-100 up 1000 down
TRW	GESN	FSS	4 GEO 15 MEO	Yes	Yes	3.4	1.5-1555

2.5 Multimedia Applications

2.5.1 DTH Broadcasting

Satellite broadcasting is a one-way data transfer by a Service Provider from a hub station, to receivers in the downlink footprint. Direct-to-Home (DTH) TV broadcasting has driven the commercial broadcasting market and currently occupies 80% of Europe's transponder capacity [EC, 1998]. The remaining capacity is available for radio and data services. The introduction of digital services using compression techniques has vastly improved bandwidth efficiency and increased the economics of DTH services.

Historically, broadcasters leased a whole 36 MHz transponder for an analogue channel. Using the digital MPEG-2 (Moving Pictures Expert Group-2) coding standard [MPEG, 1994] 9 Mbit/s is comparable to studio quality TV [ITU-R, BT601]. At 6 Mbit/s the quality exceeds conventional systems such as NTSC, PAL and SECAM. These bit rates refer to video signals only, as additional capacity is required for sound channels and other overheads.

The majority of commercial broadcast systems operate geostationary satellites providing BSS (Broadcast Satellite Services) using C-band and Ku-band frequencies. Modern high power commercial satellites carry as many as 118 transponders[5], providing many hundreds of digital channels to millions of DTH subscribers. It is desirable from the consumer point of view, to minimise the size of DTH antennas down to a size that corresponds to a beamwidth of approximately 3° below which boresight alignment becomes a difficult practical issue. The latest commercial DTH systems make use of spot beams with shaped coverage to match national requirements.

[5] http://www.hughesspace.com

2.5.2 Interactive Video Broadcast

Interactive video broadcast (IVB) [Livingstone, 1999] combines video & data channels to provide interactive TV content. One example is an internet overlay synchronized to a video broadcast, allowing subscribers to browse information related to the current program, such as particular camera views or player statistics during sports coverage. IVB lends itself to home shopping, where impulse buying consumers can find additional product information such as cost, availability and purchase information.

2.5.2.1 IVB Implementation

The presence of a permanently connected return channel from the subscriber to the content provider greatly simplifies the local hardware needed to support interactive applications. Receive only satellite systems employ terrestrial return paths and which utilise techniques designed to limit the return path traffic. These techniques help prevent inefficient use of resources when large numbers of interactive users request the same information.

Commercial Service Providers (e.g. OpenTV, PowerTV) multiplex relevant topical data into the MPEG-2 outbound transport stream. When a consumer tunes to a new video channel, software and data to enable interaction is cached in the subscriber's set-top box. To reduce the local storage requirements the data streams are broadcast cyclically, and stored in a data carousel [Milenkovic, 1998]. The carousel acts as a large serial disk caching data as it arrives. The subscriber uses an interactive overlay screen to browse MPEG-2 images or data from the carousel.

2.5.3 Video-on-Demand

Broadcast TV is a passive service in which the subscriber has no control over the session. Video-on-Demand (VoD) enables the user to select programs from a library and view them at any time using VCR type interactions, such as forward, reverse play, freeze, pause & random positioning. Delivery may be via a dedicated video stream to each customer. To deliver MPEG digital video at VCR quality, requires a transmission data rate of at least 1.544 Mbit/s [Chariglione, 1995] per stream. Provisioning such services via an individual point to point satellite link is unpractical when considering a high number of users, due to the high financial cost of satellite bandwidth. To be able to compete with standard video rental services the costs must be reduced by limiting on-demand functions offered by the system.

2.5.3.1 Near VoD

Improved scalability is achieved by multicasting the video stream to many users simultaneously. In practice, multiple streams of the same content are broadcast at staggered intervals of around 15-20 minutes [Almeroth and Ammar, 1996]. This time delay is a compromise between the bandwidth resources and the tolerable delay to the subscriber.

Buffering of the downlink stream in a set top box may introduce limited interactivity. For example pause, rewind and forward depending on the size of the buffer. If the subscriber delays the stream beyond the capacity of the buffer, it may be possible to switch reception to another time phased stream.

2.5.3.2 True VoD

True VoD gives the user complete control over the presentation of the program. Due to the high cost of implementing separate channels for each subscriber, alternative methods must be considered. The falling cost of digital storage devices (such as hard drives, magnetic tapes, re-writeable CDs and DVDs) allow whole programs to be stored locally for unlimited re-viewing. However, this introduces legal issues concerning property rights and illegal reproduction [Little and Venkatesh, 1994]. Some encryption techniques currently implemented allow the subscriber to watch but not record a program through their set top box.

A more promising technique called the Split and Merge (SAM) protocol [Liao and Li, 1997] initiates delivery via multicasting. If interaction is requested, the SAM protocol splits off the interactive user from the original multicast and temporarily assigns a new video stream. With a dedicated video stream, the user can perform any interactions desired. As soon as the user interaction terminates, the system merges this user back to the nearest ongoing video stream.

2.5.4 Internet

The World Wide Web (WWW) is a collection of documents and services available through the global interconnection of computers. Web servers distribute content on request from a client (a *browser*) through a graphical web page. Each document or web page consists of a number of individual files, i.e. text – usually Hypertext Markup Language (HTML) and multimedia (images, sounds), while services include file transfer (FTP), electronic mail and streaming multimedia (video, audio).

In a bi-directional satellite system, HTTP (Hypertext Transfer Protocol) browser requests are transmitted via the satellite to a local server at the satellite gateway, or directly into the terrestrial network. The server returns requested content through the gateway to the satellite and down to the user terminal.

An important characteristic of web applications is the highly asymmetric nature of the traffic. [Gedney] estimates received data from downloaded information is on average 9 times greater than the amount utilised by the requests. It follows that the forward channel (from server to clients) requires a significantly larger bandwidth than the return channel (from client to server).

2.5.4.1 HTTP

Hypertext Transfer Protocol (HTTP) is a request-response protocol designed to transfer the files constituting the parts of web documents [Bernes-Lee, et al., 1996]. Transfers consist of the client requesting a file from the server, then the server replying with the requested file (or an error notification). Each file is delivered reliably using a separate TCP connection. TCP requires an acknowledgement that each packet has been delivered correctly or it is resent [Tannenbaum].

2.5.4.2 HTTP Traffic Characteristics

Studies [Mah, 1997] on terrestrial HTTP networks provide statistics on typical HTTP traffic behaviour. Such information is useful when dimensioning system capacity of future distribution systems.

(1) When a WWW user clicks on a hypertext link, several Uniform Resource Locator (URL) requests may follow. Each request opens a new TCP connection for retrieving the files from which the page is composed. Statistics show the request length for an average multi-file HTML page is in the order of 1100 bytes (23 ATM cells).

(2) The length of each HTTP reply is the number of bytes returned over a single TCP connection. Typically, the reply consists of either HTML text or multimedia data (images or audio). The mean file size of HTTP replies range from 8-10 kilobytes with median files sizes around 1.5-2.0 kilobytes.

The rapid growth of the WWW and the popularity of novel multimedia applications (such as peer-to-peer networks for file sharing), can significantly change internet traffic patterns over very short periods of time. In the timescale considered for the development of V-band satellite distribution systems, the WWW is likely to evolve even further, most likely beyond prediction.

2.5.5 Web Caching

Web caching [Baentsch, et al., 1997] is the technique of storing frequently requested documents close to where they are needed, significantly reducing access latency and bandwidth usage. It is particularly suited to WWW browsing, in which web content is stored locally in cache memory or at cache servers, preventing unnecessary file transfers and improving response times.

Satellite broadcast systems can exploit web caching by automatically updating the local cache memory of remote terminals during off-peak periods. This can be achieved by refreshing browser bookmarks and scheduled downloading media subscriptions, such as online newspapers etc.

2.5.6 Multicasting

Satellite multicasting is a technique which allows a sender to deliver the same information to a group of users using a single transmit operation saving network capacity and reducing server requirements. Unlike broadcasting, multicasts are selective to whom they deliver. Multicasting is more efficient at delivering data that is required by a set of clients at the same time or more often, when the receivers are able to cache common data until needed. In terrestrial data networks multicast packets are transmitted to the first client on the group list, which copies and retransmits to the next client, in order to avoid flooding the network with duplicate broadcast packets.

Satellites naturally support multicast delivery, as the same packets can be delivered to all satellite receiver terminals simultaneously. Software filters at the remote terminals, identify packets destined for the authorised multicast group. Satellite multicasting is seen as a major new application, utilizing the return channel to register for downloads to be delivered off peak. One specific application is for the distribution and upgrading of licensed software (including patches, upgrades, free trials). Such a facility provides a more cost effective method

of keeping software up to date, than continuous manual distribution on media such as floppy disks, CD or DVD.

2.5.7 Video Conferencing

Video Conferencing employs data compression techniques in order to enable real-time two-way multi-user video and audio connections over bandwidth limited channels. Broadband satellite access supports enhanced quality images and sound. A suitable minimum data rate for commercially acceptable quality video conferencing is 384 kbit/s duplex.

2.5.8 Distance Learning

Distance learning facilitates access to educational resources remotely from businesses or direct to the home. There is huge potential for universities and further education classes that wish to increase student numbers, by attracting those that would be otherwise unable to attend classes (i.e. those employed, with children, disabled, isolated). DTH return channel satellite systems will be an ideal platform for providing affordable broadband digital video broadcast and network access, providing students with access to supplementary material or software during a class [Yoshida and Kimura, 1999]. An email window on the receive end allows students to ask questions or submit course work.

Many universities [Little, 1998, Harris, 1999] in the US already employ distance learning through the Hughes DirecTV Ku-band satellite system. DirecTV is readily available in millions of homes for TV and internet access.

2.6 Fade Mitigation Techniques

In order to ensure an acceptable quality of service (QOS) to end users of the system, adaptive fade mitigation techniques (FMT) are necessary to improve link performance. Various techniques have already been proposed and are the subject of a major new study in which the author has participated [COST280]. FMTs have been divided into three complementary classes [Allnutt and Haidara, 2000, Castanet, et al., 2002]:

(1) Power Control – varying the EIRP of the signal to enhance E_b/N_0 (uplink power control, downlink power control or on-board antenna beam shaping);

(2) Signal Processing – changing the parameters of the signal to improve BER (adaptive processing, adaptive modulation or coding scheme);

(3) Diversity – fading is avoided by use of another less impaired link (site, frequency, or time diversity).

2.6.1 Power Control

2.6.1.1 Uplink Power Control

If an earth station is equipped with uplink power control (ULPC), the effect of a reduction in received power at the satellite due to fading, may be compensated by an increase in the uplink EIRP. The objective is to maintain a constant power level at the satellite transponder input, thereby retaining each carriers original allocation of downlink power onboard transparent transponder satellites. ULPC can be implemented open loop or closed loop and with detection and control at remote terminals, onboard the satellite or at the main control centre.

Beacon Measurements. Monitoring a satellite beacon provides the most accurate indication of varying downlink attenuation. At the earth station, short term frequency scaling [Gremont and Filip, 1999] is necessary to translate downlink measurements into attenuation predictions on the uplink frequency, and adjusting transmitter power accordingly. An additional earth station beacon receiver is required, with a measurement accuracy of at least 1 dB, significantly increasing the cost per unit of VSAT equipment. Errors due to frequency translation dictate that the downlink beacon frequency should be as close as possible to the uplink frequency. Frequency scaling over 10GHz as required in a V-band system (50GHz uplink, 40 GHz downlink) may not be sufficiently accurate, as found during experiments on 20/30 GHz systems [Baptista Poiares and Salonen, 1997, Allnutt and Haidara, 2000].

Closed loop approaches to ULPC require that the uplink power (or signal characteristics) be measured onboard the satellite and the resultant information transmitted to the earth terminal in a control channel for subsequent action by the ULPC unit. In a V-band implementation this may imply a more robust lower frequency (C or Ku-band) and low data rate control channel which is less susceptible to fading than the 40 GHz downlink allocation.

[Gremont, et al., 1996, Castanet, et al., 2002] have investigated models which predict short term fluctuations in uplink attenuations, based on downlink beacon measurements, allowing earth stations to apply fade countermeasures in real-time.

Signal Measurements. Measurement of the downlink digital stream, i.e. measuring E_b/N_0 or BER, may be used to infer the equivalent fade on the uplink. This requires two translations, one from E_b/N_0 or BER, to downlink attenuation and a second from downlink attenuation to uplink attenuation. When FEC is used, a small change in signal power (E_b/N_0) can produce a very large increase in BER, reducing the ULPC function to that of an ON/OFF type for example see Figure 2.6-1.

Large satellite ground stations use ULPC, usually based on information telemetered from the satellite concerning the received uplink power. Commercial DTH VSAT systems with transmit capability have the ability to automatically control uplink power from around 0.5W to 2W [ETSI, DVB-RCS]. This is about the limit for small terminals without replacing inexpensive SSPAs with more powerful TWTAs, or exceeding frequency coordination constraints.

2.6.1.2 Downlink Power Control

If only one carrier accesses the satellite transponder, the downlink EIRP may be held constant for a range of uplink signal powers by the transponder automatic gain control (AGC). If operating multiple carriers per transponder, then the transponder AGC will not compensate for a fade on only one of the uplinks.

2.6.2 Signal Processing

2.6.2.1 Adaptive Modulation

Efficient modulation schemes such as 16PSK, 64PSK and 256QAM allow the transmission of high data rates without increasing bandwidth. However, increasing the modulation order results in an increased E_b/N_0 threshold for the same BER performance. This may be achievable at low frequencies and during clear-sky conditions, but will the link budget required to meet this will be difficult at Ka-band or V-band, especially in the presence of cloud and rain.

Adaptive modulation allows the modulation order to be optimized to channel conditions. More robust schemes such as QPSK or BPSK reduce the E_b/N_0 requirements during non clear-sky conditions. Since reduced modulation order corresponds to reduced data rate throughput, high data rate transmissions will be delayed if no spare capacity exists.

2.6.2.2 Adaptive Coding

Improvements in Bit Error Ratio (BER) during fading are achieved by introducing redundant bits in to the data packet, in order to detect and correct errors. Adding forward error correction (FEC) coding increases the bandwidth for the transmission but reduces the energy per information bit, E_b/N_0 required to achieve the same BER. If the final output BER from the decoder is achieved with a lower value E_b/N_0 than for the same BER without coding then the reduction is called coding gain, as shown in Figure 2.6-1.

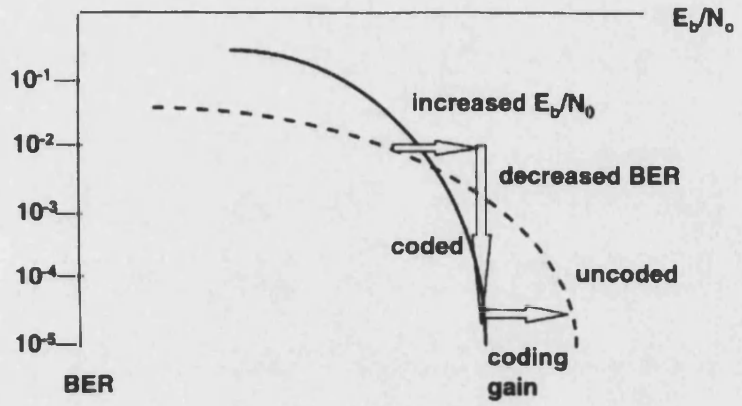

Figure 2.6-1 Effect of Forward Error Correction [Saunders, 1998]

The most common FEC scheme used in DVB-S satellite communications is a robust concatenation of a Reed-Solomon (RS) block code and a convolutional code. The RS outer code (applied first, removed last) is efficient at correcting burst errors whereas the convolutional inner code (applied last, removed first) corrects random errors.

Adaptive coding implements variable coding rates in order to compromise between bandwidth and BER to match fading on channels. In the concatenated scheme mentioned above, the coding rate can be reduced by omitting the outer code or reducing the inner coding rate. Table 4 shows a comparison between the E_b/N_0 performance at the decoder for a BER of 2×10^{-4} for different inner coding rates, including RS(204,188) and modem implementation margin.

Table 2-2 Required E_b/N_0 (dB) for BER of 2×10^{-4} [ETSI, EN 300 421]

Inner Code rate	½	2/3	3/4	5/6	7/8
E_b/N_0	4.5	5.0	5.5	6.0	6.4

Turbo Codes

Turbo codes offer bandwidth efficient coding with very low E_b/N_0 for a given BER. Uncoded QPSK with K=2 bit/symbol requires an E_b/N_0 of 9.6 dB for a BER of 10×10^{-5}. A rate ½ convolutional rate code with a soft-decision Viterbi decoder, achieves an E_b/N_0 of 4.2 dB for the same BER. In comparison, [Sklar, 1997] reports a turbo code which requires an E_b/N_0 of 0.7 dB for at BER of 10×10^{-5}.

A turbo encoder (Figure 2.6-2) consists of two recursive convolutional encoders separated by an interleaver with an optional puncturing mechanism. The input bits feed the first encoder and after having been scrambled by the interleaver enter the second encoder. The codeword of the parallel concatenated code consists of the information bits followed by the parity check bits of both encoders.

The two encoders are not necessarily identical, but two recursive systematic convolutional (RSC) codes achieve the best performance. Soft-decision decoding is performed on each systematic code. The output of the first decoder feeds into the second decoder to form one turbo decoder iteration. Each iteration improves the coding gain but requires more memory and decoder hardware complexity. A simple soft-output MAP (*maximum a posteriori*) decoding algorithm has been proposed to find the most likely information bit to have been transmitted in the coded sequence.

The efficiency savings through reduced bandwidth and power requirements have already become attractive to commercial Ku-band service providers, whose transponder lease tariffs are calculated taking into account the terminal uplink EIRP, modulation and coding scheme. Lease tariffs are encouraging Turbo coding and ensuring it is slowly becoming standard on all Ku-band point to point FDMA accesses.

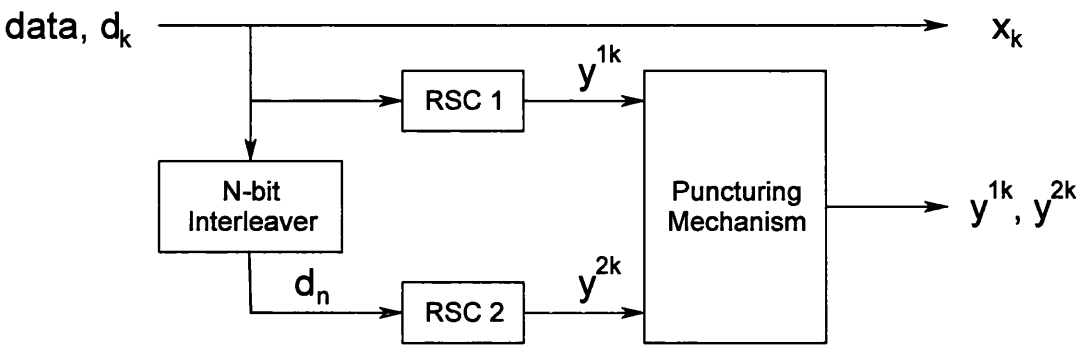

Figure 2.6-2 Turbo Encoder block diagram [Sklar, 1997]

2.6.3 Diversity

2.6.3.1 Site Diversity

Site diversity exploits two or more geographically dispersed earth stations, to establish more than one propagation path to the satellite. Since heavy rain typically occurs in geographically small cells with horizontal dimensions of a few kilometres, link availability may be maintained by switching transmissions to sites outside the rain cell. The probability of rain affecting both sites simultaneously reduces with station separation.

Site diversity is only applicable to major satellite earth stations, since DTH terminals are fixed at a single location. Duplication of major earth station facilities is complex and costly, but the advantage in preserving high availability satellite downlinks (by maintaining the uplink on the outbound link) is worth the expense [Rogers, 2000]. The implementation of site diversity also has the advantage of removing single points of failure from the satellite network.

The performance of site diversity can be calculated by evaluating the diversity gain and the diversity improvement factor using [ITU-R, P618-6]. Diversity gain is the difference (dB) between the single-site and diversity attenuation values for the same time percentage. Diversity improvement factor is the ratio of single-site time percentage and the diversity time percentage, at the same attenuation level. Site diversity calculations in [ITU-R, P618-6] are only recommended for frequencies between 10 and 30 GHz and at availabilities higher than 99.9%, such as that for V-band systems. At time percentages below 99.9%, the availability is generally not dependant on rainfall rate and the corresponding diversity improvement is not significant.

Studies by [Hodge, 1978, 1982] observe that diversity gain increases rapidly with increasing site separation until the separation exceeds 10 to 15km, after which benefits from further increases become small. Beyond this separation simultaneous rain events at two sites can be considered uncorrelated, since the probability of a single rain event affecting both sites is minimal.

2.6.3.2 Frequency Diversity

Frequency diversity [Carassa and Tartara, 1988] is applicable when in a satellite system, each link can operate in a high frequency band (Ka or V-band) as well as in lower frequency bands (C or Ku-band). The majority of traffic is carried in the high frequency band, until margin on a particular link becomes insufficient to maintain the BER, so the link is switched on to lower frequency carriers.

The amount of traffic which can be restored using frequency diversity is limited by the available capacity in the lower frequency band. A design decision is needed on the percentage of total traffic which is to be supported at the lower frequency, likely at a reduced data rate and QoS, in order to size the system and to provide a minimum service level guarantee. The lower frequency band can be used for pre-emptible low priority and low cost traffic, which can be removed if the spectrum is required as back to the higher frequency traffic.

Figure 2.6-3 illustrates the cumulative annual probability of outage on an earth station (Cambourne, UK) to satellite (longitude of 13.2°E) link, for frequencies in the range 12 to 50 GHz, using the KAW propagation model described in section 3.6. The graph shows that for an outage probability due to atmospheric attenuation better than 0.1% at 50 GHz, impractical power margins are required. However, the same outage probability can be achieved at 12 GHz using a more practical power margin of around 2-3 dB. The diversity gain in this case would be around 20dB.

Figure 2.6-3 is also a good illustration of how fixed power margins become impractical at high frequencies. It is in such conditions that adaptive countermeasures become not just useful but essential.

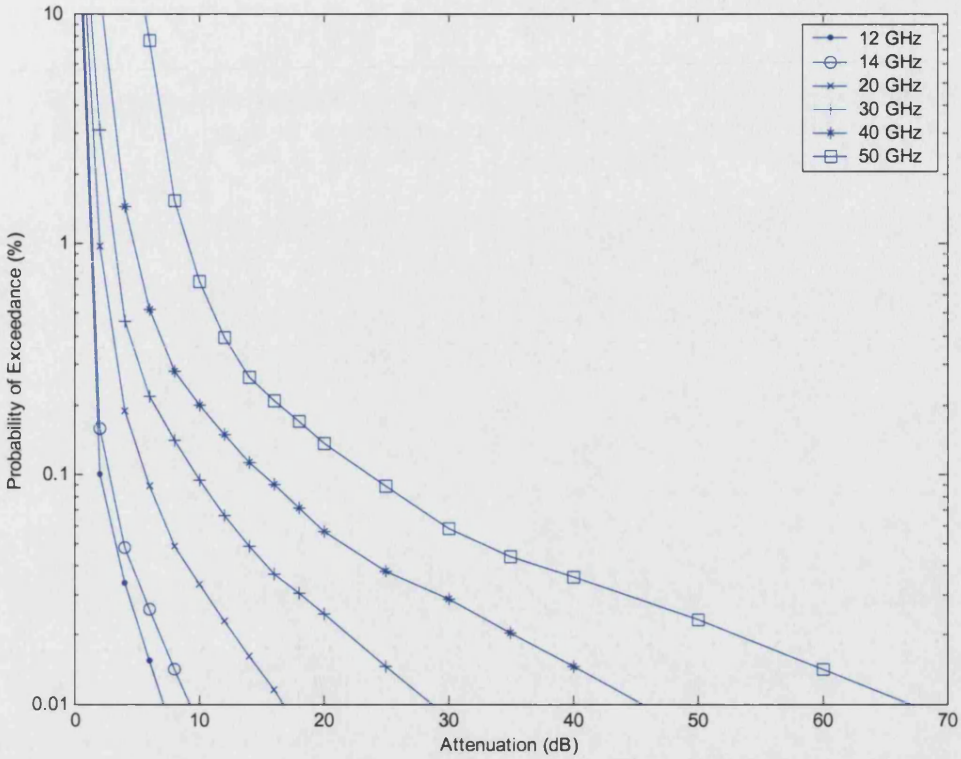

Figure 2.6-3 Cumulative annual attenuation distributions in the 12-50 GHz frequency bands, earth station at Cambourne (50.13°N, 5.59°W), 13.2°E GEO satellite.

2.6.3.3 Time Diversity

Time Diversity can be implemented by adapting the traffic delivery in time, in order to preclude disruption to the service [Fukuchi, et al., 2000]. Here it is possible to make use of low cost mass storage devices in remote terminal equipment, which can cache large amounts of data for playback when the link is unavailable. Such a technique will be invaluable in the V-band, high data rate low availability environment, although it is unsuitable for real-time interactive traffic, where such delays would be intolerable. Time diversity is suited to delivery of digital broadcasts such as TV programmes and cached web content.

2.7 Satellite Broadcast Technology & Systems

The majority of present day geostationary satellites act as passive repeaters of RF transmissions received from earth. From an uplink location, a signal is retransmitted through the satellite amplification system to the chosen downlink footprint. These footprints can encompass entire continents or areas as small as individual countries. Apart from amplification and frequency shifting, no modifications are made to the signals flowing through the satellite.

New satellite technology is being developed which is better suited to higher operating frequencies and packet based traffic. This includes efficient multiple-access techniques (such as MF-TDMA), and more robust protocol and modulation schemes based on commercial standards developed for the DTH market. The following sections describe some of the technology being developed or already in use, which is suitable for consideration in the design of a V-band multimedia satellite systems.

2.8 Onboard Processing

Onboard processing (OBP) provides greatly improved performance and efficiency over transparently transponded satellite systems. It can be used advantageously in four places in a communications satellite :

(1) Intermediate Frequency (IF) and Radio Frequency (RF) communications switching;

(2) Support processing;

(3) Phased array antenna control and beam forming;

(4) Baseband processing and switching.

IF and RF switching is generally the simplest, requiring the least amount of processing power. It involves electronically controlled RF/IF switches, usually in matrix format that can be controlled statically or dynamically and has been used for some time to route communications traffic between downlink beams.

Support processing has traditionally been associated with control of the satellite bus and includes such functions as attitude control, power management and telemetry and tracking and control. These functions can be handled by onboard computer systems.

Phased array antennas forming many independently steerable spot beams require a large number of radiating elements with individual phase (and amplitude) control for each beam. The control signal can be implemented with analogue circuits (for a small number of beams) or digitally. Digital implementation requires substantial digital processing, probably more than with the baseband processing and switching system. Phased array antennas are already in use, mainly in military satellite systems, due to the their ability to provide discrimination between legitimate and illegitimate terminals and the very high cost of implementation.

Baseband processing especially regeneration and switching involves functions similar to those performed in terrestrial local area networks and telephone switches. In addition demodulation, de-multiplexing, error detection and correction, switching, congestion control and notification, buffering, re-multiplexing, re-modulation and network synchronization may be performed. Most of these functions require specialized processors in order to be size/mass/power efficient. Baseband switching is particularly appropriate for packet switched systems with a large number of earth stations.

2.8.1 Regeneration

A regenerative payload implies onboard demodulation of the uplink carriers. The bit stream is then used to modulate a new carrier at the downlink frequency. Since the demodulation/ modulation process decouples the up/down links, noise from the uplink does not appear on the downlink, improving overall link quality. Hence, uplink and downlink power can be optimised for each link separately, leading to reduced uplink EIRP and smaller earth stations. For digital transmissions using error correction coding, onboard decoding / encoding corrects uplink errors, reducing the number of uncorrectable bits at the downlink receiver.

Intermodulation noise can be avoided by combining several carriers onboard into a single high data rate downlink carrier (TDM). As the transmitter amplifier is no longer required to operate in multi-carrier mode, it can be operated at saturation and hence maximum power efficiency [Wittig, et al., 1994].

2.8.1.1 SKYPLEX

SKYPLEX [EUROSKYWAY] is an onboard processor developed by Alenia Aerospazio[6] which combines several digital TV uplinks onboard the satellite, to form a single broadcast downlink. Traditionally, digital TV programs from different sources have been multiplexed at a single earth station before being uplinked to the satellite. SKYPLEX allows each service provider to access the satellite directly through a low cost uplink station, located at their own premises.

The first SKYPLEX transponder was operational on the Eutelsat Hotbird 4 satellite (spring 1998) with an enhanced version on Hotbird 5 (Oct. 1998) [SpaceDaily, 1998]. Each Hotbird 4 transponder (33 MHz) can accommodate 6 uplink channels with a data rate of 6 Mbit/s. A SKYPLEX processor regenerates and multiplexes these into a 40 Mbit/s TDM downlink [Elia and Colzi, 1996]. The use of ETSI DVB-S modulation and coding standards for the downlink, ensures DTH receivers are not able to distinguish between programmes broadcast via conventional DVB-S networks and those processed by the SKYPLEX multiplexer.

Figure 2.8-1 shows the functional block diagram of the SKYPLEX system. In order to reduce the complexity of the receiver and onboard technology, the outer Reed-Solomon encoding takes place on the ground. Onboard the separate carriers are extracted, demodulated, decoded and multiplexed, then re-encoded according to the DVB-S standard. The master control station coordinates the assignment of the transmission frequency and time slots to the uplink stations.

Although initially designed for TV broadcasting, the inherent ability of MPEG-2 transport stream packets to encapsulate higher layer protocols (IP, ATM, etc.), has enabled audio & data to be supported. The SKYPLEX payload onboard Hotbird 5 accommodates up to 18 uplinks with data rates down to 1 Mbit/s. Satellite bandwidth can be booked dynamically through the master control station given 20-60 minutes advance notice. Advanced SkyPlex processors form the basis of the SKYPLEXNET system [Dorides and Tomasicchio, 1999] which was launched commercially in 2001.

[6] http://www.alespazio.it

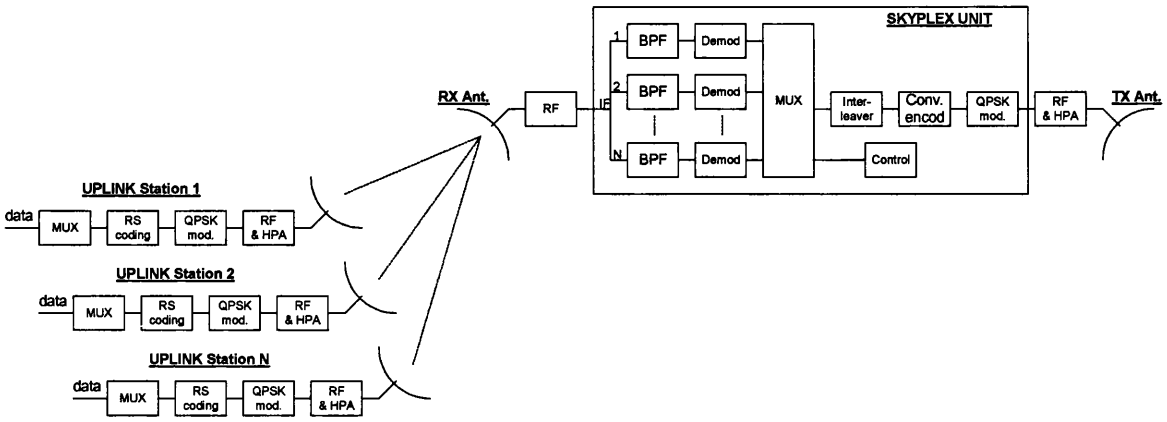

Figure 2.8-1 SkyPlex system functional block diagram [Elia and Colzi, 1996]

2.8.1.2 STENTOR

The STENTOR technology demonstrator satellite has been developed by a consortium of French space companies and was to be launched in late 2002. It was to space qualify several advanced satellite and communications technologies. These include an onboard multiplexer for digital TV signals, similar to the SKYPLEX system, called the DVB PROCESSOR [Duverdier, et al., 1999]. After a launch failure, it is unknown at this time whether the STENTOR spacecraft will be replaced.

The DVB PROCESSOR can receive up to 12 separate bit streams, containing up to 4 programs (overall limit of 41) accessed by FDMA/SCPC. Uplink bit rates vary from 1.1Mbit/s to 7.6Mbit/s depending on data and convolutional coding rate. The MPEG-2 packets are demultiplexed, decoded then remultiplexed and coded into a 38 Mbit/s (information rate) TDM downlink (according to DVB-S standards). Only one convolutional coding rate of 3/4 has been chosen for the downlink (for operation at Ku-band).

2.8.2 Switching

The efficiency and performance of multiple spot beam systems can be greatly improved by interbeam connectivity. Onboard switching allows earth terminals to connect directly to terminals in any satellite beams. Previously, the traffic would have to be routed back to the hub for retransmission on a channel corresponding to the required downlink beam. This introduces a 4 hop propagation delay of around 500ms. Using onboard switching the propagation delay is reduced to 2 hops (~250ms).

Interbeam connectivity can be based on circuit or fast packet switch architectures depending on the target user location. If users are geographically dispersed, an analogue circuit switch requires the ground network to centralise traffic at a single uplink terminal, where it can be multiplexed for efficient bandwidth usage [Bever, et al., 1999]. The circuit switching function is similar to that performed in telephone exchanges (i.e. ISDN type). ATM is well-suited to circuit switching, as it requires a connection (virtual path) to be established in order to guarantee QOS (quality of service) [Gilderson and Cherkaoui, 1997].

Fast packet switches do not require a centralized uplink for efficient downlink bandwidth usage, as the payload interprets the data and discards empty slots and packets (statistical multiplexing). Increased uplink efficiency is obtained by demand-assigned multiple access (DAMA) protocols. Packet switching is suited to bursty connectionless protocols such as IP, in which all address and data information is included in the packet, although IP address tables (e.g. DNS look up tables) must be maintained onboard or at the hub.

Throughput analysis for different types of switches is described in [Bever, et al., 1999]. The conclusion is that bent pipe and circuit switch architectures are ideally suited to broadband services such as TV, but do not efficiently transport multimedia applications from a large number of users. Cell switching maintains the highest throughput bit rate for different applications (video, voice, www) and can take advantage of statistical multiplexing to maximize bandwidth. OBP will become more common in satellite architectures, but it comes at the cost of added complexity, risk and price.

2.9 Satellite Antenna

2.9.1 Multi-beam Antenna

Early satellite systems were used to distribute signals over a large geographic area with low effective isotropic radiated power (EIRP) towards the earth. This led to the requirement for large and powerful earth stations. More recently, the trend towards DTH service reception has led to a demand for geostationary satellites providing higher EIRP and G/T in order to accommodate smaller cheaper earth terminals.

As frequency increases the beamwidth for a given antenna decreases. A reduction in satellite antenna beamwidth increases gain and therefore, EIRP at the expense of coverage. Therefore, many more spot beams are needed in order to cover the same area as those operating at a

lower frequency. As long as the beams do not overlap or touch, the frequency allocated to a spot beam can be reused, increasing the total capacity of the network without additional bandwidth.

Frequency reuse can also be achieved within each beam using two carriers with orthogonal polarisations (i.e. horizontal/vertical, RHCP/LHCP). In multi-beam systems the isolation due to the diversity of downlink spot beams can also be exploited, allowing the same frequency to be reused in another beam. Another advantage of multi-beam systems comes from using onboard switching described in 2.8.2.

A multi-spot beam coverage pattern has been proposed for the SECOMS (Satellite EHF Communications Multimedia Services) project [Losquadro, 1997, Losquadro and Schena, 1999], using 64 spots in the EHF (Figure 2.9-1). [Luglio, et al., 1998] proposes a method for setting the downlink power of each beam, according to long term predictions of atmospheric attenuation for the region. Further enhancements suggested by [Dissnayake, et al., 2000] to include instantaneous power control based on Meteosat weather images.

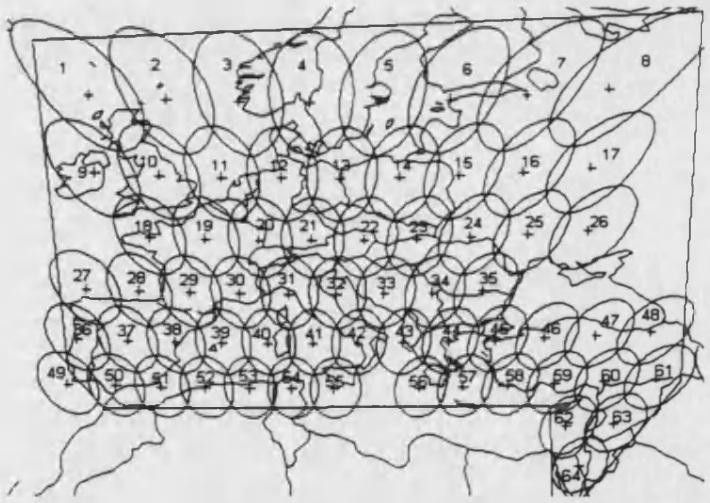

Figure 2.9-1 SECOMS EHF Spot Beam Coverage [Losquadro, 1997, Losquadro and Schena, 1999]

2.9.2 Shaped Reflector Antenna

Further optimisation in satellite power can be achieved by shaping the downlink beam to areas of land or population. Downlink beams may also be shaped to compensate for long-term climatic conditions on the ground. Before the development of shaped reflector antennas, engineers modified the transmitted downlink beam by the arrangement of feed horns. These

feed horns had to be excited in proper phase and amplitude by complex beam forming network, adding mass and therefore, extra launch cost [Rosen, 2000].

The surface of shaped reflectors is mechanically formed (see Figure 2.9-2) to generate a contoured beam coverage from a single horn. Removing horn arrays and beam forming networks reduces weight, signal losses and improves effective radiated power. For fixed contoured beams, this approach is extremely attractive, combining mechanical simplicity with a high level of RF performance [Stirland, et al., 2000]. Coverage optimisation requires the use of accurate long term coverage prediction patterns such as those given in 0.

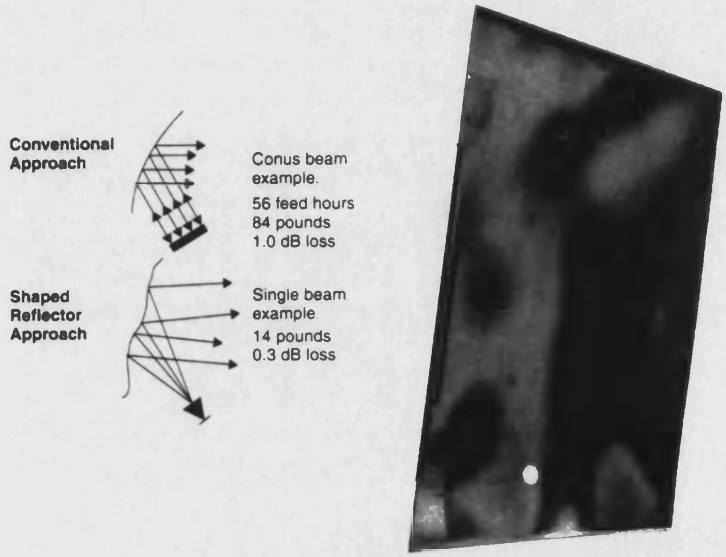

Figure 2.9-2 Shaped Reflector Antenna [Saunders, 1998]

2.9.3 Active Phased Array Antenna

A Direct Radiating Array (DRA) is composed of a large number of individually fed radiating elements or subarrays. These subarrays could be dipoles, waveguide slots, horns or microstrip patches depending on the application, frequency band and polarisation. In an active phased array the reflector and its feed array are most often replaced by a DRA of size comparable to that of the original parabolic reflector [Lisi, 2000]. A phased array is named "active" when each subarray is individually connected to controllable receive (Low Noise Amplifiers, LNA) or transmit (power amplifier) modules.

Active antennas provide reconfigurable beams and generation of overlapping spot or contoured beams with high aperture efficiency [Stirland, et al., 2000]. Beam forming is

controlled electronically by altering the amplitude and phase of each element. Introducing onboard signal processing for digital beamforming allows beams to be dynamically configured (steered, shaped, interference rejection, nulling, etc.) to take account of traffic routing or atmospheric conditions over regional areas.

ESA are developing imaging phased arrays (IPA) in which small active arrays are magnified by a single or double reflector optic [Lisi, 2000]. Using additional sub-reflectors increases aperture efficiency and reduces the size and weight of the feed array. In the long term it is likely that active antennas will become established at Ku, Ka and higher frequency bands. At these frequencies the IPA offers an attractive multi-beam solution.

2.10 Power Amplifiers

The main element of a satellite payload is the transmitter, consisting of a power amplifier and its power supply. The amplifier provides the power at the output of each channel and combined with the antenna gain determines the Effective Isotropic Radiated Power (EIRP).

Ideally, amplifiers are operated close to saturation in order to attain high efficiency, converting DC energy from the solar arrays in to RF power. Operating in the amplifier non-linear region, with a number of carrier frequencies within the same transponder produces inter-modulation products which degrade the signal to noise ratio of the signal. In practice, TWTA's are operated 'backed-off' as a compromise between efficiency and noise. Two types of transmitters are used in commercial satellites, Travelling Wave Tube Amplifiers (TWTAs) and Solid State Power Amplifiers (SSPAs).

2.10.1.1 TWTA's

TWTA's are the most commonly used transmitters on commercial and military satellites. They are advantageous for multimedia systems because they offer high RF power and broadband amplification, while minimising the power consumption due to their excellent efficiency.

Efficiency is defined as the ratio of RF output power to direct current (DC) electric power consumed [Maral and Bousquet, 1998]. The difference is dissipated in the form of heat. High efficiency leads to a reduction in the electrical power requirements reducing mass.

Another requirement for high quality data transmission is good linearity. TWTA non-linearity may be compensated with a pre-distortion linearizer. This device drives the TWTA and

generates non-linearities inverse of those of the TWTA so that the whole chain is highly linear [Andre, et al., 1999]. The amount of back off required is reduced and this results in better efficiency. Linearizes also compensate for temperature and the effect of aging. It is estimated approximately 40% of present systems use linearised as opposed to non-linearised[7] TWTAs .

2.10.1.2 TWTA Market

The worldwide TWTA market (including commercial and military ground and space applications) is in the order of $500 million [ITRI, 1998]. There are three main manufacturers of space qualified TWTAs in the world, AEG/Thompson Tubes, NEC and Hughes Electron Dynamics Division. Hughes specialises in the development of C-band and Ku-band tubes, whereas Thompson has tended towards Ka-band. NEC is a smaller manufacturer and makes TWTAs in S-band to V-band and their tubes have flown mostly on Japanese programs. All manufacture varying RF output power levels for ground and space based applications, nominally with a lifetime in excess of 15 years.

Table 2-3 gives the performance of current TWTAs. Both Thompson and Hughes are developing 60 GHz TWTAs for broadband multimedia applications (5 GHz bandwidth). Output power is expected to be 20-40 W, with an efficiency of 30-35% using a helix system [ITRI, 1998]. While a comb design (see [ITRI, 1998]) can deliver 60-100 W, 25% efficiency requiring several comb tubes to cover the 5 GHz bandwidth.

Table 2-3 TWTA Performance

Frequency Band	RF O/P Power (W)	Comments
S-band	50-150	
C-band	15-150	
Ku-band	15-150	Growth to 200W
Ka-band	20-100	Growth to 150W
V-band	35	~41% Efficient

2.10.1.3 SSPA's

Solid state power amplifiers use cascaded Field Effect Transistors (FETs). The available power and operating frequency are continually increasing as technology progresses.

[7] http://complextoreal.com

C-band SSPAs can deliver upto 400W, but they are unable to match the efficiencies of TWTs and are more commonly used at low power (<20W).

The improved linearity of SSPAs compared with tube amplifiers increases their useful capacity for multi-carrier operations owing to improved inter-modulation performance. Also, their robust and reliable design makes them ideal for DTH VSAT's, in which cost is a major factor. Typical VSAT output powers are in the range of 1-3W, although this is usually limited by frequency coordination constraints rather than technological issues.

The growing use of phased array antennas is leading to satellites with large numbers of low power SSPAs. An example, the STENTOR payload carries antenna array consisting of 48 elements, each fed by its own SSPA.

2.11 MF-TDMA

Multi-Frequency TDMA [Ohlson and Huff, 1983, Davies, et al., 1986] has been developed specifically for applications in which large numbers of geographically dispersed VSATs need to access satellite resources. MF-TDMA consists of a hybrid FDMA/TDMA scheme, whereby each VSAT can transmit bursts of data in a combination of orthogonal time and frequency slots. The scheme offers efficient over-the-air access to satellite resources and reduced VSAT complexity and cost, through the use low data rate TDMA carriers (typically up to 2Mbit/s [Ananasso, et al., 1992]).

In commercial single carrier MF-TDMA systems, each ground terminal contends for access to a dedicated slot within the frame (or on a separate carrier), to request a number of data slots from the Master Control Station (MCS). Subject to priority and traffic loading the MCS allocates a number of data bursts within the orthogonal grid and informs the remote terminals by broadcasting access tables on the outbound link [ETSI, EN300421]. Each remote terminal bursts into an allocated slot, and this may involve hopping to different frequency carriers with the orthogonal grid to make full use of available capacity, as shown in Figure 2.11-1. This technique allows flexible and efficient allocation of capacity with reduced uplink blockage.

In a TDMA system, after accessing a time slot, the remote terminal must withhold from transmitting until the next allocated slot in the frame. In order to achieve the same aggregate data throughput as MF-TDMA, a single carrier TDMA system must operate at a higher burst rate, leading to increased EIRP from the remote terminal.

MF-TDMA is employed in the ASTRA Return Channel System at Ka-band using a transparent transponder payload. ESA[8] have funded the development of an onboard Multi-Carrier Demodulator (MCD), enabling satellite multiplexing of MF-TDMA uplinks into a single efficient TDM downlink. This technology was to be demonstrated on the payload of the STENTOR experimental satellite (but unfortunately suffered a launch failure)..

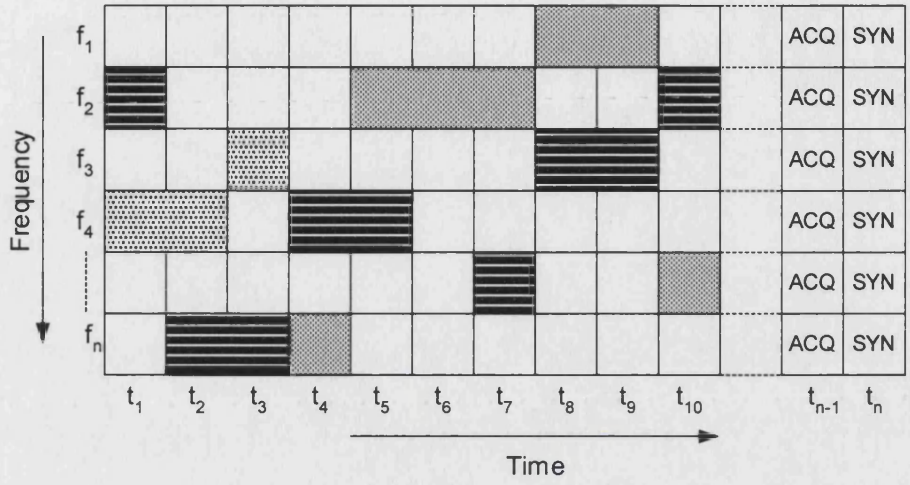

Figure 2.11-1 MF-TDMA frame structure

2.11.1 Power Requirements

In TDMA systems, the satellite transponder downlink power margin is designed to accommodate the least tolerant remote terminal. This can reduce the efficiency of the network which contains terminals of different sizes and fade margins. Individual MF-TDMA channel powers can be matched to the requirements of earth terminals. For example, terminals experiencing fading can be allocated slots on a higher power carrier to maintain its link margin. Alternatively, large terminals can use lower power channels to reduce the link margin and increase utilization of transponder power. The advantages of frequency diversity can also be exploited, depending on the hop bandwidth of the remote terminals.

[8] European Space Agency, http://telecom.estec.esa.nl

2.11.2 Synchronization

In order to utilize high frame efficiency with short data bursts and to control access to the separate TDMA carriers, synchronization of the system is essential. This is achieved by transmitting a stable clock reference (from onboard the spacecraft or from the Main Control Station(MCS)) on all downlink spot beams, to which all remote terminals constantly adjust their clocks to remain fully synchronised at all times. This eliminates the need for inter-burst guard-times, bit synchronization and unique word portions of traditional TDMA preambles.

2.11.3 Intermodulation

As MF-TDMA operates several channels in the transponder, output backoff is required to avoid intermodulation interference due to amplifier non-linearity. Typical output backoff is in the range 3-6 dB [Ohlson and Huff, 1983]. Two recent developments have reduced the significance of the backoff requirements. SSPA's with a more linear characteristics permit operation closer to saturation. Robust error correction techniques, e.g. Reed Solomon and Turbo codes produce acceptable link performance at higher levels of intermodulation interference.

2.11.4 Medium Access Control

The slot assignment in a MF-TDMA scheme has a significant effect on system performance. In order to efficiently share bandwidth between a large number of terminals a Medium Access Control (MAC) protocol layer is needed [Hung, et al., 1996]. The MAC layer determines how the terminals request capacity and its selection strongly depends on the nature of the traffic.

A slot allocation algorithm determines slots the number of slots available to each terminal, while a slot assignment algorithm resolves which of the time and frequency slots in the frame are assigned to each remote terminal. All slots are reallocated and reassigned every superframe [Shvodian, 1998], as this simplifies algorithms and ensures regular synchronisation of remote terminals.

2.11.5 Acquisition

The initial request by remote terminals for slots takes place on a separate acquisition carrier [Ananasso, et al., 1990] or through slots in the uplink frame assigned for signaling and synchronization (as illustrated in Figure 2.11-1) [Gilderson and Cherkaoui, 1997]. The ETSI Return Channel Standard [ETSI, 1999] defines a contention scheme based on slotted Aloha. Each remote terminal contends for request slots by transmitting its individual MAC address and slot volume requirement. In the absence of an allocation of data slots from the MCS (in the form of tables multiplexed in the downlink) the terminal must assume a collision and retry after a random backoff. To minimize contention delays, remote terminals are assigned MAC addresses in groups at logon, thereby restricting the maximum number per group.

2.11.6 Allocation

MAC layer protocols can be categorized into four basic classes :

(1) *fixed assignment* – static allocation which is independent of the stations activity. This is highly inefficient for bursty traffic as slots are wasted when remote terminals have no information to transmit.

(2) *demand assignment (DAMA)* – allocates slots dynamically as requested. There are two basic types: fixed rate in which a fixed number of slots are allocated per frame for the duration of the connection. Variable rate DAMA allocates slots only when data is queued for transmission. Efficiency is increased using a reservation process which automatically reserves a slot in the following frame. This allows dynamic allocation of satellite power and bandwidth based on changing traffic loads [Peyravi, 1999].

(3) *random assignment* – involves no control, is simple to implement but can be wasteful of capacity due to collisions. Contention schemes include, Aloha, slotted Aloha and selective-reject Aloha.

(4) *hybrid random access & reservation* – e.g. Combined/Free DAMA (CFDAMA) [Le-Ngoc and Mohammed, 1993] first allocates slots on the basis of requests pending in its queue similar to a DAMA scheme. In the absence of such requests it freely assigns the remaining slots according to a defined strategy. One such strategy is hierarchical round robin by [Shvodian, 1998], which prioritizes allocation prioritises requests according to

traffic class (CBR, VBR, etc.). If there are more requests than available slots, slots are allocated in a round robin manor until no more remain.

2.11.7 Implementation

Using onboard processing (such as a multi-carrier demodulator (MCD)) hardware in the satellite payload isolates up and down links, allowing the uplink traffic to be remultiplexed onboard the satellite into an efficient TDM downlink. This type of regenerative payload leads to cheaper, higher performance VSATs due to link budget improvements. STENTOR will be the first satellite to space qualify MCD hardware, but already the majority of future Ka-band VSAT system designs, propose to use the technology, including: Spaceway, Astrolink, Cyberstar, Teledesic, Celestri, West and Euroskyway [Mertzanis, et al., 1999].

2.12 DVB-S

MPEG-2 [MPEG, 1994] defines the syntax of the digital video signal and does not define the other necessary features of satellite transmission such as coding, modulation and encryption. In Europe the Digital Video Broadcasting (DVB) project has produced specifications for digital broadcasting based on the MPEG-2 coding and multiplex system. The DVB for satellite (DVB-S) standard [ETSI, EN 300 421] describes a "satellite channel adapter" defining coding and modulation schemes (refer Figure 2.12-1).

Since satellite services are particularly affected by power limitations, the DVB-S scheme has been designed to protect against noise and interference rather than spectrum efficiency. It is based on a powerful forward error correction (FEC) scheme using a concatenation of convolutional and Reed-Solomon (RS) codes. This advanced scheme is designed to achieve a bit error ratio (BER) of 2×10^{-4} after Viterbi decoding, to meet a quasi-error free quality target set by DVB.

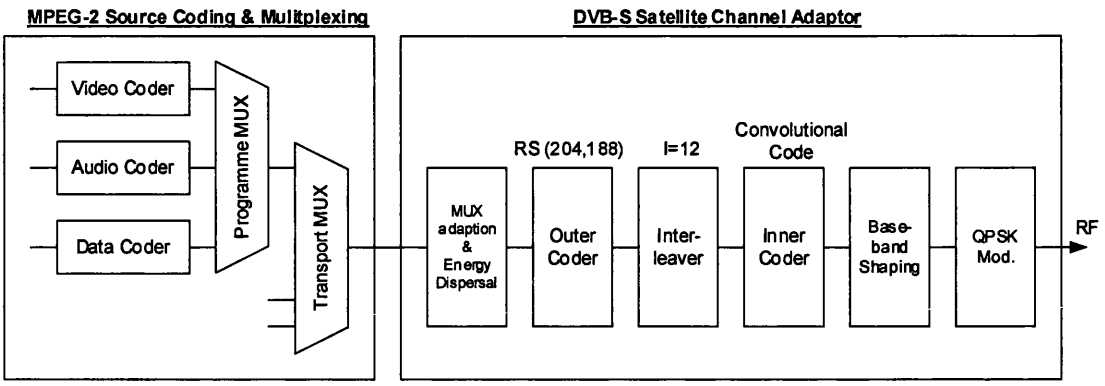

Figure 2.12-1 DVB-S Channel Coding & Modulation System [ETSI, EN 300 421]

2.12.1 MPEG Multiplex

DVB-S framing structure is based on the MPEG-2 transport stream multiplex. MPEG-2 transport stream (TS) packets encapsulate higher layer services (video, audio, data) and protocols (ATM, IP) into fixed length 188 byte packets. Each packet begins with a 1 byte synchronization word, 3 header bytes (including priority and packet identifier, PID) and 184 bytes of data (refer [ETSI, EN300421]). The 13 bit packet identifier descriptor references up to 2^{13} independent packets.

2.12.2 Energy Dispersal

In order to comply with ITU radio regulations and to ensure adequate binary transitions the TS packets are randomised to assist clock recovery at the receiver, and maintain a smooth modulated spectrum. The scrambling is performed by a Pseudo-Random Binary Sequence (PRBS) generator which multiples (modulo 2) the data stream.

2.12.3 Reed-Solomon Coding

A Reed-Solomon outer code is applied to the randomized transport packet. Each packet is appended with a checksum generated using two polynomial functions. The resulting coded block consists of K information symbols, R parity symbols and a code word consisting of $(K+R)$ symbols. $R/2$ symbols can be corrected, expressed as $RS(K+R,K,R/2)$. MPEG-2 TS packets use a RS(204,188,8) code, the additional 16 redundancy bytes provide the capability to detect and correct 8 bytes of errors in the 204 byte packet [Richharia, 1995]. RS codes are well suited to burst error correction but are inefficient in correcting random errors.

The DVB-S polynomial functions given are :

code generator polynomial : $g(x) = (x + \lambda^0)(x + \lambda^1)(x + \lambda^2)....(x + \lambda^{15})$, where $\lambda = 02_{HEX}$

field generator polynomial : $p(x) = x^8 + x^4 + x^3 + x^2 + 1$

2.12.4 Interleaving

In the DVB-S concatenated coding scheme, the errors at the output of the soft-decision Viterbi decoder at the receiver are grouped into bursts. To improve the burst error correcting capability of the RS code, convolutional interleaving (with depth I=12) is applied to the error protected packets.

2.12.5 Convolutional Coding

Unlike block codes which operate on each block independently, convolutional codes retain several previous bits in memory. Information bits are convolved with the impulse response of a shift register encoder. The number of shift register stages, *K* defines the constraint length of the code (typically *K*=7). For each information bit entered into the shift register *n* bits appear at the output, which are then transmitted sequentially (refer Figure 2.12-2). The convolutional coding rate can be adjusted (by puncturing) to operate at different rates according to service requirements. *1/n* represents the coding rate, typically 1/2 (50% added redundancy), 2/3, 3/4, 5/6 or 7/8. Increasing redundancy improves error correcting ability, but requires more satellite bandwidth.

The Viterbi algorithm is a cost effective decoding algorithm widely used in satellite communications. It estimates the path of the coded message by truncating the depth of search to typically 4-5 times the constraint length. Only those paths which give the least error counts are retained and others discarded, reducing the decoder complexity.

[ETSI, DVB-RCS] provides the punctured code definition (including convolutional coding rate, constraint length and generator polynomials) to ensure compatibility throughout DVB standard equipment.

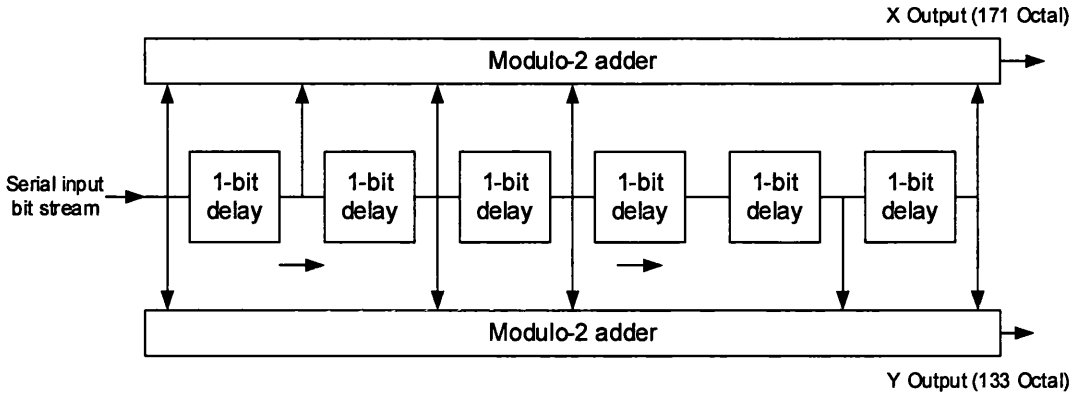

Figure 2.12-2 Convolutional Coder of Rate ½ [ETSI, DVB-RCS]

2.12.6 Modulation

Finally, in the DVB-S system the coded bits are mapped to a Gray coded QPSK constellation, and are filtered at baseband to generate a square-root raised cosine spectrum with a roll-off factor $\alpha = 0.35$. The roll-off factor determines the spectrum width after filtering.

2.12.7 Bit Rate vs. Transponder Bandwidth

DVB-S standards are flexible to allow the modulation, symbol rate and coding rate to optimise the satellite link performance (spectrum occupancy and power requirements). Typical digital DTH services broadcast from Ku-band satellites operate single carrier per transponder, with TDM (Time Division Multiplexing) to achieve maximum satellite power efficiency by operating the TWTA close to saturation [Cominettie, et al., 1995]. This requires all the data to be assembled at a single site to uplink to the satellite. Other applications such as satellite news gathering, in which the satellite is accessed from multiple locations, require multiple carriers per transponder. For this reason, multiple access schemes (FDMA, MF-TDMA) are allowed, which give better flexibility with reduced power and spectral efficiency.

In single carrier per transponder configurations, the transmission symbol rate R_s is matched to the transponder bandwidth BW to achieve maximum transmission rate. The BW/R_s ratio determines the symbol rate transmitted in the satellite transponder for any particular bandwidth. Decreasing BW/R_s increases the symbol rate and therefore available capacity. However decreasing BW/R_s also increases distortion due to inter symbol interference (ISI) caused by the satellite filters (IMUX and OMUX). Choosing the optimum BW/R_s ratio is a

compromise between acceptable E_b/N_0 degradation and useful symbol rate. Figure 2.12-3 has been taken from [Cominettie, et al., 1995] as an example of the E_b/N_0 degradation at a BER of 2×10^{-4} due to simulated transponder bandwidth limitations (combination of IMUX and OMUX filters). For multi-carrier operation, R_s can be matched to the frequency slot allocated by the frequency plan within the transponder, to optimise transmission capacity while maintaining acceptable interference levels.

Table 2-4 gives examples of useful bit rate capacity R_u achievable for different transponder bandwidths and coding rates, using a BW/R_s ratio of 1.35 (i.e. with negligible E_b/N_0 degradation), QPSK modulation and RS(204,188).

Table 2-4 DVB-S Bit Rates versus Transponder Bandwidth

BW	R_s	R_u	R_u	R_u	R_u	R_u
	BW/Rs	1/2 rate RS(204,188)	2/3 rate RS(204,188)	3/4 rate RS(204,188)	5/6 rate RS(204,188)	7/8 rate RS(204,188)
[MHz]	[Mbaud]	[Mbit/s]	[Mbit/s]	[Mbit/s]	[Mbit/s]	[Mbit/s]
72	53.3	49.1	60.3	73.7	81.9	86.0
54	40.0	36.9	45.3	55.3	61.4	64.5
33	24.4	22.5	30.0	33.7	37.5	26.0

where, $R_s = \frac{BW}{1+\alpha}$ for $\alpha = 0.35$ and $R_u = R_s \times \left[\frac{k}{n}\right]_{RS} \times \left[\frac{k}{n}\right]_{conv.} \times [2]_{QPSK\,(2bits\,/\,symbol)}$

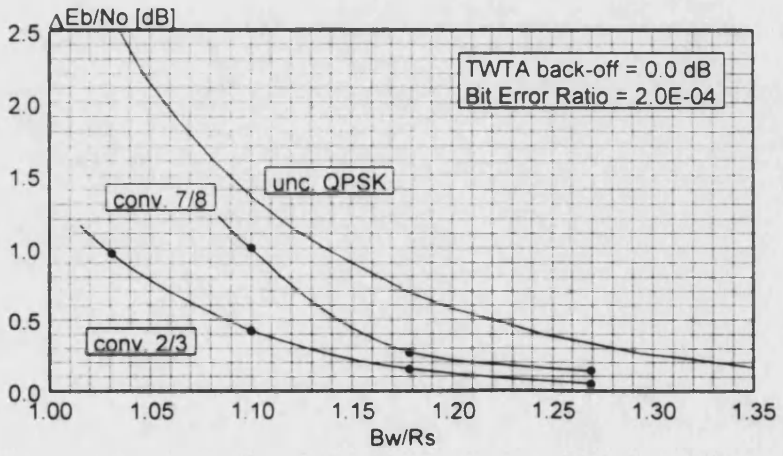

Figure 2.12-3 E_b/N_0 degradations due to transponder bandwidth limitations [ETSI, EN300421]

3 Long Term Propagation Prediction

3.1 Introduction

The V-band (40/50 GHz) propagation environment for satellite-earth links is markedly different to that experienced at lower frequencies. In particular the effects of clouds and light rain dominate link availability for systems with modest fade margins (say 10 to 15 dB). This is in contrast to 20/30 GHz and lower frequency bands where, in most climates, heavy rain occurrences would be the dominant factor in outage calculations for the same fade margins.

Evidently at V-band we must consider the contributions of widespread and showery rains, atmospheric gases (oxygen and water vapour), clouds and scintillation from atmospheric turbulence. These effects show pronounced climatic dependencies including, in some climates, strong seasonal effects. Also the effects are not independent and one must consider methods for their combination. A review of the basis for relevant propagation factors is given in the following chapter.

Availability is expressed as a percentage of time over which a link maintains a specified performance criteria (e.g. Carrier-to-Noise Density ratio, C/N_0). As availability reduces, the percentage of time the link exceeds the criteria increases proportionally. System designers refer to an unavailable link as an outage and often describe system performance by outage time over a year.

European commercial satellite multimedia systems, such as ARCS quote link availability of 99.5% for business users and 95% for residential customers for Ka-band users. The only available EHF specification, which is for the SECOMS (to be EUROSKYWAY system) aims for 99.8% across the whole of Europe [Luglio, et al., 1998].

3.2 Atmospheric Attenuation

At V-band we must consider the contributions of widespread and showery rain, atmospheric gases (oxygen & water vapour), clouds and scintillation from atmospheric turbulence. These effects are not independent and must be combined to evaluate total atmospheric attenuation. Figure 3.2-1 shows a cumulative graph of atmospheric attenuation for Stoneway in the UK (58.13N, 6.5W, 50 GHz, satellite longitude 19.2°E) for probabilities of time exceeded, using the model described in section 3.6.

Various possibilities exist for statistical combination of attenuation distributions [COST255]. The model described in section 3.6 uses the method of equi-probability summing, in which attenuation levels for equal probabilities are added, as given in Eqn. 3-1.

Eqn. 3-1 $$A_{tot}(P) = A_o(P) + A_{wv}(P) + A_c(P) + A_r(P) + A_{ml}(P)$$

where A_o, A_{wv}, A_c, A_r and A_{ml} are respectively the attenuation due to oxygen, water vapour, clouds, rain and the melting layer.

This method assumes that the different effects are fully correlated. In practice, two (or more) attenuation phenomena are not fully correlated and therefore equi-probability summing gives pessimistic values for low outage times. Thus, the equi-probability summing may be used for the worst case approximation.

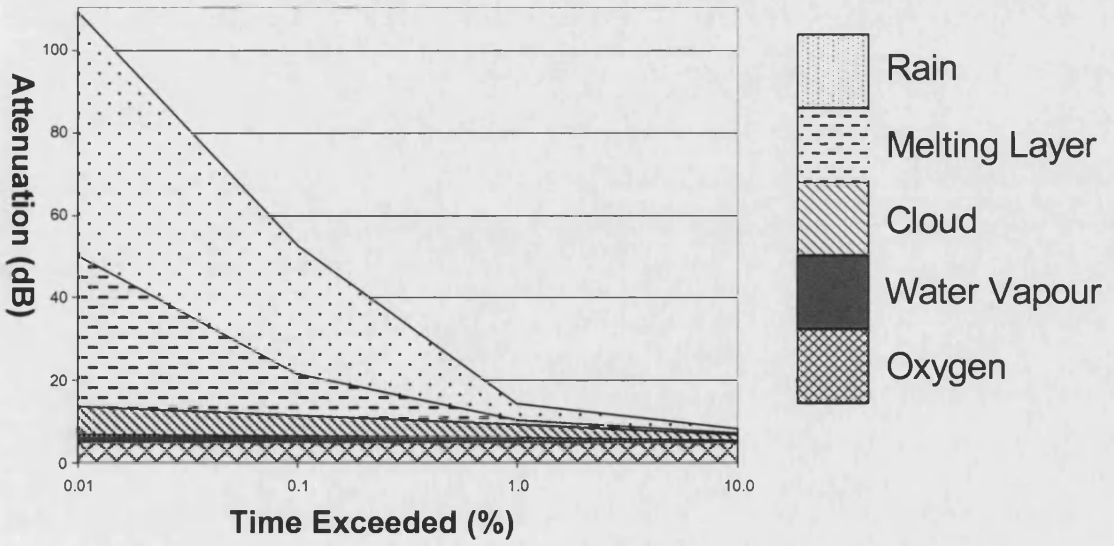

Figure 3.2-1 Cumulative Atmospheric Attenuation against Time Exceeded

3.3 Gaseous Attenuation

All the constituent gases of the atmosphere (O, H_2O, O_3, CO, SO_2, N_2O, NO_2) contribute to the radio refractivity of air. However this effect is negligible compared to the absorption by oxygen and water vapour [Brussard and Watson, 1995].

3.3.1 Absorption

Attenuation caused by absorption depends mainly on frequency, elevation angle, atmospheric pressure, temperature and humidity. It can normally be neglected below 10 GHz but requires consideration at higher frequencies. Absorption due to oxygen does not vary significantly with time or location, while that due to water vapour varies slowly in response to variations in water vapour content. The model given in [ITU-R, P676-4] can be used to predict statistics of gaseous absorption from 0 to 1000 GHz.

Water Vapour molecules have a permanent electric dipole which causes them to rotate when influenced by an electric field. The direction of alignment tends to oppose the applied field, and leads to increased loss [Brussard and Watson, 1995]. Water vapour causes resonant absorption at particular frequencies, which can be observed by the peaks in Figure 3.3-1. Water vapour density can vary from location to location, season to season and time of day.

Oxygen has a permanent magnetic moment which causes resonant absorption at particular frequencies (see Figure 3.3-1). The total zenith attenuation at 50 GHz is approximately 1 dB and increases with frequency to over 100 dB at 60 GHz.

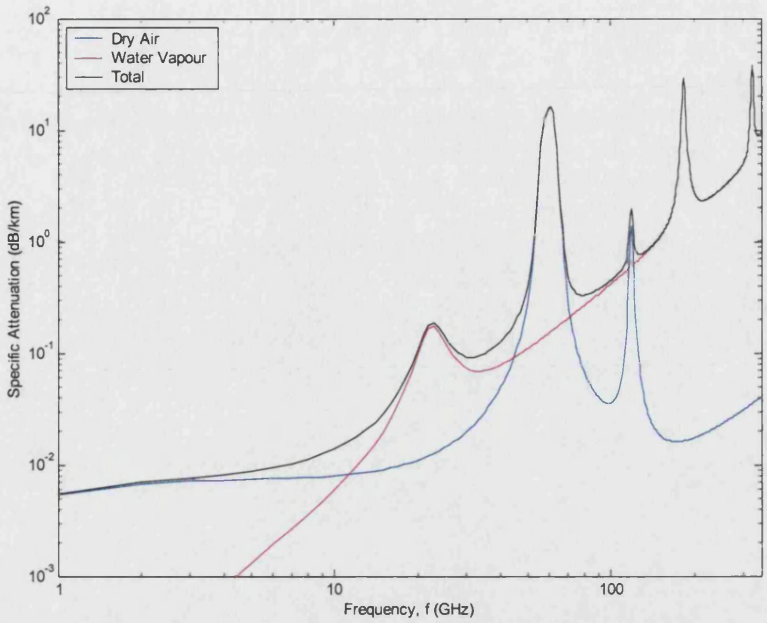

Figure 3.3-1 Total Zenith Attenuation due to Atmospheric Gases from sea level (pressure = 1013 mb, temperature = 15 °C, water vapour content = 7.5 g/m^3)

3.3.2 Refractivity

As electromagnetic waves propagate through the atmosphere they are refracted (bent) and scattered. Refraction is caused by changes in the refractive index at different heights due to variations in pressure, temperature and water vapour pressure. The atmospheric radio refractive index n is the ratio of the speed of radio waves in a vacuum to the speed through the air. As height increases the refractive index $n = 1+N\times10^{-6}$, decreases and the radio wave bends towards the region of higher refractivity. Radio refractivity can be calculated using [ITU-R, P453-7] which defines:

Eqn. 3-1 $$N = N_{dry} + N_{wet} = \frac{77.6}{T}\left(P + 4810\frac{e}{T}\right)$$

where P is atmospheric pressure (hPa), e is water vapour pressure (hPa), T is absolute temperature (K). The dry term $N_{dry} = 77.6\frac{P}{T}$, consists of the atmospheric gases which remain fairly constant with location and height. The wet term $N_{wet} = 3.732\times10^5\frac{e}{T^2}$, is due to water vapour and has a major contribution to the refractivity.

3.4 Cloud Attenuation

Cloud attenuation is highly dependent on frequency. The effect is not significant below 10 GHz, but becomes increasingly important for low margin systems around 30 GHz. Clouds consist of suspended non-precipitating water particles. Typically the cloud particles are in liquid form above 0°C and in ice form below about –20°C to -40°C depending on cloud type [Salonen and Uppala, 1991]. Between 0°C and -20°C water can occur in super-cooled form. Below the 0° isotherm height the temperature increases and ice particles start to melt forming rain. The thickness of this band called the melting layer is typically 300m to 500m.

Attenuation due to cloud is a function of the particle size distribution, shape, density, temperature, index of refraction, wavelength and cloud extent, though when the cloud droplets are small compared to the wavelength the Rayleigh scattering approximation may be applied [Brussard and Watson, 1995].. The attenuation is primarily due to absorption by the cloud droplets (below 50 GHz) with smaller losses due to scattering. For clouds above the 0° isotherm, absorption by ice particles can be neglected because the imaginary component of the index of refraction of ice is very small.

When there is no precipitation we can assume that clouds below the zero degree isotherm have a composition similar to fog. Thus clouds consist entirely of small droplets with diameters generally less than 0.1mm [Altshuler, 1989]. This allows the Rayleigh scattering approximation to be applied for frequencies below 200 GHz.

For uniform cloud cover it is reasonable to assume that the attenuation is proportional to the distance through the cloud. Therefore the total attenuation should be proportional to the cosecant of the elevation angle. The typical range of the 0° isotherm height (h_R in Figure 3.4-1) is between 2-4 km, although cloud can extend to ground level.

Attenuation due to clouds for a given probability can be calculated from statistics of total columnar liquid water content (kg/m^2), or equivalently, mm of precipitable water for a given site [ITU-R, P840-3]. Total columnar liquid water content may be obtained from radiometric measurements or from radiosonde launches. Complex models by [Liebe, et al., 1989, Salonen and Uppala, 1991] predict cloud attenuation by using statistical measurements. The model of [Konefal, et al., 2000] can be used to predict the monthly exceedance probabilities of cloud attenuation that reflect seasonal variation.

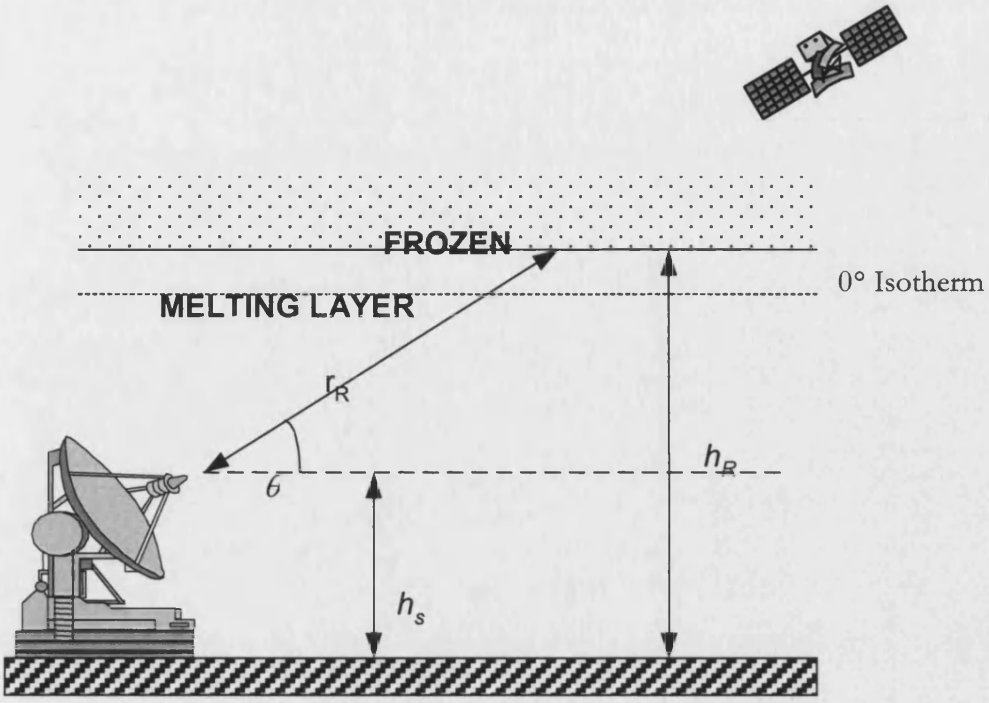

Figure 3.4-1 Height of Cloud and Rain

3.5 Rain Attenuation

Rain attenuation is the most significant propagation mechanism for satellite communications systems operating above 10 GHz. Rain fades of 30dB or more can occur due to a combination of absorption and scattering. Complex interactions take place when drop diameters (0.1 to 8 mm) and radio wavelengths become comparable (i.e. in the Mie region) see [Brussard and Watson, 1995]. Therefore, it is very important to accurately predict rain attenuation when considering EHF systems.

For coherent scattering the total attenuation due to rain is the sum of the contributions of each individual drop, assuming single scattering see [Brussard and Watson, 1995]. The contribution of each drop depends on the temperature, size distribution, terminal velocity and shape of the raindrops. This is integrated along the total rain filled slant path length (r_R in Figure 3.4-1). The effective rain height *(h_R)* is usually taken to be the same as the height of the top of the melting layer and changes with the season.

Rainfall intensity (mm/hr) at different sites can be accurately measured using radars and rain gauges. [ITU-R, P838-1] relates the specific attenuation γ_R (dB/km) to the rain rate R (mm/hour) using the power-law relationship :

Eqn. 3-1 $\gamma_R = kR^{\alpha}$ (dB/km)

where k and α are frequency dependant coefficients

This model is used in the derivation of Figure 3.5-1, which shows how the attenuation increases with frequency and rain rate. In the UK rainfall rates of 100 mm/hr occur infrequently and in short bursts (typically 1-2 minutes). More typical in the UK are rainfall rates of 1.25 mm/hr and 25 mm/hr for light and heavy rain respectively [Hall, et al., 1996].

For areas where no rainfall data exists, [ITU-R, P837-2] provides global rain rate maps for different exceedance times. These maps were derived from 15 years of data from the European Centre of Medium-range Weather Forecasting (ECWMF). Much higher rain rates are expected in equatorial and tropical regions.

In C-band, Ku-band and Ka-band satellite systems, light rain can be accommodated with a small link margin and therefore produces less outage time than the same amount of rain falling in occasional heavy storms. At 40/50 GHz light rain has such a strong effect that even FMT will not prevent link outages. In this situation it is more efficient to reallocate satellite resources than to try and maintain the link availability. Time diversity can protect services through short fades but introduces a delay. The optimum time to restart transmissions to faded cells can be predicted using models of fade slope and fade duration [Matricciani, et al., 1987, Paulson and Gibbins, 2000].

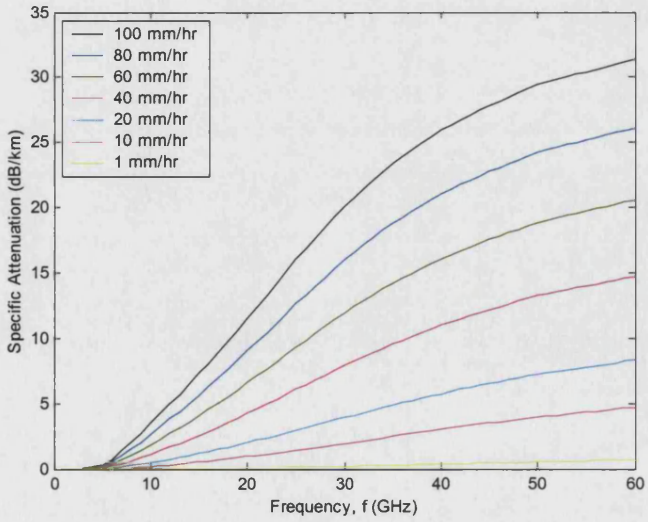

Figure 3.5-1 Specific Attenuation Through Rain as a Function of Frequency (horizontal polarisation)

3.6 Long Term Propagation Prediction Model

A propagation model (KWSA) [Konefal, et al., 2000] has been used to provide predictions of radio link availabilities at frequencies from 10 to 50 GHz. This model was based on an extension of the [Watson, et al., 1977, Leitao and Watson, 1986, Watson and Hu, 1994] models to facilitate more accurate prediction using monthly meteorological data.

[Watson, et al., 1977, Leitao and Watson, 1986] had drawn two fundamental observations, namely (i) the dominance of variations in rain height for slant path attenuation prediction for middle latitudes and (ii) seasonal variations of rain intensity over the European region. As a consequence a proposal for a new approach to prediction of annual cumulative statistics was drawn up based on the use of monthly meteorological data, especially monthly rain intensity data. This resulted in the Konefal, and Watson model [Konefal, et al., 2000]. Note the prediction is essentially for monthly data and the annual data is presented as a sum of the monthly contributions.

3.6.1 Overview

A detailed description of the mathematical model can be found in [Konefal, et al., 2000]. The database contains two sources of climatic data:

Potsdam Institute for Climatic Research (PIK) – observations, 30 years, 1931 - 1960

- monthly precipitation;
- monthly number of rainy days;
- monthly mean temperature;

European Space Agency (ESA) - radiosonde profiles, over 10 years, 1980 - 1989

- surface humidity;
- humidity at 0°C isotherm.

Both sets of data are global, but measurements were only based on land and were interpolated into a regular grid with a 1.5° latitude / longitude spacing. The data base is then manipulated by different models depending on the required output:

(1) monthly or annual probability of exceedance for a given attenuation:

- rain model – [Tattelman and Scharr, 1983] method used to predict monthly 1 minute rainfall rates at exceedance levels : 0.01, 0.05, 0.1, 0.5, 1.0, 2%;
- melting layer model – based on [Russchenberg and Ligthart, 1996];
- cloud model – [Salonen and Uppala, 1991] uses integrated liquid water content as input, which is varied to produce seasonal fluctuations;
- water vapour model – [Salonen and Uppala, 1991] annual water vapour database gives annual exceedance statistics for integrated water vapour content;
- oxygen model – [ITU-R, P676-4] calculated using model atmosphere at 15°C and 1013 ± 50 mbar.

(2) monthly attenuation associated with probability of exceedance:

- rain attenuation – rainfall rates are turned to attenuation using [Leitao and Watson, 1986], showery rain coefficients are used below 0.1% exceedance and widespread coefficients above 0.1%;
- cloud attenuation – [Salonen and Uppala, 1991] gives annual zenith cloud attenuation for the length of path through cloud;
- water vapour attenuation – [ITU-R, P676-4] model with temperature correction over 15°C;
- oxygen attenuation – [ITU-R, P676-4].

The program flowchart for a satellite-to-earth link is shown in Figure 3.6-1.

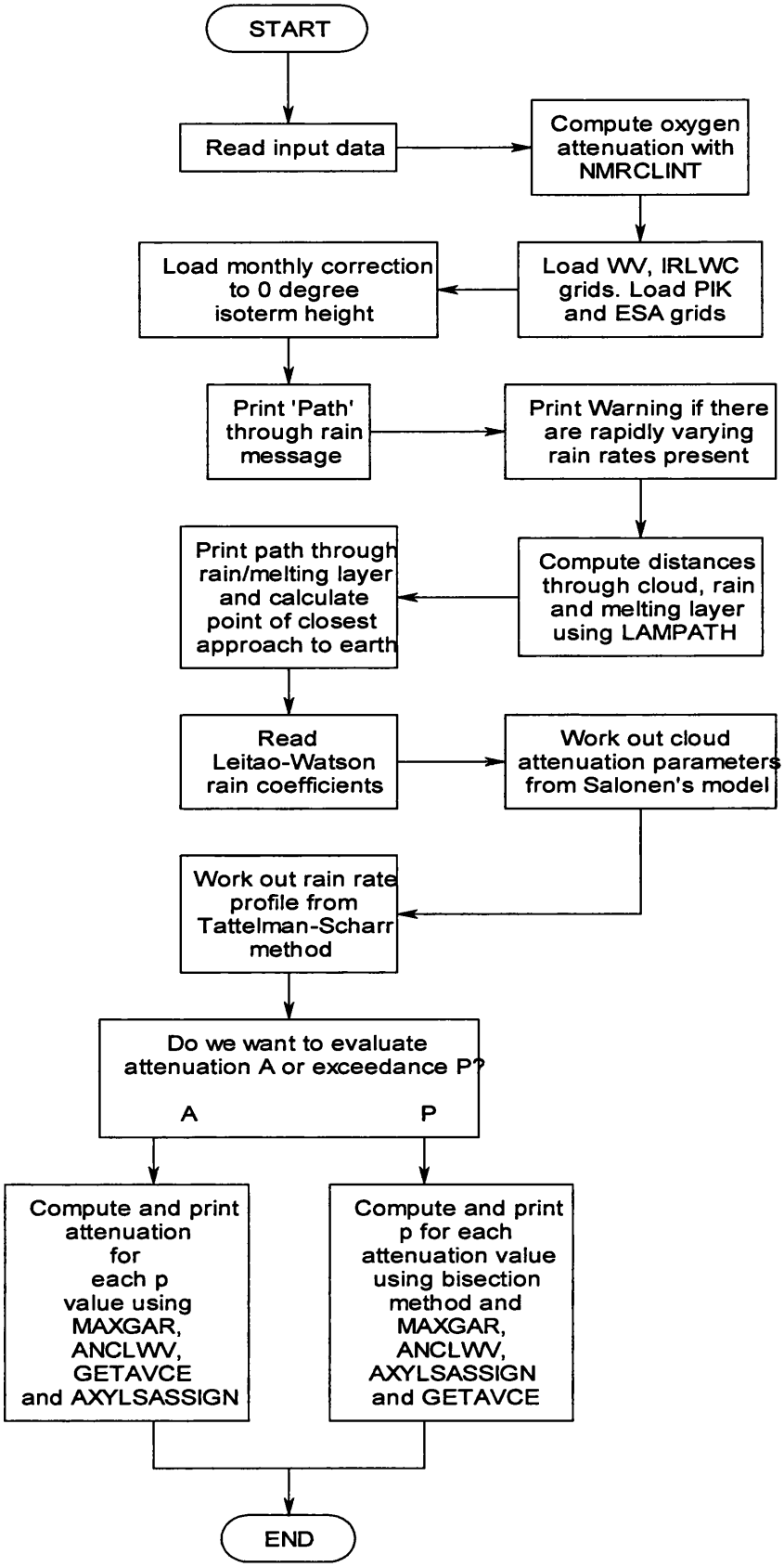

Figure 3.6-1 KWSA Propagation Prediction Model Flowchart

3.6.2 Pseudo-Satellite Geometry

The original KWSA software was developed for calculating atmospheric attenuation on aircraft-to-aircraft links. For this reason, the software takes as input the positions of two planes (latitude, longitude and height). Subsequently, the software calculates the range for line of sight paths and divides the link into a number of segments. The height above the earths surface for each segment is used to determine the water vapour statistics and hence atmospheric conditions along the path.

For application to earth-to-satellite links, the satellite geostationary orbit was represented by a pseudo-satellite position with a height between 30-50 km. If the actual orbit height were to be used, segmentation of the link paths would result in segment lengths too large to adequately follow the changing water vapour and oxygen specific attenuations close to the earth.

The calculation of the pseudo-satellite position is given below and the geometry is illustrated in Figure 3.6-2. The procedure simply transforms polar coordinates into Cartesian form and scales by a fraction (λ) of the satellite path. Using λ of 0.001 gives a pseudo-satellite height between 30-50 km for mid-latitude points, and λ is increased for higher latitudes to ensure the pseudo-satellite height remains above 15 km (to ensure the full path through the troposphere is evaluated).

Eqn. 3-2 $$x_p = r_e.sin\theta.cos\phi + \lambda\,[(r_e+h).cos(-\omega) - r_e.sin\theta.cos\phi]$$

Eqn. 3-3 $$y_p = r_e.sin\theta.sin\phi - \lambda\,[(r_e+h).sin(-\omega) + r_e.sin\theta.sin\phi]$$

Eqn. 3-4 $$z_p = r_e.cos\theta.(1-\lambda)$$

where ϕ is ground station longitude, ω is geostationary satellite longitude, r_e is the earth radius using the straight ray model (8500 km), h is geostationary orbit height * 4/3 (48447.59252 km) and θ = 90 - ground station latitude.

Eqn. 3-5 $$\text{pseudo-satellite latitude} = 90 - \cos^{-1}\left(\frac{z_p}{r_p}\right) \quad (degrees)$$

Eqn. 3-6 $$\text{pseudo-satellite longitude} = \tan^{-1}\left(\frac{y_p}{x_p}\right) \quad (degrees)$$

Eqn. 3-7 pseudo-satellite height = $\sqrt{x_p^2.y_p^2.z_p^2} - r_e$ *(km)*

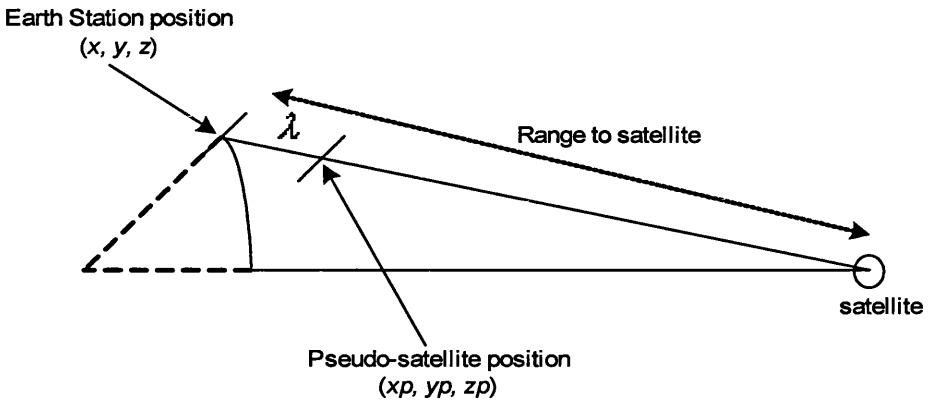

Figure 3.6-2 Pseudo Satellite Geometry

3.6.3 Long Term Point Predictions

3.6.3.1 Comparison with ITALSAT

The ITALSAT propagation experiment was started in 1991 and has provided published CDFs of total attenuation measured along satellite slant paths suitable for comparison with predictions from the KAW model. ITALSAT F2 (13°E) carries a payload including three beacon transmitters at 18.7, 39.6 and 49.5 GHz. Results of beacon measurements recorded at an earth station at Spino D'Adda in Italy (45.4°N, 9.5°E), are available for an observation time of three years [Polonio and Riva, 1998].

Figure 3.6-3 taken from [Polonio and Riva, 1998] shows the annual cumulative distribution of total attenuation measured at Spino D'Adda (37.6° elevation) for 39.6 and 49.5 GHz for three years from 1994 to 1996. Superimposed in the graphs are annual CDFs for the same slant path (using the satellite pseudo geometry) predicted with the KAW model. The average exceedance between the three years for attenuations of 10, 15 and 20 dB are used for comparison with the predictions in Table 3-1 [Watson, et al., 2000].

It can be seen that the model provides very satisfactory estimates of attenuation statistics over the full range of availabilities. It is worth noting that the prediction model uses the average of 30 years of rainfall rate data. Only three years of experimental data are available, which is not really sufficient time to enable valid comparisons to be made with long term software predictions. There is considerable variation in experimental data between years (see Figure 3.6-3) and very good agreement was found between the software prediction and the attenuation data for 1995.

Table 3-1 Comparisons between predicted and measured attenuation for Spino D'Adda

Fade Margin (dB)	Link Availabilities (% time) at 39.6 GHz		Link Availabilities (% time) at 49.5 GHz	
	Predicted	Measured	Predicted	Measured
10	99.72	99.6	99.30	99.1
15	99.84	99.8	99.69	99.6
20	99.90	99.9	99.80	99.8

3.6.3.2 COST 255

Further point predictions were undertaken for Riva[9] in the framework of [COST255] for comparison between prediction models used in the project. Predicted total attenuation values were supplied for the time percentages and slant path characteristics given in the COST255 project. The results of the comparison are to published in the COST 255 Final Report.

Also in the framework of COST 255, Martellucci[10] collaborated on a short term scientific mission (STSM) to make further comparisons between the KWSA model and [Liebe, 1989]. Liebe's MPM93 model is based on a different approach and database:

- ESA-FUB database of radiosonde data (interpolated up to 30km);
- Liquid water density profile estimated using Salonen's model based on critical humidity;

[9] Politecnico di Milano; riva@elet.polimi.it

[10] Radiocommunications Dept., Fondazione Ugo Bordoni; martellucci@fub.it

- Equi-probability summing of oxygen, water vapour and cloud attenuation;
- Attenuation along the slant path calculated assuming longitudinal homogeneity.

The original KWSA software predicted monthly cloud attenuation from annual upper-air data taken from radiosondes by applying monthly weighting factors. Monthly upper-air data was unavailable to Konefal and Watson at the time of publication. Subsequently ESA/ESTEC processed the full monthly upper-air records from ECWMF data and Martellucci[11] collaborated with us to check the two approaches. This led to an upgrade of the KWSA software to include improved monthly upper-air databases.

Martellucci[11] also validated the results in section 0 to create maps of attenuation over Europe, by comparison with those produced by the MPM93 model.

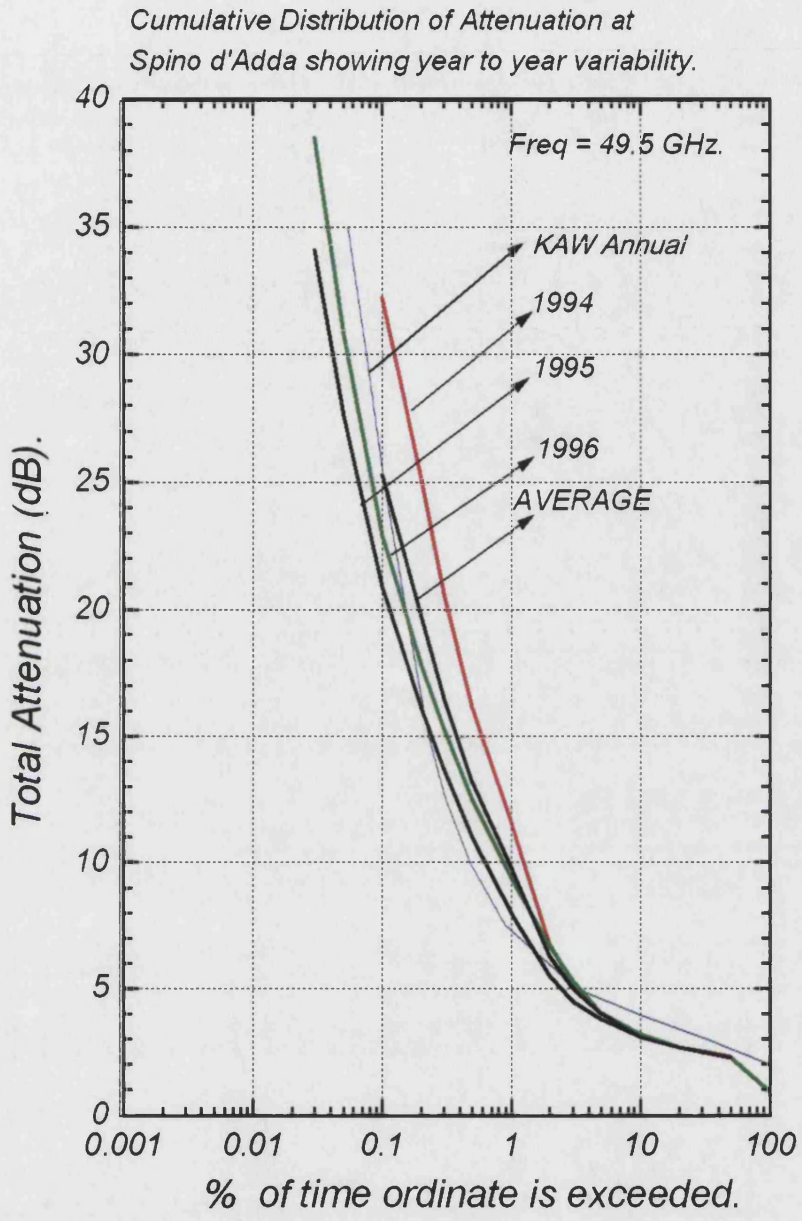

Figure 3.6-3 Measured cumulative distribution of total attenuation at 39.6 and 49.5 GHz (Spino D'Adda, 1994-1996) [Polonio and Riva, 1998].

3.6.3.3 Monthly Cumulative Distributions

Predicted monthly cumulative distributions from the KWSA model are shown in Figure 3.6-4 for Spino D'Adda. Note the large seasonal variation and the dominance of the summer months.

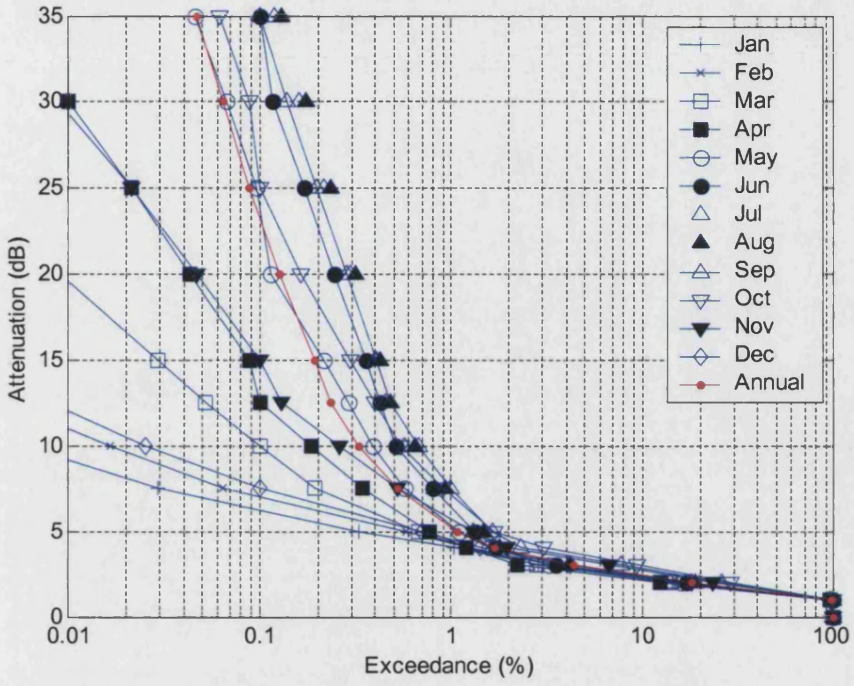

Figure 3.6-4 Predicted Monthly attenuation statistics at 49.5 GHz for Spino D'Adda

3.7 Link Performance Analysis for a European Coverage

To determine the minimum link power margin required, the annual attenuation associated with gaseous and cloud attenuation, for an availability of 99% has been evaluated for the highest frequency (worst case). The static margin must at least overcome the combined effect of gases and cloud with a high probability of occurrence. Figure 3.7-1 shows the attenuation due to these effects for an availability of 99% at 50 GHz over the coverage area. It can be seen from this plot, that a margin of at least 10 dB is required over the majority of Europe and the UK.

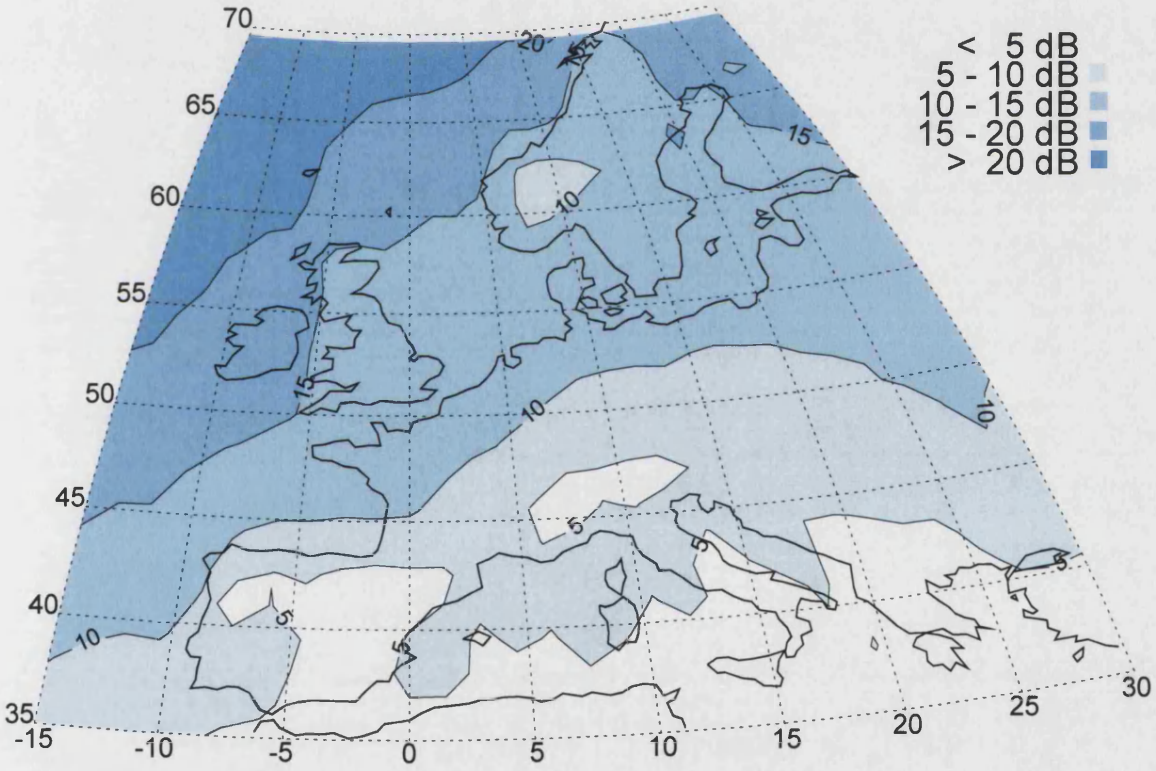

Figure 3.7-1 Attenuation due to atmospheric gases and cloud for an availability of 99%

3.7.1 Conclusions

In this chapter the KWSA model has been used to predict statistics of annual and monthly availability for V-band for specific European locations where it observations have been made. The predicted results have been validated against empirical data from OLYMPUS and ITALSAT propagation experiments, and are seen to give good agreement. Such agreement gives confidence in the component models used in the KWSA approach, in particular the Leiteo-Watson rain model, Salonen cloud attenuation models and ITU-R gaseous absorption models. This approach is thus of direct value to the prediction of attenuation for system design, especially in the context of long term availability i.e. annual or monthly. It is also anticipated that the same or similar component models will be of relevance to time series prediction of attenuation for simulation purposes.

At V-band the specific attenuation due to atmospheric gases is an order of magnitude greater than at Ku-band. This equates to slant path attenuation of ~3dB, which is a significant proportion of the excess power margin required for a commercial system. In addition, cloud attenuation at typical availabilities of 99.9% can contribute around 10dB of loss. However, the occurrence of rain dominates link availability at V-band frequencies in the range 99% to 99.9% and above.

4 System Design

This system study explores the area of convergence between satellite broadcast systems and VSAT technology. Such systems can exploit the point-to-multipoint nature of the satellite channel to provide interactive multimedia services.

Multimedia traffic can be characterized by the degree of traffic asymmetry. At the highest degree the system may be regarded as a low data rate return channel for applications such as pay-per-view TV, impulse buying from TV commercials and audience polling or participation. The system may be further extended to support IP based applications ranging from a limited hub based server for specific applications linked to direct broadcast TV services (home shopping for example), to full world wide web browsing.

4.1 Architecture

The system provides broadband data transfer between thousands of VSAT terminals, through a bent-pipe geostationary satellite (19.2°E). These represent the majority of commercial satellite payloads, but further gains can be realized using on-board regeneration, processing and switching. Transmission frequencies have been chosen in the range allocated by the ITU for EHF Fixed Satellite Services (37.5–40.5 GHz downlink and 47.2-50.2 GHz uplink). The data rates are flexible depending on the volume of packets received.

The bandwidth per transponder is considered to be 72 MHz, re-useable in spot beams and orthogonal linear polarizations. A practical multispot beam pattern covering Europe (similar to Figure 2.9-1) will be assumed, with a specific test case taking a hub at Spino D'Adda in Italy (45.4°N, 9.5°E) and a VSAT station at Cambourne in the UK (50.22°N, 5.3°W), as shown in Figure 4.2-1. These sites correspond to locations for which statistics of atmospheric attenuation are available.

4.2 Return Channel

The return channel uses fixed Very Small Aperture Terminals (VSAT's) to provide 2-way communication with the hub. As described earlier, the use of higher frequencies allows the use of smaller more desirable 30cm antennas. A single transponder is considered, with a total data capacity of 32.768 Mbit/s (applting to DVB-S modulation & coding, see section 2.12), divided

into 64 separate 512 kbit/s channels (on each of two linear polarisations). The channels are grouped into blocks of 8, accessed with MF-TDMA. All channels are separated by a guard band and the amplifier operates backed off to avoid intermodulation interference associated with satellite transponder non-linearities.

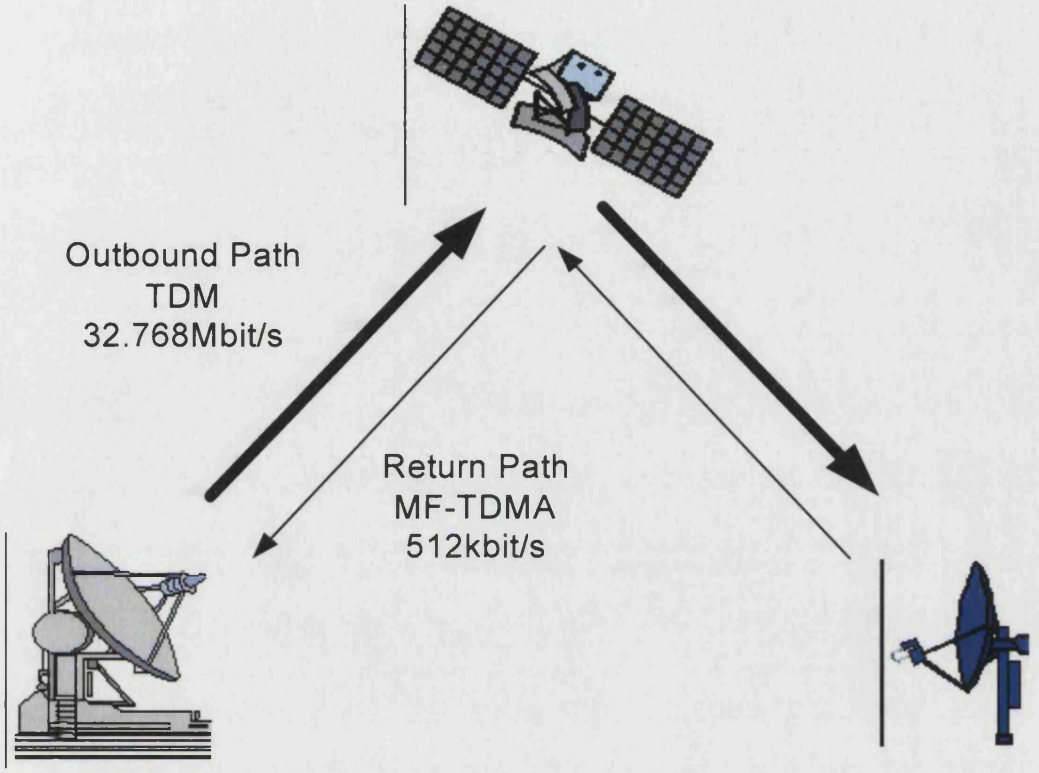

Figure 4.2-1 Test Case System Architecture

Each MF-TDMA channel contains 32 time slots with a user data rate of 16 kbit/s, although the actual number of transmitted bits will be 23 kbit/s after coding. Each user can request capacity on a slot by slot basis up to a maximum of 30 slots depending on traffic. On slot is per frame is reserved for synchronisation and another for contending for bandwidth using a DAMA scheme (typically slotted aloha). One ATM data packet (48 bytes) is transmitted in each data slot, with a total frame time of 24 ms (see Figure 4.2-2).

frame time = 24 m, therefore 41.66 frames/sec

ATM data packet = 384 bits × 41.66 frames/sec = **16 kbit/s**

Data + header (5 bytes) + RS coding (16 bytes) = 552 bits × 41.66 frames/sec = **23 kbit/s**

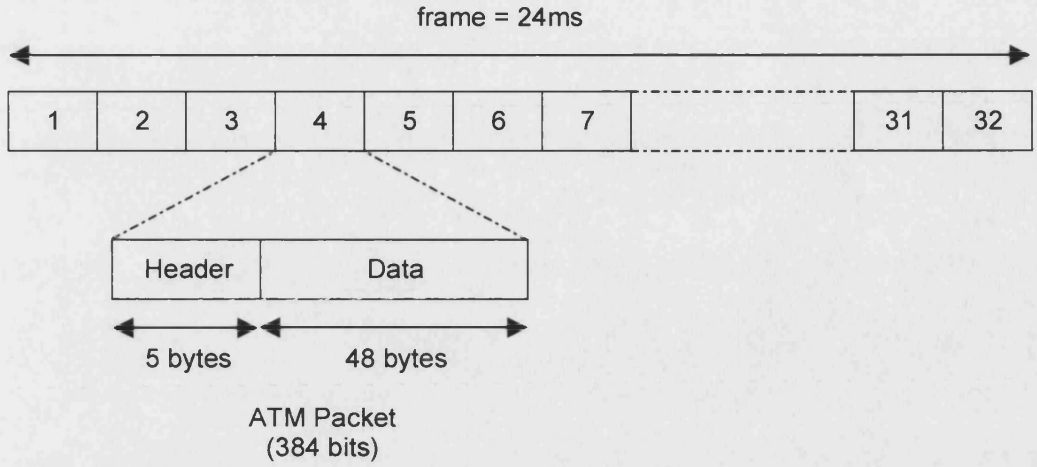

Figure 4.2-2 Single MF-TDMA Data Frame Structure

4.2.1 Transponder Utilisation

The satellite transponder resource allocation for the return channel is given in Table 4-1.

Table 4-1 Return channel transponder utilisation

Space Segment Utilisation		
Data Rate	0.512	Mbps
RS Coding	0.546	Mbps
FEC (1/2 rate)	1.093	Mbps
Symbol Rate (QPSK)	0.546	Sym/sec
Occupied Bandwidth (roll-off = 0.35)	0.737	MHz
Carrier Spacing (= 1.5)	0.819	MHz
Transponder Bandwidth	72	MHz
Usable Transponder Bandwidth, Rs	53.333	MHz
Percentage BW used	1.54	%
Max. carriers by transponder BW	65.09	

Considering Groups of 8 channels = ~64 data channels.

Total Data Rate, R_b = 512 kbit/s/channel × 64 channels = 32.768 Mbit/s.

But it is noted that the same spectrum can be reused in an orthogonally polarised transponder, so that capacity in orbit is 2 × 32.768Mbps = 65.5Mbit/s.

4.2.2 Number of Users

4.2.2.1 Low Bit Rate Serial Applications

For a broadcast return channel system, the number of simultaneous users is limited by the capacity of the return channel. Many subscribers could be on-line receiving broadcast data (e.g. TV) though not transmitting. The proposed system is intended to support at least 100,000 users per spot beam using the total return channel data capacity of 65.536 Mbit/s (considering both polarisations). The number of active transmitters will be highly variable depending on time, tariffing and interactive options.

Considering a minimum return channel granularity of one time slot (~41 ATM packets) per terminal, around 3840 (30 slots × 128 carriers) users can be supported simultaneously. However, many applications such as on-line polling and messaging will require only a few ATM packets allocated on a frame by frame basis, therefore, increasing the number of supported users to maximum of 126,000 (3084 slots × 41 ATM packets/slot).

4.2.2.2 Packet Based Applications

Internet browser applications are characterized by the asymmetric ratio of the received data to the size of the request. Measurements show a ratio of about 10:1, which will increase with the use of more image, sound and video in web page design. The total outbound capacity (98.24 Mbit/s) is shared by the number of users. Reducing the number of users increases the maximum bandwidth available to each user. Assuming an average web page size of 20 kbytes, the system can support around 4900 simultaneous web users.

This number could underestimate the actual number of users, since HTTP requests consist of a number of separate TCP transfers (1.5 – 2.0 kbytes long). Also the number of transfers per page will be affected by the browsers cache size and user think time.

4.3 Outbound Channel

On the outbound link (hub to VSAT) the broadcast nature of the system is exploited. The available transponder bandwidth (53.3MHz) is used to carry a single TDM channel with a data rate (49.12 Mbit/s). Using single carrier TDM allows the satellite transmitter amplifier to be driven into saturation without output backoff, but with the loss of flexibility associated with multiple access schemes.

The TDM multiplex contains a number of data streams compatible with high quality MPEG-2 compressed video (6 Mbit/s). Each time slot contains an MPEG-2 transport stream packet protected by DVB-S coding. These packets contain a destination address to identify individual terminals in the broadcast stream.

4.3.1 Transponder Utilization

The satellite transponder resource allocation for the return channel is given in Table 4-2.

Table 4-2 Return channel transponder utilisation

Space Segment Utilisation		
Data Rate	49.120	Mbps
RS Coding	53.300	Mbps
FEC (1/2 rate)	106.600	Mbps
Symbol Rate (QPSK)	53.300	Sym/sec
Occupied Bandwidth (roll-off = 0.35)	53.300	MHz
Carrier Spacing (= 1.5)	53.300	MHz
Transponder Bandwidth	72	MHz
Usable Transponder Bandwidth, Rs	53.333	MHz
Percentage BW used	99.94	%
Max. carriers by transponder BW	1.00	

But it is noted that the same spectrum can be reused in an orthogonally polarised transponder, so that capacity in orbit is 2 × 49.12Mbps = 98.24Mbit/s.

4.3.2 Link Budgets

The link power budget is given in Table 4-3 (without atmospheric or interference losses).

Table 4-3 Test Case Link Budget

	Inbound Link:	**Outbound Link:**	
	VSAT to Hub	**Hub to VSAT**	
Transmit Terminal			
Uplink Frequency	50.20	47.20	GHz
Uplink Wavelength	0.00598	0.00636	m
Transmit Power	0.58	100.00	W
Transmit Antenna Diameter	0.30	3.00	m
Transmit Antenna Efficiency	70	70	%
Transmit Antenna Gain	42.4	61.9	dBi
Transmit Saturated EIRP	40.0	81.9	dBW
Transmit EIRP back Off	0.0	3.0	dB
Transmit EIRP	40.0	78.9	dBW
Uplink			
Uplink Slant Range	38799	38029	km
Uplink Free Space Path Loss	218.23	217.52	dB
Satellite			
Satellite beamwidth	0.4	0.4	deg
Satellite Antenna Diameter	1.09	1.09	m
Satellite Antenna Efficiency	70	70	%
Satellite Antenna Gain	53.6	53.1	dBi
Satellite Rx Figure of Merit (G/T)	24.0	23.5	dB/K
Uplink C/N0	**74.5**	**113.5**	**dBHz**
Transponder TWTA power	100.00	100.00	W
Transponder OBO	9.00	5.00	dB
Transponder power per carrier	-7.1	15.0	dB
Effective Transmit Antenna Gain	51.7	51.1	dBi
Transponder Signal EIRP	44.6	66.1	dBW
Downlink			
Downlink Frequency	40.50	37.50	GHz
Downlink Wavelength	0.00741	0.00800	m
Downlink Slant Range	38029	38029	km
Downlink FSPL	216.2	215.5	dB
Receive terminal			

Receive Antenna Diameter	3.0	0.3	m
Receive Antenna Efficiency	70	70	%
Receive Antenna Gain	60.5	39.9	dBi
Receive Figure of Merit (G/T)	35.8	15.1	dB/K
Downlink C/N0	**92.8**	**94.2**	**dBHz**
Total Link			
Total Link C/N0	74.4	94.2	dBHz
Required Modem (Eb/N0)	6.30	6.30	dB
Modem Implementation Loss	1.00	1.00	dB
Required Modem C/N0	64.4	84.2	dBHz
Link Feasibility			
Close Link C/N0	YES	YES	
C/N0 Margin	10.0	10.0	dB

4.3.3 Test Case Link Analysis

Using the typical system parameter given in this chapter, the outward and return link budgets have been designed to provide the 10 dB margin identified in Table 4-3. The link availability performance has been assessed. Table 4-4 gives the predicted annual availability performance for this threshold using the KWSA model. The overall link availability for the outbound link is 99.2% and 98.0% for the return channel.

Table 4-4 Test Case Predicted Annual Link Availability

	Location	Link	Frequency (GHz)	Availability (%)
Outbound	Spino D'Adda	Uplink	47.2	99.46
	Cambourne	Downlink	37.5	99.75
Inbound	Cambourne	Uplink	50.2	98.27
	Spino D'Adda	Downlink	40.5	99.68

4.3.4 Annual European Availability

Figure 4.3-1 and Figure 4.3-2 show annual availability maps for the European region for 40 GHz and 50 GHz and a link margin of 10 dB. The maps have been created by executing the KWSA prediction model for a grid of earth locations with a 1.5° resolution (latitude and longitude). These calculations include ground elevation, interpolated into a regular grid using the MIN_CURVE_SURF procedure in IDL. Finally, the CONTOUR procedure projects the data onto a surface map.

The maps show geographical variations of annual total attenuation (oxygen, water vapour, cloud, rain and melting layer) on each link.

4.3.5 Seasonal Availability

Further maps have been produced using the KWSA model, on a monthly basis to show the strong seasonal variations in the link availability. For example, a 50 GHz uplink in Southern England / Northern France has at least 99.0% availability from January to April, but falls to between 98.0 to 99.0% for the rest of the year. Figure 4.3-3 and Figure 4.3-4 show examples of these monthly plots.

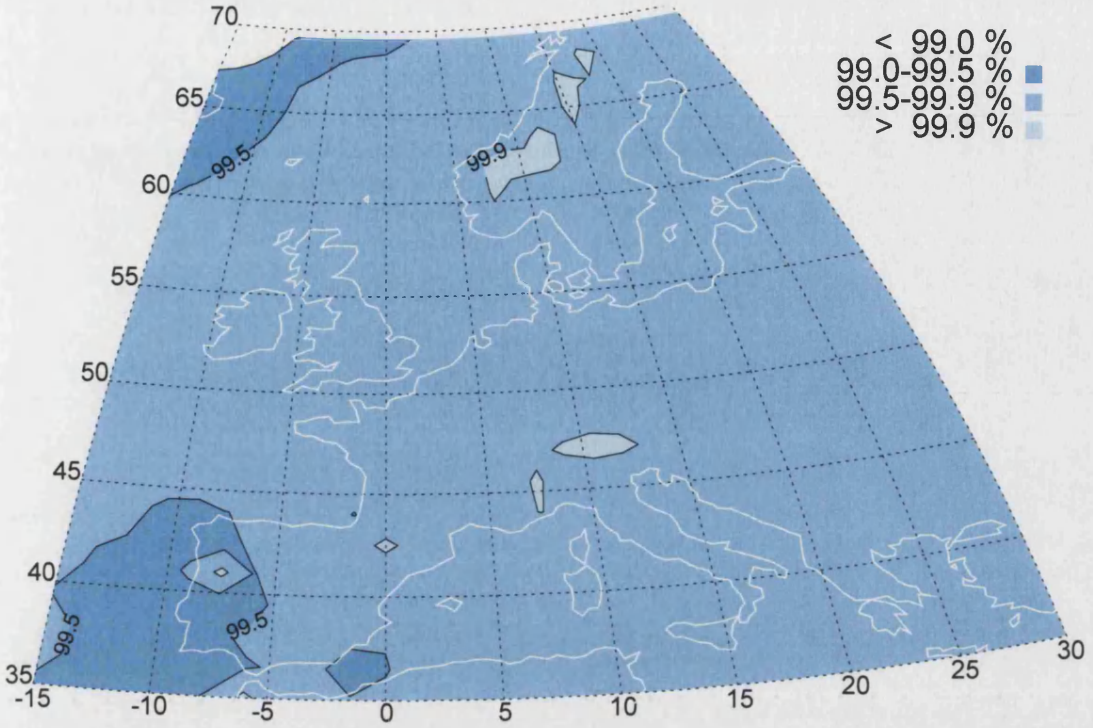

Figure 4.3-1 Annual Availability contours for a threshold of 10dB at 40GHz, 19.2°E (Note : excludes antenna pattern and range loss)

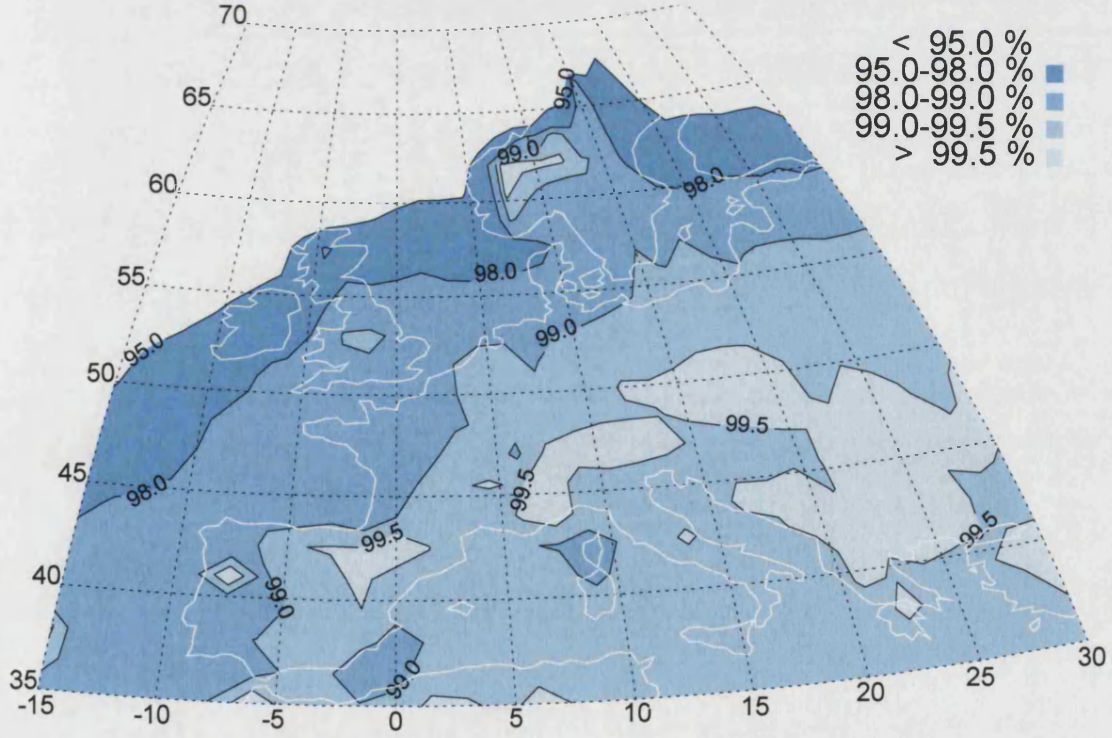

Figure 4.3-2 Annual Availability contours for a threshold of 10dB at 50GHz, 19.2°E (Note : excludes antenna pattern and range loss)

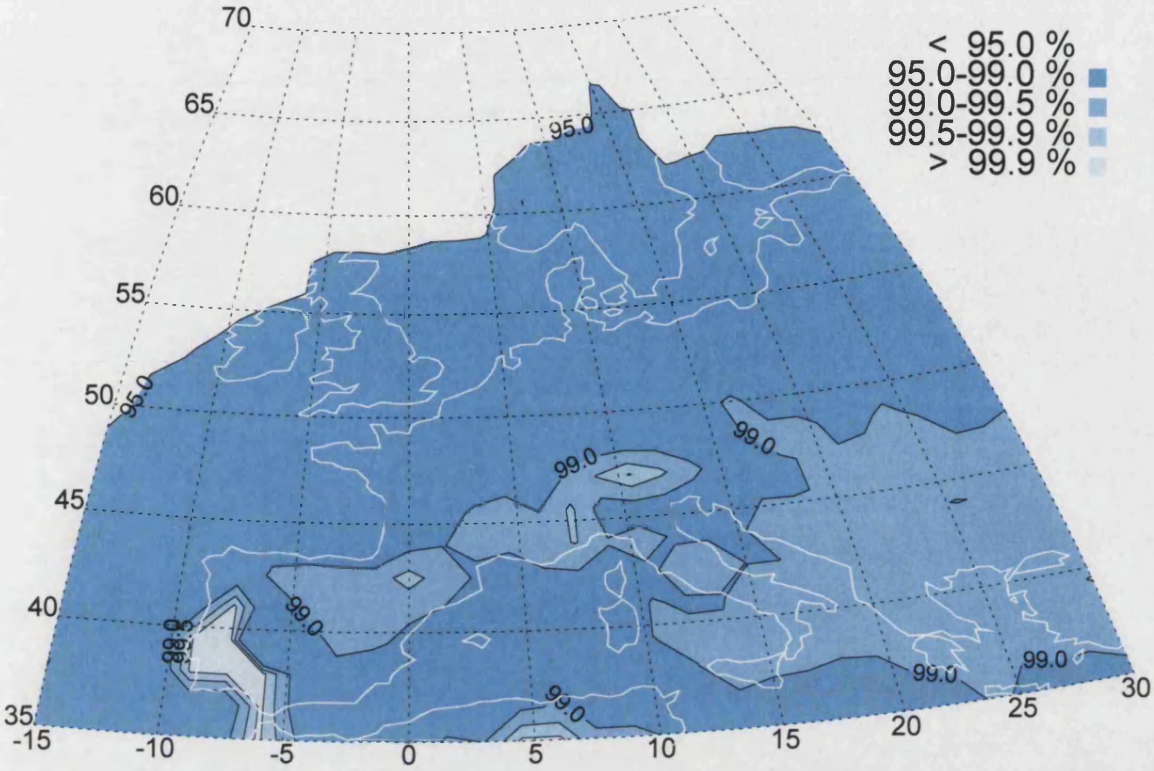

Figure 4.3-3 Availability contours for January for a threshold of 10dB at 50 GHz, 19.2°E

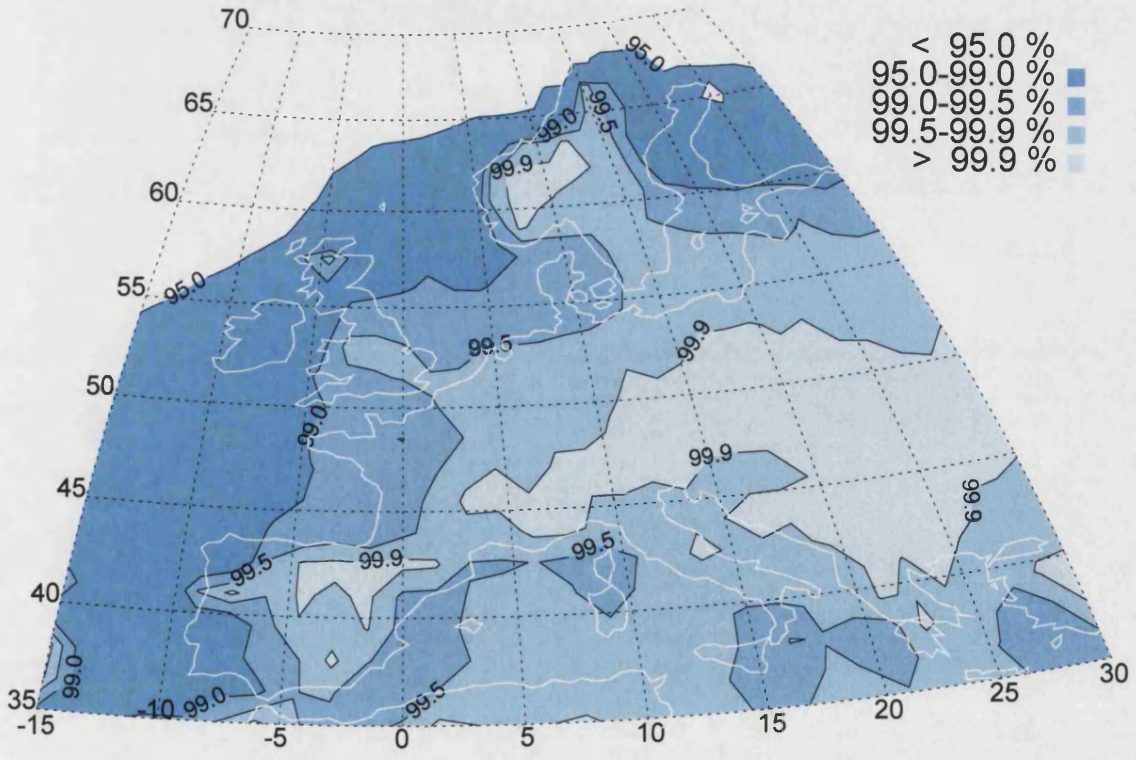

Figure 4.3-4 Availability contours for July for a threshold of 10dB at 50 GHz, 19.2°E

4.4 Conclusions

A V-band (40/50 GHz) system has been evaluated for a European coverage, taking as a specific test case a hub station at Spino D'Adda in Italy and a VSAT station at Cambourne in the UK. Annual availabilities are given for 40 and 50 GHz. Thus the system would be considered more than adequate by the DVB Return Channel standards, which propose lower link availabilities (99.5% for business users and 95% for residential customers [ETSI, DVB-RCS]).

The combined availability performance of the uplink and downlink can only be evaluated if atmospheric attenuation is considered to be statistically independent on each link. Given the large spatial separation of between earth stations, this can confidently be assumed for rain events. Further work is needed on the spatial correlation of cloud, which can extend over large distances, to determine the probability of this effect on both links and thus the optimum static margin. Adaptive techniques such a power control, modulation and coding are needed to maintain a high availability when attenuation due to atmospheric gases and cloud is present.

Despite a lower probability of occurrence, the severe attenuation due to rain will almost always cause a link outage when operating at V-band. Service quality for broadcast applications can be maintained through short rain fades with extensive use of memory in user terminals. When individual terminals experience prolonged outage due to rain fade, satellite resources should be maximized by reallocating the link capacity to unaffected terminals throughout the duration of the fade. Although this removes any possibility of service to the affected terminals, it is more economical for the overall system, which may otherwise be affected by an increased amount of satellite power and bandwidth to faded users. The optimum time to restart transmissions can be found from statistics of fade duration, while statistics of fade slope provides an indication of the ability of adaptive techniques to mitigate atmospheric fades.

The hub to VSAT path is the most demanding for sustaining large numbers of users in an asymmetric multi-media mode, but by making use of adaptive techniques and memory at the hub and VSAT stations satisfactory service availability should be achieved. On the VSAT to hub path further work must be undertaken on the MF-TDMA multiplex, based on a practical HPA performance model to quantify intermodulation and hence backoff requirements. Also,

consideration must be given to the implementation of contention-less protocols and the related delays incurred with a large number of users.

Although not illustrated here, the use of a regenerative scheme, where bit errors are corrected onboard the satellite, will help to improve the end to end BER, and reduce the link power requirement (as the end Eb/N0 on the ground will be reduced). In addition, on-board multiplexing using combined schemes such as MF-TDMA/TDM would increase throughput and spectral efficiency.

Finally, it is worth noting that the link analysis provided in this chapter excludes other sources of link impairments such as interference. In a practical system, frequency coordination between adjacent spacecraft operating within the same frequency spectrum would require careful planning, especially when considering a large number of remote terminals operating with automatic uplink power control.

5 Approaches to Time Series Generation

5.1 Introduction

The ability to derive or predict time series of attenuation in the 10 to 50 GHz frequency range is of current interest in simulating the performance of multi-media satellite-to-earth (or high altitude platform-to-earth) links. Analysis using on-average statistical properties leading to conventional links budgets may be a starting point, but is not sufficient to examine the performance of the large variety of fade mitigation techniques that are applicable to such systems including power control, space-diversity and time-diversity (see for example [Castanet, et al., 1998]). On-board processing techniques including regeneration, resource sharing, switching and ground station control must also be considered. Fade mitigation techniques must inevitably be used if the upper range of the EHF band is to be exploited efficiently.

One approach might be to use measured data but this is restricted to a very small number of sites and link configurations, so that it is necessary to generate realistic time series by some other means. Two approaches can be considered here. (1) where an attenuation time series is derived from time series of meteorological data (the approach taken in this thesis). (2) where artificial or synthetic time series are generated to confirm to published overall statistical properties of measured attenuation. Note that in approach (2) there is no means of including short distance spatial variation or spatial correlation between time series. The latter property is an essential requirement in determining the performance of a system with a group of closely spaced earth stations.

In order to generate synthetic time series for simulation, several authors have proposed the use of dynamic mathematical models as in [Maseng and Bakken, 1981, Fiebig, 1999, Paulson and Gibbins, 2000]. Such simulators are based on long-term statistics from experimental radio links. The main drawback of statistical methods is the inability to transition between periods of rain and clear sky, as well as the inclusion of spatial correlation. Furthermore, such simulators could not be extended into real-time control.

This chapter describes a new approach which derives time series of attenuation based on meteorological forecast and radar data. Since the model has a physical basis it permits the generation of realistic time series for multiple sites, including dynamic temporal and spatial correlation properties inherent in weather systems. Preliminary results generated by the

simulator show promising similarity with those measured on an Earth-space link for the same time period. Furthermore, the technique opens up the possibility of use in real-time control of operational systems with response time measured in hours.

5.2 Statistical Models

5.2.1 Maseng-Bakken Model

[Maseng and Bakken, 1981] have proposed a mathematical model for rain attenuation which has found widespread use in simulating radio link performance [Filip and Vilar, 1990, Alouini, et al., 1997, Gremont and Filip, 1999]. The model is based upon experimental observations [Lin, 1973] which identify two properties of dynamic rain attenuation, A (in decibels):

- that rain attenuation in decibels (A) is lognormally distributed as given in Eqn. 5-1.

Eqn. 5-1
$$p(A) = \frac{1}{\sigma_{\ln a} A\sqrt{2\pi}} e^{\frac{\left(\ln\left(A/m_a\right)\right)^2}{2\sigma_{\ln a}^2}}$$

with, m_a = the long term median of attenuation A (dB)

σ_{lna} = the long term standard deviation of $\ln(A)$

- [Maseng and Bakken, 1981] show that the random rate of change of $A(t)$ increases in proportion to A, and also that θ_A, the time derivative of the variance, is proportional to A^2 as given in Eqn. 5-2.

Eqn. 5-2
$$\theta_A(t, A) = 2\beta A^2 \sigma_{\ln a}{}^2$$

[Maseng and Bakken, 1981] derive the mathematical model for the distribution of A, by applying these two properties as inputs to the Fokker-Planck equation. Solving results in a first order Markov process of the Ornstein-Uhlenbeck type, with a Gaussian distribution of $\ln(A)$[11]. The model allows the stationary distribution function of rain attenuation to be described by the mean attenuation, m and standard deviation, σ of $\ln(A)$.

[11] A random variable X is said to have a lognormal distribution with parameters μ and σ, if $y=ln(X)$ has the normal (Gaussian) distribution with mean μ and standard deviation σ, $X = e^Y$.

The dynamic behaviour of the process is determined by an additional parameter, β (in Eqn. 5-2) which controls the rate of change of the fade. These three parameters (m, σ, and β) determine the statistics of the stochastic process and allow other properties such as the PSD and autocorrelation function to be determined analytically. The theoretical power spectrum of the Ornstein-Uhlenbeck process is given by Eqn. 5-3.

Eqn. 5-3
$$W(f) = \frac{1}{\left(1+\left(2\pi f / \beta\right)^2\right)}$$

5.2.1.1 Discrete Sampled Implementation

A discrete sampled implementation of the Maseng-Bakken model as published by [Gremont, 2001], is easily achieved in MATLAB. A block diagram of the discrete sampled approach is shown in Figure 5.2-1. The theoretical solution of the PSD given in Eqn. 5-3, has the form of an analogue Butterworth filter[12] of order one with the cutoff frequency ω_c given by β. An equivalent digital implementation given in Eqn. 5-4 [Gremont, 2001], is found by conversion of the analogue function $H(\omega)$, in to the discrete transfer function $H(z)$, through the bilinear transformation.

A sequence of independent normally distributed random numbers, with zero mean and unity variance, are filtered using $H(z)$ to produce the correct power spectrum. Typical values for β in [Maseng and Bakken, 1981] are in the order of 1.68×10^{-3} (s^{-1}) or 1.85×10^{-3} (s^{-1}). Small values of β produce a slowly varying process.

Eqn. 5-4
$$H(z) = \sqrt{\frac{2}{\beta}} \cdot \left(\frac{1}{1+\frac{1}{\tan(\pi\beta)}} \right) \cdot \frac{1+z^{-1}}{1+Bz^{-1}}, \quad B = \frac{1-\frac{1}{\tan(\pi\beta)}}{1+\frac{1}{\tan(\pi\beta)}}$$

The Gaussian noise is then normalised to zero mean and unity variance before being modified to match the required input statistics. The two parameters m and σ can be determined for a

---

[12] $\left|H(\omega)^2\right| = \frac{1}{1+\left(\omega/\omega_c\right)^{2N}}$, where N is the filter order and ω_c is the cut off frequency.

specific site, from first order statistics of long-term propagation measurements or the CDF of exceeded rain attenuation, e.g. ITU-R P618 or [Konefal, et al., 2000].

The PDF of the output rain attenuation, y (dB) is now lognormal as given in Eqn. 5-5.

Eqn. 5-5
$$f(y) = \frac{1}{\sqrt{2\pi}\sigma y} \exp\left[\frac{-\left(\ln(y) - m\right)^2}{2\sigma^2}\right]$$

Figure 5.2-1 Block diagram of the discrete sampled implementation of the Maseng-Bakken model

5.2.1.2 Results

Figure 5.2-2 shows a stochastic rain attenuation time series produced by the discrete sampled implementation of the Maseng-Bakken model. By definition (due the use of a first order Butterworth filter), for high frequencies the PSD demonstrates the f^{-2} roll off property that has also been given in other published results.

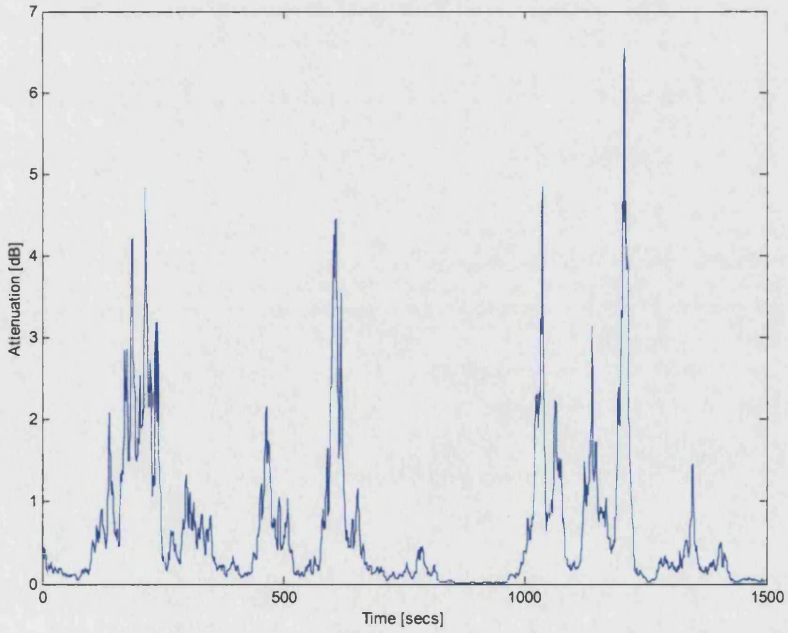

Figure 5.2-2 Maseng-Bakken rain attenuation time series example

5.2.1.3 Conclusions

The Maseng-Bakken model and its DSP implementation simulates realistic synthetic rain attenuation time series with statistics and physical properties observed in real events. Since the model is mathematically derived, other useful statistics such as fade duration, can be described analytically. However, the model has one fundamental drawback. Since the model is based upon a stationary lognormal distribution, it is only applicable during periods of rain and there is no mechanism to include transitions between periods of clear sky and rain.

5.2.2 Fractals

[Mandelbrot] proposed the idea of a *fractal* (short for "fractional dimension") which he defined to be any geometric pattern that is repeated at ever smaller scales to produce irregular shapes and surfaces that cannot be represented by classical geometry. Fractals generally exhibit *self-similarity* (the appearance of a fractal pattern remains unchanged when shrinking or enlarging) and *scale invariance* (the same statistics of variation on all scales). They are especially useful in describing irregular patterns and structures in nature, such as snowflakes, clouds and turbulence. Several different classes of self-similar processes exist and have been exploited in the formulation of stochastic temporal-spatial models of rainfall.

Pulse models describe rain experiments at a point or an area, as a result of a hierarchy of different physical processes on different scales. Typically, they model features such as rain cells arriving with random inter-arrival time distributions, typically negative exponential. Early models considered rain cells as circular regions of constant rain rate [Cowpertwait, 1995] and more recently, as populations of rain cells with negative exponential profiles[13] [Capsoni, et al., 1987, Crane and Shieh, 1989]. The latter models yield accurate predictions of annual rain fade exceedances statistics, but are not adequate for predicting short-term variations [Paulson and Gibbins, 2000].

Multiscaling models of rainfall describe variations on smaller scales using a fractal model structure. The majority of models are based on *multiplicative cascades* (multiplying independent processes) at different scales, to represent the physical processes contributing to the structure of rainfall. Such multiplicative models have useful spectral properties which can provide insight in to the structure of rainfall.

[Crane and Shieh, 1989, Veneziano, et al., 1996] observed the temporal power spectrum of log rainfall, exhibited the segmented power law form illustrated in This spectrum is consistent with theoretical models of rain as a passive tracer in a turbulent two-dimensional flow [Kraichnan and Montgomery, 1980, Lovejoy and Schertzer, 1992]. The corner frequencies are associated with the scale of convective storms and the scale of turbulence within storms.

---

[13] i.e. $R(\rho) = R_m \exp\left(-\rho/\rho_o\right)$, where ρ is the distance from the centre of the rain cell, R_m is the maximum rain rate and ρ_o is a size parameter.

[Veneziano, et al., 1996, Paulson and Gibbins, 2000] generate stochastic temporal rainfall models as a stationary lognormal process with log amplitude spectrum as shown in Figure 5.2-3. The corner frequencies are taken from empirical measurements. In addition, [Veneziano, et al., 1996] describes how the build up and decay of storm intensity can be modelled using fractional Brownian motion as the phase spectrum of the model. Controlling the moments (μ and σ) of the phase model controls the intensity and duration of the event. Following inverse Fourier transformation in to the time domain, the first order statistics can be matched to long term annual measurements.

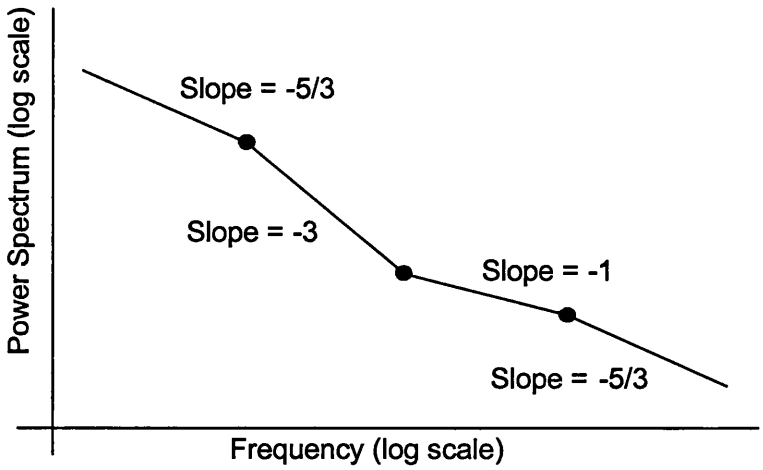

Figure 5.2-3 Idealised power spectrum of log rainfall

5.3 Empirical-Statistical Models

5.3.1 Matricciani-Riva

While not designed to produce attenuation time series, several studies by Matricciani-Riva on the analysis of satellite beacon data at V-band frequencies, are particularly relevant to this study. [Matricciani, et al., 1995] analyses the spectral characteristics of slant path beacon measurements, and identifies that which can be attributed to rain and scintillation. They find the spectral density of rain attenuation to show the theoretical -20dB/dec slope at frequencies up to 0.07 Hz for a slant path at 49.6 GHz. They also find it possible to extract high frequency components which clearly show the $f^{8/3}$ relation predicted for scintillation beyond 0.07 Hz.

The most interesting observation is the derivation of a statistical relationship between scintillation and simultaneous rain attenuation (mainly at low attenuations), through regression analysis of empirical data. A model of the log form is proposed, which links the level of rain attenuation, A with the standard deviation of scintillation σ.

Such a model has obvious application in the development of synthetic time series, in which the inclusion of such properties will improve the integrity of the result. In addition, it confirms the additive nature of the time series (in dB's).

5.3.2 Fiebig Model

[Fiebig, 1999, 2000, 2002] proposes a novel rain attenuation time series model which uses parameters from satellite beacon measurements to simulate stochastic rain fading with equivalent statistics (PDF). These parameters depend on the specific conditions of measured data, such as climatic zone, frequency, elevation angle, season and time of day.

5.3.2.1 Processing Measured Data for Fiebig Model

The approach has been to classify time series measurements of satellite beacon attenuation (in decibels) into three segment types, depending on the short term fluctuations of attenuation, as shown in Figure 5.3-1.

- C segments – almost constant received power,
- D segments – more or less monotonically decreasing received power,

- U segments – more or less monotonically increasing received power.

An assumption is made that the attenuation level $a(t)$, at a given time is dependant on the attenuation level at a previous time $\Delta\tau$, and on the type of the signal segment (C, D or U). Statistics are generated for each segment type for the PDF of $P(y|x)$, which is the likelihood that the attenuation is y (dB) conditioned that it has been x (dB) $\Delta\tau$ seconds before. Figure 5.3-2 gives examples of the measured PDF's of $P(y|x)$ for various values of x and $\Delta\tau = 64$s for each segment types. Observing that the PDFs have a Gaussian like shape, the first order statistics, for the mean $(\mu_j(x), j \in \{C, D, U\})$ and standard deviation $(\sigma_j(x), j \in \{C, D, U\})$ of attenuation at time $\Delta\tau$ are recorded.

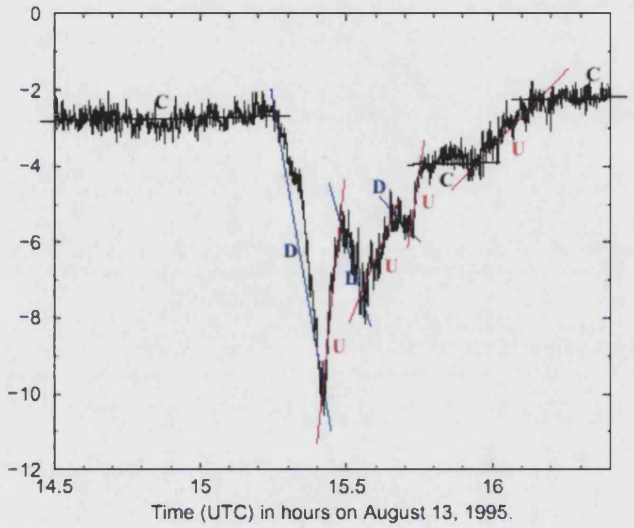

Figure 5.3-1 Fiebig-Schnell Classification of received signal type by segmentation [14]

[14] http://www.dlr.nr.de/projects/kaband

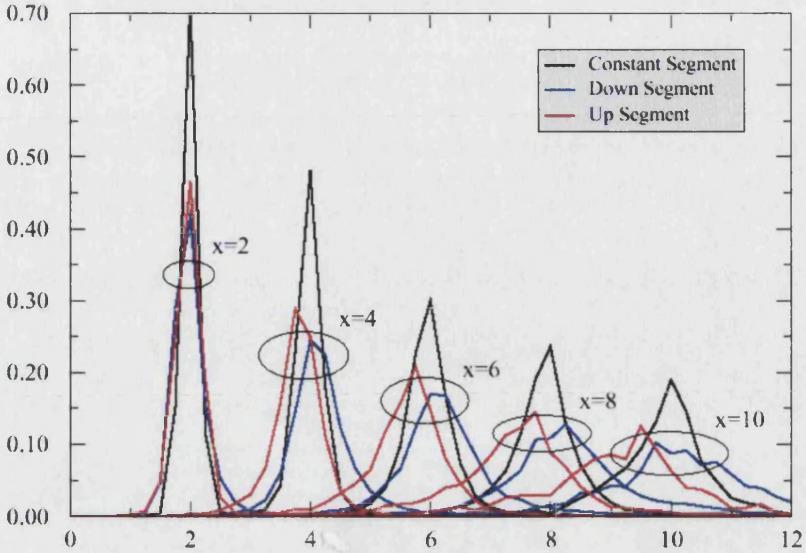

Figure 5.3-2 Measured PDF's of P(y | x) *for various values of* x *and* $\Delta\tau$ = *64s.* [14]

5.3.2.2 Channel Model

The channel model generates an attenuation time series such that every sample $y_s(iT_s)$, $i=1,2,\ldots n$ is the outcome of a single experiment of the Gaussian random variable z. Mean value $\mu(x)$ and standard deviation $\sigma(x)$ of z depend on both the previous sample $x = y_s((i-d_1)T_s)$ and the type of signal segment $\Delta(iT_s)$, where $\Delta(iT_s)$ is defined as:

Eqn. 5-6
$$\Delta(iT_s) = \begin{cases} C \Rightarrow y_s((i-d_1)T_s) - y_s((i-d_2)T_s) = 0 \\ D \Rightarrow y_s((i-d_1)T_s) - y_s((i-d_2)T_s) > 0 \\ U \Rightarrow y_s((i-d_1)T_s) - y_s((i-d_2)T_s) < 0 \end{cases}$$

where d_1, d_2 are integers defining the time interval which is the basis for the classification of signal segments and $d_1 < d_2$. T_s is the sampling period and y_s is the attenuation in decibels given in Eqn. 5-7 [Fiebig, 1999, 2000, 2002].

Eqn. 5-7
$$y_s = \begin{cases} 0, y_s < 0.5 \\ \lfloor y_s + 0.5 \rfloor, 0.5 \le y_s < 40.5 \\ 40, 40.5 \le y_s \end{cases}$$

5.3.2.3 Fiebig Time Series

[Fiebig, 2002] gives the model parameters based on a propagation measurement campaign recording a 40 GHz beacon of the Italsat satellite. The mean and standard deviation for different values of attenuation and segment type are given by the equation of a polynomial fit to the recorded data in Figure 5.3-2. Appropriate values for T_s, d_1 and d_2 have been found empirically comparing the statistics obtained from the time series generator and those obtained from recorded data. An example rain attenuation time series obtained from the model is shown in

Figure 5.3-3 for $T_s = 64s$, $d_1 = 1$ and $d_2 = 2$.

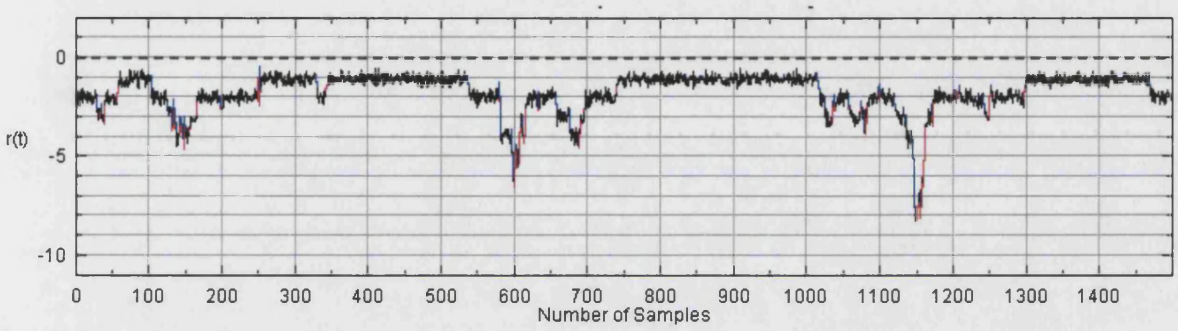

Figure 5.3-3 Fiebig rain attenuation time-series example [14]

5.3.2.4 Conclusions on Fiebig Model

The model captures the dynamic nature of rain attenuation time-series, producing a non-stationary rain attenuation time-series where adjacent samples are spaced about a minute apart. It can also be shown that the first order output statistics match those of the recorded satellite beacon data upon which they were based.

The greatest disadvantage of the Fiebig model is the need to have recorded satellite beacon data for the location and conditions required. The author proposes modelling seasonal and diurnal variations by switching the equation of the mean and standard deviation of each segment type for different recorded periods. There is no facility to model different earth stations cofigurations (including antenna characteristics, elevation angle, and location) or climatic conditions. Indeed, if beacon measurements were available in the first instance these could simply be used directly in these applications.

5.3.3 Matricciani Model

[Matricciani, 1991, 1994] has developed a model which converts rainfall rate time series in to rain attenuation time series for any frequency, polarisation and slant path. It can be used to generate statistics such as long-term PDFs, fade slope, fade duration and power spectra [Matricciani, 1994].

5.3.3.1 Theory for Matricciani Model

Converting rainfall rate time series into attenuation directly (using the well known power law[15]) is only likely to be accurate for vertical paths. Attenuation along a slant path is not only a function of the rainfall amount measured at any single point in the path, but the contribution along the whole path. This effect is highlighted when considering the duration of rain and attenuation events, as shown in Figure 5.3-4. Rainfall events can have a short duration as the storm moves over the rain gauge, but can remain present on the slant path producing a longer and smoother attenuation fade.

[Matricciani, 1991] uses the synthetic storm technique to convert rainfall rate measured at a rain gauge and averaged over 1 minute, to a rainfall space-series along a line, using an estimate of the storm translation speed v to transform time to distance. This method provides an estimate of the distribution of rainfall rate with distance and has been successfully used to predict attenuation on terrestrial radio links [Watson, et al., 1977]. An average value for v at the 0°C isotherm height can be taken from meteorological measurements (radar or radiosonde profiles) or using ITU-R P839. Alternatively, the generated statistics are found to be nearly insensitive to v if $v \geq 6$ m/s and a value of $v = 10.6$ m/s has been suggested [Matricciani, 1991].

[15] $A = kR^{\alpha}.L$ as given by [ITU-R, P838-1]

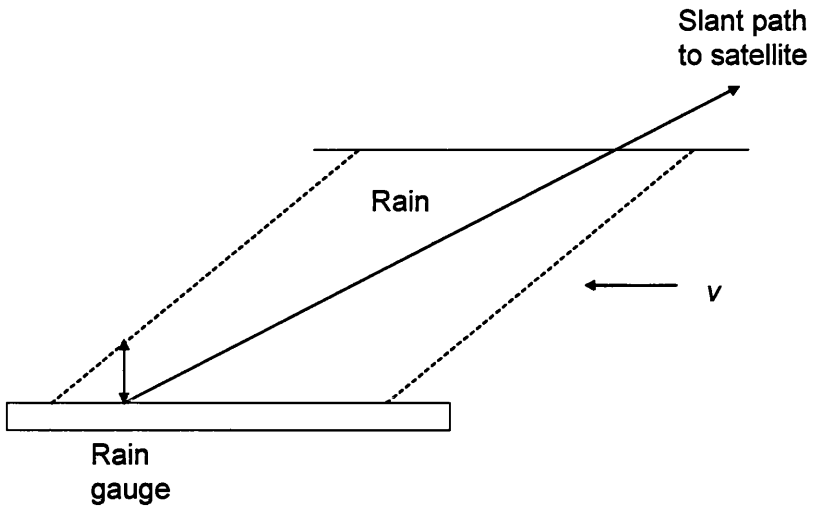

Figure 5.3-4 Geometrical structure of rain events

5.3.3.2 Results for Matricciani Model

Due to the lack of 1 minute rainfall rate time series data, it has not been possible to reproduce the Matricciani model. [Fiebig and Lemorton, 2002] shows a good comparison between generated rain attenuation time series and Italsat beacon data at 18.7 GHz.

Using the storm translation speed the same rainfall rate time series yields a rain attenuation time series of proportionally shorter total duration but with higher average attenuation for values above 10.6 m/s. While it yields rain attenuation time series of longer total duration and lower average attenuation for values below 10.6 m/s.

5.3.3.3 Conclusions from Matricciani Model

The Matricciani model results in a close comparison with real beacon data. However, this is not too surprising, considering the use of high resolution rainfall time series measurements from the same site.

6 Sources of Data for Development of Time Series Generator

The success of an empirical temporal time series model will be entirely dependant upon the measurements upon which it is based. Several different sources of suitable meteorological data were considered during this study.

6.1 Satellite Beacon Data

Beacon measurements from satellite propagation experiments such as ITALSAT [Carducci and Francesi, 1995], provides the ultimate source of attenuation time series data. The ITALSAT F1 satellite carries a propagation payload with three beacons at 18.7, 39.6 and 49.5 GHz. During its operational lifetime (1993 to January 2001), a huge amount of attenuation data, usually sampled at 1 Hz, has been recorded at around a dozen sites across Europe. Analysis has led to many important EHF propagation statistics and studies are ongoing [COST280].

Due to the high cost and limited number of measurement sites, satellite beacon data is not readily available for studies outside sponsoring institutions. Fortunately, two periods of ITALSAT measurements were available during this study:

(1) 20 non-consecutive rainy days recorded at Spino D'Adda, Italy, made available through the framework of [COST255];

(2) 2 years of measurements recorded at Sparsholt, UK, kindly supplied by the Rutherford Appleton Laboratory[16].

A single example of a rainy day measurement from (1) is shown in Figure 6.1-1. This data has been used to investigate modelling approaches and the properties of the power spectral density of attenuation. Data from (2) has been used to validate the proposed time series model.

[16] Radio Communications Research Unit (RCRU) at Rutherford Appleton Laboratory, http://www.rcru.rl.ac.uk

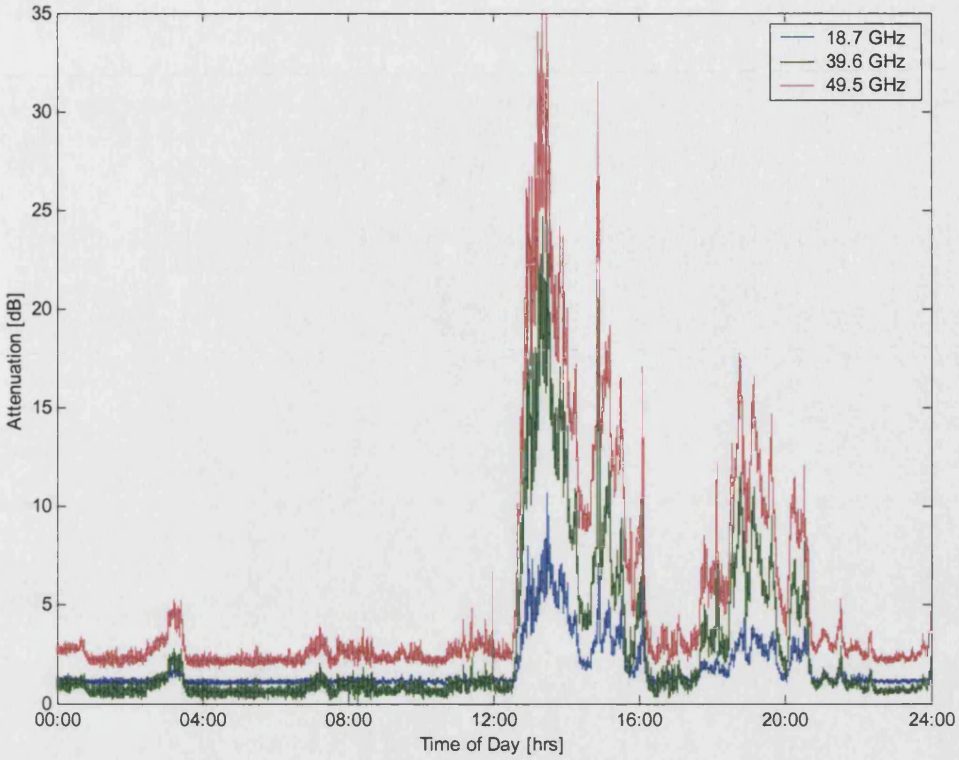

Figure 6.1-1 ITALSAT beacon measurement at Spino D'Adda, 07 January 1994

6.2 Hourly Synoptic Data

Meteorological Office hourly synoptic data from 141 European stations is available from the BADC[17]. The parameters include present and past weather, rainfall amount (resolution 0.1mm), cloud amount, type and base height, wind direction and speed, visibility, temperature measurements, water vapour pressure, relative humidity, mean sea level pressure, rainfall and gust speed and direction. Data is currently available for the period 1990 to 1996.

The hourly rainfall amount was considered as a possible foundation for the rain attenuation time series model. However, it became clear from hourly temporal plots that simple bilinear interpolation results in smoothed, long duration rain events. One method considered for the introduction of high frequency components of rainfall was fractal interpolation [Puente, et al., 1999]. Using this approach, satellite beacon data would be decomposed to extract its *fractal*

[17] British Atmospheric Data Centre, http://www.badc.rl.ac.uk

dimension[18]. A space-filling fractal interpolation function, scaled by fractal dimension, is derived and passes through each rainfall point. The mathematical theory underpinning this technique is still being studied and its use was considered too complex for this model.

In an approach used by [Howell and Watson, 2001] for a study into the planning of fixed millimetre wave radio links, hourly synoptic rainfall rates (R_{60}) have been scaled to 1 minute intensities (R_1). This scaling factor (R_{60}/R_1) is the ratio of rainfall intensities exceeded for a given percentage time (in this case 0.01%) measured using rain gauges having integration times of 1 minute and 1 hour.

6.3 One Minute Rain Gauge Network

The UK Meteorological Office have a database of 1 minute rainfall rates collected from 53 sites in UK and Northern Ireland over the period 1986 to 2000. These measurements recorded using Solid State Event Recorder (SSER) raingauges, record the amount of rainfall (typically in multiples of 0.2mm) during a period that is dependent on the rainfall intensity. At rainfall rates greater than about 12 mm/hr the time between recordings is 1 minute.

The SSER dataset has been used in further studies by [Howell and Watson, 2001] into the R60/R1 scaling ratio, in which the mean ratio is around 0.36% (for 0.01% exceedance time). However, the ratio is highly climate, and hence location, dependant. In an extension, the BADC hourly records have been combined with the SSER sites, to produce contour maps of the rainfall intensity (mm/hr) exceeded for 0.01% of the time.

The high temporal resolution of the SSER dataset would make it an ideal driver of the time series model of rain attenuation. Improvements to the low spatial resolution between UK sites by combining with the BADC dataset has already been demonstrated in previous studies. The main disadvantage was the desire to model larger European coverage areas, such as those used in current commercial geostationary satellite systems. Consideration was given to the generation of rain cells with high temporal resolution which could be moved across a European area to simulate rainfall. This type of approach introduces the possibility of producing climates with disjoint ground (rainfall) and upper air (cloud) conditions due the combination of measured and simulated conditions.

[18] fractal dimensions quantify the static geometry of an object.

6.4 Radiosonde Data

A dataset consisting of radiosonde data from stations worldwide, including from 28 UK launch sites is available from the BADC[17]. The data comprise vertical profiles of temperature, dew-point temperature, wind speed and direction at standard and significant pressure levels. The standard pressure levels are 1000, 925, 850, 700, 500, 400, 300, 250, 200, 150, 100, 70, 50, 30, 20 and 10 mb (from the surface to approximately 20-30 km). Significant pressure levels are calculated according to the Meteorological Office criteria and constitute levels at which significant events occur in the profile for example turning points.

The period of coverage in 1997 to present (some European stations are available from 1990), is updated weekly. Stations conduct ascents up to four times daily at the hours of 00, 06, 12, 18 GMT, when synoptic records are taken.

Radiosonde profiles are a good source of data for the calculation of cloud attenuation. They have an acceptable vertical resolution ideal for the calculation of cloud attenuation. The spatial distribution of stations across Europe is relatively low, but a composite interpolated 2D grid can be compiled, albeit losing small scale structure. The low temporal resolution for an individual radiosonde site is problematical, as temporal interpolation would also remove the small scale structure of cloud. It is such temporal characteristics which are of prime importance for time series generation. It will be seen later (section 6.6) that it is much better to use assimilated radiosonde profiles as input into the Unified Model (UM) of the atmosphere which can give model outputs of higher temporal resolution.

6.5 Meteorological Satellites

Meteorological images from METEOSAT earth observation satellites are available from the University of Nottingham[19]. The field of view from its geostationary orbit includes Europe, North Atlantic and North Africa at both visible and infra-red wavelengths, using an onboard radiometer. Extracted meteorological products include percentage cloud cover and motion, and hence the apparent wind speed and direction. Estimated cloud top height (by fitting the cloud top temperature to the forecast pressure-temperature profile) for up to three different

[19] http://www.nottingham.ac.uk/meteosat

cloud layers at 6 hourly intervals and 15 km horizontal resolution are available. Representative water vapour in the upper atmosphere between approximately 300 and 600 hPa is available.

Processed images taken every half hour are available from November 1999 to the present. Pixelated JPEG images at visible wavelengths have a resolution of approximately 2.5 km. A METEOSAT second generation satellite [ESA, 2002] currently undergoing in-orbit tests with an advanced radiometer payload, will be able to send back images every 15 minutes at 1 km resolution at visible wavelengths.

METEOSAT images deducing the presence of cloud over Europe is not enough to calculate cloud attenuation along a satellite path, which requires high resolution data concerning the vertical structure of clouds. [Paraboni, et al., 2002] describes a fade restoration system combining METEOSAT images and numerical weather prediction data (from the ECWMF) to determine subregions where rain is likely to occur. It assumes as rainy areas those where ECWMF predict rainfall provided that METEOSAT data indicate the presence of cloud and hence the possibility of rain.

Rainy areas are then transformed into attenuation areas through the EXCELL [Capsoni, et al., 1987] method and are used to optimise downlink satellite power across spot beams. A 6 hour updating time has been proposed limited by current ECWMF time-steps. It seems that such a system could be improved by combining second generation cloud images and weather radar images where available. Providing predictions of higher spatial and temporal (15 minute) resolution may enable dynamic optimisation of satellite downlink power and where possible, downlink coverage (for satellites with active or steerable antennas).

6.6 Unified Model

The Unified Model [Met.Office, 1998] is a numerical weather prediction model (realised in software) developed by the UK Meteorological Office to describe the time evolution of the atmosphere. Meteorological measurements provide the initial conditions to a set of hydrostatic equations[20] relating to the horizontal motion of wind, potential temperature and specific humidity. Further observations (e.g. radiosonde profiles) are assimilated in to an analysis

[20] the model is always in hydrostatic balance which means there are no vertical accelerations.

correction scheme over the model period, which iteratively "nudges" the forecast solution towards the observations.

The physical processes represented by the model include [Met.Office, 1998]:

- Atmospheric radiation allowing for the effects of clouds, water vapour, ozone, carbon dioxide and a number of trace gases;
- Land surface processes including a multi-layer soil temperature and moisture prediction scheme;
- A treatment of the form drag due to the sub-grid scale variations in orography;
- Vertical turbulent transport within the boundary layer;
- Large-scale precipitation determined from the water or ice content of a cloud;
- The effects of convection through a scheme based on initial buoyancy of a parcel of air. It includes entrainment, detrainment and the evaporation of falling precipitation.

6.6.1 Spatial & Temporal Resolution

The Meteorological Office uses the Unified Model (UM) operationally to provide numerical weather forecasts for periods of a few hours to a few days ahead. At present we have used hourly outputs, but in the longer term improvements in computing power should allow higher resolution outputs to be practical. Both global and regional configurations are possible, with the larger scale model providing lateral boundary values for higher resolution regional models. The current UK Mesoscale Model covers the UK and northern France with a horizontal grid size in the order of $11km^2$ (3.3km by 3.3km) but improvements in modelling and data inputs (particularly from meteorological satellites and weather radars) should improve this further.

In the vertical, diagnostic outputs occur on 38 terrain-modified pressure levels from the surface to an altitude of approximately 15km. The distance between pressure levels is linearly related to the surface pressure at each point, providing the highest resolution (~100m) close to the surface and gradually flattening towards the upper most layers (~1km at 15km altitude). Thus providing the greatest level of detail close the surface where weather conditions are most variable.

6.6.2 Mesoscale Model Outputs

UK Mesoscale Model data has been provided for this study by the University of Reading, under the auspices of the Universities Weather Research Network (UWERN) [Panagi and Dicks, 1997]. Periods of data were supplied to correspond to those for which concurrent satellite beacon data was also held (06 to 13 August 1999 and 30th October to 5 November 2000).

A complete list of available prognostic, diagnostic and derived Mesoscale model output fields is given in Appendix A. Due to the large data processing requirements a smaller subset of output fields was requested as given in Table 6-1. It is worth noting that future studies could make use of additional output fields (e.g. precipitation, cloud liquid water content).

The "raw" Mesoscale model data was processed to derive the required meteorological data fields according to the equations given in Appendix B to Appendix I. The resulting three dimensional data grid for each field and at each time-step was interpolated to extract vertical profiles of pressure, temperature and humidity for specific locations. This data was thus used for the background fading effects (water vapour losses, cloud losses and scintillation intensity) but for rain at present we resort to using radar data with higher temporal & spatial resolution.

Table 6-1 Supplied subset of Mesoscale Model output fields

STASH[21]	Field	Symbol	Units
1	Surface pressure	P_*	pa
2	U component of wind	U	ms^{-1}
3	V component of wind	V	ms^{-1}
33	Orographic height	Z_*	m
3236	Temperature at 1.5m	T	k
3237	Specific humidity at 1.5m	Q	$kgkg^{-1}$
4201	Large Scale rain amount		kg/m^2
5201	Convective rain amount		kg/m^2
4004	Temperature on model levels	T	k
4010	Specific humidity on model levels	Q	$kgkg^{-1}$
16210	Height of freezing level	h_z	m

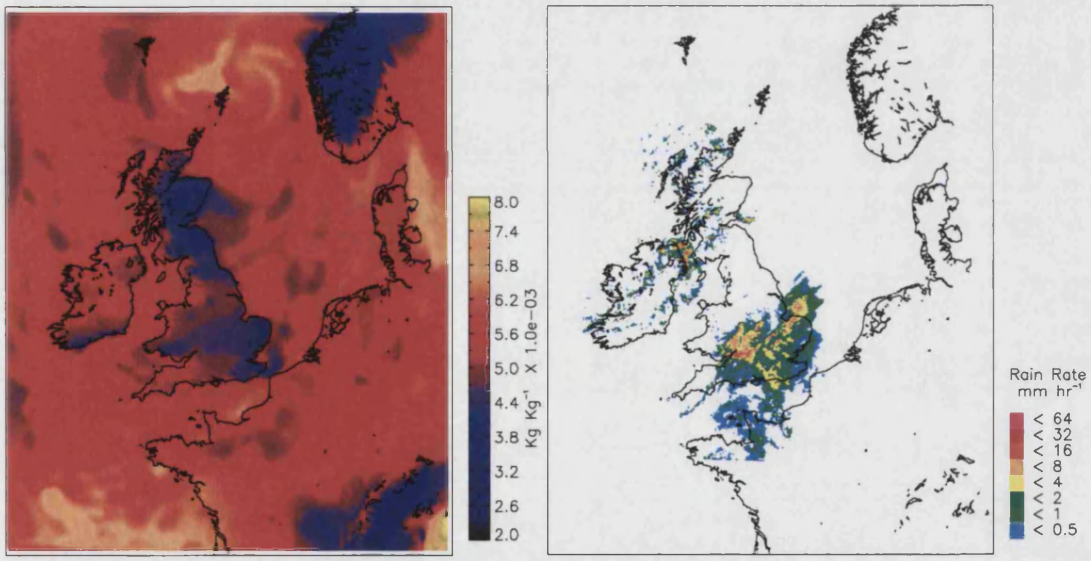

Figure 6.6-1 Illustrative left *a) Mesoscale Model Output – Specific Humidity grid on pressure level;* right *b) Network Radar Image*

6.7 Weather Radar

The UK and Irish weather radar network [Smith and Kitchen, 1999] has been developed over the last 30 years and currently includes fifteen C-band (5.65 GHz) radars. Of these 15 radars, two are in the Republic of Ireland and one is in Jersey. The network produces a composite

[21] Meteorological Office field code identifier.

image consisting of a 5km resolution 256x256 grid of surface rainfall rate estimates covering the whole of the UK and the Republic of Ireland. An example output of the weather radar network can be seen in Figure 6.6-1b)

The individual radar systems operate routinely on a cycle that repeats every 5 minutes. Radar reflectivity data (Z) is collected is collected in PPI (plan position indicator) mode at elevations of 0.5, 1.5, 2.5 and 4.0 degrees. The data is then processed to produce estimates of surface rainfall data (RR) on a 5km resolution Cartesian grid. Ground clutter suppression is achieved using a fixed clutter map and infilling contaminated data from higher elevation scans. Rainfall rate estimation is made using a Z-R power law relationship.

Every 15 minutes, at a predefined period, each radar transmits its latest image to the Meteorological Office in Bracknell where a composite image of 256×256 cells is generated. Each grid cell in the image contains the data from a single radar. If there are data available from two radars, the 'best' data is selected according to a hierarchy map. The hierarchy map ranks for each location, which radars are able to provide the highest quality estimates. In practice this normally means that the data chosen for a particular grid cell is the closest available to the ground at that location.

Weather radar images were supplied by the University of Reading under the auspices of UWERN for the same periods as UM data. The processing of "raw" radar images to extract point rainfall rates (mm/hr) is given in Appendix H.

7 New Approach to Time Series Generation

7.1 Introduction

The time series approach is based on three underlying assumptions:

(1) The short-term (15 minutes or less) statistics of fading between fixed radio links are statistically independent;

(2) The intermediate-term (15 minutes to a few days) statistics of fading are described by the movement of weather systems as observed on meteorological radars (15 minutes to a few hours) or by Mesoscale weather forecasting techniques (hours to a few days);

(3) The long-term spectral and statistical properties of fading during aggregated events are stationary.

Assumption (1) covers short-term scintillation fading which is essentially determined on a local scale (typically a few metres [Tatarskii, 1961]). This assumption also covers the fine scale structure of rain that leads to independent fading over a few kilometres [Allnutt, Fukuchi, 1988]. Within assumption (2) we take account of the larger scale background effects that apply to rainy conditions, including the occurrence of cloud and water vapour both of which lead directly to loss of signal but also to enhanced scintillation intensity. Assumption (3) is not essential but has been taken for expedient in this initial work. If the technique that we describe were to be used over a long period of time then stationary could be the subject of continuous evaluation.

Figure 7.1-1 shows schematically the system that we have adopted to generate slant path attenuation time series, and lists the models used in determining the attenuation outputs from the meteorological input data. The prediction models that we have adopted have all been tested against real fading data, several of them in the context of COST 255 [Leitao and Watson, 1986].

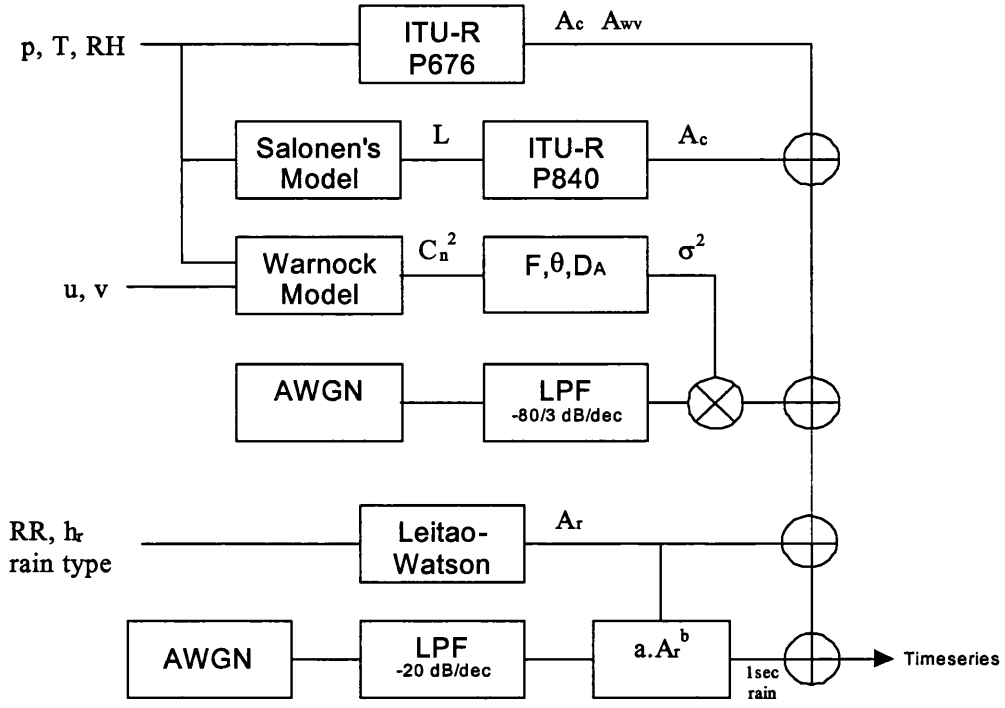

Figure 7.1-1 Outline block diagram of the time series generator

7.1.1 Power Spectrum

EHF fading caused by the effects of rain, cloud, water vapour and scintillations typically shows three spectral regimes. We have used 40 and 50 GHz time series data supplied in the framework of EC COST 255 [COST255] to illustrate this point. Similar conclusions have been drawn in [Matricciani, et al., 1995]. We have thus set an objective for our time series generator to reproduce the an on-average power spectrum during rain as shown in Figure 7.1-2.

The lower part of the spectrum ($f < f_L$) rolls-off at –20 dB/dec during rain or remains stationary in clear air. Above f_L the spectrum represents scintillation caused by atmospheric turbulence along the path. Between ($f_L < f < f_C$) the spectrum depends on how the turbulence was created and has no describing formula (it is usually seen to be flat), followed by a region ($f > f_C$) that rolls-off at –80/3 dB/dec predicted by turbulence theory [Tatarskii, 1961].

The spectrum up to the radar sampling frequency f_l, is determined from the physical evolution of rain over time. Theoretically, the corner frequency of turbulence f_c can be related to the transverse wind velocity v_n (m/s) given by the UM data (refer to Appendix I). However for simplicity both f_L and f_C have been taken from beacon observations and correspond to 0.07 and 0.3 Hz respectively.

Through combining all of these components we are thus able to represent the lower frequency (> 0.0011 Hz) background loss variations from cloud, gases and rain with the smaller scale rain intensity fluctuations (0.0011 to 0.7 Hz) and also the finer scale scintillations relating to rain, gases and clouds (> 0.3 Hz).

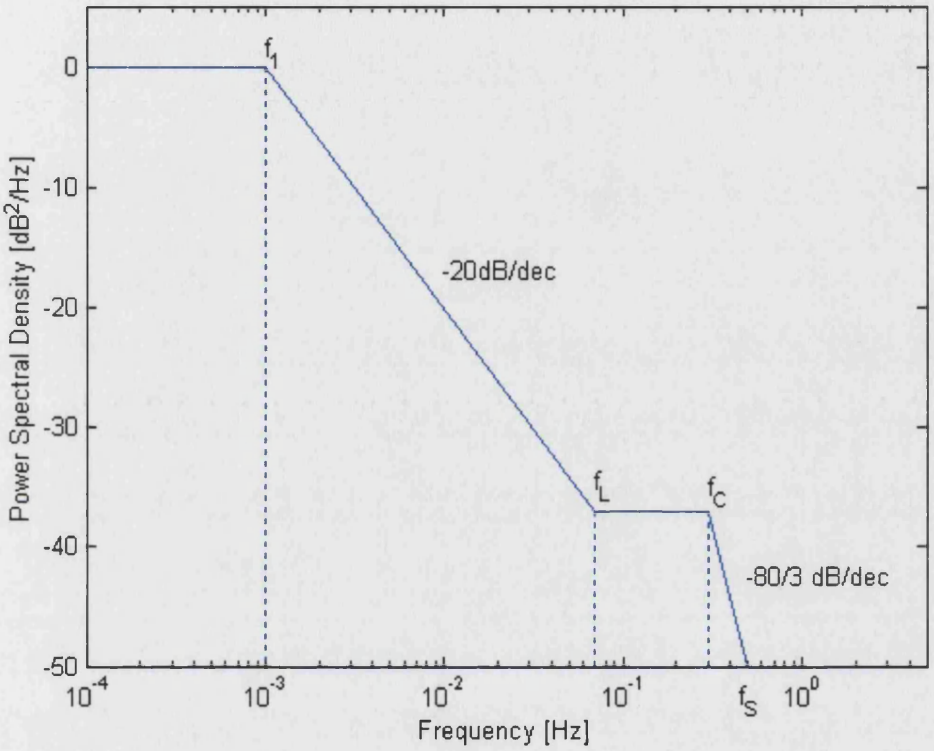

Figure 7.1-2 Ideal on average power spectral density of slant path attenuation

7.1.2 Cumulative Distribution

The long-term cumulative statistics of SHF and EHF fading (dominated by rain) are well described by a distribution of the log-normal form (see for example [Lin, 1973, ITU, 1996]). This observation, in keeping with the modelling of attenuation by rain as a multiplicative process [Lin, 1973], defines the type of long-term target distribution for our time series generator. The moments of the distribution will depend upon the climate and location of each site.

7.2 Rain Attenuation Time Series Model

7.2.1 Low frequency Components

The duration and intensity of rain events for any location within the composite image are determined from weather radar observations. Rainfall rate is first converted to attenuation using an appropriate model. Here an approach able to deal separately with the occurrence of widespread and showery rains is most appropriate [Leitao and Watson, 1986, Watson and Hu, 1994] showing good results when compared to Italsat and Olympus satellite beacon data [Konefal, et al., 2000]. The type of rain is determined from the UM prognostic fields large scale rain amount and convective rain amount by applying the following rule:

- widespread rain if large scale rain amount > convective rain amount
- showery rain if convective rain amount > large scale rain amount

Figure 7.2-1 and Figure 7.2-2 illustrate the difference between simulated rain attenuation assuming showery and widespread rain types compared to Italsat satellite beacon data. It illustrates the importance of increasing the predicted attenuation during convective storms.

Alternatively, [ITU-R, P838-1] could be used, but does not distinguish showery and widespread rain. Experiments showed the ITU-R model underestimated rain attenuation during particularly during storm periods.

7.2.2 High Frequency Components

Higher frequency fluctuations in the rain attenuation time series are added using a filtered Gaussian noise generator with a -20 dB/decade spectral roll-off. The non-stationary nature of real events, in particular the build up and fall off periods, are represented by modulating high frequency fluctuations with the local intensity of the underlying shape. A scaling law is applied to control the intensity variation of the high frequency rain components.

Optimum coefficients for the short example dataset were determined through inspection. A much larger dataset will be required to define long-term scaling coefficients.

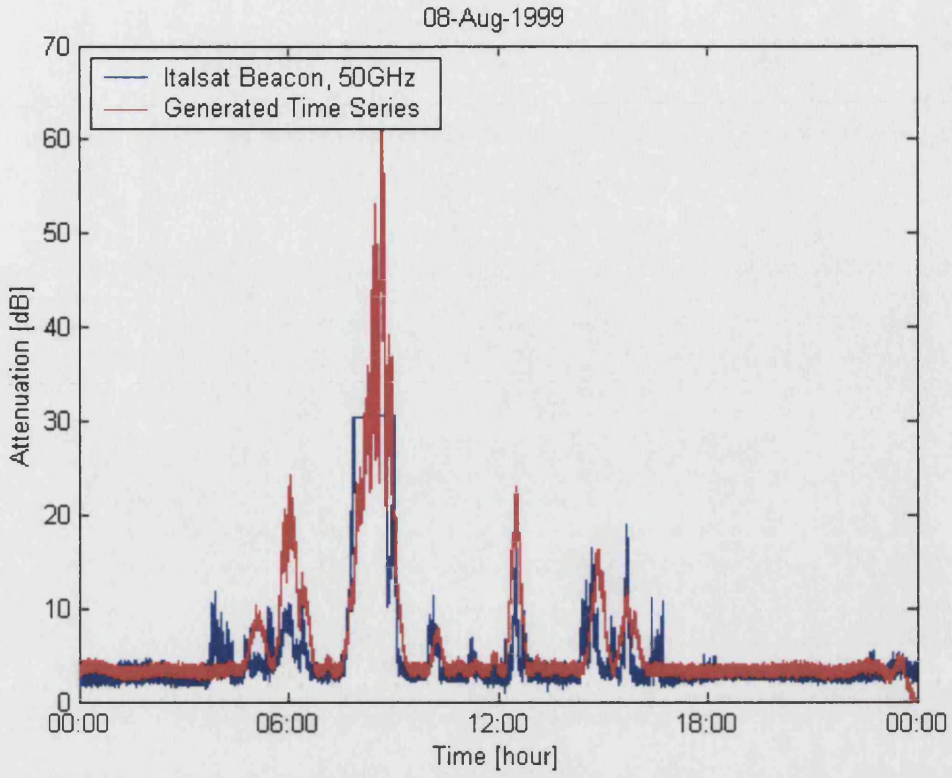

Figure 7.2-1 Comparison of simulated rain attenuation time series for widespread rain

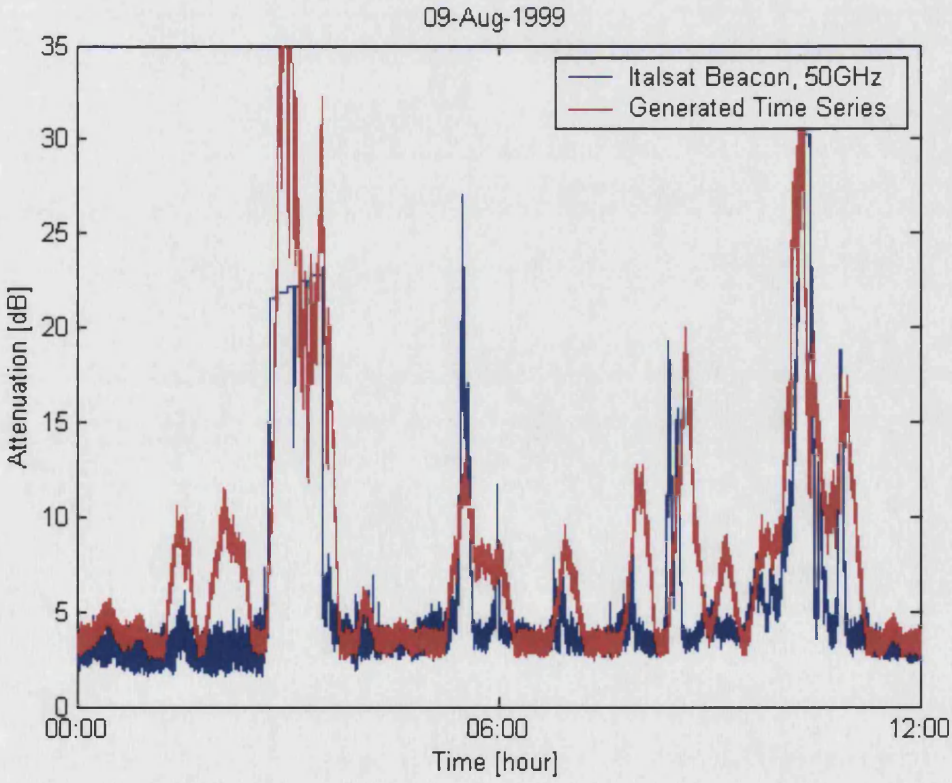

Figure 7.2-2 Comparison of simulated rain attenuation time series for showery rain

7.3 Gaseous Attenuation

The attenuation due to oxygen and water vapour in the atmosphere has been calculated at each time-step from UM surface data using Annex 2 of [ITU-R, P676-4].

7.4 Cloud Attenuation Model

In the Earth's atmosphere, regions in which the local supersaturation of water vapour exceeds more than a few percent rapidly become filled with cloud in liquid or ice phase (depending on temperature). The UM Large-Scale cloud parameterization scheme returns as a prognostic variable for each grid box, an instantaneous fractional cloud cover, which can be more accurately thought of as "non-clear sky fraction". Secondly, it partitions the total water content in a grid box between water vapour content and mean cloud water content.

Initial proposals were to use these UM fields as inputs to the calculation of slant path cloud attenuation. However, the large vertical separation between layers of mean cloud water content, produced a smooth vertical profile and thus over exaggerated total cloud water content. For this reason, the UM cloud prognostic variables were not used directly.

7.4.1 Cloud Liquid Water Content

Before the calculation of cloud attenuation the cloud liquid water content is determined from UM upper-air outputs using the approach of [Salonen and Uppala, 1991]. Salonen has already demonstrated this method on numerical weather prediction data to produce statistics of reduced liquid water content. (Note that the specific attenuation due to clouds depends on frequency, liquid water content and temperature. The reduced liquid water content of cloud is the columnar liquid water content normalised to 0°C.)

The presence of cloud in a vertical profile of relative humidity is detected using a critical humidity function given in Eqn. 7-1. When the local value of critical humidity (U_c) is exceeded, the measurement is assumed to be in cloud. Figure 7.4-1 shows an example critical humidity profile based on a vertical profile of relative humidity from the UM. The height of the cloud base and top are determined through linear interpolation of graph intersections.

Eqn. 7-1 $$U_c = 1 - \sigma(1-\sigma)\left(1+\sqrt{3}(\sigma-0.5)\right)$$

where σ is the ratio of pressure on the considered level and at the surface level.

Subsequently, the liquid water content (g/m^3) is calculated as a function of temperature, t (°C) and height, h_c (m) from the cloud base. An integral of the function for determining liquid water content between two heights is given Eqn. 7-2 of [OPEX, 1994]. In the calculations the temperature is approximated by the mean temperature of the heights h_j and h_{j+1}.

Eqn. 7-2 $$\int_{h_j}^{h_{j+1}} w dh_c = w_o(1+c\times t)\times\frac{h_{j+1}^{a+1}-h_j^{a+1}}{(a+1)\times h_r^a}\times p_w(t,t_i)$$

where a = 1.4; c = 0.04; w_o = 0.14; $p_w(t)=\begin{Bmatrix}1 & 0°C<t\\ 1+\frac{t}{20} & -20°C<t>0°C\\ 0 & t<-20°C\end{Bmatrix}$

7.4.2 Cloud Attenuation

Finally, the slant path cloud attenuation can be predicted from the work of [Liebe, et al., 1989] as now also embodied in [ITU-R, P840-3]. This combined approach has been shown to give good predictions by [Davies, et al., 1999].

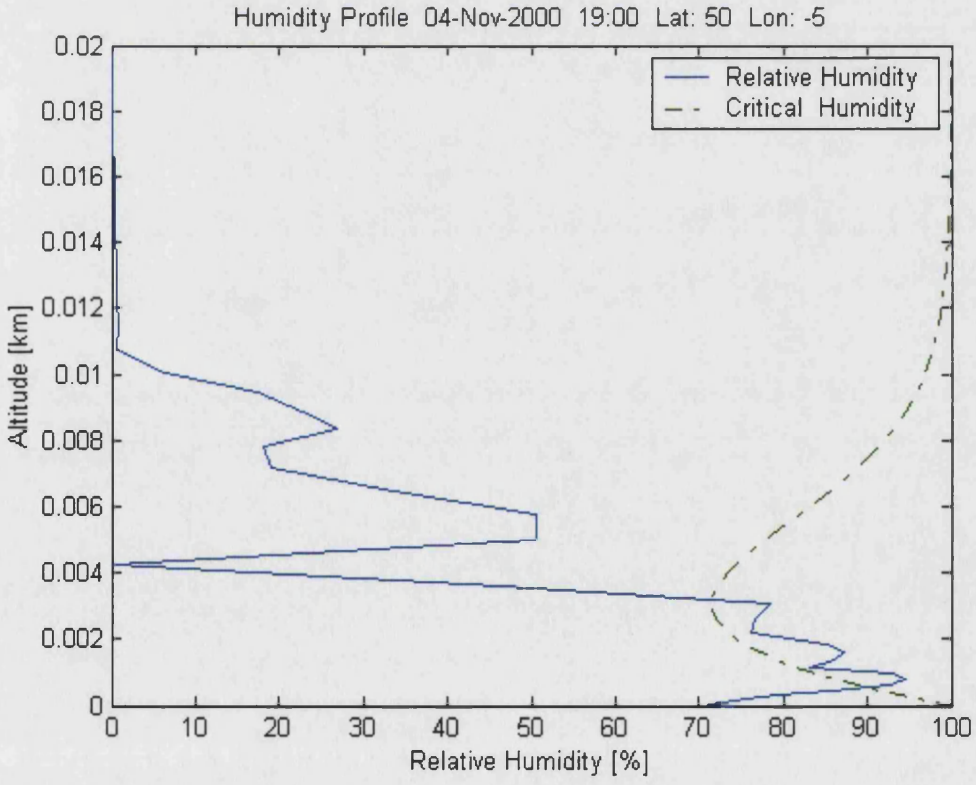

Figure 7.4-1 Example of critical humidity profile using a UM vertical profile

7.5 Scintillation

Atmospheric turbulence causes random variations of refractive index, producing small fluctuations in the amplitude of the received signal. Scintillation occurs in clear sky, but is predominately induced by turbulent eddies, formed by mixing air masses of different temperatures and humidities in cloud [Vanhoenacker, et al., 1991]. The effect of scintillation is important when considering low availability systems (<99%) operating above 10GHz, especially those at low elevation angles (<10°) with small receiving antennas.

7.5.1 Scintillation Power Spectrum

The observed temporal power spectrum of scintillation [Vanhoenacker and Vander Vorst, 1985, Matricciani, et al., 1995, Otung, et al., 1998] has the form predicted by Kolmogorov theory for fully developed turbulence. The lower part of the spectrum ($f < f_o$) depends on how the turbulence was created and has no describing formula (near constant spectral density). Followed by a region ($f > f_o$) that rolls off according to a $f^{-8/3}$ power law. [Tatarskii, 1961] suggests the theoretical corner frequency (f_o) can be related to the transverse wind velocity v_n (m/s), at a Fresnel zone radius $\sqrt{\lambda L}$, given by Eqn. 7-3. Although, [Savvaris, et al., 2001] finds only a moderate correlation between f_c and wind velocity which decreases with frequency, from recent experimental results

Eqn. 7-3 $$f_c = \frac{0.57 v_n}{\sqrt{\lambda L}} \quad \text{(Hz)}$$

7.5.2 Scintillation Intensity

Empirical studies [Moulsley, et al., 1981, Ortgies, 1985, Otung and Evans, 1995] have shown that short scintillation intervals (up to 10 minutes) can be characterized as stationary periods with a log-normal amplitude distribution (Gaussian in decibels). Over longer periods scintillation intensity σ^2, varies due to changing turbulence conditions along the path, and has been modeled using a log-normal [Moulsley and Vilar, 1982] or gamma distribution [Karasawa, et al., 1988].

Statistical prediction models for σ^2 are based upon empirical results scaled using theoretical formula to match the link (frequency, elevation, antenna diameter). Climate conditions are included through values of monthly surface temperature and humidity. These models have the

drawback of being dependant on the experiment on which they were based, without knowledge of the physical turbulence on the path.

From the theory of wave propagation through a turbulent medium [Tatarskii, 1961], σ^2 of a stationary event can be related to the atmospheric refractive index structure parameter, C_n^2 given in Eqn. 7-4 [Vasseur, 1999].

Eqn. 7-4 $$\sigma^2 = 42.48 \frac{k^{7/6}}{(\sin\theta)^{11/6}} \int_{height} C_n^2(z) z^{5/6} dz \qquad (dB^2)$$

where $k = 2\pi/\lambda$ with λ the wavelength (m), θ is the elevation angle, z is the height above ground level (m). C_n^2 ($m^{-2/3}$) depends upon the refractive index gradient which can be calculated from vertical profiles of pressure (mbar), temperature (K), relative humidity (%), wind speed (m/s) and azimuthal direction (deg).

Following the method of [Warnock, et al., 1985], the structure parameter is estimated for horizontal slabs whose thickness define the resolution of turbulent flows in the atmosphere. Embedded in large scale laminar flows in the slabs, are many fine scale turbulent flows which extend down to scales of a few meters. The stability and wind shear of these flows are estimated from meteorological profiles, giving the Richardson number, R_i (dimensionless ratio of buoyancy to square wind shear) which is used to assess the stability of the layer. When $R_i < 0.25$ the flow becomes unstable and horizontally stratified turbulent layers are formed.

The refractive index structure parameter at a height z, is given by [Tatarskii, 1961, Ishimaru, 1978].

Eqn. 7-5 $$C_n^2 = aM(z)^2 L_0^{4/3} \qquad (m^{-2/3})$$

where $a \approx 2.8$, $M(z) = \delta n(z)/\delta z$ is the vertical refractive index gradient (m^{-1}) and L_0 is the outer scale of turbulence (m). By summing together the C_n^2 for all the layers in the slab we could directly calculate the profile structure parameter. In practice, a probabilistic approach must be used to estimate the mean refractive index structure parameter $\langle C_n^2(z) \rangle$, due to the insufficient fine scale of the meteorological data [Warnock, et al., 1985] :

Eqn. 7-6 $$\left\langle C_n^2(z)\right\rangle = aM_O(z)^2\left\langle R(z)\right\rangle \int_0^\infty L_0^{4/3} P_{L_0} \int_0^\infty P_S \int_{-\infty}^{\delta^2 Ric} \left(N^2\right)^2 P_{N^2} dN^2 dS dL_0 \qquad (\mathrm{m}^{-2/3})$$

where $M_O(z) = M_O N^2 R^{1/2}$ and R represents the humidity contribution to M^2. L_0, S and N^2 are random variable representing the outer scale of turbulence, the wind shear and the buoyancy forces, respectively and characterised by the PDF P_{L0}, P_S and P_{N^2}.

Appendix I details all the parameters involved in Eqn. 7-6 and how they are derived from meteorological parameters. Due to the low resolution of the UM vertical layers compared to the fine scale of turbulent flows (< 10m), linear interpolation was used to increase their resolution to 50m. An example C_n^2 profile using UM data is shown in Figure 7.5-1.

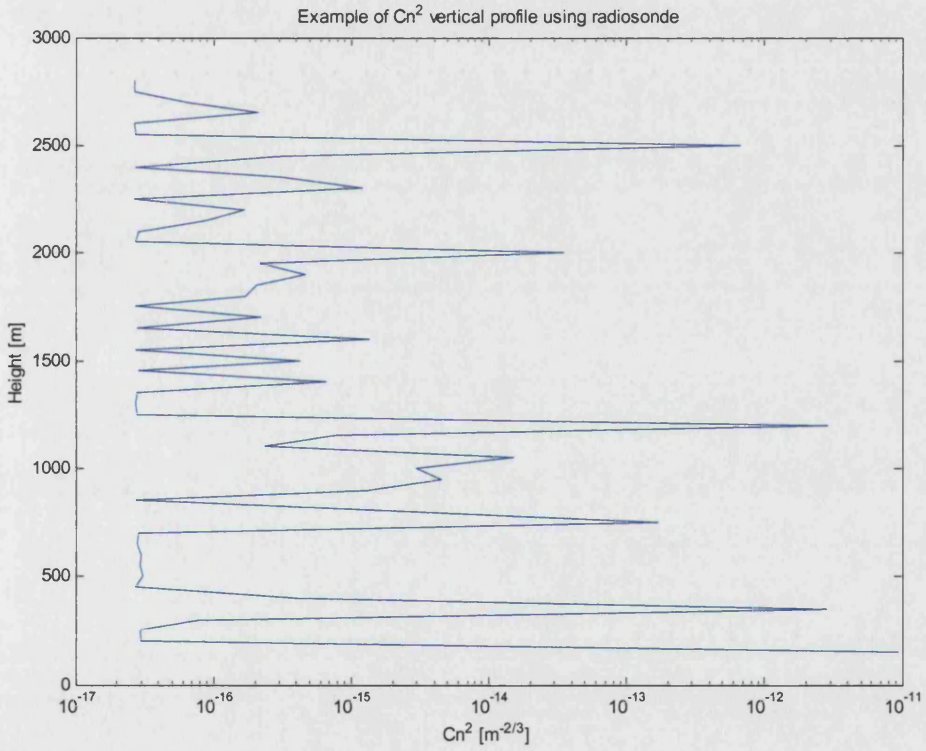

Figure 7.5-1 Example refractive index structure parameter C_n^2 using UM profile

7.6 Results

We should now be able to place satellite earth stations at arbitrary locations in the UK and generate time-series of attenuation that retain the temporal and spatial characteristics evident in measurements obtained in real weather systems. Figure 7.6-1, Figure 7.6-2 and Figure 7.6-3

illustrate a set of simulated attenuation time series at 49.5 GHz generated for three locations in the UK for 8th August 1999. The potential of the technique as a tool for the simulation of the performance of a network of stations is clear.

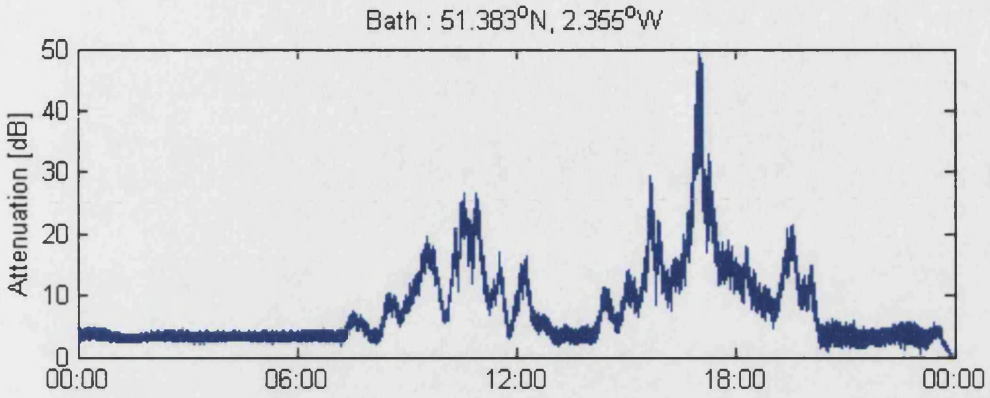

Figure 7.6-1 Example of Generated Time series from Bath

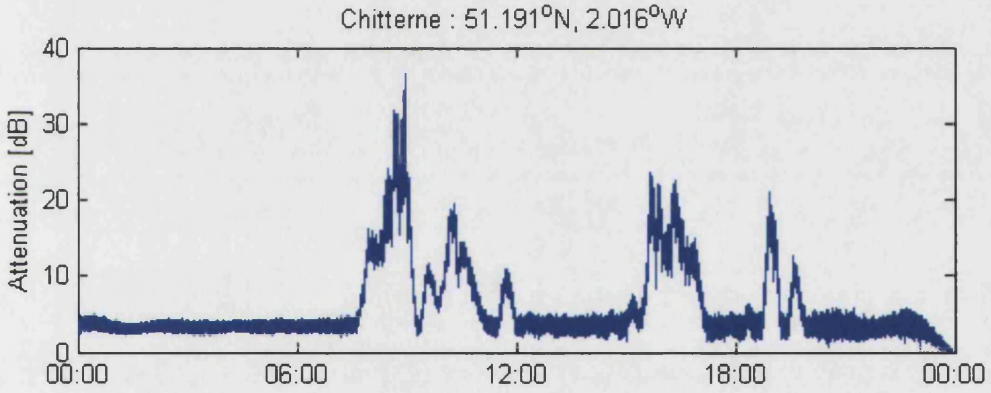

Figure 7.6-2 Example of Generated Time series from Chitterne

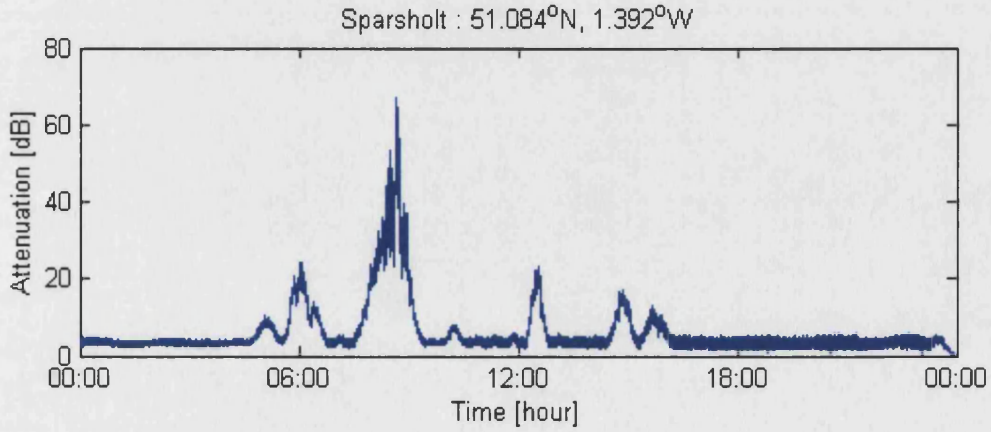

Figure 7.6-3 Example of Generated Time series from Sparsholt

7.7 Validation of Time Series Simulator

7.7.1 Power Spectrum

Given the original objective of the simulator, the obvious method of validation is to verify that the power spectrum of the generated time series is consistent with that of our idealised power spectrum shown in Figure 7.1-2. The power spectrum of the generated time series for Sparsholt is shown in Figure 7.7-1 and shows similar spectral characteristics to those in Figure 7.1-2. Bearing in mind that the simulated time series has been generated from a small sample of data this result is encouraging. Further long term comparisons should be made with a much larger data set.

7.7.2 Comparison with Measured Attenuation Time Series

A further attempt to validate the time series simulator, has been made using real satellite beacon data (supplied by the Rutherford Appleton Laboratory). We have attempted to validate the time series by comparing the attenuation time series generator output for Sparsholt to that directly obtained from an Italsat beacon receiver sited at Sparsholt (θ = 30°, D_A = 61cm). Figure 7.7-2 illustrates the measured time series at Sparsholt for the same period as simulated in Figure 7.6-3. It is important to note here that although the time series and simulated data are encouragingly similar, we should not expect to see 100% correlation, especially in the fine scale structure. The objective is to create a representative fading environment for periods of ~1 hour to 6 hours with a fine scale structure that will be useful to test the dynamic control systems associated with fade mitigation techniques. A further comparison is shown for 5th November 2000 in Figure 7.7-3, which also shows good agreement.

A more detailed validation process must of course compare the cumulative distributions of simulated and measured time series. We propose to compare the cumulative distributions of simulations and measurements for a number of 6 hourly periods. In order to observe the long-term spectra and cumulative distributions we should, of course have to make observations over a much longer period, but the general the form of these distributions is well known and in any case is dependent on location and climate [Baptista Poiares and Salonen, 1997, Konefal, et al., 2000].

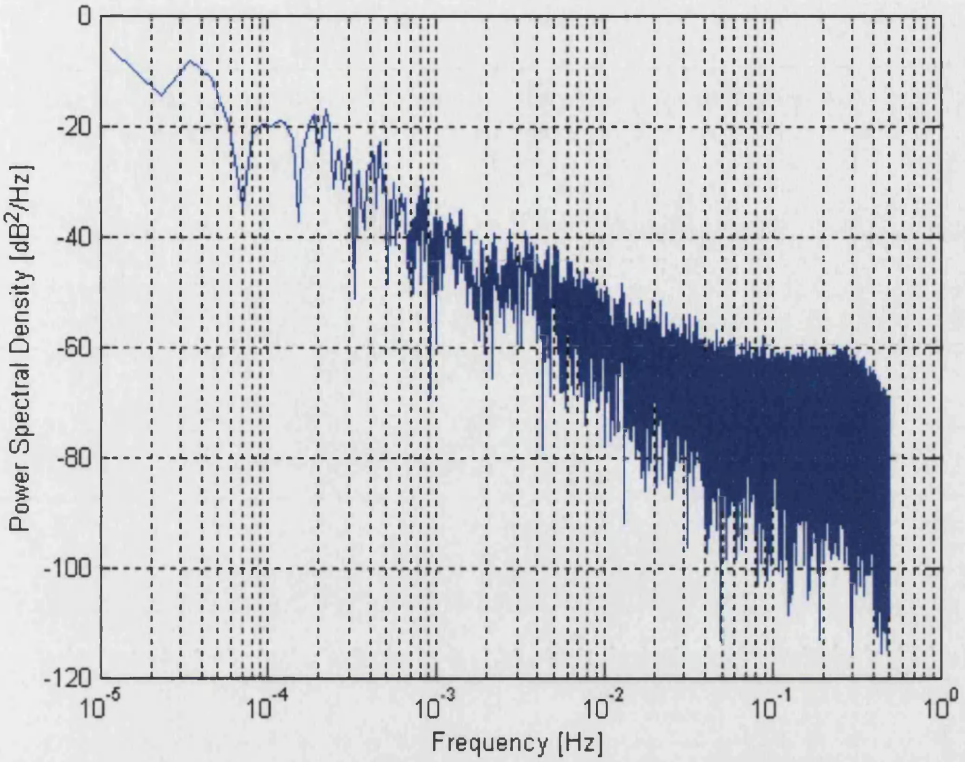

Figure 7.7-1 Power spectral density for the simulated Sparsholt time series shown in Figure 7.6-3

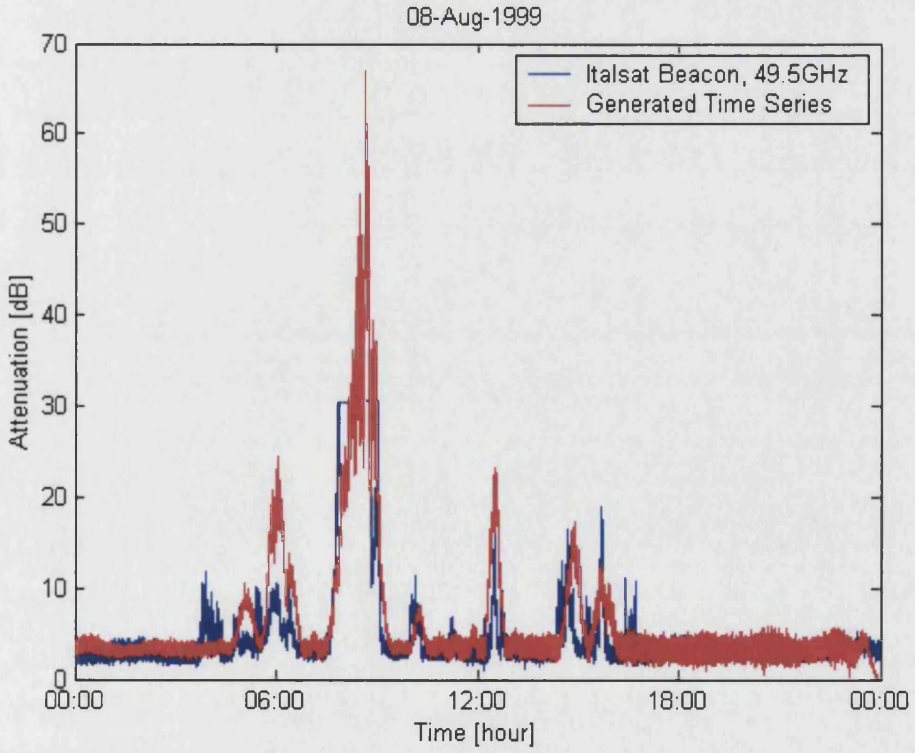

Figure 7.7-2 Comparison between measured Italsat link data and simulated time series

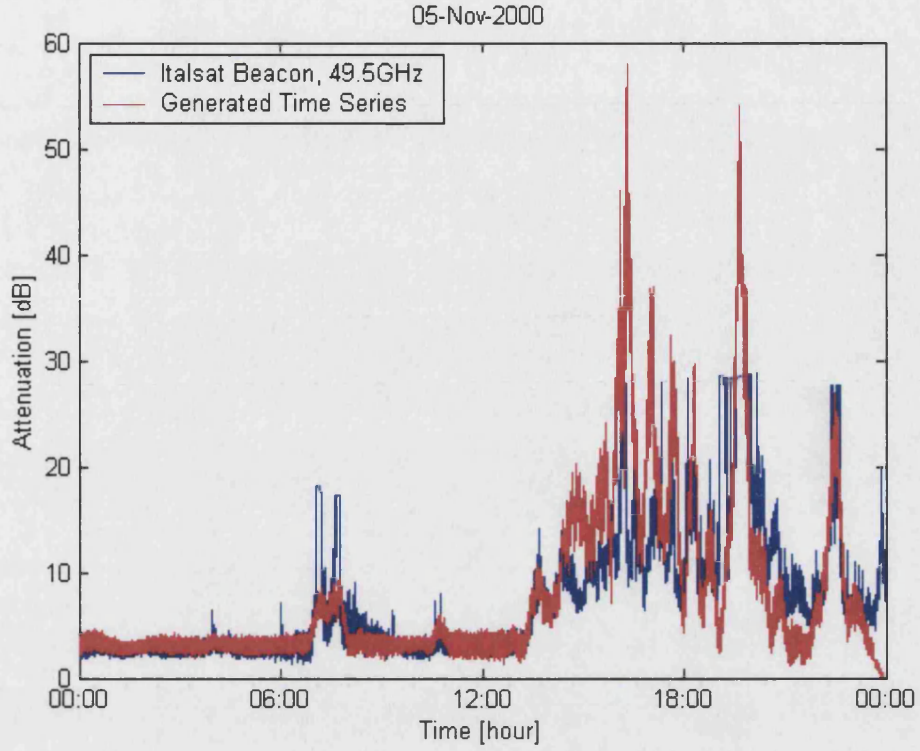

Figure 7.7-3 Comparison between measured Italsat link data and simulated time series

7.8 Conclusions

We have described a new approach to the realisation of an attenuation time series generator and demonstrated its potential for representing both the spatial and temporal properties of fading on EHF links. The simulator has immediate application to performance evaluation for EHF links that include fade-mitigation techniques, and the approach has longer term potential in terms of the operational management of links.

For use in performance evaluation, VSAT or DVS-RCST terminals can be arbitrarily located in the UK (or in the European region) and time series generated for all stations simultaneously. Such time series may then be used in conjunction with a network level simulator (such as OPNET) to determine the throughput and delay of networks of earth stations using various fade mitigation techniques to provide acceptable QoS.

8 System Modelling

8.1 Introduction

In preceding chapters, the short term atmospheric variability of the RF channel has been discussed, and a novel approach has been proposed for the generation of empirically based short-term physical layer fluctuations. In an extension to this study, the physical layer model has been integrated into an end-to-end simulation of a satellite multimedia network. The objective was to illustrate the end-to-end system performance as experienced by an end user of the test case system proposed earlier.

It is common for system engineers to include long term fixed propagation margins in satellite network models. Furthermore it is possible to simulate the end-to-end performance of point-to-point links using empirical beacon data [Gremont and Filip, 1999, Castanet, et al., 2002]. In this thesis a novel approach has been taken that aims to model realistic short term link performance across a typical geostationary coverage zone, with a large number of distributed subscribers in a satellite network. Such an approach is particularly significant when considering systems and technologies that have yet to be widely exploited, in view of the high financial risk associated with the introduction of unproven technology.

In the case of commercial multimedia V-band systems, the greatest risk is associated with the variability of the propagation environment and whether an acceptable service can be guaranteed to the customer through the application of fade mitigation techniques. In such a situation, simulation of end-to-end system performance is the only means of verifying the system design and fulfilling subscriber service delivery expectations.

8.2 Modelling Philosophy

The principle objectives of the system simulation model are to:

- Demonstrate integration of a simulated V-band physical layer into a network simulation;
- Illustrate the effect of physical layer variations on network subscriber performance;
- Provide a basis for the development and verification of fade mitigation techniques above OSI Layer 1;

- Evaluate dynamic performance of the network architecture, e.g. time to set up and availability of link connections.

As the simulation model is principally designed to evaluate the propagation environment, the DVB-RCS framework has been adopted as a realistic future system. Software Considerations

The use of Commercial Off The Shelf (COTS) software was necessary to develop an integrated software model within the timescale of the study, the principal objective being the evaluation of the validity of an integrated approach, rather than the development of the software itself. Several COTS package were evaluated, as illustrated in Figure 8.2-1.

8.2.1 Software Considerations

The use of Commercial Off The Shelf (COTS) software was necessary to develop an integrated software model within the timescale of the study, the principal objective being the evaluation of the validity of an integrated approach, rather than the development of the software itself. Several COTS package were evaluated, as illustrated in Figure 8.2-1.

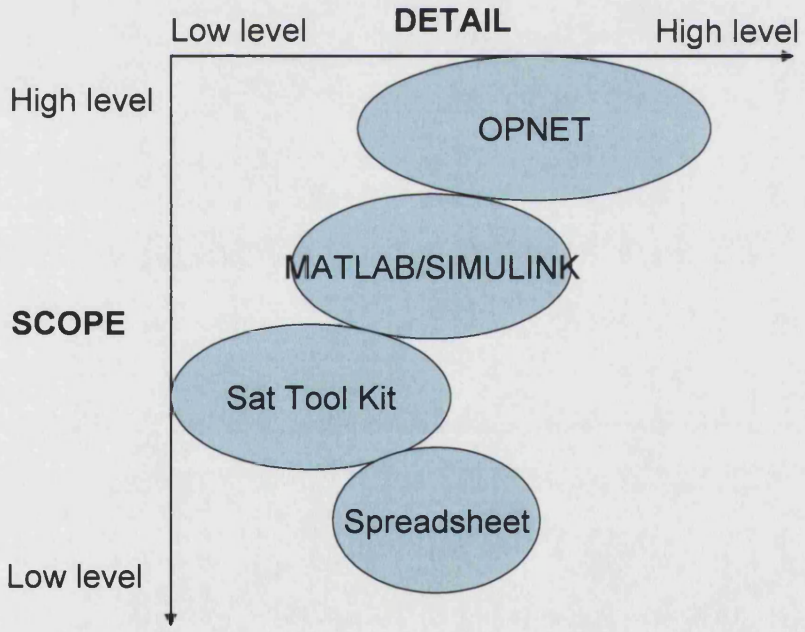

Figure 8.2-1 COTS software scope

8.2.1.1 Spreadsheets

Spreadsheet software products such as Microsoft Excel, provide a flat table ideal for the implementation of static calculations such as RF link budgets. Custom macros developed in MS Visual Basic are easily integrated. However, spreadsheets are not designed for dynamic functional modelling or simulation.

8.2.1.2 Matlab Simulink

Matlab[22] is a technical programming language, which includes a library of mathematical and visualisation functions. Simulink is an extension package, designed for modelling, simulating and analyzing dynamic systems. Systems are modelled as hierarchical block diagrams in a graphical user environment. The package is intuitive to operate, and allows custom Matlab functions to be integrated within the Simulink environment. A typical application includes the simulation and analysis of a single point-to-point communications path. From traffic source, standard model blocks from the communications blockset can be combined to represent modem functionality (modulation and coding), with an appropriate transfer function block for the RF channel.

Detail below bit level can be modelled using simple mathematical approximations for chains of modulation and coding schemes, greatly reducing simulation complexity and run time when considered higher layer operation. However, Simulink is limited to modelling a single communications path, which is insufficient for this application which requires a large distributed network.

8.2.1.3 Satellite Tool Kit (STK)

Satellite Tool Kit[23] (STK) is the leading COTS software package for the space industry. STK provides an easy to use graphical user interface for the time dependant visualisation of satellite networks. The STK/Comm add on module enables the capability for dynamic link performance analysis and modelling, including RF radiowave propagation (including ITU-R P models), antenna modelling and interference analysis. As expected STK is a comprehensive

[22] www.mathsworks.com

[23] www.stk.com

professional package, ideal for modelling and visualisation of the time varying physical layer on a geographic map. Unfortunately, STK is currently limited to modelling OSI Layer 1 variations.

Since the culmination of this study, STK and OPNET Technologies have begun discussions on the possible integration of the two packages. Such an integration would be ideal for this area of study, providing a single comprehensive COTS package capable of modelling and analysis of the physical and higher layers of the end–to-end communication path.

8.2.1.4 OPNET

OPNET[24] (Optimized Network Engineering Tool) is a comprehensive development environment for network simulation and performance analysis. It provides a library of standard ISO-OSI layer protocol models and common network configurations. OPNET has a hierarchical modelling structure, consisting of a number of tools for each stage of a simulation study (model design, simulation, data collection and data analysis).

System behaviour is built around discrete-event simulations modelled through objects and distinct events such as the arrival of packets in a network. Each object has associated attributes that control its behaviour in the simulation. Models can be constructed from the standard library (including transport protocol – IP, ATM or traffic profiles – HTTP, FTP) or custom built by the user, through a graphical user interface.

Each simulation model is operated at four hierarchical levels, to describe and control the network under analysis. These are the network, node, process and link level. More levels can be added depending on the complexity of the system including external program interfaces.

Network Level

The network level defines the topology of the system. It consists of fixed or mobile nodes that can be connected by simplex or duplex communication links. Nodes and links are deployed within a geographical context and their attributes are passed to lower layers. Nodes can be chosen from a library of standard models or customized, as in this case. The satellite orbit toolbox can be used to generate orbits of any height or inclination.

---

[24] www.opnet.com

Node Level

The node level, models the communication devices that are employed and interconnected at the network layer. Node models consist of a number of modules of different types. Each type is predetermined and defines the functionality and interaction capabilities of the modules. These include packet generators, transmitters, receivers, processors and queues. The latter two are highly programmable using a lower level process model.

Connections between modules occur along packet streams or statistic wires. Packet streams allow formatted message packets to sent from one module to another. Statistic wires convey numeric signals or control information used to monitor other modules. These simple building blocks and links form the basis of all protocol and function models.

Figure *8.2-2* illustrates the node model for a generic radio terminal, created from the library of standard OPNET blocks. Attributes associated with each module tailor the model towards specific system designs. For example the *client* module can be modified to simulate different applications such as HTTP, FTP, email, with traffic loads and inter-arrival times determined from user specified PDFs. Other principal attributes, such as the terminal IP address can be specified individually or passed to a higher layer.

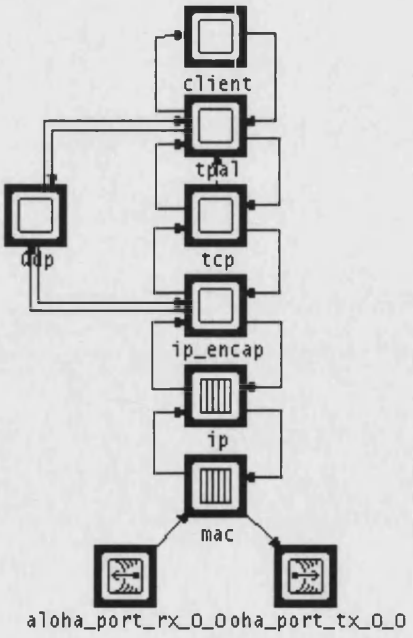

Figure 8.2-2 Standard Radio Terminal Node Model

Process Level

Process models operate on packets as they flow through processor and queue modules of the higher node level. Their operation is determined by state transition diagrams (STDs) supported by additional kernel commands written in PROTO-C or C++ programming language. A process model STD defines a set of primary states that the process can enter and for each state, the conditions needed to move to another state. The condition needed for a particular change in state is called a transition, responding to interrupt events such as a packet arrival or expiry of a timer. Figure 8.2-3 illustrates the process model designed to simulate TDMA operation.

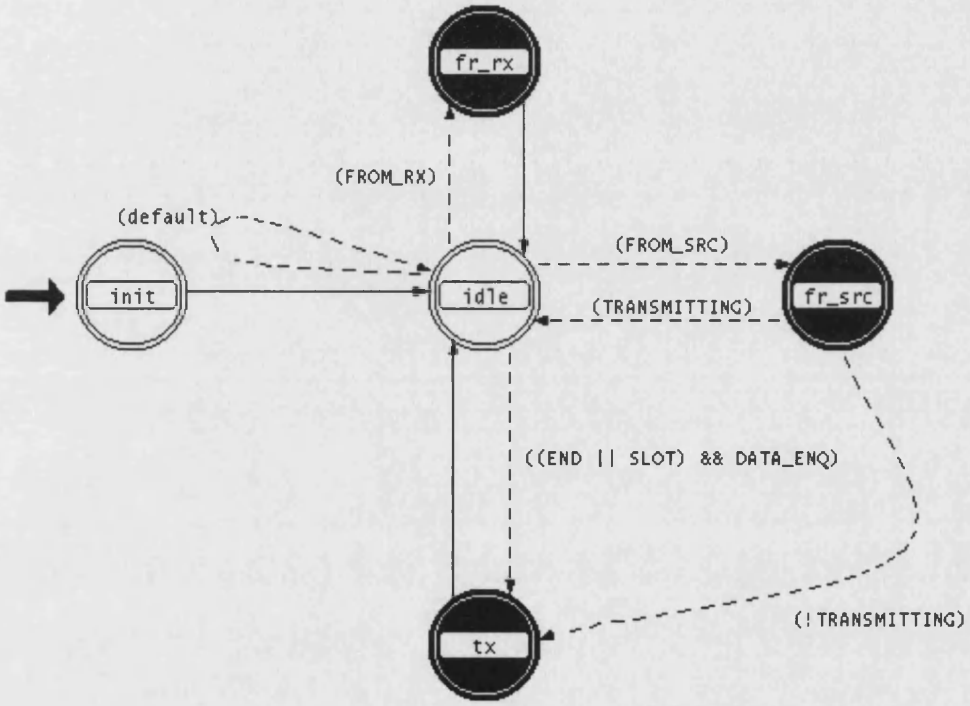

Figure 8.2-3 TDMA Process Model

Physical Level

At the physical level the transmitter and receiver blocks exchange packets through a radio transceiver pipeline stage. This consists of fourteen stages which must be executed whenever a transmission occurs. Because radio links provide a broadcast medium, each transmission can potentially affect multiple receivers throughout the network model. In addition, the radio link to each receiver may exhibit different behaviour and timing. Therefore a separate pipeline must be executed for each eligible receiver.

Figure 8.2-4 illustrates the transceiver pipeline execution sequence. Each stage is implemented in C or C++ language functions, with additional OPNET kernel commands to transfer attributes between model objects. The majority of these stages have been customized in order to comply with the test case system link budget given earlier. In particular, modifications to extract values of total atmospheric attenuation from a European coverage table for arbitrary terminal positions. This leads to the concept of introducing time-series data for a network of VSAT terminals in order to model the performance of a dynamically faded system. Because wireless transmissions can be received by a potentially large number of recipients, modelling every possible connection can be a time-intensive task. When modelling wireless networks, up to 90 percent of OPNET simulation run time is consumed by modelling the interaction between the transmitter and each possible receiver.

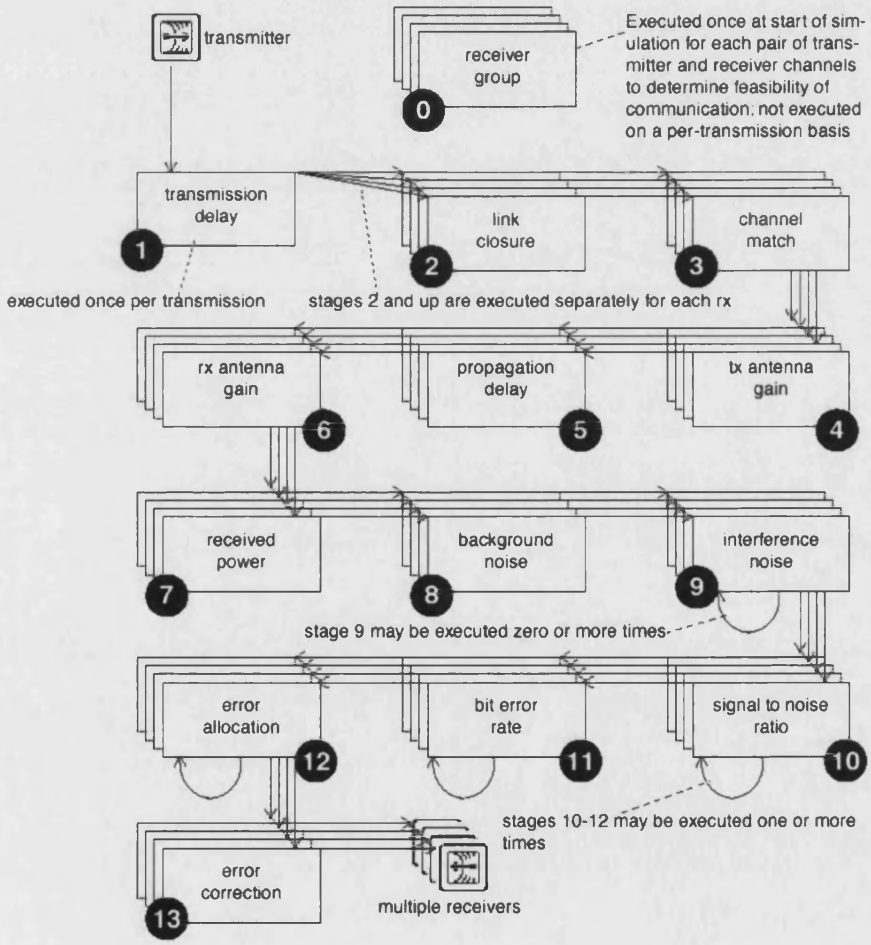

Figure 8.2-4 Transceiver Pipeline Stages

8.3 Test Case Protocol Stack

The architecture of the Test Case system as described previously was implemented in OPNET. ETSI DVB-RCS standards were followed and unmodified OPNET node models were used wherever possible.

8.3.1 Outbound Channel

Figure 8.3-1 illustrates the protocol stack for the DVB-RCS outbound path. The outbound link is a broadcast channel for video, audio and data streams. Traffic streams from within the application layer are segmented into fixed length (188 byte) MPEG-2 transport stream (TS) packets. Video and Audio are carried in variable length Program Elementary Stream (PES) packets, before being encapsulated in to TS packets using a defined mapping. Data applications (such as web browsing or file transfer) may use TCP or UDP for end-to-end session control as required. Broadband PES applications are point-to-multipoint applications, and therefore provide no guarantee of delivery or possibility of retransmission. Data transfer sessions are segmented into variable length IP packets and mapped onto TS packets using Multi-Protocol Encapsulation (MPE).

At the physical level, each packet is coded and modulated according to the DVB-S standard [ETSI, EN 300 421].

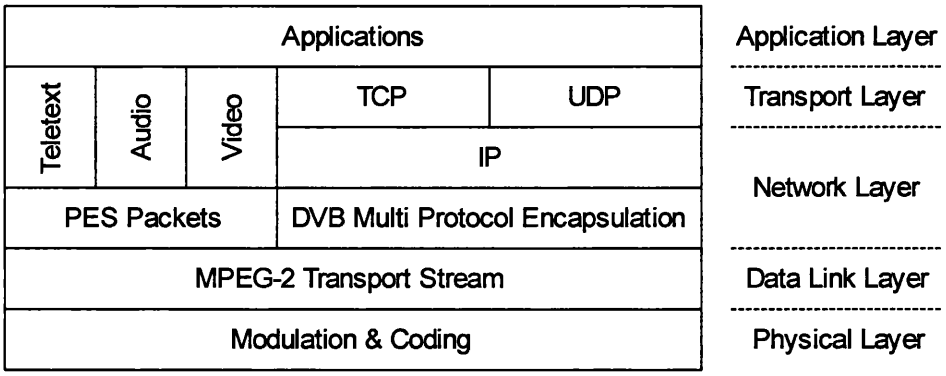

Figure 8.3-1 Outbound Path Protocol Stack

8.3.2 Return Channel

Figure 8.3-2 illustrates the protocol stack for the DVB-RCS return path. The application layer consists of different end user applications. This can range from simple file transfer (FTP), electronic mail (SMTP), to web browsing (HTTP). OPNET provides configuration of simulated user applications, including statistical traffic usage distributions. Due to time constraints, application layer simulations were not comprehensively modelled and simple random packet sources were used.

End-to-end application sessions are controlled by the Transmission Control Protocol (TCP) to assure packet delivery (e.g. for file transfer) or by User Datagram Protocol (UDP) if no delivery guarantee is required (e.g. audience polling & multimedia streaming). The transport layer fragments outgoing data streams into variable length IP packets for compatibility with conventional networks.

At the data link layer, IP packets (up to 64 kbytes) are fragmented into fixed length ATM size packets (48 data bytes + 5 byte header). The shorter packet size is more efficient for applications with a range of message sizes, but the DVB-RCS standard does not provide any ATM QoS guarantees. At the Multiple Access Control (MAC) layer data packets from the higher levels are queued while requests are made for channel capacity.

Access schemes may introduce delays which can considerably affect the end user performance. In accordance with DVB-RCS standards, each time a SIT affiliates to the network it is assigned an carrier group number as part of the MAC address. This mechanism ensures tight control of the maximum number and blocking probability of each user group.

At the physical level, each packet is coded and modulated according to the DVB-S standard. One protected packet is transmitted in each MF-TDMA slot.

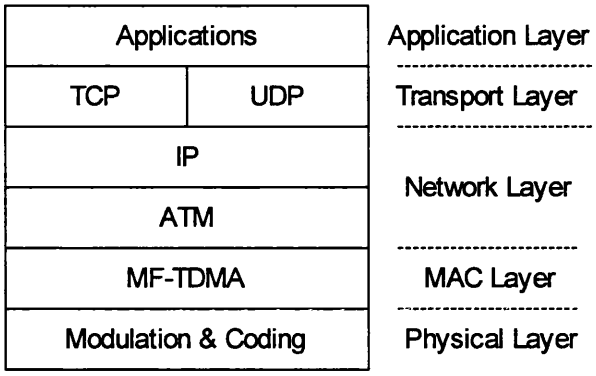

Figure 8.3-2 Return Path Protocol Stack

8.4 Results

Figure 8.4-1 illustrates the OPNET user interface environment. In the top left, the window shows the network layer with the distributed VSAT sites. At the bottom left is the node model of the setup module which is used to initialise the simulation with the "raw" UM data. Top left if the process model with the setup node, and the two windows at the bottom right illustrate coding with these process states.

The model allows VSATs to be located anywhere within the map boundary (which is set to correspond to UM data coverage) and the link budget and propagation time-series are generated automatically.

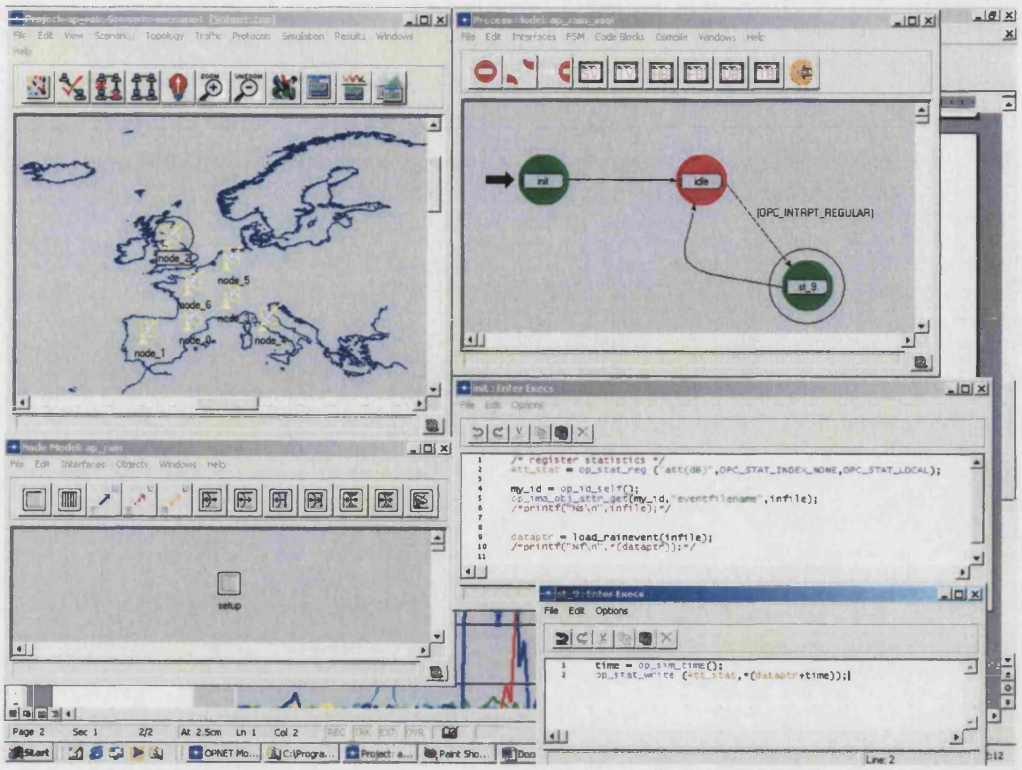

Figure 8.4-1 Screenshot of the OPNET User Interface

Figure 8.4-2 illustrates how the time-series generator for a number of dispersed sites, appears within the OPNET statistics package. Each time-series represents a one second resolution, and the graph shows the attenuation on each link during a 24 hour period.

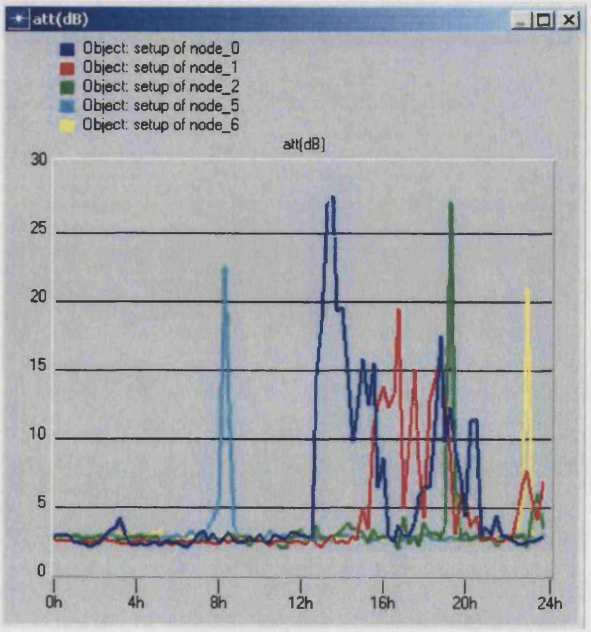

Figure 8.4-2 Example of time-series attenuation integrated into the OPNET physical layer

8.5 Conclusions

In order to aid development of FMTs within higher layers of the ISO-OSI model, work was untaken to integrate the physical layer model into an event driven network model in the simulation environment. The approach was to illustrate the real-time performance of a distributed multi-media satellite network, under a benign scenario (i.e. no packet loss due to the physical layer). The performance was then re-assessed including simulated atmospheric attenuation time-series. Thereafter, future studies could use the model to evaluate new FMTs and optimise protocol performance.

The OPNET environment was selected and a simulation developed based on the architecture of the test case system, including a hub station and several remote terminals at arbitrary locations. The synthetic time series generator was integrated into the physical layer radio pipeline stages of the model and slaved to the simulation clock. At the C programming layer, this was implemented by reading in the "raw" input data required by the time-series model at the beginning of the simulation. C language programs were then executed each time a packet passes over the OPNET radio pipeline stage (the physical layer). During simulation setup OPNETs system clock is set to correspond the same time period as the "raw" meteorological data set. The appropriate ITU-R P and other models (as described in an earlier chapter) are implemented in C to convert these raw data into the path attenuation loss value.

Unfortunately, the time constraints of this study only allowed demonstration of the integrated model and not full investigation of end-to-end performance. Professional all encompassing software often has a large learning curve associated with it and OPNET is no exception. However, the feasibility of the basic approach has been successfully demonstrated. Future studies will be able to use the models developed and in particular the method of integrating the external Unified Model output data arrays with terminal locations and simulation time.

Although its disappointing not to have produced any quantitative results at this stage, the novel approach has been demonstrated to work at the physical layer.

9 Conclusions

9.1 Prediction of Monthly Availabilities

The attenuation prediction model proposed by Konefal, et al., [2000], has been enhanced to permit the production of monthly availability maps for a global coverage. This work was validated under the auspices of the COST 255 programme and results published for Ka-band and V-band test cases.

9.2 Development of Novel Time Series Generator

A novel attenuation time-series generator has been developed based on the use of assimilated meteorological forecast data from the Meteorological Office Unified Model, for the calculation of hourly gaseous and cloud attenuation (via profiles of pressure, temperature and humidity). Since the data is provided in horizontal data grids covering Northern Europe, this approach applies to any arbitrary location within the boundary of the operational Unified Model.

Hourly output fields from the Unified Model were not considered to be of high enough spatial or temporal resolution for the generation of realistic attenuation time series, for use with FMT techniques. Instead concurrent weather radar images were accessed providing rain rate measurements with 5km spatial resolution and 15 minute temporal resolution and a coverage encompassing the UK and northern France. These data provide the outline definition of each rain event, including the spatial correlation between different sites.

High resolution characteristics of rain attenuation have been included in the synthetic time series using random high frequency components with the theoretical power spectrum of f^{-3} found in literature. Scintillation models were included that use profiles of wind speed and direction from the Unified model, providing the hourly intensity and the $f^{8/3}$ roll-off given in Kolmogorov's theory of turbulence.

2.3 Testing of Novel Time Series Generator

The new attenuation time series generator has been tested against 40 and 50 GHz Italsat data and it has been shown to give remarkably similar time-series to those captured from real satellite beacon measurements for the same time and ground location. It was also found that correlation was improved by using a rain model [Leitao and Watson, 1986] which can differentiate between showery and widespread rains, based on the rain type from the Unified Model. In addition, the short term spectral characteristics can be shown to match empirical beacon characteristics. Furthermore the power spectrum of the artificial time-series are seen to approximate to those observed for the real data. It is emphasized that these are preliminary results and that more data should be assessed in further studies (see next chapter).

In conclusion, the new model proposed in this study has succeeded in providing a physically based, high resolution, tropospheric time series generator. It allows generation of time-series with temporal and spatial properties of real events and can be used to model earth to space links at arbitrary locations within the bounds of the data coverage.

2.4 Demonstration of Approach to System Simulation

An approach to simulation of the higher layers of ISO-OSI model has been developed using Opnet. The synthetic time series generator has been integrated into the physical layer radio pipeline stages of the model and slaved to the simulation clock. The feasibility of the approach has been illustrated, which again has laid the foundations for further work.

2.5 Proposal for Use of Unified Model in Real-Time as a Fade-Mitigation Technique

Since the simulation model could in future be fully based on metrological forecast data, the approach lends itself to becoming an FMT in itself. By exploiting the ability of the Unified Model to accurately forecast weather conditions several days in advance, system operators could identify areas susceptible to link outage and optimise resources appropriately. Prior to outage this could include updating cached web pages, buffering large amount of service content, constructing fallback plans such as switching to more robust waveforms, or affiliating terrestrial return links where available.

10 Future Work

An approach for the design of a time-series generator for signals on V-band VSAT and DVB-RCST [ETSI, DVB-RCS] has been described. The initial results on a small amount of data are extremely promising. The time-series generator should be fully validated on a larger data set and could be implemented using a higher resolution Unified Model. In addition, there are many more UM fields which could also be used as input to the model.

In addition to the time-series generator, a V-band VSAT system based around an extension of DVB-RCS architecture was evaluated and shown to have the potential to provide high capacity multi-media messaging services. The ultimate performance and optimisations of this system using various FMT should be possible using the time-series generator.

Future studies to integrate OPNET network simulations with physical layer models, should be aided by the integration of the STK (Satellite Tool Kit) product. Whereas, OPNET provides a very basic low level C programming interface and requires custom propagation models to be developed. STK already provides a easy static design of propagation and interface on satellite links. Running together STK will replace the OPNET pipeline stages.

Following further validation work, a similar approach could be considered for real-time network management, to optimise high frequency multimedia satellite networks. In the future UM short term forecasts (including the rain fields) could be used to predicted areas of high tropospheric loss and to allocate satellite resources and FMT accordingly. This would only be of real benefit once Ka-band and V-band systems with dynamic allocation schemes (including MF-TDMA) enter service.

In the shorter term an end-to-end system and propagation models could be used to investigate potential problems associated with the ETSI DVB-RCS MF-TDMA access scheme, when operated at V-band frequencies including recovery protocols when large areas of the network are affected by rain.

Appendix A Unified Model Output Fields

Table 10-1 Unified Model Output Fields

STASH	Field	Units
1	Surface pressure	Pa
2	U component of wind	ms^{-1}
3	V component of wind	ms^{-1}
4	Theta (Temperature)	
10	Specific Humidity	
24	Surface Temperature	
33	Orographic height	M
3225	10m wind U-component	
3226	10m wind V-component	
3229	Evaporation from soil surface	$Kg/m^2/s$
3230	Evaporation from canopy	$Kg/m^2/s$
3232	Evaporation from sea	$Kg/m^2/s$
3234	Surface Latent Heat Flux	w/m^2
3236	Temperature at 1.5m	K
3237	Specific humidity at 1.5m	$KgKg^{-1}$
4004	Temperature on model levels (η)	K
4201	Large scale rain amount	Kg/m^2
4202	Large scale snow amount	Kg/m^2
4203	Large scale rainfall amount	Kg/m^2
4204	Large scale rainfall amount	Kg/m^2
4205	Cloud liquid water after large precipitation	
4206	Cloud ice content after large precipitation	
4010	Specific humidity on model levels	$KgKg^{-1}$
5201	Convective rain amount	Kg/m^2
5202	Convective snow amount	Kg/m^2
5205	Convective rainfall amount	Kg/m^2
5206	Convective snowfall amount	Kg/m^2
5207	Pressure at convective cloud base	
5208	Pressure at convective cloud top	
5209	Temperature after convection	
12201	Omega (In advection) on model levels	
12201	Omega (In advection) on pressure levels	
15201	U comp. (Westerly) of wind on pressure levels	
15202	V comp. (Southerly) of wind on pressure levels	

15216	Temperature on pressure levels	
15222	Omega on pressure levels	
15226	Specific Humidity on pressure levels	
16202	Geopotential height on pressure levels	
16203	Temperature on pressure levels	
16210	Height of freezing level	M

Appendix B Pressure on UM Levels

Each UM output field is stored as a two dimensional array, on vertical model levels (η_k). The pressure (mb) on model levels, $p(\eta_k)$ and model half-levels $(\eta_{k-1/2})$, refer to Figure 9.2-1, is calculated using Eqn. B-1 [Goddard, 1998].

Eqn. B-1 $$p(\eta) = Ak + (Bk \times p^*) \quad \text{(Pa)}$$

where A_k and B_k are the coefficients at full model levels, $p(\eta_k)$ and model half-levels $(\eta_{k-1/2})$ given below and p_* is the surface pressure.

```
 AK   = [0.000000, 0.000000, 0.000000, 0.000000, 0.000000, 0.000000,…
         0.000000, 0.000000, 0.000000, 0.000000, 0.000000, 22.30000,…
         220.9000, 695.5000, 1521.500, 2752.200, 4402.000, 6432.900,…
         8632.600, 10643.50, 12181.50, 13326.00, 14098.20, 14525.60,…
         14757.00, 14821.60, 14703.00, 14384.70, 13850.40, 13083.70,…
         12068.10, 10786.90, 9223.200, 7359.300, 5174.600, 2959.400,…
         1479.700, 460.6000]

 BK   = [0.998803, 0.995233, 0.988198, 0.977703, 0.964946, 0.948982,…
         0.930496, 0.910986, 0.890482, 0.868984, 0.846477, 0.822258,…
         0.792756, 0.755497, 0.709723, 0.654886, 0.590865, 0.518018,…
         0.441003, 0.368408, 0.308075, 0.256618, 0.213944, 0.182185,…
         0.154870, 0.129215, 0.105398, 0.083571, 0.063903, 0.046558,…
         0.031697, 0.019485, 0.010086, 0.003666, 0.000396, 0.000000,…
         0.000000, 0.000000]

AK1/2 = [0.000000, 0.000000, 0.000000, 0.000000, 0.000000, 0.000000,…
         0.000000, 0.000000, 0.000000, 0.000000, 0.000000, 0.000000,…
         87.80000, 409.0000, 1045.700, 2064.100, 3500.400, 5345.500,…
         7527.400, 9700.100, 11521.20, 12781.40, 13794.30, 14351.60,…
         14660.60, 14811.10, 14786.60, 14570.80, 14147.40, 13500.20,…
         12612.60, 11468.60, 10051.60, 8345.400, 6333.600, 4000.000,…
         2000.000, 1000.000, 50.00000]

BK1/2 = [1.000000, 0.997600, 0.992900, 0.983500, 0.971900, 0.958000,…
         0.940000, 0.921000, 0.901000, 0.880000, 0.858000, 0.835000,…
         0.809122, 0.775910, 0.734543, 0.684359, 0.624996, 0.556545,…
         0.479726, 0.402999, 0.334788, 0.282186, 0.232057, 0.196484,…
         0.168394, 0.141889, 0.117134, 0.094292, 0.073526, 0.054998,…
         0.038874, 0.025314, 0.014484, 0.006546, 0.001664, 0.000000,…
         0.000000, 0.000000, 0.000000]
```

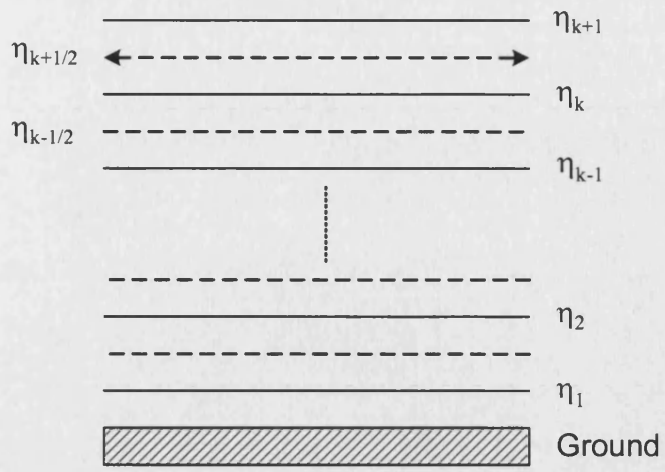

Figure 9.2-1 Distribution of UM vertical layers

Appendix C Geopotential Height on UM Model Levels

The geopotential height (m) on UM model levels $Z(\eta)$ is calculated from [Goddard, 1998]. Required UM output fields are orography (Z_*), surface pressure (p_*), temperature on model levels ($T(\eta)$), specific humidity on model levels ($q(\eta)$), A, B coefficients at full model levels (η_k) and model half-levels ($\eta_{k-1/2}$).

From the hydrostatic equation the height of each η layer boundary is given by Eqn. C-2.

Eqn. C-2 $$z_{k-\frac{1}{2}} = z_* + \frac{c_p}{g}\sum_{m=1}^{m=k-1}(\theta_v)_m(\pi_{m+\frac{1}{2}} - \pi_{m-\frac{1}{2}})$$

with k = 2, 3,...top. The height (z_i), at a pressure (p_i), within layer k (bounded at k-½, k+½), is then calculated using a second order approximation to the thickness of the layer between p_i and $p_{k-1/2}$ given by Eqn. C-3.

Eqn. C-3 $$z_i = z_{k-\frac{1}{2}} + \frac{c_p}{g}\left\{(\theta_v)_k\left[\pi_{k-\frac{1}{2}} - \pi_k\right] - \frac{1}{2}\left(\frac{\partial\theta}{\partial\pi}\right)_k\left[\pi_i(\pi_i - 2\pi_k) - \pi_{k-\frac{1}{2}}\left(\pi_{k-\frac{1}{2}} - 2\pi_k\right)\right]\right\}$$

where the specific heat capacity of dry air, c_p = 1005.0 J/Kg/K, the surface gravity, g = 9.80665 m/s^2 and θ_v is the virtual potential temperature in terms of temperature T and specific humidity q, given by Eqn. C-4.

Eqn. C-4 $$\theta_v = \frac{T(1+0.61q)}{\pi}$$

with the EXNER pressure defined by Eqn. C-5 for π, $\pi_{k+\frac{1}{2}}$ and $\pi_{k-\frac{1}{2}}$.

Eqn. C-5 $$\pi = \left(\frac{p}{100000}\right)^{\kappa}$$

where $\kappa = \frac{R}{c_p}$, and the gas constant of dry air, R = 287.05 J/Kg/K.

Further, the full model level value of π_k is given by Eqn. C-6.

Eqn. C-6 $$\pi_k = \frac{\pi_{k+\frac{1}{2}} p_{k+\frac{1}{2}} - \pi_{k-\frac{1}{2}} p_{k-\frac{1}{2}}}{(\kappa+1)\left[p_{k+\frac{1}{2}} - p_{k-\frac{1}{2}}\right]}$$

Finally, the derivative,

Eqn. C-7 $$\left(\frac{\partial\theta}{\partial\pi}\right) = \frac{1}{\pi_k}\left[\frac{T_{kp} - T_{km}}{\pi_{kp} - \pi_{km}} - \theta_k\right], \quad km = max(1,k\text{-}1),\ kp = min(top,k+1)$$

Once the height z_i at pressure p_i has been calculated, vertical interpolation between pressure surfaces is assumed to be logarithmic according to Eqn. C-8

$$F_K = \begin{cases} F_{top} & p_i < p_{top} \\ \alpha F_j + (1-\alpha) F_{j-1} & p_j < p_i < p_{j-1} \\ F_1 & p_i > p_1 \end{cases}.$$

Eqn. C-8 $$F_K = \begin{cases} F_{top} & p_i < p_{top} \\ \alpha F_j + (1-\alpha) F_{j-1} & p_j < p_i < p_{j-1} \\ F_1 & p_i > p_1 \end{cases}$$

where F_K represents the UM output field to be interpolated and the interpolation coefficient a is given by Eqn. C-9 $$\alpha = \frac{\ln\left[\frac{p_i}{p_{j-1}}\right]}{\ln\left[\frac{p_j}{p_{j-1}}\right]} \qquad j-1 < i < j.$$

Eqn. C-9 $$\alpha = \frac{\ln\left[\frac{p_i}{p_{j-1}}\right]}{\ln\left[\frac{p_j}{p_{j-1}}\right]} \qquad j-1 < i < j$$

Appendix D Relative Humidity on UM Levels

Relative Humidity RH (%) using pressure p (mbar), Temperature T (K) and specific humidity q (KgKg) using [Trevelyan, 1993]

Eqn. D-1 $$RH = \frac{r}{q_{sat}} \times 100 \qquad (\%)$$

where humidity mixing ratio r, using [Panagi, 2000]

Eqn. D-2 $$r = \frac{q}{1-q}$$

and saturation mixing ratio q_{sat}, using [Smith, et al., 1997]

Eqn. D-3 $$q_{sat} = \frac{0.622 e_s}{p}$$

saturation vapour pressure es, at the temperature t (°C) using [ITU-R, P453-7]

Eqn. D-4 $$e_s = a \times \exp\left(\frac{b \times t}{t + c}\right) \qquad (\text{hPa})$$

where the coefficients a, b, c are

for water (between –20° to +50°)	for ice (between –50° to 0°)
a = 6.1121	a = 6.1115
b = 17.502	b = 22.452
c = 240.97	c = 272.55

Appendix E Water Vapour Density

Water vapour density ρ (g/m^3) given RH (%), T (K) and e_s (hPa) using [P453-7, 1999]

Eqn. E-1 $$\rho = \frac{216.7 \times e}{T} \qquad \text{(g/m3)}$$

where water vapour partial pressure e (hPa),

Eqn. E-2 $$e = \frac{RH \times es}{100} \qquad \text{(hPa)}$$

Appendix F UM Position Grid

UM mesoscale output fields use a latitude-longitude grid in which the celestial poles are translated along a meridian onto an equatorial grid (see Figure 9.2-2). The equatorial grid is uniform and avoids the need for stability filtering at high latitudes.

On the standard grid, a point on the earths surface is given as a latitude ϕ_p and longitude λ in degrees. Using the new pole at latitude ϕ_p and longitude λ_p, the transformation onto the equatorial grid (ϕ',λ') is given by [Goddard, 1998].

Eqn. F-1 $$\lambda_o = \lambda_p + \pi$$

Eqn. F-2 $$\phi' = \sin^{-1}\left(-\cos\phi_p \cos(\lambda - \lambda_o)\cos\phi + \sin\phi_p \sin\phi\right) \quad \text{(degrees)}$$

Eqn. F-3 $$\lambda' = \gamma \cos^{-1}\left[\frac{\cos\phi_p \sin\phi + \sin\phi_p \cos(\lambda - \lambda_o)\cos\phi}{\cos\phi'}\right] \quad \text{(degrees)}$$

where from global symmetry $\gamma = 1$ if $0 \le \lambda - \lambda_o \le \pi$ and $\gamma = -1$ if $-\pi \le \lambda - \lambda_o < 0$.

A reverse transformation from the equatorial grid to the standard grid is given by

Eqn. F-4 $$\phi = \sin^{-1}\left(\cos\phi_p \cos\lambda' \cos\phi' + \sin\phi_p \sin\phi'\right) \quad \text{(degrees)}$$

Eqn. F-5 $$\lambda = \lambda_o + \gamma \cos^{-1}\left[\frac{-\cos\phi_p \sin\phi' + \sin\phi_p \cos\lambda' \cos\phi'}{\cos\phi}\right] \quad \text{(degrees)}$$

where from global symmetry $\gamma = 1$ if $0 \le \lambda' \le \pi$ and $\gamma = -1$ if $-\pi \le \lambda' < 0$.

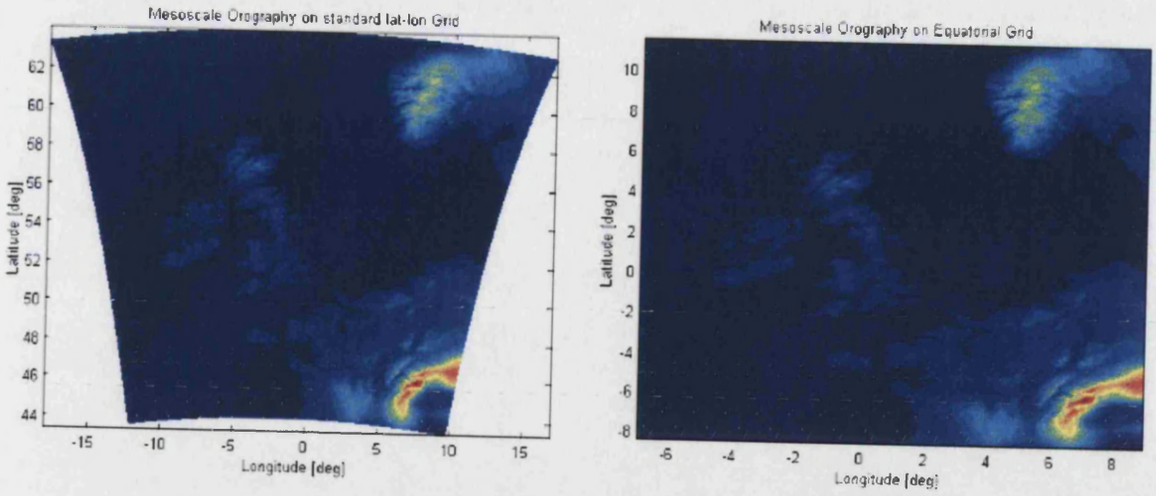

Figure 9.2-2 Example UM field on standard & Equatorial Lat-Lon Grids

Appendix G Wind Speed & Direction

Horizontal wind is a vector quantity defined by two components *u, v*, at the centre of each pressure square. This staggered grid is first re-mapped on the horizontal pressure grid. Since the staggered grid has *NX-1* and *NY-1* dimensions, the last row/column of the wind arrays are filled with the same values *(NUX-1,NUY-1)*, making the interpolation easier. Then a standard 4 point bi-linear interpolation is used [Panagi, 2000].

Eqn. G-1 $$w_{ij} = \frac{1}{4}\left(w_{ij} + w_{i-1,j} + w_{i-1,j-1} + w_{i,j-1}\right)$$ where *w* represents *u* or *v*.

The wind components are now given *wrt* the Mesoscale equatorial grid and they must be rotated onto the standard latitude – longitude grid [Panagi, 2000]

Eqn. G-2 $$ut = c1u + c2v$$

Eqn. G-3 $$vt = c1v - c2u$$

where the coefficients c_1, c_2 are given by

Eqn. G-4 $$c1 = -\sin(\lambda - \lambda o)\sin\lambda' \sin\phi p + \cos(\lambda - \lambda o)\cos\lambda'$$

Eqn. G-5 $$c2 = \sin\phi \sin\lambda' \cos(\lambda - \lambda o)\sin\phi p - \sin\phi \cos\lambda' \sin(\lambda - \lambda o) - \sin\lambda' \cos\phi \cos\phi p$$

Finally, the true wind direction (deg) *wrt* 0 deg North is computed so that 0 deg winds are true southerly and 90 deg winds are true westerly on a lat-lon grid [Panagi, 2000].

Eqn. G-6 $$u \geq 0, v \geq 0: \quad 0\ deg \geq dirn \leq 90\ deg$$

Eqn. G-7 $$u \geq 0, v \geq 0: \quad 90\ deg \geq dirn \leq 180\ deg$$

Eqn. G-8 $$u \geq 0, v \geq 0: 180\ deg \geq dirn \leq 270\ deg$$

Eqn. G-9 $$u \geq 0, v \geq 0: 270\ deg \geq dirn \leq 360\ deg$$

Wind strength *v* (ms-1), is the vector magnitude [Panagi, 2000]

Eqn. G-10 $$V = \sqrt{u^2 + v^2} \qquad \text{(ms-1)}$$

Appendix H Rain Rate

Rain rate (mm/hr) was processed from UKMO network radar 'raw' data files using the procedure taken from the UM visualisation software 'JPLOT', kindly supplied by the UKMO. The UK network radar data is a composite of precipitation rate data from 15 individual Radar sites spread across the UK. The Radar data consists of a grid of data, of size 256×256 boxes, at an approximate spatial resolution and a temporal resolution of 15 minutes.

The network radar data uses the file naming convention raYYMMDDHHMM.dat, where YY=year (last 2 digits only), MM=month, DD=year, HH=hour and MM=minute.

The 'raw' radar data is read into an array using the FORTRAN 77 routine 'read_network_radar', producing a 256×256 array, representing rain rate at 0.5mm/hr. This value is scaled to 1mm/hr, and the rain rate at a specific latitude/longitude point is evaluated using the MATLAB function 'griddata'. Griddata takes the rain rate array, and two arrays representing the longitudes and latitudes of the cell centres of the radar grid. It fits a surface to the rain rate array, then interpolates for the required latitude/longitude point. The true latitude/longitude position arrays are read from the JPLOT data file 'uk_rad_latlon'.

Appendix I Scintillation Variance

Scintillation variance σ_χ^2 (dB^2) is given by

Eqn. I-1 $$\sigma_\chi^2 = 42.48\frac{k^{7/6}}{(\sin\theta)^{11/6}}\sum_z \overline{\langle C_n^2(z)\rangle} z^{5/6}\Delta z$$

where $k = 2\pi/\lambda$ with λ the wavelength (m^{-1}), θ the elevation angle, z is the height (m) and $\langle C_n^2(z)\rangle$ is the height dependant refractive index structure parameter (m$^{-2/3}$).

Eqn. I-2 $$\langle C_n^2(z)\rangle = 2.8 M_O(z)^2 \langle R(z)\rangle \int_0^\infty Lo^{4/3} P_{LO} \int_0^\infty P_S \int_{-\infty}^{S^2 Ric} (N^2)^2 P_{N^2} dN^2 dS dLo$$

Eqn. I-3 $$M_O(z) = M_O N^2 R^{1/2}$$

and R represents the humidity contribution to M^2, Lo, S and N^2 are random variable representing the outer scale of turbulence, the wind shear and the buoyancy forces, respectively and characterised by the pdf P_{LO}, P_S and P_{N^2}. $Ric \approx 0.25$ is the critical value of the Richardson number (dimensionless ratio of the buoyancy to square wind shear) used to access the instability of the medium.

Eqn. I-4 $$M_o(z) = -77.6\times10^{-6}\frac{p(z)}{gT(z)}$$

with $g = 9.81$ m/s^2.

Eqn. I-5 $$\langle R(z)\rangle = \left[1 + 1.55\times10^4\frac{q(z)}{T(z)} - \frac{1.55\times10^4}{2}\frac{g\frac{\partial q}{\partial z}(z)}{\langle N^2(z)\rangle T(z)}\right]^2$$

with specific humidity,

Eqn. I-6 $$q(z) = 0.6225\frac{e(z)}{p(z)}, \qquad \text{(dimensionless)}$$

mean value of buoyancy forces,

Eqn. I-7 $$\left\langle N^2(z)\right\rangle = g\frac{\partial \ln\theta}{\partial z}, \qquad (s^{-2})$$

specific temperature,

Eqn. I-8 $$\theta = T(z)\left(\frac{1000}{p(z)}\right)^{0.2858}, \qquad (K)$$

P_{LO} is a uniform distribution between Lo_{min} = 3m and Lo_{max} = 100m

Eqn. I-9 $$P_{LO} = \frac{1}{Lo_{\max} - Lo_{\min}} \text{ if } Lo_{min} \le Lo \le Lo_{max} \text{ or 0 otherwise}$$

Ps is a Rice distribution (inferred from the assumption of Gaussian distribution for both components of vector shear).

Eqn. I-10 $$Ps = \frac{S}{\sigma_s^2}\exp\left(-\frac{S^2 + \left\langle S(z)\right\rangle^2}{2\sigma_s^2(z)}\right) I_o\left(\frac{S\left\langle S(z)\right\rangle}{\sigma_s^2(z)}\right)$$

with the mean wind shear,

Eqn. I-11 $$\left\langle S(z)\right\rangle = \sqrt{\left(\frac{\partial v\cos\varphi}{\partial z}(z)\right)^2 + \left(\frac{\partial v\sin\varphi}{\partial z}(z)\right)^2} \qquad (s^{-2})$$

Eqn. I-12 $$\sigma_s = 0.18 Lo^{-0.3}\left|\left\langle N^2(z)\right\rangle\right|^{0.25}\rho(z)^{-0.15}$$

mean density of dry air in the slab,

Eqn. I-13 $$\rho(z) = 0.348\left(\frac{p(z)}{T(z)}\right), \qquad (kg/m^3)$$

P_{N^2} is a Gaussian distribution

Eqn. I-14 $$P_{N^2} = \frac{1}{\sqrt{2\pi}\sigma_N(z)}\exp\left(-\frac{\left(N^2 - \left\langle N^2(z)\right\rangle\right)^2}{2\sigma_N^2(z)}\right)$$

Eqn. I-15 $$\sigma_N(z) = \sqrt{\frac{6}{5}}\sigma_s(z)\sqrt{\left|\left\langle N^2(z)\right\rangle\right|}$$

References

Akram A., Shukla A.K., Konefal T., and Watson P.A., 'MIDAS: A monthly link budget and signal coverage tool for frequencies between 10 and 50 GHz', presented at IEE ICAP International Conference on Antennas and Propagation, pp.152-155, 1999.

Allnutt J.E., 'Nature of space diversity in microwave communications via geostationary satellites: a review', *Proceedings of the IEE*, vol. 125, pp.376-396, 1998.

Allnutt J.E. and Haidara F., 'Uplink power control strategies for low data rate Ka-band satellite services', presented at AP2000 Millennium conference on antennas and propagation, Davos, Switzerland, 2000.

Almeroth K.C. and Ammar M.H., 'The use of multicast delivery to provide a scalable and interactive video-on-demand service', *IEEE Journal on Selected Areas in Communications*, vol. 14, No.6, pp.1110-1122, 1996.

Alouini M.S., Borgsmiller S.A., and Steffes P.G., 'Channel characterization and modeling for Ka-band very small aperture terminals', *Proceedings of the IEEE*, vol. 85, No.6, pp.981-97, 1997.

Altshuler E.E., 'Cloud attenuation at millimetre wavelengths', *IEEE Transactions on Antennas and Propagation*, vol. 37, No.11, pp.1473-1479, 1989.

Ananasso F., Chiassarini G., Ambrosio A.D., Franti L.F., and Gallinaro G., 'A multi-carrier demodulator and its front-end for MF-TDMA', *Space Communications*, vol. 7, No.4-6, pp.531-542, 1990.

Ananasso F., Chiassarini G., Del Re E., Fantacci R., Rousset D., and Saggese E., 'A multirate digital multicarrier demodulator: design, implementation, and performance evaluation', *IEEE Journal on Selected Areas in Communications*, vol. 10, No.8, pp.1326-42, 1992.

Andre F., Bosch E., Nunn R., and Pelletier A., 'Broadband linearized TWT for multimedia communications', presented at ECSC5, Fifth European Conference on Satellite Communications, 1999.

Baentsch M., Baum L., Molter G., Rothkugel S., and Sturm P., 'World Wide Web caching: The

internet application level view of the internet', *IEEE Communications Magazine*, pp.170-177, 1997.

Baptista Poiares J.P.V. and Salonen E., 'Rainfall rate modelling and mapping', presented at COST 255: Radiowave Propagation Modelling for SatCom Services at Ku-band and Above, 1997.

Bernes-Lee T., Fielding R.T., and Nielson H.F., 'Hypertext Transfer Protocol - HTTP/1.0', *Internet Request for Comments*, 1996.

Bever M., Freitage J., and Linsky S., 'Fast packet vs. circuit switch and bent pipe satellite network architectures', *International Journal of Satellite Communications*, vol. 17, No.2-3, pp.83-105, 1999.

Brussard G. and Watson P.A., *Atmospheric Modelling & Millimetrewave propagation*: Chapman & Hall, 1995.

Burgueno A., Vilar E., and Puigcerver M., 'Spectral analysis of 49 years of rainfall rate and relation to fade dynamics', *IEEE Transactions on Communications*, vol. 38, No.9, pp.1359-66, 1990.

Capsoni C., Fedi F., Magistroni C., Paraboni A., and Pawlina A., 'Data and theory for a new model of the horizontal structure of rain cells for propagation applications', *Radio Science*, vol. 22, No.3, pp.395-404, 1987.

Capsoni C., Fedi F., and Paraboni A., 'A comprehensive meteorologically oriented methodology for a variety of compact terminals', *Radio Science*, vol. 22, No.3, pp.387-393, 1987.

Capsoni C., Fedi F., and Paraboni A., 'A comprehensive meteorologically oriented methodology for the prediction of wave propagation parameters in telecommunication application beyond 10 GHz', *Radio Science*, vol. 22, No.3, pp.387-393, 1987.

Carassa F. and Tartara G., 'Frequency diversity and its applications', *International Journal of Satellite Communications*, vol. 6, pp.313-322, 1988.

Carducci F. and Francesi M., 'The ITALSAT F1 satellite system', *International Journal of Satellite*

Communications, vol. 13, pp.49-81, 1995.

Castanet L., Bousquet M., and Mertens D., 'Simulation of the performance of a Ka-band VSAT videoconferencing system with uplink power control and data rate reduction to mitigate atmospheric propagation effects', *International Journal of Satellite Communications*, vol. 20, pp.231-249, 2002.

Castanet L., Lemorton J., and Bousquet M., 'Fade mitigation techniques for new SatCom services at Ku-band and above: a review', presented at Fourth Ka Band Utilization Conference, Venice, Italy, pp.119-172, 1998.

Chariglione L., 'MPEG: A technological basis for multimedia applications', *IEEE Multimedia*, vol. 2, pp.85-89, 1995.

Clarke D., Lampard G., Merret R.P., Smith D.W., Wakeling J.F., Whitley T.J., and Young G., 'Emerging Broadband access technologies', *BT Technology Journal*, vol. 16, No.4, pp.187-195, 1998.

Cominettie M., Mignone V., Morello A., and Visintin M., 'The European system for digital multi-programme television by satellite', *IEEE Transactions on Broadcasting*, vol. 41, No.2, pp.49-62, 1995.

Consulting P., 'Global broadband satellite investment,' in *Satellite News*, 2000.

COST 255, EC, 'Radiowave Propagation Modelling for SatCom Services at Ku-band and Above'.

COST280, EC, 'Propagation Impairment Mitigation for Millimetre Wave Radio Systems'.

Cowpertwait P.S.P., 'A generalised Spatial-Temporal model of rainfall based on a cluster process', *Proceedings of Royal Society of London*, vol. 450, No.38, pp.163-175, 1995.

Crane R.K. and Shieh H.-C., 'A two component rain model for the prediction of site diversity performance', *Radio Science*, vol. 24, No.6, pp.641-665, 1989.

Davies O.T., Howell R.G., and Watson P.A., 'Measurement and modelling of cloud attenuation at millimeter wavelengths', presented at COST 255 First International Workshop on Radiowave Propagation Modelling for SatCom Services at Ku-band and

above, Noordwijk, Netherlands, pp.77-8, 1999.

Davies R.S., Huff R.J., and Ohlson J.E., 'Application of MF-TDMA for satellite communications', presented at Conference on satellite systems, pp.152-158, 1986.

Dissnayake A., Viskum H., and Haidara F., 'Propagation modelling for optimising spacecraft antenna coverage', presented at IEE Conference on Antennas and Propagation, 2000.

Dorides C. and Tomasicchio G., 'SKYPLEXNET system: an advanced platform for satellite multimedia services', presented at ECSC 5 Fifth European Conference on Satellite Communications, 1999.

Duverdier A., Comte M., Ribes A., Zarragoza J.L., and Tanguy Y., 'The DVB Processor on STENTOR', presented at ECSC5, Fifth European Conference on Satellite Communications, 1999.

European Commision, Directorate B: Satellite working group, 'Draft report on research and development : Advanced Communications technologies & Services', Jan, 1998.

Elia C. and Colzi E., 'SKYPLEX: Distributed Uplink for digital television via satellite', *IEEE Transactions on Broadcasting*, vol. 42, No.4, 1996.

ESA, 'MSG-1 weather satellite ready for commissioning', *www.esa.int*, 2002.

ETSI, DVB-RCS Draft report, 'Interaction channel for satellite distribution systems', 1999.

ETSI, EN 300 421, 'Digital Broadcasting systems for television, sound and data services: Frame structure, channel coding and modulation for 11/12GHz satellite services', EN 300 421.

EUROSKYWAY Technical Report, http://www.euroskyway.alespazio.it, 'SKYPLEX'.

Fiebig U.C., 'Modelling rain fading in satellite communications links', presented at Gateway to 21st Century Communications Village. VTC 1999-Fall. IEEE VTS 50th Vehicular Technology Conference, Piscataway, NJ, USA, pp.1422-6, 1999.

Fiebig U.C., 'A Rain Fading Channel Model for Satellite Communications Links', presented at Millennium Conference on Antennas and Propagation, Davos, Switzerland, pp.176-9,

2000.

Fiebig U.C., 'A Time-Series Generator Modelling Rain Fading and its Seasonal and Diurnal Variations', presented at COST 280 1st International Workshop, Toulouse, France, 2002.

Fiebig U.C. and Lemorton J., 'Overview of available channel models for time-series generation', presented at COST 280: 1st International Workshop, Malvern, UK, 2002.

Filip M. and Vilar E., 'Optimum utilization of the channel capacity of a satellite link in the presence of amplitude scintillations and rain attenuation', *IEEE Transactions on Communications*, vol. 38, No.11, pp.1958-65, 1990.

Foley T., 'A Space Odyssey,' in *Communications Week International*, March, 1998.

Fukuchi H., 'Correlation properties of rainfall rates in the United Kingdom', *IEE Proceedings*, vol. 135, No.2, pp.83-88, 1988.

Advanced Communications Technology (ACT) Co., 'Satellite access techniques for efficient WWW communications', 1998.

Ghani N. and Dixit S., 'TCP/IP enchancements for satellite networks', *IEEE Communications Magazine*, pp.64-72, 1999.

Gilderson J. and Cherkaoui J., 'Onboard switching for ATM via satellite', *IEEE Communications Magazine*, vol. 35, No.7, pp.66-70, 1997.

Meteorlogical Office, UM Doc. S1, 'Interpolation techniques and grid transformations used in the Unified Model', 1998.

Gremont B.C., 'Stochastic/Dynamic Model of Rain Attenuation', presented at COST 280 Propagation Impairment Mitigation for Millimetre Wave Radio Systems, Toulouse, 2001.

Gremont B.C. and Filip M., 'Modelling the instaneous frequency scaling factor (IFSF) of rain attenuation and applications', presented at ESTEC Workshop, Noordwijk, The Netherlands, 1999.

Gremont B.C. and Filip M., 'Simulation of a high frequency satellite link with a fade countermeasure', presented at IEE National Conference on Antennas and Propagation (IEE Conf. Publ. No.461). IEE. 1999, pp.164-8. London, UK., 1999.

COST 255, CP33001, 'Predictive fade countermeasures for Ka band satellite systems', 1996.

Technical research report CSHCN, T.R. 99-2 http://www.isr.umd.edu/CSHCN, 'Broadband access via satellite', 1999.

Hall M.P.M., Barclay L.W., and Hewitt M.T., *Propagation of radiowaves*: IEE, 1996.

Harris D.A., 'Online distance education in the United States', *IEEE Communications Magazine*, vol. 37, No.3, pp.87-91, 1999.

Hodge D.B., 'Path diversity for Earth-space communications links', *Radio Science*, vol. 13, pp.481-487, 1978.

Hodge D.B., 'An improved model of diversity gain on Earth-space paths', *Radio Science*, vol. 17, pp.1393-1399, 1982.

Final Report for the Radiocommunications Agency under Research Contract AY3362, 'Rainfall Intensity data for use in prediction of attenuation on terrestrial fixed links', 2001.

Hung A., Montpetit M.J., Kesidis G., and Takats P., 'A framework for ATM via satellite', presented at GLOBECOM 1996. Communications: The Key to Global Prosperity. Conference Record, New York, USA, pp.1020-5, 1996.

Ishimaru A., *Wave Propagation and scattering in a random media*, vol. 2. New York: IEEE press, 1978.

International Technology Research Institute, 'Global satellite communications technology and systems', 1998.

Radiocommunication Bureau, 'Handbook on Radiometeorology', Geneva, 1996.

ITU-R, 'Studio encoding parameters of digital television for standard 4:3 and wide screen 16:9 aspect ratios', BT601.

ITU-R, 'The radio refractive index: its formula and refractivity data', P453-7.

ITU-R, 'Propagation data and prediction methods required for the design of earth-space telecommunication systems', P618-6.

ITU-R, 'Attenuation by atmospheric gases', P676-4.

ITU-R, 'Characteristics of precipitation for propagation modelling', P837-2.

ITU-R, 'Specific attenuation model for rain for use in prediction models', P838-1.

ITU-R, 'Attenuation due to clouds and fog', P840-3.

ITU-R, 'Nomenclature of the frequency & wavelength bands used in telecommunications', V431.

Karasawa Y., Yamada M., and Allnutt J.E., 'A new prediction method for tropospheric scintillation on Earth-space paths', *IEEE Transactions on Antennas & Propagation*, vol. 36, No.11, pp.1608-14, 1988.

Konefal T., Watson P.A., Shukla A.K., and Akram A., 'Prediction of monthly and annual availabilities on 10-50 GHz satellite-Earth and aircraft-to-aircraft links', *IEE Proceedings-Microwaves Antennas & Propagation*, vol. 147, No.2, pp.122-7, 2000.

Kraichnan R.H. and Montgomery D., 'Two dimensional turbulence', *Rep. Prog. Phys*, vol. 43, pp.547-619, 1980.

Leitao M.J. and Watson P.A., 'Method for prediction of attenuation on earth-space links based on radar measurements of the physical structure of rainfall', *IEE Proceedings, Part F: Communications, Radar & Signal Processing*, vol. 133, pp.429-40, 1986.

Le-Ngoc T. and Mohammed J.I., 'Combined free/demand assignment multiple access (CFDAMA) protocols for packet satellite communications', presented at 2nd International Conference on Universal Personal Communications. Personal Communications: Gateway to the 21st Century. Conference Record (Cat. No.93TH0573-6). IEEE. 1993, pp.824-8 vol. 2. New York, NY, USA., 1993.

Liao W. and Li V.O.K., 'The Split and Merge protocol for interactive video-on-demand',

IEEE Multimedia, vol. 4, No.4, pp.51-52, 1997.

Liebe H.J., 'MPM - An atmospheric Millimeter-wave propagation model', *International Journal of infrared & millimeter waves*, vol. 10, No.6, pp.631-650, 1989.

Liebe H.J., Manabe T., and Hufford G.A., 'Millimeter-wave attenuation and delay rates due to fog/cloud conditions', *IEEE Transactions on Antennas and Propagation*, vol. 2, pp.165-8, 1989.

Lin S.H., 'Statistical behaviour of rain attenuation', *Bell System Technical Journal*, vol. 52, No.4, pp.557-81, 1973.

Lin S.H., 'More on rain rate distributions and extreme value statistics', *Bell System Technical Journal*, vol. 57, pp.1545-1568, 1978.

Lisi I.M., 'Satellite antennas into the 21th century: A system engineering perspective', presented at IEE Antennas & Propagation, 2000.

Little T., 'Satellite based distance learning using digital video and internet', *IEEE Multimedia*, vol. 5, No.3, pp.72-77, 1998.

Little T. and Venkatesh D., 'Prospects for video-on-demand', *IEEE Multimedia*, vol. 1, No.3, pp.14-23, 1994.

Livingstone A., 'Interactivity via digital satellite', presented at IEE Colloquiumon Multimedia Services and digital television by satellite, London, 1999.

Losquadro G., 'SECOMS: advanced interactive multimedia satellite communications for a variety of compact terminals', presented at IEE Colloquium on EU's Initiatives in Satellite Communications - Mobile (Ref. No.1997/087). IEE. 1997, pp.3/1-7. London, UK., 1997.

Losquadro G. and Schena V., 'The SECOMS project satellite service demonstration results', presented at Gateway to 21st Century Communications Village. VTC 1999-Fall. IEEE VTS 50th Vehicular Technology Conference (Cat. No.99CH36324). IEEE. Part vol.5, 1999, pp.2744-9 vol.5. Piscataway, NJ, USA., 1999.

Lovejoy S. and Schertzer D., 'Multifractals in rain', *New Concepts in Hydrology and water resources*,

1992.

Luglio M., 'Application of frequency diversity for dimensioning a Ka-band satellite system', *International Journal of Satellite Communications*, vol. 14, pp.53-56, 1996.

Luglio M., Marinelli M., and Paraboni A., 'Provision of multimedia services over Europe by means of geostationary satellites with multispot coverage using small terminals', *Wireless Networks*, vol. 4, No.2, pp.125-39, 1998.

Mah B.A., 'An emprical model of HTTP network traffic', presented at INFOCOM'97, Japan, pp.5c.1.1-5c.1.9, 1997.

Mandelbrot.

Maral G. and Bousquet M., *Satellite communication systems*: Wiley & Sons, 1998.

Maseng T. and Bakken P.M., 'A stochastic dynamic model of rain attenuation', *IEEE Transactions on Communications*, vol. COM-29, No.5, pp.660-9, 1981.

Matricciani E., 'Rain Attenuation Predicted with a Two-Layer Rain Model', *European Transactions on Telecommunications*, vol. 2, No.6, pp.715-727, 1991.

Matricciani E., 'Physical-mathematical model of dynamics of rain attenuation with application to power spectrum', *Electronics Letters*, vol. 30, No.6, pp.522-4, 1994.

Matricciani E., Mauri M., and Paraboni A., 'Dynamic Characteristics of Rain Attenuation: Duration and Rate of Change', *Alta Frequenza*, vol. 106, No.2, pp.33-45, 1987.

Matricciani E., Mauri M., and Riva C., 'Scintillation and simultaneous rain attenuation at 49.5 GHz', *Ninth International Conference on Antennas and Propagation (Conf. Publ. No.407). IEE.*, vol. 2, pp.165-8, 1995.

Mertzanis I., Sfikas G., Tafazolli R., and Evans B.G., 'Protocol architectures for satellite ATM broadband networks', *IEEE Communications Magazine*, pp.46-54, 1999.

Meteorological Office, 'Unified Model User Guide', http://www.rdg.ac.uk/~panagi, 1998.

Milenkovic M., 'Delivering interactive services via digital TV infrastructure', *IEEE Multimedia*,

pp.34-43, 1998.

Moulsley T.J., Haddon J., Lo P., and Vilar E., 'Measurement and modelling of the probability density function of amplitude scintillations on an X-band satellite down-link', *Electronics Letters*, vol. 17, No.18, pp.625-6, 1981.

Moulsley T.J. and Vilar E., 'Experimental and theoretical statistics of microwave amplitude scintillations on satellite down-links', *IEEE Transactions on Antennas & Propagation*, vol. AP-30, No.6, pp.1099-106, 1982.

ISO/IEC 13818-1, 'MPEG-2 System', 1994.

Ohlson J.E. and Huff R.J., 'Multi-Frequency TDMA for satellite communications', presented at International Conference on Communications, pp.892-896, 1983.

OPEX, *Radiometry & Metrological Measurements*, vol. 3: ESA, 1994.

Ortgies G., 'Probability density function of amplitude scintillations', *Electronics Letters*, vol. 21, No.4, pp.141-2, 1985.

Otung I.E., Al-Nuaimi M.O., and Evans B.G., 'Extracting scintillations from satellite beacon propagation data', *IEEE Transactions on Antennas & Propagation*, vol. 46, No.10, pp.1580-1, 1998.

Otung I.E. and Evans B.G., 'Short term distribution of amplitude scintillation on a satellite link', *Electronics Letters*, vol. 31, No.16, pp.1328-9, 1995.

Over T.M. and Gupta V.K., 'A space-time theory of mesoscale rainfall using random cascades', *Journal of Geophysical Research*, vol. 101, No.D21, pp.26,319-26,331, 1996.

Padmanabhan V.N. and Mogul J.C., 'Improving HTTP latency', presented at 2nd International World Wide Web conference, Chicago, 1994.

Page A., 'Validation of Propagation Prediction for systems test cases', presented at Final Meeting & Closing Workshop COST255 Radiowave propagation at Ku band and above, 1999.

Page A. and Watson P.A., 'Use of V-band in multimedia messaging services via geostationary

satellites', presented at AP2000: Millennium conference on Antennas and Propagation, Davos, Switzerland, 2000.

Page A. and Watson P.A., 'Use of V-band in multimedia messaging services via geostationary satellites', presented at URSI Symposium, Hosted by RAL, Abingdon, Oxford, 2000.

Page A. and Watson P.A., 'Time-series of attenuation on EHF and SHF fixed radio links derived from meteorological forecast and radar data', presented at RAINMAP'01 WORKSHOP, hosted by the DTI, London, 2001.

Page A. and Watson P.A., 'Time-series of attenuation on EHF and SHF fixed radio links derived from meteorological forecast and radar data', presented at 1st International Workshop COST280 Propagation Impairment Mitigation for Millimetre Wave radio systems, Toulouse, France, 2001.

MDIAG, 'MDIAG: A Fortran 90 Program to Compute Diagnostics on Pressure levels from UM data on Model Levels', 2000.

University of Reading, 'Met. Office Unified Model Data, diagnostics, graphical programs and other observational data available from the JCMM through the aegis of the Universities Weather Research Network - UWERN', 1997.

Paraboni A., Capsoni C., Masini G., Poiares Baptista J.P.V., and Riva C., 'Dynamic fade restoration in Ka-band satellite systems', *International Journal of Satellite Communications*, vol. 20, pp.283-291, 2002.

Paulson K.S. and Gibbins C.J., 'Rain models for the prediction of fade durations at millimetre wavelengths', *IEE Proceedings-Microwaves Antennas & Propagation*, vol. 147, No.6, pp.431-6, 2000.

Peyravi H., 'Medium access control protocols performance in satellite communications', *IEEE Communications Magazine*, vol. 37, No.3, pp.62-71, 1999.

Polonio R. and Riva C., 'ITALSAT propagation experiment at 18.7, 39.6 and 49.5 GHz at Spino D'Adda: three years of CPA statistics', *IEEE Transactions on Antennas & Propagation*, vol. 46, No.5, pp.631-5, 1998.

Puente C.E., Obregon N., Robayo O., Puente M.A., and Simsek D., 'Projections

off fractal functions: a new vision of natures complexity', *Fractals*, vol. 7, No.4, pp.387-401, 1999.

RFC2488, 'Enchancing TCP over satellite channels using standard mechanisms', 1999.

Richharia M., *Satellite Communcations systems: design principles*. Macmillan, 1995.

Rogers D.V., 'Aspects of site diversity for multimedia satellite services', presented at AP2000: Millennium conference on Antennas and Propagation, Davos, Switzerland, 2000.

Rosen H.A., *Direct broadcast satellite communications: An MPEG enabled service*. Addision & Wesley, 2000.

Russchenberg H.W.J. and Ligthart L.P., 'Backscattering by propagation through melting layer of precipitation: A new polarimetric model', *IEEE Transactions on Geoscience and Remote sensing*, vol. 34, No.1, pp.3-14, 1996.

Salonen E. and Uppala S., 'New prediction method of cloud attenuation', *Electronics Letters*, vol. 27, No.12, pp.1106-8, 1991.

Saunders S., *Antennas & Propagation for Wireless Communications Systems*, 1998.

Savvaris A., Kassianides C.N., and Otung I.E., 'Observed effects of wind on the intensity and spectrum of scintillation', presented at Eleventh International Conference on Antennas and Propagation (IEE Conf. Publ.No.480). IEE. Part vol.2, 2001, pp.546-50 vol.2. London, UK., 2001.

Schmitt F., Vannitsem S., and Barbosa A., 'Modeling of rainfall time series using two-state renewal processes and multifractals', *Journal of Geophysical Research*, vol. 103, No.D18, pp.23,181 - 23,193, 1998.

Shvodian W.M., 'Multiple priority distributed round robin MAC protocol for satellite ATM', presented at IEEE Military Communications Conference. Proceedings. MILCOM 98 (Cat. No.98CH36201). IEEE. Part vol.1, 1998, pp.258-62 vol.1. New York, NY, USA., 1998.

Sklar B., 'A primer on Turbo concepts', *IEEE Communications Magazine*, pp.94-101, 1997.

Sklar B., *Digital Communications Fundamentals & Applications*, 2003.

Smith A.H. and Kitchen M., 'A review of the quality control and quality evaluation of radar rainfall measurements carried out by the UK Met. Office', *COST 75 Advanced weather radar systems, published by European Commission*, pp.68-81, 1999.

Meteorological Office, UM Doc. 29, 'Calculation of Saturated Specific Humidity and Large-Scale Cloud', 1997.

SpaceDaily, 'SKYPLEX Multimedia in the Sky,' in *Space Daily*, 1998.

Stirland S.J., Fox G.P.D., and Cols J., 'Multi-beam reflector antennas for space', presented at IEE Antennas & Propagation, 2000.

Tannenbaum A.S., *Computer Networks*, third ed: Prentice-Hall International, 2000.

Tatarskii V.I., *Wave propagation in a turbulent medium.* New York: McGraw-Hill, 1961.

Tattelman P. and Scharr K.G., 'A model for estimating one minute rainfall rates', *Journal of Climate and Applied Meteorology*, vol. 22, pp.1575-1580, 1983.

Tozer T.C. and Grace D., 'High-Altitude platforms for wireless communications', *Electronics and Communication Engineering Journal*, No.June 2001, 2001.

Meteorological Office, UM Doc. 80, 'Physical & Dynamic Diagnostics as calculated within the Unified Model', 1993.

Meteorological Office, 'Unified Model User Guide', 1998.

Vanhoenacker D. and Vander Vorst A., 'Atmospheric fluctuation spectra and radio system implications', presented at Fourth International Conference on Antennas and Propagation (ICAP 85) (Proceedings No.248). IEE. 1985, pp.67-71. London, UK., 1985.

Vanhoenacker D., Vasseur H., and Amaya-Byrne C., 'Simulation of the effects of atmospheric scintillation on digital transmissions at centimeter and millimeter wavelengths', *International Journal of Infrared & Millimeter Waves*, vol. 12, No.10, pp.1215-24, 1991.

Vasseur H., 'Prediction of tropospheric scintillation on satellite links from radiosonde data',

IEEE Transactions on Antennas & Propagation, vol. 47, No.2, pp.293-301, 1999.

Veneziano D., Bras R.L., and Nieman J.D., 'Nonlinearity and self-similarity of rainfall in time and a stochastic model', *Journal of Geophysical Research*, vol. 101, No.D21, pp.26,371-26,392, 1996.

Warnock J., VanZandt T., and Green J., 'A statistical model to estimate mean values of parameters of turbulence in the free atmosphere', presented at 7th symposium Turbulence Diffusion, Boulder, CO, pp.156-159, 1985.

Watson P.A. and Hu Y.F., 'Prediction of attenuation on satellite-earth links for systems operating with low fade margins', *IEE Proceedings-Microwaves Antennas & Propagation*, vol. 141, pp.467-72, 1994.

Watson P.A., Konefal T., Page A., Shukla A.K., and Akram A., 'Propagation prediction for V-band systems', presented at AP2000: Millennium conference on Antennas and Propagation, Davos, Switzerland, 2000.

COST255 Radiowave propagation at Ku band and above, CP73003, 'V-band asymmetric system (Test Case 3): System Specification', May, 1999.

COST255, Final Report, 'Test Case 3: V-band VSAT asymmetrical data communication system', 1999.

Watson P.A., Papaioannou G., and Neves J.C., 'Attenuation and cross-polarisation measurements at 36-GHz on a terrestrial path', presented at URSI F Open Symposium, La Baule, pp.283-287, 1977.

Wittig M., Dinwiddy S.E., and Chatterton J., 'OBP for Private Networks and Residential Users', presented at Tenth International conference on Digital Satellite Communications, London, UK, pp.653-60, 1994.

List of Publications

Page A. and Watson P.A., "Time-series of attenuation on EHF and SHF fixed radio links derived from meteorological forecast and radar data", presented at 1st International Workshop COST280 Propagation Impairment Mitigation for Millimetre Wave radio systems, Toulouse, France, 2001.

Page A. and Watson P.A., "Time-series of attenuation on EHF and SHF fixed radio links derived from meteorological forecast and radar data", presented at RAINMAP'01 WORKSHOP, hosted by the DTI, London, 2001.

Page A. and Watson P.A., "Use of V-band in multimedia messaging services via geostationary satellites", presented at AP2000: Millennium conference on Antennas and Propagation, Davos, Switzerland, 2000.

Watson P.A., Konefal T., Page A., Shukla A.K., and Akram A., "Propagation prediction for V-band systems", presented at AP2000: Millennium conference on Antennas and Propagation, Davos, Switzerland, 2000.

Page A. and Watson P.A., "Use of V-band in multimedia messaging services via geostationary satellites", presented at URSI Symposium, Hosted by RAL, Abingdon, Oxford, 2000.

Watson P.A., Page A., and Martellucci A.,"Test Case 3: V-band VSAT asymmetrical data communication system", COST255, Final Report, 1999.

Page A., "Validation of Propagation Prediction for systems test cases", presented at Final Meeting & Closing Workshop COST255 Radiowave propagation at Ku band and above, 1999.

Watson P.A., Larsen J., Martellucci A., and Page A.,"V-band asymmetric system (Test Case 3): System Specification", COST255 Radiowave propagation at Ku band and above, CP73003, May 1999.

STSM Report :

VALIDATION OF PROPAGATION PREDICTION FOR SYSTEMS TEST CASES

[1]Andrew Page

[1]Department of Electronic and Electrical Engineering,
University of Bath, Claverton Down, Bath, BA2 7AY, UK
Tel +44 (0) 1225 826061, Fax +44 (0) 1225 826305.
Email: A.Page@bath.ac.uk

1 INTRODUCTION

As part of COST 255, "Test Case" systems have been proposed in the frequency range 20-50GHz. Propagation prediction modelling has been applied to quantify tropospheric effects on these systems. In particular, work was carried out through the STSM to process predictions for Test Case 2, namely "Ka Band VideoConference System[1]". The model[2,3] predicts annual and monthly availability for a low fade margin, due to the contributing components of attenuation, including rain, cloud and atmospheric gases.

2 MODEL SPECIFICATION

The model specification was defined by the Test Case 2 link budget[1]. The Test Case comprises of a link between two USATs in Belgium, Louvain-la-Neuve (5.25 °E longitude - 50.22 °N latitude) and Lessive (4.62 °E longitude - 50.67°N latitude) through a geostationary satellite (19 °W). The link was modelled as two separate uncorrellated links, for both uplink and downlink. The modelled frequencies and link margins are given in table 1 below.

	Frequency	Link Margin
Uplink	29.625 GHz	1.75 dB
		4.75 dB
		10.75 dB
Downlink	19.7 GHz	1.9 dB
		10.9 dB

Table 1 : Model Parameters

The results from the propagation prediction model for these parameters are given in the Appendices. Rain Rate values are included to enable comparisons with measurements taken at CERT-ONERA.

3 CONCLUSION

The propagation prediction model has been applied to Test Case 2 as proposed for the STSM. The results will help evaluate the availability performance of the videoconference service. Comparisons can now be made with the predictions from CERT-ONERA, to validate the propagation results.

In addition, monthly availability maps for the European region have been drawn for the system. These highlight coverage areas where tropospheric effects degrade system performance below the system requirements (99% availability with USATs, 99.5% with VSATs and 99.9% for gateways). The map has been compiled with a resolution of 1.5°.
A monthly example is included in the Appendices.

Further work is continuing to make comparisons made by the Fondazione Ugo Bordoni (Dr Martellucci) for Test Case 3[4], and also to process propagation predictions for Test Case 5 [5].

4 ACKNOWLEDGEMENTS

I would like to express my gratitude to the COST 255 Management Committee for the opportunity to participate in this mission. And also to Laurent Castanet from CERT-ONERA for his collaboration during the mission.

5 REFERENCES

[1] L.Castanet, H. Vasseur, M. Bousquet and A. Vander Vorst, "Simulation test case n°2: Ka band videoconference VSAT system requirements", COST 255, CP63002

[2] "Prediction of monthly cumulative distributions of short duration rain intensities", T. Konefal and P.A. Watson, COST 255, CP42007

[3] "Midas: A monthly link budget and decision tool for frequencies between 10 and 50 GHz", A. Akram, A. Shukla, T. Konefal and P.A. Watson, IEE NCAP, York, April 1999, pp 152 - 155

[4] P.A. Watson, J.R. Larsen, A. Martellucci, A. Page, "Simulation test case n°3: Millimetre-Wave Multimedia GEO System Specification, COST 255, CP73003

[5] J. Habetha, "Simulation test case n°5: IRIDIUM Feeder Link Ka-band System Requirements", COST 255, CP7005

6 APPENDICES

A1.1 Louvain-la-Neuve - UPLINK

latitude = 50.22 N
longitude = 5.25 E
satellite longitude = 19 W

Frequency (GHz)	Attenuation (dB)	Month	Exceedance (%)	Availability (%)	Rain Rate (mm/hr)
29.625	1.75	Jan	6.80	93.20	0.75
	1.75	Feb	6.81	93.19	0.75
	1.75	Mar	7.73	92.27	0.73
	1.75	Apr	6.80	93.20	0.61
	1.75	May	7.53	92.47	0.48
	1.75	Jun	8.26	91.74	0.40
	1.75	Jul	7.75	92.25	0.35
	1.75	Aug	8.19	91.81	0.38
	1.75	Sep	8.72	91.28	0.45
	1.75	Oct	9.50	90.50	0.59
	1.75	Nov	9.17	90.83	0.76
	1.75	Dec	7.42	92.58	0.75
		Av. Month	7.89	92.11	-

Frequency (GHz)	Attenuation (dB)	Month	Exceedance (%)	Availability (%)	Rain Rate (mm/hr)
29.625	4.75	Jan	0.15	99.85	4.00
	4.75	Feb	0.17	99.83	3.85
	4.75	Mar	0.12	99.88	3.26
	4.75	Apr	0.29	99.71	3.51
	4.75	May	0.50	99.50	2.76
	4.75	Jun	0.76	99.24	2.27
	4.75	Jul	0.85	99.15	2.05
	4.75	Aug	0.87	99.13	2.06
	4.75	Sep	0.77	99.23	2.27
	4.75	Oct	0.58	99.42	2.62
	4.75	Nov	0.31	99.69	3.24
	4.75	Dec	0.22	99.78	3.71
		Av. Month	0.47	99.53	-

Frequency (GHz)	Attenuation (dB)	Month	Exceedance (%)	Availability (%)	Rain Rate (mm/hr)
29.625	10.75	Jan	0.01	99.99	15.36
	10.75	Feb	0.01	99.99	14.33
	10.75	Mar	0.01	99.99	12.54
	10.75	Apr	0.04	99.96	12.01
	10.75	May	0.13	99.87	9.35
	10.75	Jun	0.26	99.74	7.48
	10.75	Jul	0.32	99.68	6.70
	10.75	Aug	0.32	99.68	6.69
	10.75	Sep	0.25	99.75	7.34
	10.75	Oct	0.11	99.89	8.44
	10.75	Nov	0.03	99.97	10.46
	10.75	Dec	0.02	99.98	13.07
		Av. Month	0.13	99.87	-

A1.2 Louvain-la-Neuve - DOWNLINK

Frequency (GHz)	Attenuation (dB)	Month	Exceedance (%)	Availability (%)	Rain Rate (mm/hr)
19.7	1.9	Jan	1.13	98.87	1.51
	1.9	Feb	1.14	98.86	1.49
	1.9	Mar	1.24	98.76	1.41
	1.9	Apr	1.19	98.81	1.29
	1.9	May	1.47	98.53	1.08
	1.9	Jun	1.66	98.34	0.90
	1.9	Jul	1.67	98.33	0.82
	1.9	Aug	1.71	98.29	0.84
	1.9	Sep	1.71	98.29	0.94
	1.9	Oct	1.73	98.27	1.14
	1.9	Nov	1.61	98.39	1.42
	1.9	Dec	1.29	98.71	1.48
	Av. Month		1.46	98.54	-

Frequency (GHz)	Attenuation (dB)	Month	Exceedance (%)	Availability (%)	Rain Rate (mm/hr)
19.7	10.9	Jan	0.00	100.0	0.00
	10.9	Feb	0.00	100.0	25.92
	10.9	Mar	0.00	100.0	29.02
	10.9	Apr	0.01	99.99	13.20
	10.9	May	0.05	99.95	17.93
	10.9	Jun	0.09	99.91	14.55
	10.9	Jul	0.11	99.89	14.74
	10.9	Aug	0.11	99.89	14.69
	10.9	Sep	0.09	99.91	14.29
	10.9	Oct	0.04	99.96	16.36
	10.9	Nov	0.00	100.0	20.23
	10.9	Dec	0.00	100.0	24.13
		Av. Month	0.04	99.96	-

A1.3 Lessive - UPLINK

latitude = 50.67 N
longitude = 4.62 E
satellite longitude = 19 W

Frequency (GHz)	Attenuation (dB)	Month	Exceedance (%)	Availability (%)	Rain Rate (mm/hr)
29.625	1.75	Jan	6.98	93.02	0.69
	1.75	Feb	6.97	93.03	0.69
	1.75	Mar	7.88	92.12	0.68
	1.75	Apr	6.89	93.11	0.56
	1.75	May	7.45	92.55	0.44
	1.75	Jun	7.82	92.18	0.36
	1.75	Jul	7.49	92.51	0.32
	1.75	Aug	7.53	92.47	0.33
	1.75	Sep	8.17	91.83	0.40
	1.75	Oct	9.24	90.76	0.54
	1.75	Nov	9.17	90.83	0.71
	1.75	Dec	7.65	92.35	0.71
		Av. Month	7.77	92.23	-

Frequency (GHz)	Attenuation (dB)	Month	Exceedance (%)	Availability (%)	Rain Rate (mm/hr)
29.625	4.75	Jan	0.12	99.88	3.71
	4.75	Feb	0.13	99.87	3.58
	4.75	Mar	0.10	99.90	3.93
	4.75	Apr	0.26	99.74	3.37
	4.75	May	0.48	99.52	2.70
	4.75	Jun	0.71	99.29	2.21
	4.75	Jul	0.81	99.19	2.00
	4.75	Aug	0.81	99.19	2.00
	4.75	Sep	0.71	99.29	2.20
	4.75	Oct	0.53	99.47	2.54
	4.75	Nov	0.28	99.72	3.13
	4.75	Dec	0.19	99.81	3.55
		Av. Month	0.43	99.57	-

Frequency (GHz)	Attenuation (dB)	Month	Exceedance (%)	Availability (%)	Rain Rate (mm/hr)
29.625	10.75	Jan	0.01	99.99	15.28
	10.75	Feb	0.01	99.99	14.79
	10.75	Mar	0.01	99.99	12.51
	10.75	Apr	0.03	99.97	11.97
	10.75	May	0.11	99.89	9.28
	10.75	Jun	0.25	99.75	7.43
	10.75	Jul	0.31	99.69	6.66
	10.75	Aug	0.31	99.69	6.64
	10.75	Sep	0.23	99.77	7.29
	10.75	Oct	0.10	99.90	8.38
	10.75	Nov	0.03	99.97	10.44
	10.75	Dec	0.02	99.98	13.03
		Av. Month	0.12	99.88	-

A1.4 Lessive - DOWNLINK

Frequency (GHz)	Attenuation (dB)	Month	Exceedance (%)	Availability (%)	Rain Rate (mm/hr)
19.7	1.9	Jan	1.10	98.90	1.36
	1.9	Feb	1.10	98.90	1.35
	1.9	Mar	1.21	98.79	1.29
	1.9	Apr	1.15	98.85	1.17
	1.9	May	1.43	98.57	1.00
	1.9	Jun	1.61	98.39	0.84
	1.9	Jul	1.64	98.36	0.76
	1.9	Aug	1.65	98.35	0.77
	1.9	Sep	1.65	98.35	0.87
	1.9	Oct	1.69	98.31	1.06
	1.9	Nov	1.60	98.40	1.33
	1.9	Dec	1.30	98.70	1.37
		Av. Month	1.43	98.57	-

Frequency (GHz)	Attenuation (dB)	Month	Exceedance (%)	Availability (%)	Rain Rate (mm/hr)
19.7	10.9	Jan	0.00	100.0	0.00
	10.9	Feb	0.00	100.0	25.75
	10.9	Mar	0.00	100.0	23.52
	10.9	Apr	0.01	99.99	22.75
	10.9	May	0.04	99.96	17.88
	10.9	Jun	0.09	99.91	14.50
	10.9	Jul	0.10	99.90	14.65
	10.9	Aug	0.10	99.90	14.52
	10.9	Sep	0.08	99.92	14.22
	10.9	Oct	0.04	99.96	16.31
	10.9	Nov	0.00	100.0	20.12
	10.9	Dec	0.00	100.0	23.91
		Av. Month	0.04	99.96	-

A2 Monthly European Availability Maps

Annual Availability contours for a threshold of 4.75dB at 29.7GHz,19W

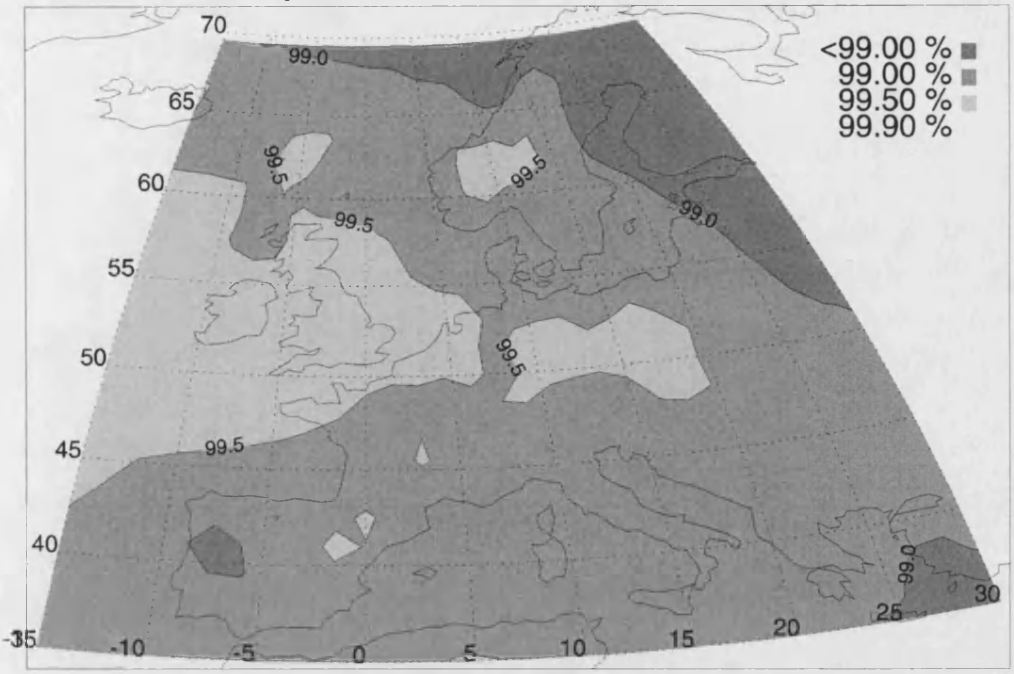

Availability contours for January for a threshold of 4.75dB at 29.7GHz,19W

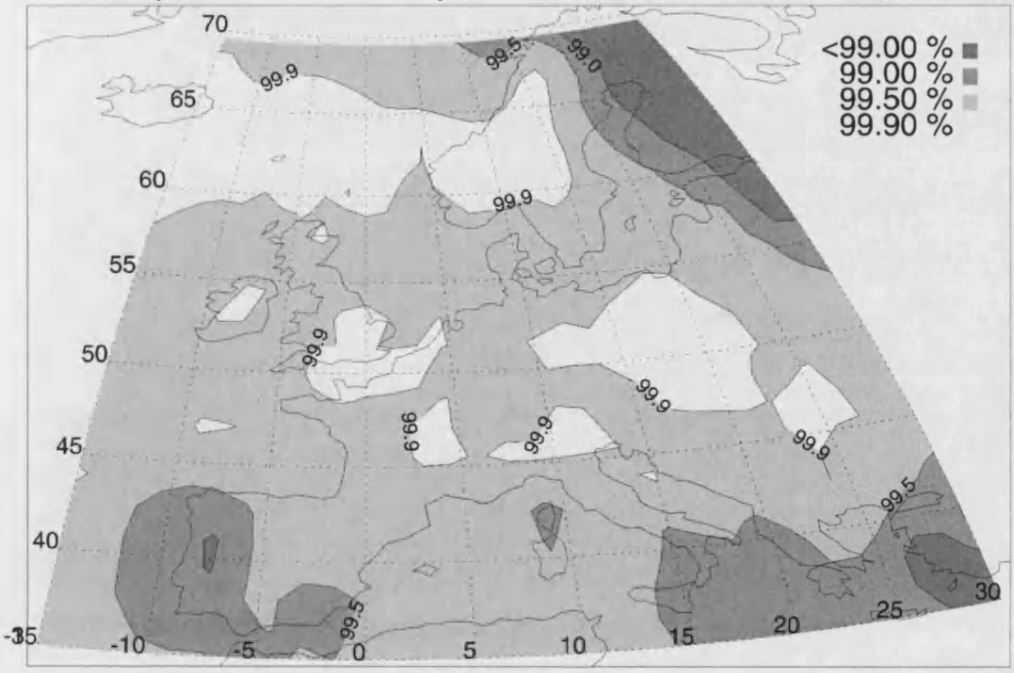

Availability contours for February for a threshold of 4.75dB at 29.7GHz,19W

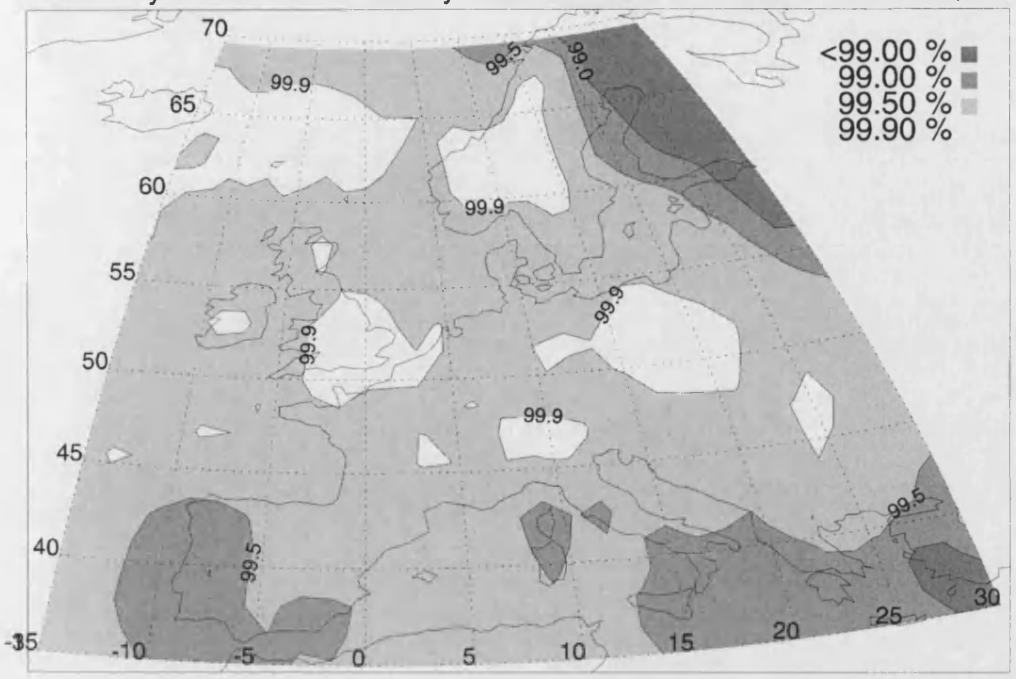

Availability contours for March for a threshold of 4.75dB at 29.7GHz,19W

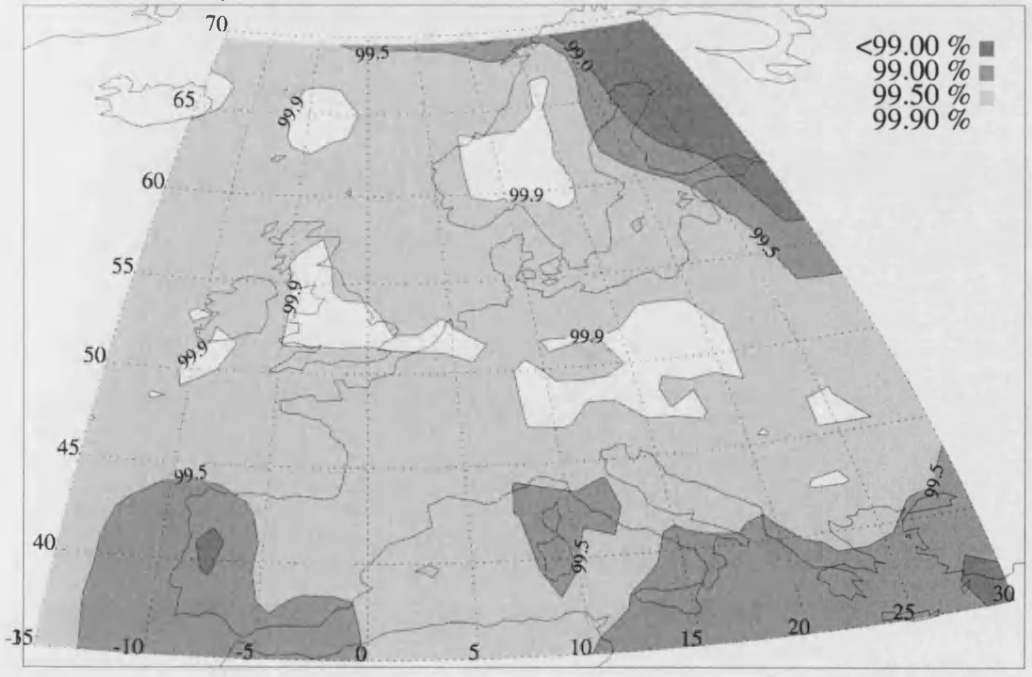

Availability contours for April for a threshold of 4.75dB at 29.7GHz,19W

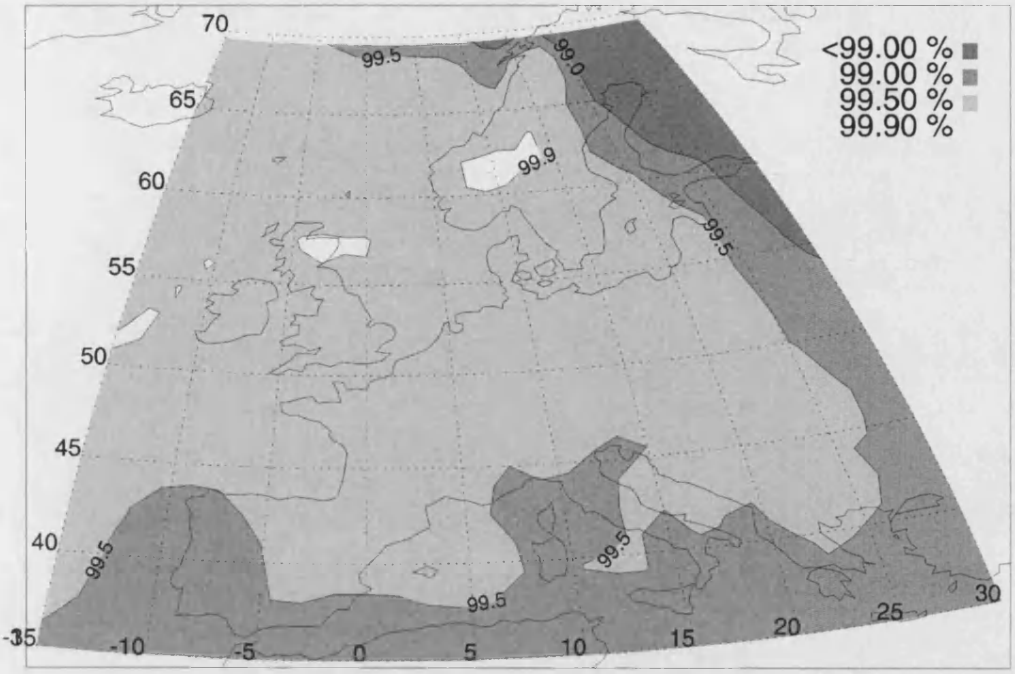

Availability contours for May for a threshold of 4.75dB at 29.7GHz,19W

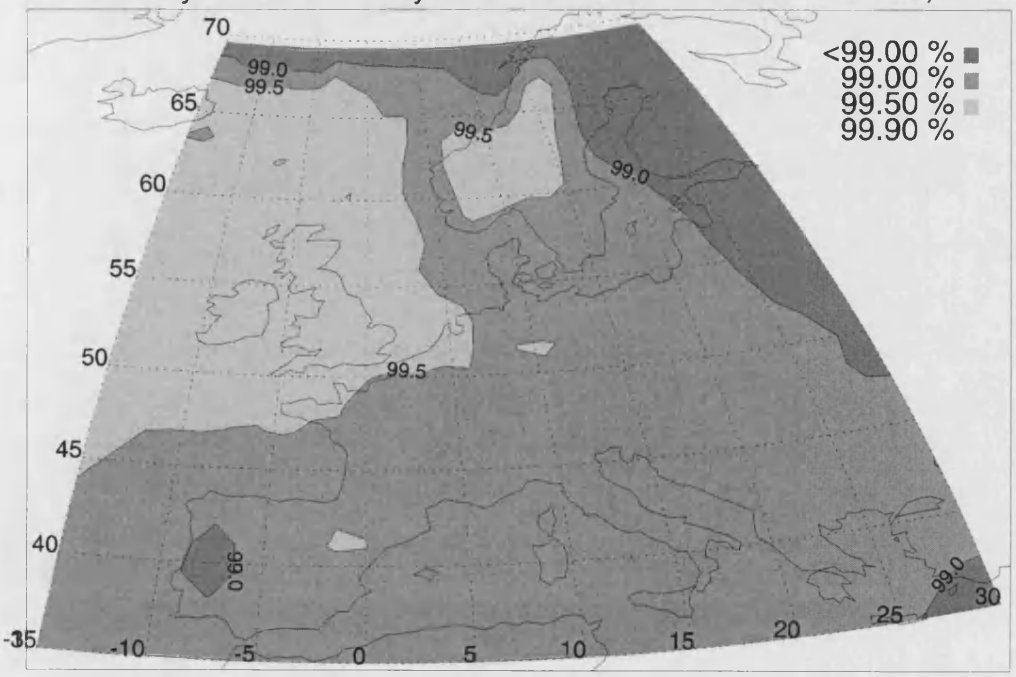

Availability contours for June for a threshold of 4.75dB at 29.7GHz,19W

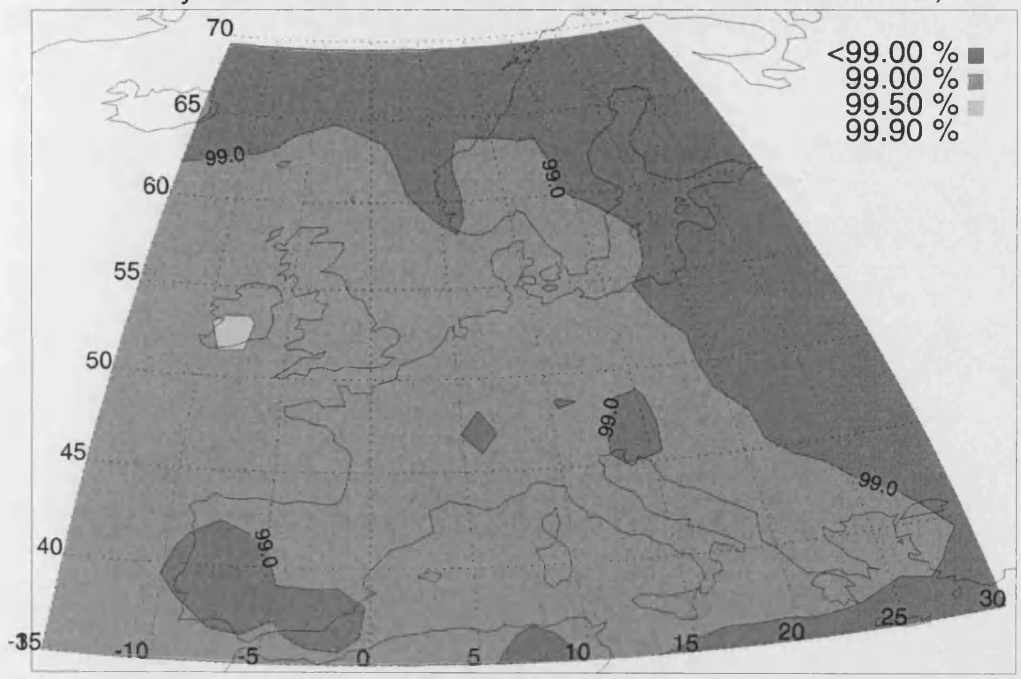

Availability contours for July for a threshold of 4.75dB at 29.7GHz,19W

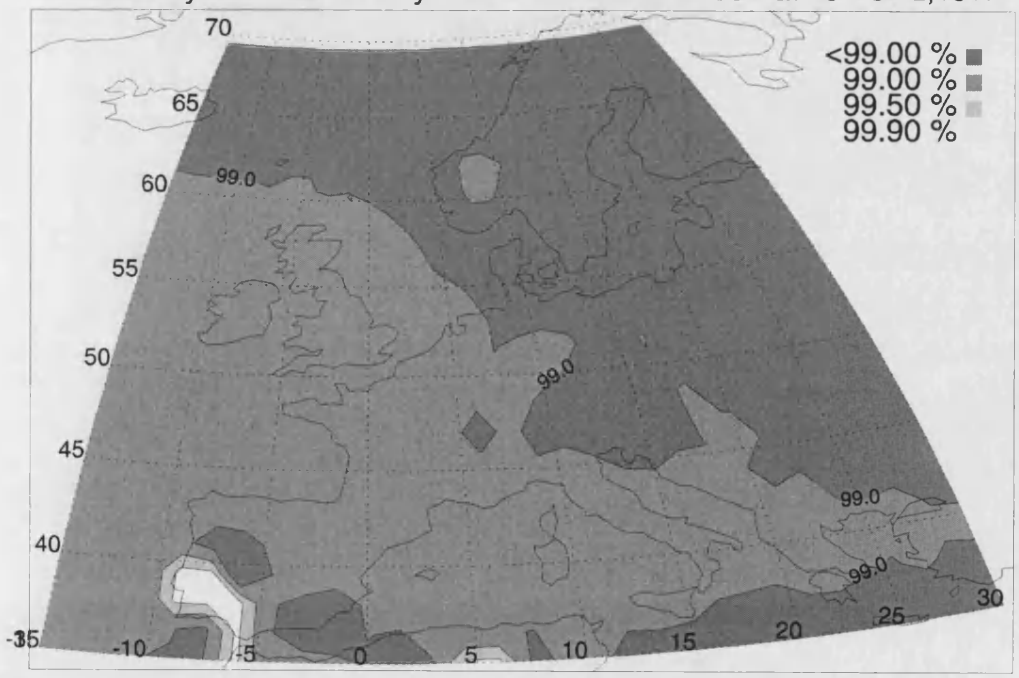

Availability contours for August for a threshold of 4.75dB at 29.7GHz,19W

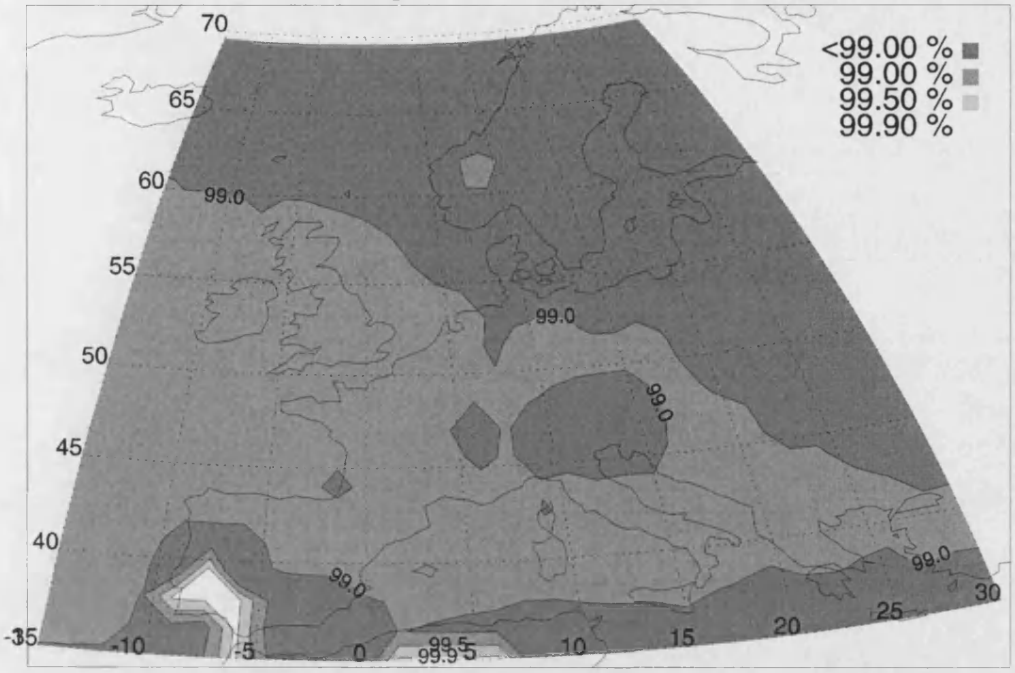

Availability contours for September for a threshold of 4.75dB at 29.7GHz,19W

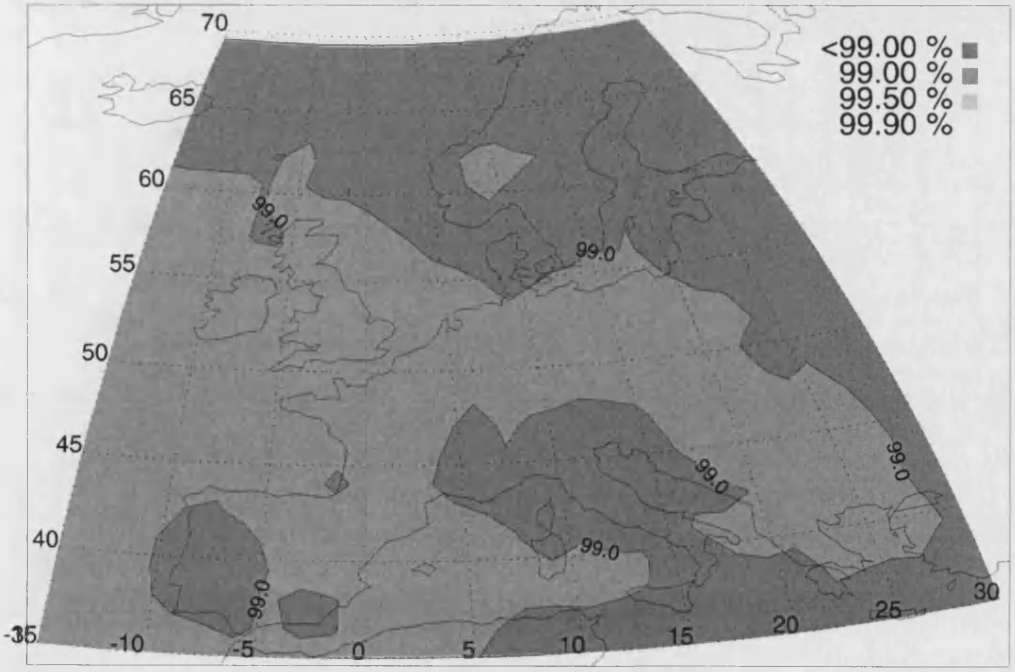

Availability contours for October for a threshold of 4.75dB at 29.7GHz,19W

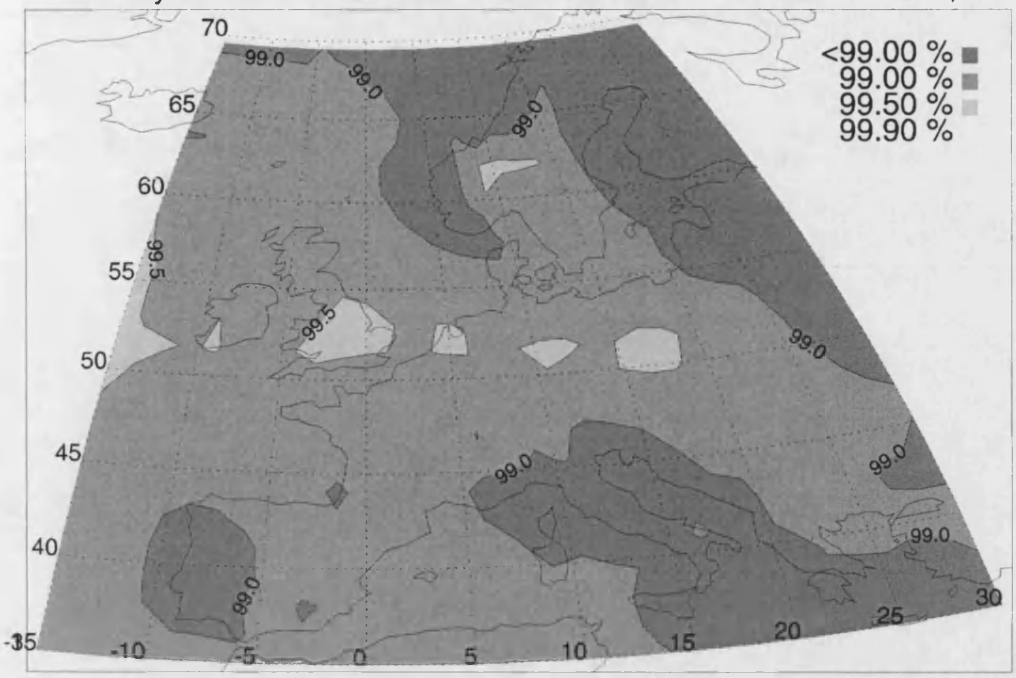

Availability contours for November for a threshold of 4.75dB at 29.7GHz,19W

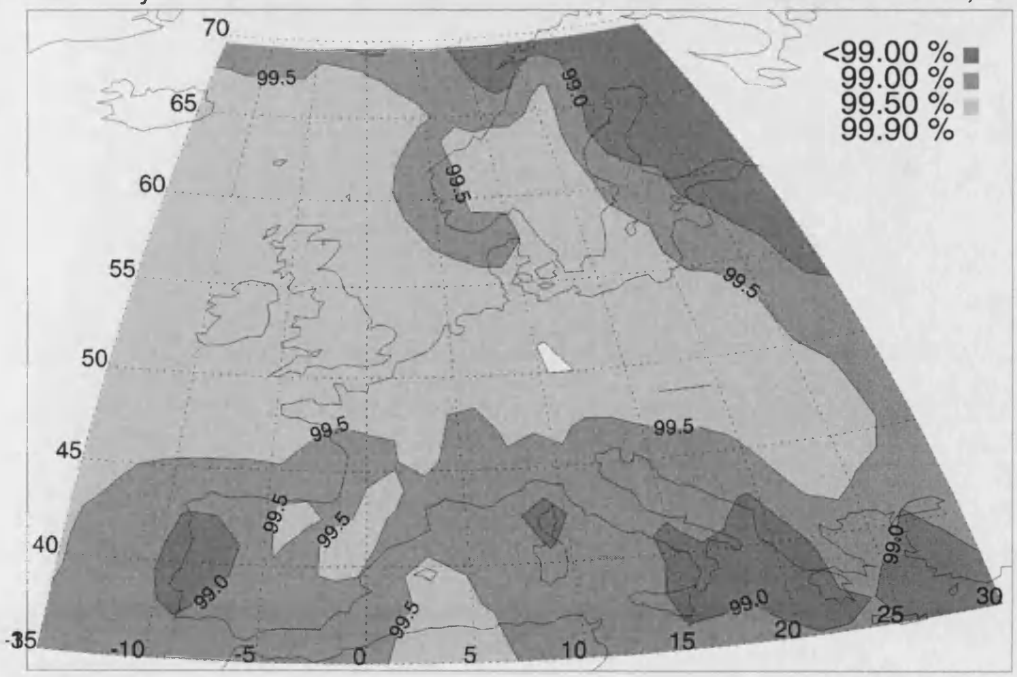

Availability contours for December for a threshold of 4.75dB at 29.7GHz,19W

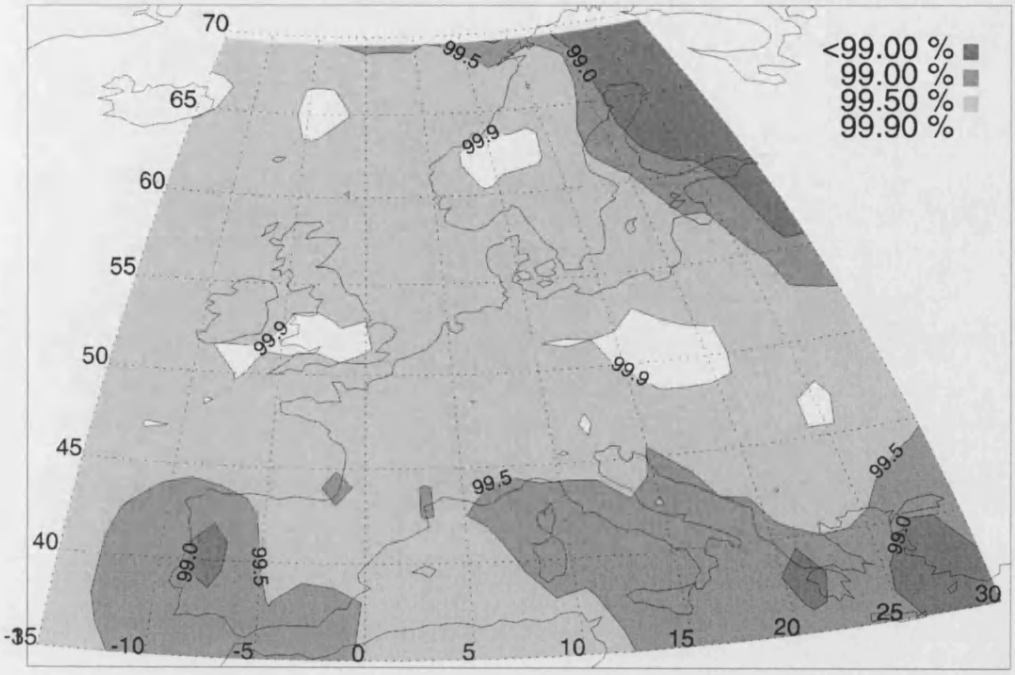

CHAPTER 6.3

Test Case 3: V-Band VSAT Asymmetrical Data Communication System

Editor: Prof. P.A. Watson[1]

Authors: Prof. P.A. Watson, Mr Andrew Page[2], Dr. A. Martellucci[3]

[1] University of Bath, Dept. of E&E Engineering, Claverton Down, Bath, BA2 7AY, UK
Tel.: +44-1225-826-6330, Fax.: +44-1225-826-6305, e-mail: P.A.Watson@bath.ac.uk

[2] University of Bath, Dept. of E&E Engineering, Claverton Down, Bath, BA2 7AY, UK
Tel.: +44-1225-826-6061, Fax.: +44-1225-826-6305, e-mail: A.Page@bath.ac.uk

[3]Fondazione Ugo Bordoni, RadioCommunications Dept., Viale Europa 190, I-00144 Rome, ITALY
Tel. : +39-6-5480-2116, Fax.: +39-6-5480-4401, e-mail: amartellucci@fub.it

Draft Report 04-10-99

6.3 V-Band VSAT Asymmetrical Data Communication System

6.3.1 Introduction

This system study explores the area of convergence between V-Sat systems and direct broadcast systems. At the highest degree of traffic asymmetry, the system may be regarded as a direct broadcast link with a low-data rate return channel for such applications as pay-per-view TV, impulse buying from TV commercials and audience polling or participation.

As a further step, the system may be extended to support a range of internet based applications, ranging from a limited system with a hub based server for specific applications linked to direct broadcast TV services (home shopping for example) to full world-wide-web access. In both cases the system will exploit the developing situation which offers extensive, low cost memory, both at hub and user stations.

As the growth of internet traffic is currently exponential and as the cable network operators are themselves having difficulty in anticipating the nature of future growth, it would be unwise for us to speculate too deeply on traffic models (the use of home based servers for example will have significant impact on traffic patterns). In this case study we merely recognise the fact that WWW access will be commonplace in the home and that there is an opportunity for IP based applications to be associated with direct broadcasting.

6.3.2 Architecture

This study is directed towards the use of a traditional bent-pipe transponder. The available bandwidth per transponder is considered to be 72 MHz, re-useable in spot beams and by polarisation re-use. For out bound channels we consider 16 carriers with 6 Mbps used in TDMA. For the return channel we consider up to 125 carriers of 512 kbps accessed by MF-TDMA. Other return path carriers/capacity (15 channels) will be used for order wire requests. All carriers are separated by a guard band of one channel width, avoiding interference due to inter-modulation of carriers when using a non-linear transponder amplifier.

6.3.3 Number of Users

6.3.3.1 Low-bit rate return path

For a broadcast return channel system, the number of simultaneous users is limited by the capacity of the return channel. More subscribers could be on-line, though not transmitting. This system supports at least 100,000 users per spot beam, using a total return channel data capacity of 64 Mbps. The actual number of active users depends on traffic and tariffing.

6.3.3.2 IP –type applications

Internet browser applications are characterised by the asymmetric ratio of the received data, to the size of the request. This ratio is highly flexible and will increase with the use of audio and video in web page design. Total outbound system capacity (96 Mbps) is shared by the number of users. Reducing the number of users increases the maximum bandwidth available for each user. Assuming that all users are web browsing and an average web page size of 20 kbps[1]

(12 kbytes per page + allowance for future growth in page sizes), the system can support approximately 5000 simultaneous users.

6.3.4 Link and Service Availabilities

The bands at 40/50 GHz offer significant spectrum for exploitation in such services, but at relatively low link availabilities. Typical values range from 99.5 to 99.8% at 40 GHz and 98.0 to 99.5% at 50 GHz, for the coverage considered in this case study and with a 10dB fade margin (see Fig. 6.3-1). Two important factors in system design are thus evident:

(a) memory must be exploited in the hub and V-Sat stations to give the user a good service availability despite the relatively poor link availability, and:

(b) it is critical that the user stations have enough link margin to accommodate the losses encountered from clouds and atmospheric gases and that adaptive techniques (resource sharing with adaptive coding, space and time diversity, application specific protocols) and outbound uplink power control are used as mitigation techniques during rainfall.

6.3.5 System Description

The system provides packet transmission from a hub to VSAT terminals, through a bent-pipe satellite. The V-band frequencies allocated by the ITU for fixed satellite services at V-band have been used (37.5-40.5 GHz downlink & 47.2-50.2 GHz uplink). The data rates are flexible depending on the volume of packets received.

6.3.5.1 Outbound Link

On the outbound link (hub to VSAT) TDMA is used at a burst rate compatible with MPEG-2 (6 Mbps). Variable length packets from higher layer applications (video, audio, data) are encapsulated in a MPEG transport stream packet (188 bytes). Individual terminals identify user data from the destination address header in the broadcast stream.

6.3.5.2 Inbound Link

The in-bound link uses ATM packets (48 bytes data+ 5 bytes header) to access the internet and communicate directly with the hub. ATM provides a guaranteed QoS and short packet sizes (16 kbps). Each frame (512 kps) contains 32 ATM cells and each user can request upto 4 cells (64 kbps = IP cell) per frame, depending on channel traffic. Both MF-TDMA and CDMA have been considered for multiple access. MF-TDMA offers efficient allocation of return path capacity in a variety of user applications and is especially suited to adaptive resource sharing in an environment where individual links may suffer occasional deep fades. In MF-TDMA users can combine non-overlapping time and frequency slots to form a frame.

Contention techniques are avoided for return path access. When large numbers of users are queued waiting to send these are dealt with by polling (i.e. pay-per-view) and selective polling (audience participation). Home shopping is dealt with as an IP application, making use of hub and V-Sat cache memory.

6.3.5.3 Modulation and Coding

The outbound and inbound links use the DVB-S standard defining modulation and coding (ETS 300 421). This ensures capability between equipment manufacturers and global performance requirements. Each time slot contains a single transmission packet (MPEG-2 or ATM), protected with a concatenated FEC scheme (16 byte Reed-Solomon outer code & 1/2 rate, K=7 convolutional inner code). Subsequently a Gray-coded QPSK modulation scheme is employed.

6.3.6 Link Performance Analysis

Propagation data for this test case have been taken from models 2-7 presented within COST255, which have been checked against Italsat data for specific sites. Cumulative attenuation distributions have been predicted initially for two test locations : one in Italy and the other in the extreme South West of the UK. The Italian location coincides with Spino d'Adda, for which extensive Italsat data are available. Tables 6.3-1 and 6.3-2 compare the predictions derived from the various models for Spino d'Adda, and include data from 2 years measurement for the nearest Italsat frequency. Tables 6.3-3 and 6.3-4 compare predictions for the SW UK site (Cambourne). Further details can be found in ref. 8

In addition a preliminary availability map for the European region has been drawn for a threshold of 10 dB (*Figs. 6.3-1 and 6.3-2*), which is the fade margin that we have built into the links on this system. The maps has been created using the models for prediction of gas, cloud and rain attenuation and the fade depth induced by scintillation described in ref. 8. The maps of altitude and wet term of air refractivity used for calculation have been put at disposal by J.P.V. Baptista (ESA/ESTEC)

Earth Station Location : 45.40N, 9.50E (Spino d'Adda)

Fade Margin	Link Availability Predicted From Various Models			
(dB)	Gas, cloud + ITU (50.2 GHz)	Gas, cloud + Excell (50.2 GHz)	Gas, cloud + T-S/K-W (49.5 GHz)	Italsat data (2 years) (49.5 GHz)
10	98.0	98.2	99.2	99.1
15	99.2	99.0	99.7	99.6
20	99.7	99.5	99.8	99.8

Table 6.3-1 Estimates of link availability at 50 GHz from prediction models and Italsat measurements

Earth Station Location : 45.40N, 9.50E (Spino d'Adda)

Fade Margin	Link Availability Predicted From Various Models			
(dB)	Gas, cloud + ITU (37.5 GHz)	Gas, cloud + Excell (37.5 GHz)	Gas, cloud + T-S/K-W (39.6 GHz)	Italsat data (2 years) (39.6 GHz)
10	99.6	99.2	99.7	99.6
15	99.9	99.8	99.8	99.8
20	99.95	99.92	99.90	99.90

Table 6.3-2 Estimates of link availability at 37/39 GHz from prediction models and Italsat measurements

Earth Station Location : 50.13N, 5.59W (Cambourne)

Fade Margin	Link Availability Predicted From Various Models		
(dB)	Gas, cloud + ITU	Gas, cloud + Excell	Gas, cloud + T-S/K-W
10	97.2	96.0	98.2
15	99.3	98.3	99.6
20	99.8	99.4	99.8

Table 6.3-3 Estimates of link availability at 50.2 GHz from prediction models and Italsat measurements

Earth Station Location : 50.13N, 5.59W (Cambourne)

Fade Margin	Link Availability Predicted From Various Models		
(dB)	Gas, cloud + ITU	Gas, cloud + Excell	Gas, cloud + T-S/K-W
10	99.5	98.7	99.7
15	99.82	99.65	99.84
20	99.93	99.86	99.90

Table 6.3-4 Estimates of link availability at 40.5 GHz from prediction models and Italsat measurements

6.3.7 Outbound Link Analysis (Hub to VSAT)

Bit rate	6 Mbps
Modulation scheme	QPSK
FEC	Concatenated Reed-Solomon (204,188)
Coding	Convolutional, K = 7, rate = 1/2
Multiple access scheme	TDMA

Uplink

Frequency	47.2 GHz
Hub power	20 dBW (100 W @ 5db OBO)
Antenna diameter	3 m
Antenna efficiency	75 %
Antenna transmitter gain	62.2 dBi
EIRP	82.2 dBW
Free-space path loss	217.7 dB

At Satellite

Antenna diameter	0.54 m
Antenna efficiency	80 %
Antenna receiver gain	47.6 dBi
Receiver noise temperature	30.92 dB/K
Uplink C/N_O	109.4 dBHz

Downlink

Frequency	37.5 GHz
TWT power	18.45 dBW (70 W @ 5db OBO)
Antenna transmit gain	45.56 dBi
EIRP per carrier	64 dBW
Free-space path loss	215.7 dB

VSAT

Antenna diameter	0.3 m
Antenna efficiency	80 %
Antenna gain	40.5 dBi
Receiver noise temperature	28.3 dB/K
Downlink C/N_O	84.1 dBHz

Overall Link

Available C/N_O	84.09 dBHz
Data rate	67.78 dBHz
E_b/N_O achieved	16.31 dB

E_b/N_O theory (BER = 10^{-8})	6.3 dB

Link Margin	10 dB

6.3.8 Inbound Link Analysis (VSAT to Hub)

Bit rate	512 kbps (64 kbps max. per user)
Modulation scheme	QPSK
FEC	Concatenated Reed-Solomon (16 bytes)
Coding	Convolutional, K = 7, rate = 1/2
Multiple access scheme	MF-TDMA

Uplink

Frequency	50.2 GHz
VSAT power	3 dBW
Antenna diameter	0.3 m
Antenna efficiency	80 %
Antenna transmitter gain	43 dBi
EIRP	46 dBW
Free-space path loss	218 dB

At Satellite

Antenna diameter	0.54 m
Antenna efficiency	80 %
Antenna receiver gain	48.1 dBi
Receiver noise temperature	30.92 dB/K
Uplink C/N_O	73.4 dBHz

Downlink

Frequency	40.5 GHz
TWT power per carrier (140)	-3 dBW (70 W @ 5dB OBO)
Antenna transmit gain	61.12 dBi
EIRP	58.12 dBW
Free-space path loss	216.4 dB

Hub

Antenna diameter	3 m
Antenna efficiency	75 %
Antenna gain	61 dBi
Receiver noise temperature	28.3 dB/K
Downlink C/N_O per carrier	103 dBHz (1000 carriers)

Overall Link

Available C/N_O	73.4 dBHz
Data rate	57.09 dBHz
E_b/N_O achieved	16.3 dB

E_b/N_O theory (BER = 10^{-8})	6.3 dB

Link Margin	10 dB

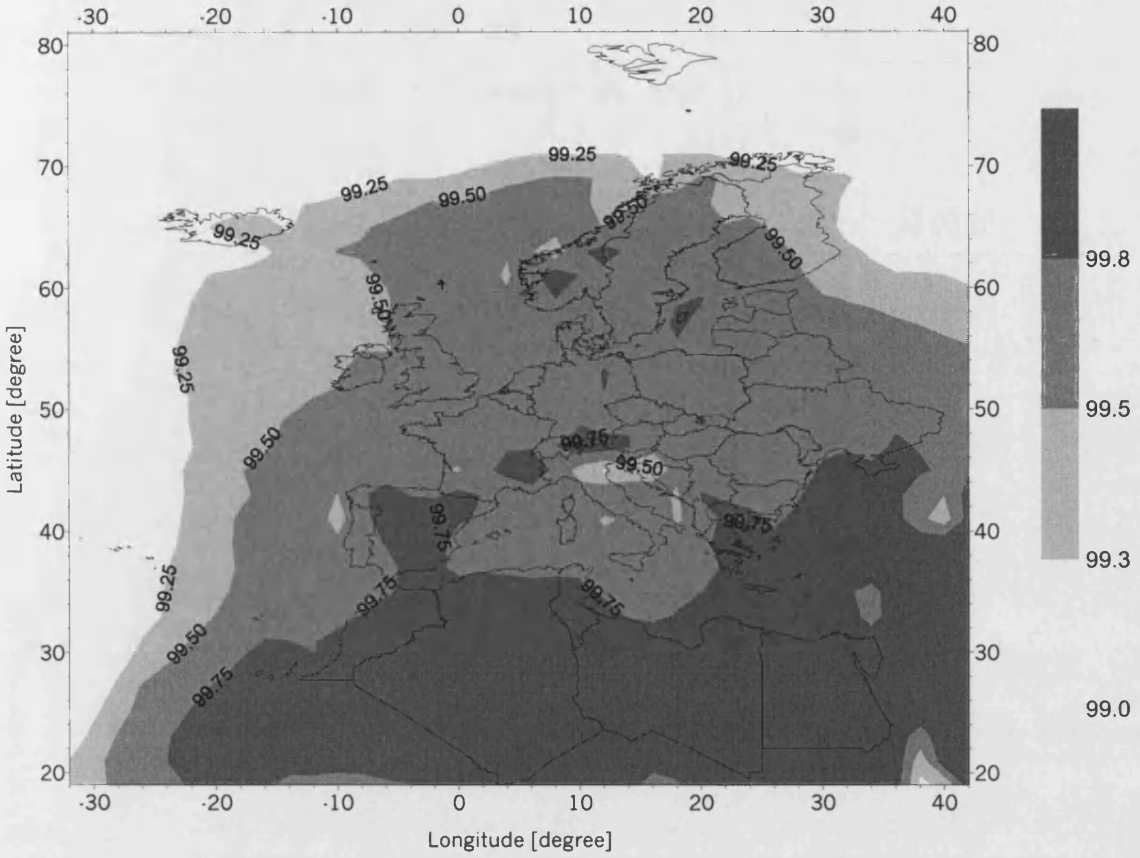

Figure 6.3-1 Annual availability contours for a threshold of 10 dB at 40 GHz (satellite at 19.2° E)

(ignoring antenna beam pattern and range losses)

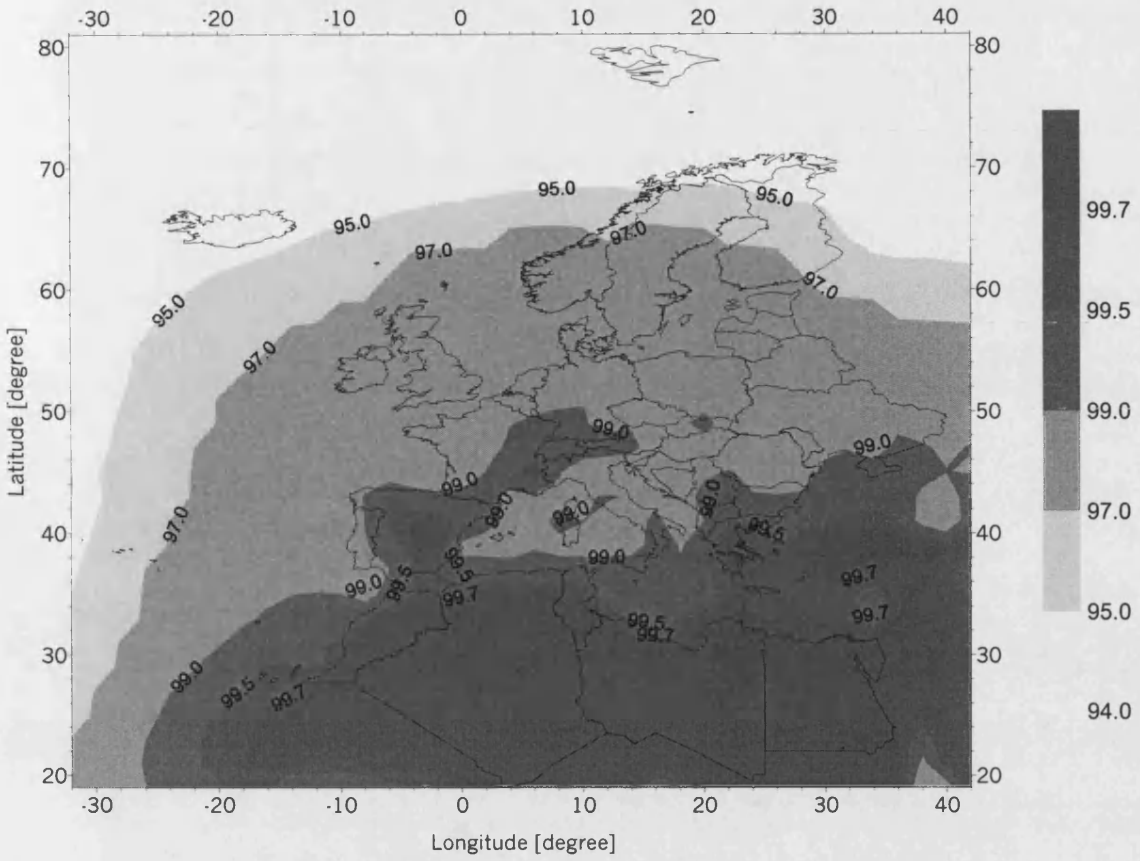

Figure 6.3-2 Annual availability contours for a threshold of 10 dB at 50 GHz (satellite at 19.2° E)

(ignoring antenna beam pattern and range losses)

6.3.9 Discussion and Conclusions

A V-band (40/50 GHz) VSAT system has been evaluated for a European coverage, taking as a specific test case a hub station at Spino D'Adda in Italy and a VSAT station at Cambourne in the UK.

The hub to VSAT path is the most demanding for sustaining large numbers of users in an asymmetric multi-media mode, but by making use of adaptive techniques and through the use of memory and intelligence at both hub and VSAT stations, satisfactory service availability should be achievable. On the VSAT to hub path further work must be undertaken on the MF-TDMA multiplex, based on a practical satellite HPA performance model. Also, consideration must be given to the implementation of contention-less protocols and the related delays incurred with a large number of users.

The link performance analysis based on COST 255 models and Italsat propagation data is sufficiently encouraging to merit consideration of the performance of these systems in greater detail.

6.3.10 References

[1] "Assessing the Impact of LEO Satellite Networks on TCP Performance", D. Chan, COST 252/253/255 Joint Workshop, Toulouse, May 1999, pp 77-88

[2] "Modelling the atmospheric attenuation by means of meteorological parameters", F. Barbaliscia, M. Boumis, A. Martellucci, J.P.V. Baptista, Alta Frequenza, Vol. 6, Num. 6, November-December 1994, pp. 101-105

[3] "Review of rainfall rate modelling and mapping", Poiares Baptista J.P.V., Salonen E.T. Procs of URSI-F Open Symposium CLIMPARA'98, Ottawa 27-29 June 1998, pp. 35-44.

[4] "Prediction of Monthly cumulative distributions of short duration rain intensities", T. Konefal and P.A. Watson, COST 255, CP42007

[5] "Midas: A monthly link budget and decision aid tool for frequencies between 10 and 50 GHz", A. Akram, A. Shukla, T. Konefal and P.A. Watson, IEE NCAP, York April 1999, pp 152-155

[6] "A prediction model that combines rain attenuation and other propagation impairments along earth-satellite paths", A. Dissanayake, J. Alnutt, F. Haidara, IEEE Transactions on Antennas and Propagation, Vol. 45, No. 10, 1546-1558, 1997.

[7] "Propagation data and prediction methods required for the design of Earth-space telecommunication systems ", ITU-R:, Propagation in Non-Ionized Media, Recommendation 618-5, Geneva, 1997.

[8] "Model based evaluation of propagation data for COST 255 Simulation Test Case 3", A. Martellucci, M. Boumis, Carlo Riva, COST 255, CP71A04, May 1999

USE OF V-BAND IN MULTIMEDIA MESSAGING SERVICES VIA GEOSTATIONARY SATELLITES

A.Page, P.A.Watson

University of Bath, Dept. of Electronic and Electrical Engineering,
Claverton Down, Bath, BA2 7AY, United Kingdom
Emails: A.Page@bath.ac.uk, P.A.Watson@bath.ac.uk

INTRODUCTION

Radio techniques for delivery of multi-media messaging services must offer cost advantages over cable techniques in order to be viable. In sparsely populated or "under developed" areas such advantage may be obvious. Also in the more populated areas of the globe, cost advantage and rapid deployment may be gained through the use of so-called high altitude platforms. However, there is a further opportunity for countries with established satellite broadcast systems in combining a return path (either radio or cable) with a broadband downlink. Such systems can exploit the point-to-multipoint nature of the satellite channel and the low cost of computer memory in making available appropriate interactive multi-media messages.

In this paper we consider the adaptive techniques necessary to support multi-media messaging services on a geostationary satellite with a radio return path. For this to be possible the propagation factors must be well characterised over the region to enable full capacity of the satellite to be exploited. Here we use a propagation prediction model which includes cloud, rain and gaseous attenuation effects and predicts attenuation distributions on a monthly basis. The MF-TDMA access technique is used to allocate satellite resources in a flexible manner.

Multi-media traffic can be characterised by the degree of traffic asymmetry. At the highest degree, the system may be regarded as a low data rate return channel for applications such as pay-per-view TV, impulse buying from TV commercials and audience polling or participation. The system may be further extended to support IP based applications, ranging from a limited hub based server for specific applications linked to direct broadcast TV services (home shopping for example) to full world-wide-web browsing.

Time-series of attenuation on EHF and SHF fixed radio links derived from meteorological forecast and radar data

Abstract

A method for deriving time-series of attenuation on fixed satellite or terrestrial links is described. The method uses meteorological forecast data and radar data and hence permits time coincident derivations for multiple sites that include the spatial correlation properties inherent in weather systems. The success of the technique depends upon insertion of the short interval temporal properties (varying typically over 1 second to 15 minutes) that are statistically independent between stations. The paper describes the methodology and illustrates examples of time-series derived at multiple-sites for satellite-earth links, comparing the spectral and statistical properties with those from real data. The technique has immediate application to simulation of the performance of multi-media satellite (or high-altitude platform) to earth links and has longer-term significance in terms of real-time operational use.

1. Introduction

The ability to derive or predict time-series of attenuation in the 10 to 50 GHz range is of current interest in simulating the performance of multi-media satellite-to-earth (or high-altitude platform-to-earth) links. Analysis using on-average statistical properties leading to conventional link budgets may be starting point but is not sufficient to examine the performance of the large variety of fade mitigation techniques that are applicable to such systems, including power control, space-diversity and time-diversity (see, for example, [1]). On-board processing techniques including regeneration, resource sharing, switching and ground station control must also be considered. Fade mitigation techniques must inevitably be used if the upper range of the EHF band is to be exploited efficiently.

In the longer term the ability to predict time-series of attenuation from meteorological forecast data opens up the possibility of use in the real-time control of operational systems with response times measured in hours.

An alternative to our approach in order to generate data for simulation, is to use an entirely synthetic event driven simulator (e.g. as in [2 and 3]). Difficulties arise here in relation to inclusion of spatial correlation in real-time. Furthermore such a simulator could not be extended into real-time control.

The paper describes the approach adopted in the technique and presents preliminary results for multiple sites in a region of the UK. The time-series, spectra and cumulative distributions generated by the simulator show promising similarity with those measured on an Earth-space link for the same period of time.

2. Approach

Our approach is based on three underlying assumptions:

(1) The short-term (15 minute or less) correlation of fading between fixed radio links is statistically independent.
(2) The intermediate-term (15 minutes to a few days) correlation of fading is described by the movement of weather systems as observed on meteorological radars (15 minutes to a few hours) or by mesoscale weather forecasting techniques (hours to a few days).
(3) The long-term spectral and statistical properties of fading during aggregated events are stationary.

Assumption (1) covers short-term scintillation fading which is essentially determined on a local scale (typically a few metres [4]). This assumption also covers the fine scale structure of rain that leads to independent fading over a few kilometres [5,6]. Within assumption (2) we take account of the larger scale background effects that apply to rainy conditions, including the occurrence of cloud and water vapour both of which lead directly to loss of signal but also to enhanced scintillation intensity. Assumption (3) is not essential but has been taken for expedience in this initial work. If the technique that we describe were to be used over a long period of time then stationarity could be the subject of continuous evaluation.

3. On-average spectral and statistical properties of EHF fading

Power Spectrum
EHF fading caused by the effects of rain, cloud, water vapour and scintillations typically shows three spectral regimes. We have used 40 and 50 GHz time series data supplied in the framework of EC COST 255 [7,8] to illustrate this point. Similar conclusions have been drawn in [8]. We have thus set an objective for our time-series generator to reproduce the an on-average power spectrum during rain as shown in Fig. 1.

The lower part of the spectrum ($f < f_L$) rolls-off at –20 dB/dec during rain or remains stationary in clear air. Above f_L the spectrum represents scintillation caused by atmospheric turbulence along the path. Between ($f_L < f < f_C$) the spectrum depends on how the turbulence was created and has no describing formula (it is usually seen to be flat). Followed by a region ($f > f_C$) that rolls-off at –80/3 dB/dec predicted by turbulence theory [4].

The spectrum up to the radar sampling frequency f_l, is determined from the physical evolution of rain over time. Theoretically, the corner frequency of turbulence f_c, can be related to the transverse wind velocity v_n (m/s) given by the UM data. However for simplicity both f_L and f_C have been taken from beacon observations and correspond to 0.07 and 0.3 Hz respectively.

Cumulative distribution
The long-term cumulative statistics of SHF and EHF fading (dominated by rain) are well described by a distribution of the log-normal form (see for example [9 and 10]). This observation, in keeping with the modelling of attenuation by rain as a multiplicative process [9], defines the type of long-term target distribution for our time-series generator. The moments of the distribution will depend upon the climate and location of each site.

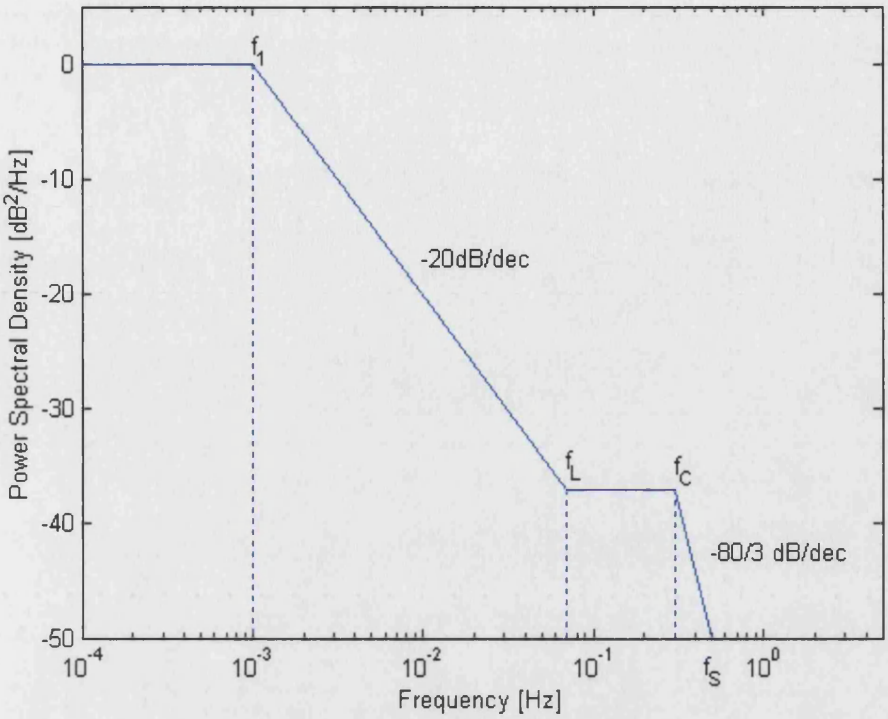

Figure 1: Ideal power spectrum

4. Meteorological data

Outputs from The Meteorological Office Unified model

The UK Met. Office Unified Model (UM [11,12]) is a numerical model (realised in software) to describe the time evolution of the atmosphere. Meteorological measurements provide the initial conditions to a set of hydrostatic equations relating to the horizontal motion of wind, potential temperature and specific humidity. Further observations are assimilated over the model period which iteratively "nudge" the forecast solution towards these observations.

It is noted that the Unified Model can be run with a choice of temporal and spatial resolutions. At present we have used hourly outputs but, in the longer term, higher resolution outputs should be practical. The current meso-scale model covers the UK and northern France with a horizontal resolution in the order of $11km^2$ (see figure 2), but improvements in modelling and data inputs should improve this further. In the vertical, diagnostic outputs occur on 38 terrain-modified pressure levels. The distance between levels is linearly related to the surface pressure at each point, providing the highest resolution (~100m) close to the surface and gradually flattening towards the upper most layers (~1km at 15km altitude).

We have thus used the UM for the background fading effects (water vapour losses, cloud losses and scintillation intensity) but for rain at present we resort to using radar data, with higher resolution.

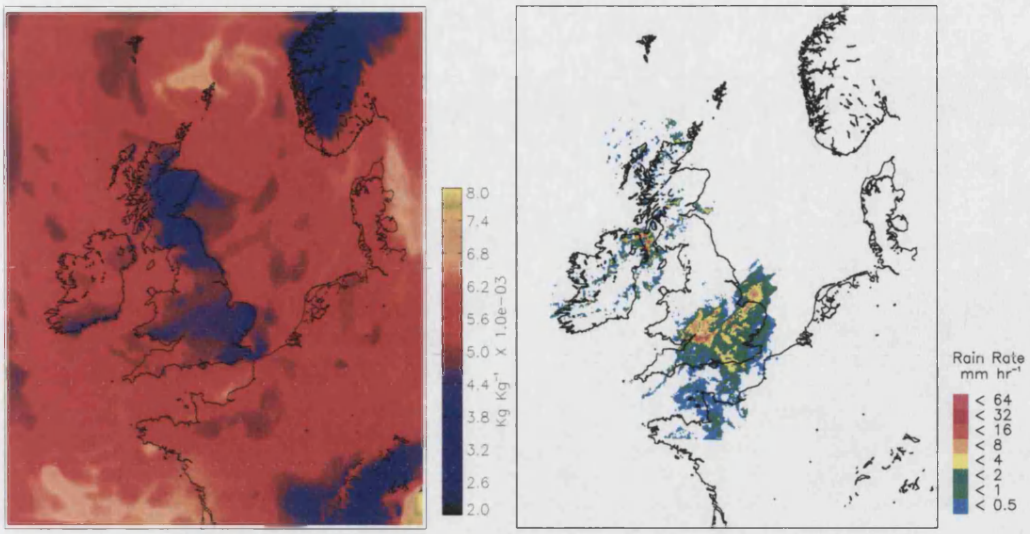

Figure 2: Example UM output specific humidity *(left)*, network radar image *(right)*

Outputs from Meteorological Office radar network
The UK and Irish weather radar network [13] has been developed over the last 30 years and currently contains 15 C-band (5.65GHz) radars. Of these 15 radars, two are in the Republic of Ireland and one is in the state of Jersey. The network produces a composite image consisting of a 5km resolution 256x256 grid of surface rainfall rate estimates covering the whole of the UK and the Republic of Ireland. An example output of the weather radar network can be seen in Figure 2.

The individual radar systems operate routinely on a cycle that repeats every 5minutes. Radar reflectivity data (Z) is collected is collected in PPI (plan position indicator) mode at elevations of 0.5, 1.5, 2.5 and 4.0 degrees. The data is then processed to produce estimates of surface rainfall data (RR) on a 5km resolution Cartesian grid. Ground clutter suppression is achieved using a fixed clutter map and infilling contaminated data from higher elevation scans. Rainfall rate estimation is made using a Z-R power law relationship.

Every 15 minutes, at a predefined period, each radar transmits its latest image to the Met. Office in Bracknell where a composite image of 256x256 cells is generated. Each grid cell in the image contains the data from a single radar. If there are data available from two radars, the 'best' data is selected according to a hierarchy map. The hierarchy map ranks for each location, which radars are able to provide the highest quality estimates. In practice this normally means that the data chosen for a particular grid cell is the closest available to the ground at that location.

5. Generation of attenuation time-series

Figure 3 shows schematically the system that we have adopted, and lists the models used in determining the attenuation outputs from the meteorological input data. The prediction models that we have adopted have all been tested against real fading data, several of them in the context of COST 255[7].

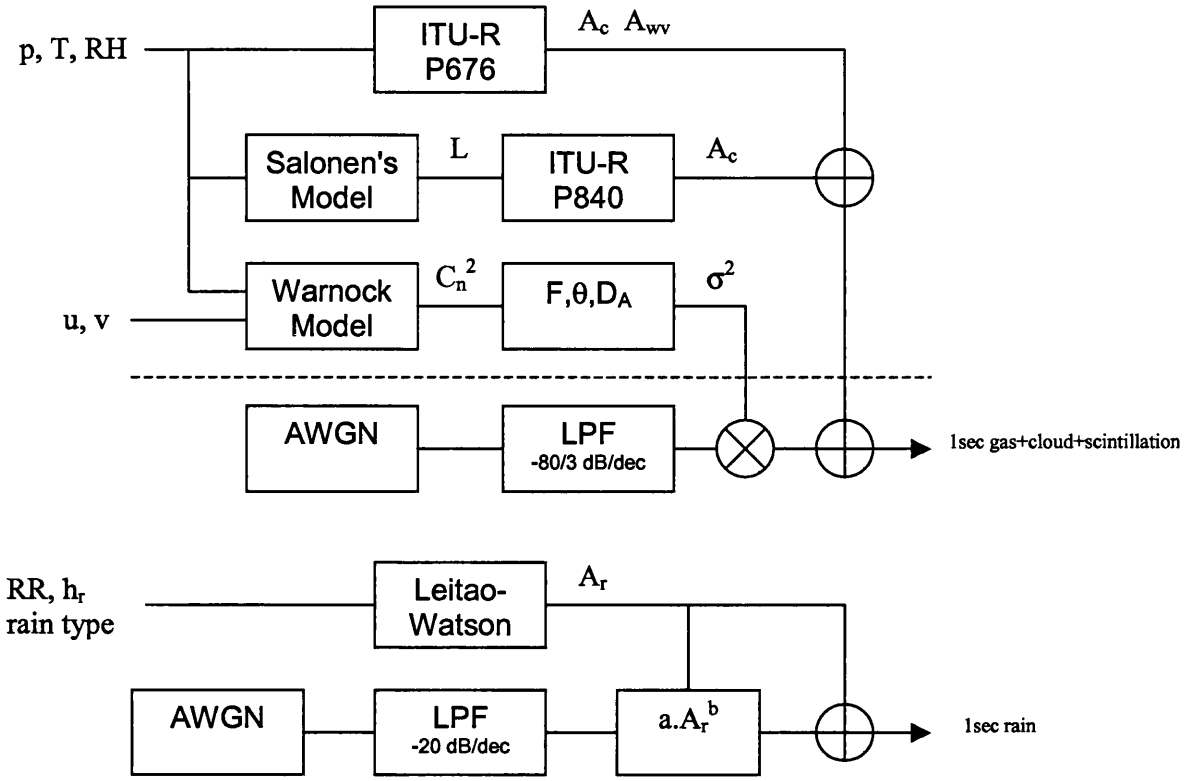

Figure 3: Outline block diagram of the time-series generator

Before the calculation of cloud attenuation the cloud liquid water content is determined from UM upper-air outputs using the approach of Salonen [14]. The presence of cloud is detected using a critical humidity function, with the cloud base and top determined through linear interpolation. Subsequently, the liquid water content (g/m^3) is calculated as a function of temperature and height from the cloud base. Salonen has already applied this method to a numerical weather prediction model for an on average statistical predication of liquid water content. Finally the slant path cloud attenuation can be predicted from the work of Liebe et al. [15] as now also embodied in ITU-R P840-3. This combined approach has been shown to give good predictions by Davies et al. [16].

For scintillations we take the UM upper-air outputs and use these to define the hourly scintillation intensity (σ^2), modulating a Gaussian noise generator with spectral roll-off of –8/3. From the theory of wave propagation through a turbulent medium [3], σ^2 is related to the measured refractive index structure parameter (C_n^2). This is, in turn, dependent upon the refractive index gradient which can be readily calculated from vertical profiles of pressure, temperature, humidity and wind direction / speed. Following the method of Warnock et al. [17], the structure parameter is calculated for horizontal slabs whose thickness defines the resolution turbulence scale. Due to the lower resolution of the UM vertical layers compared to radiosonde observations, linear interpolation was used to produce layers with 50 m thickness. The duration and intensity of rain events for any location are determined from radar observations. Rain rate is first converted into attenuation using an appropriate model. Here an approach able to deal separately with the occurrence of widespread and showery rains is most appropriate [18,19] showing good results when compared to Italsat and Olympus data [20].

Alternatively ITU-R P838 could be used, but does not distinguish showery and widespread rain. Higher frequency fluctuations in the rain attenuation time-series are added using a gaussian noise generator with a –20 dB/dec spectral roll-off as given in [8]. The non-stationary nature of real events, in particular the build up and fall off periods, are represented by modulating the high frequency fluctuations with the local intensity of the underlying shape. A power law function allows the control of intensity variation and scaling of the high frequency rain components. Optimum coefficients for the short example dataset were determined through inspection. A much larger dataset will be required to define long-term coefficients.

Through combining all of these components we are thus able to represent the lower frequency [> 0.0011 Hz] background loss variations from cloud, gases and rain with the smaller scale rain intensity fluctuations [0.0011 to 0.7 Hz] and also the finer scale scintillations relating to rain, gases and clouds [> 0.3 Hz].

6. Example output from time-series generator

We should now be able to place satellite earth stations at arbitrary locations in the UK and generate time series of attenuation that retain the temporal and spatial characteristics of evident in real weather systems. Figures 4a,b,c illustrate a set of simulated attenuation time-series at 49.5 GHz generated for three locations in the UK for 8th August 1999. The potential of the technique as a tool for the simulation of the performance of a network of stations is clear.

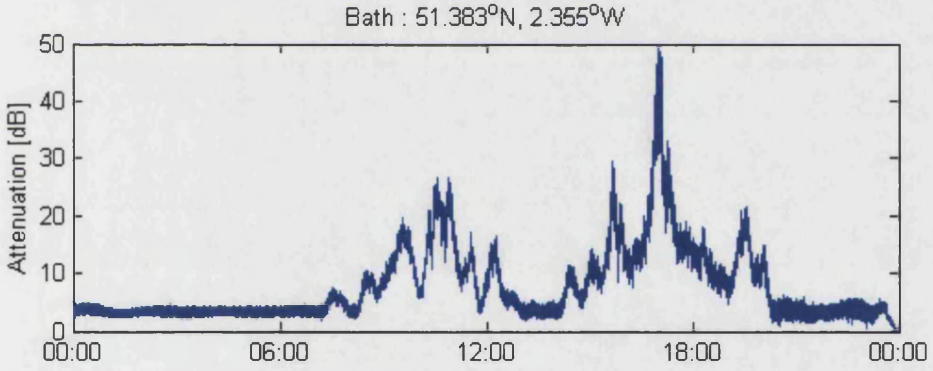

Figure 4a: Time-series from Bath

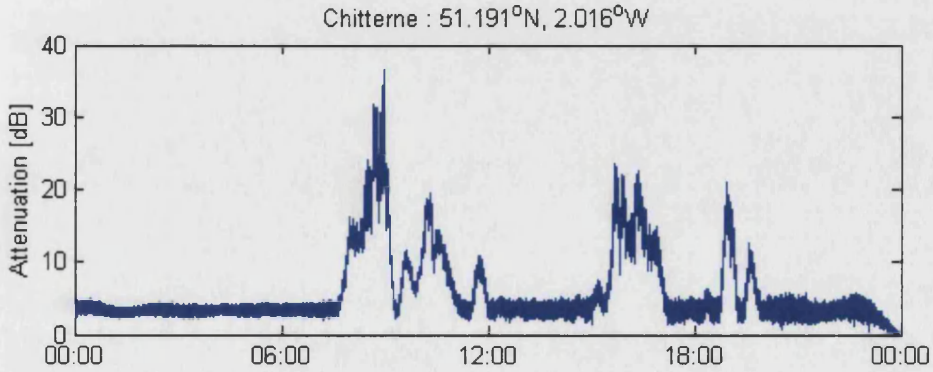

Figure 4b: Time-series from Chitterne

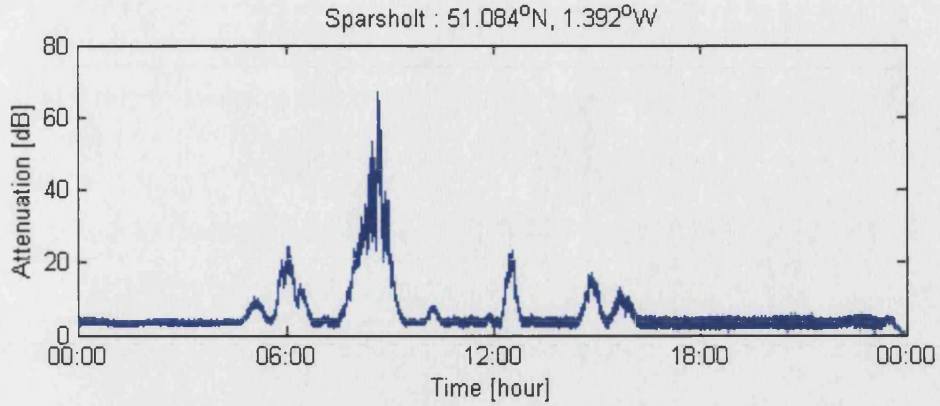

Figure 4c: Time-series from Sparsholt

7. Validation of the time-series simulator

Given the original objective of the simulator, the obvious method of validation is to verify that the power spectrum of the generated time-series is consistent with that of our idealised power spectrum shown in Fig.1. The power spectrum of the generated time-series from Sparsholt data of the same period is shown in Fig. 5. It can be seen that there is good agreement between the two, despite there being considerable differences in the spatial and temporal resolution of the data used to derive each of the spectra

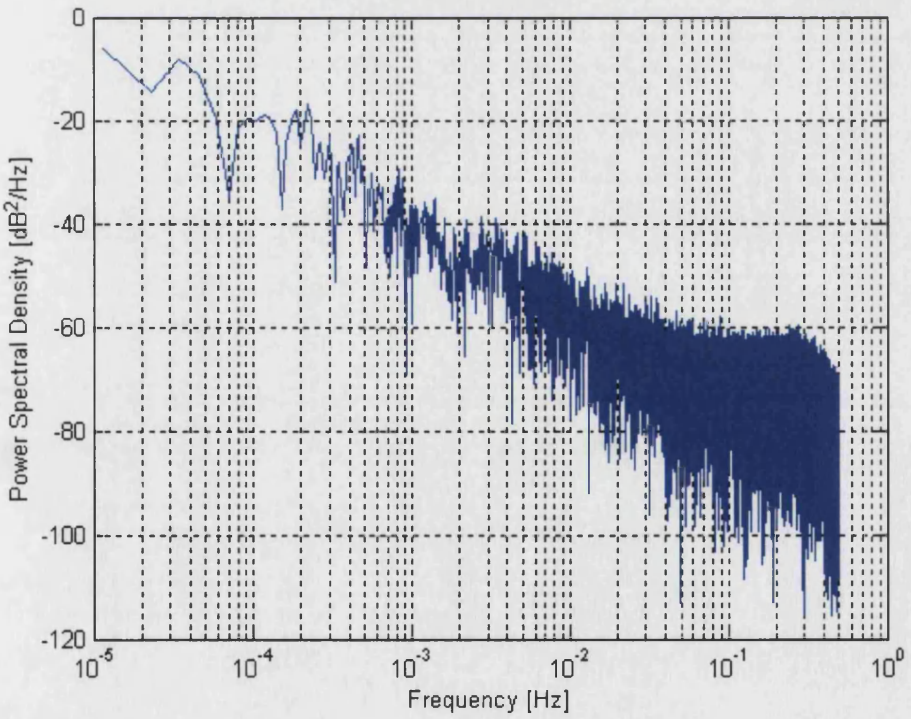

Figure 5: Power spectral density for the simulated Sparsholt time-series shown in Fig. 4c.

A further attempt to validate the time-series simulator, has been made using real satellite beacon data (supplied by the Rutherford Appleton Laboratory). We have attempted to validate the time-series by comparing the attenuation time-series generator output for Sparsholt to that directly obtained from an Italsat beacon receiver sited at Sparsholt (θ = 30°, D_A = 61cm). Figure 6 illustrates the measured time-series at Sparsholt for the same period as simulated in Fig. 4. It is important to note here that although the time-series and simulated data are encouragingly similar, we should not expect to see 100% correlation, especially in the fine scale structure. The objective is to create a representative fading environment for periods of ~1 hour to 6 hours with a fine scale structure that will be useful to test the dynamic control systems associated with fade mitigation techniques. A further comparison is shown for 5th November 2000 in Fig. 7, which also shows good agreement.

A more detailed validation process must of course compare the cumulative distributions of simulated and measured time-series. We propose to compare the cumulative distributions of simulations and measurements for a number of 6 hourly periods In order to observe the long-term spectra and cumulative distributions we should, of course have to make observations over a much longer period, but the general the form of these distributions is well known and in any case is dependent on location and climate [20,21].

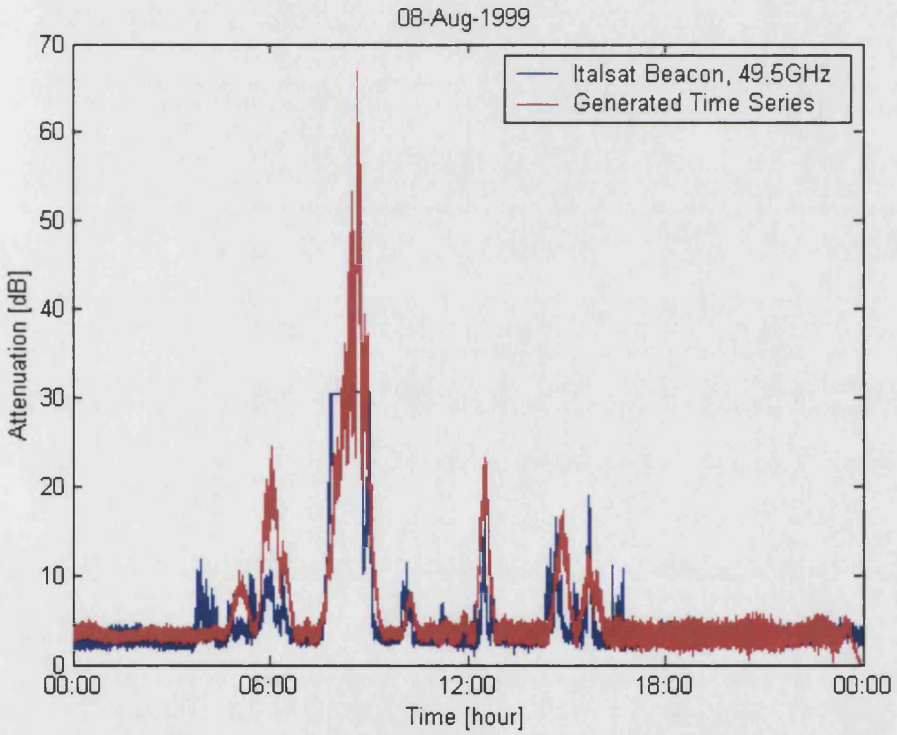

Figure 6: Comparison between measured Italsat link data and simulated time-series

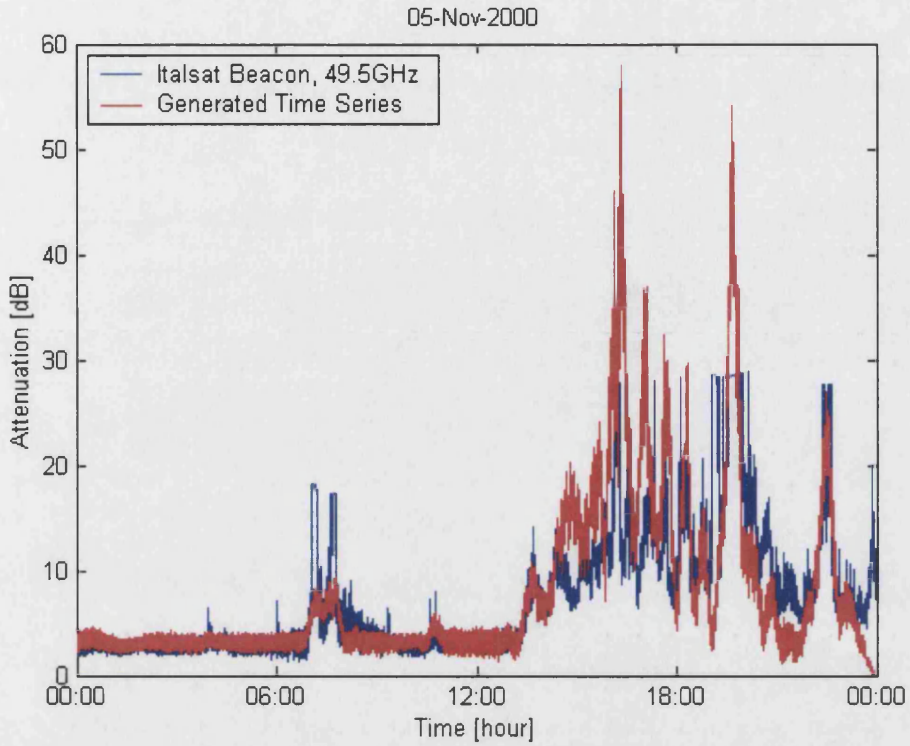

Figure 7: Comparison between measured Italsat link data and simulated time-series

8. Conclusions

We have described a new approach to the realisation of an attenuation time-series generator and demonstrated its potential for representing both the spatial and temporal properties of fading on EHF links. The simulator has immediate application to performance evaluation for EHF links that include fade-mitigation techniques, and the approach has longer term potential in terms of the operational management of links.

9. Acknowledgements

The authors are grateful for the support of Dr. Peter Panagi at University of Reading for supplying the UM data through UWERN (Universities Weather Research Network). We also thank the Radio Communications Research Group at the Rutherford Appleton Laboratory for the Italsat beacon data.

10. References

[1] M. J. Willis, "Fade counter-measures applied to transmissions at 20/30 GHz," *Electronics & Communication Engineering Journal*, vol. 3, pp. 88-96, 1991.

[2] BC. Gremont, M. Filip, "Design and Simulation of High Frequency Satellite Links: An Overview", *COST 255' 5th International Workshop on Radiowave Propagation Modelling for SatCom Services at Ku-band and Above. 1998.*

[3] K. S. Paulson and C. J. Gibbins, "Rain models for the prediction of fade durations at millimetre wavelengths," *IEE Proceedings-Microwaves Antennas & Propagation*, vol. 147, pp. 431-6, 2000.
[4] V. I. Tatarskii, "Wave propagation in a turbulent medium", McGraw-Hill, 1961.
[5] H. Fukuchi, "Correlation properties of rainfall rates in the United Kingdom," *IEE Proceedings-H Microwaves Antennas & Propagation*, vol. 135, pp. 83-8, 1988.
[6] Allnutt, J.E. "Nature of space diversity in microwave communications via geostationary satellites: a review". Proc IEE, Vol. 125, 396-376
[7] EC COST Action 255 "Radiowave Propagation Modelling for SatCom Services at Ku-band and Above".
[8] E. Matricciani, M. Mauri, and C. Riva, "Scintillation and simultaneous rain attenuation at 49.5 GHz," *Ninth International Conference on Antennas and Propagation (Conf. Publ. No.407). IEE*, vol. 2, pp. 165-8, 1995.
[9] S.H. Lin, "Statistical behaviour of rain attenuation", Bell System Technical Journal, Vol. 52, No.4, April 1973, pp 557-581
[10] ITU Handbook on Radiometeorology, Radiocommunication Bureau, Geneva, 1996
[11] Metrological Office, "Unified Model User Guide", 1998, http://www.rdg.ac.uk/~panagi
[12] P. Panagi, E. Dicks, "Met. Office Unified Model data, diagnostics, graphics programs and other observational data available from the JCMM through the aegis of the Universities Weather Research Network UWERN", University of Reading, 1997.
[13] A.H. Smith and M. Kitchen, "A review of the quality control and quality evaluation of radar rainfall measurements carried out by the UK Met. Office", 1999, COST 75 Advanced weather radar systems, published by European Commission, ISBN 92-828-4907-4, pp68-81
[14] E. Salonen and S. Uppala, "New prediction method of cloud attenuation," *Electronics Letters*, vol. 27, pp. 1106-8, 1991.
[15] H. J. Liebe, T. Manabe, and G. A. Hufford, "Millimeter-wave attenuation and delay rates due to fog/cloud conditions," *IEEE Transactions on Antennas & Propagation*, vol. 37, pp. 1617-12, 1989.
[16] O. T. Davies, R. G. Howell, and P. A. Watson, "Measurement and modelling of cloud attenuation at millimeter wavelengths," presented at `COST 255' First International Workshop on Radiowave Propagation Modelling for SatCom Services at Ku-band and above (ESA-WPP-146). ESA. 1999, pp.77-8. Noordwijk, Netherlands.
[17] J. M. Warnock, T. E. Vanzandt, and J. L. Green, "A Statisitical model to estimate mean values of parameters of turbulence in the free atmosphere," presented at 7th Symposium of Turbulence Diffusion, 1985.
[18] M. J. Leitao and P. A. Watson, "Method for prediction of attenuation on earth-space links based on radar measurements of the physical structure of rainfall," *IEE Proceedings, Part F: Communications, Radar & Signal Processing*, vol. 133, pp.429-40, 1986.
[19] P. A. Watson and Y. F. Hu, "Prediction of attenuation on satellite-Earth links for systems operating with low fade margins," *IEE Proceedings-Microwaves Antennas & Propagation*, vol. 141, pp. 467-72, 1994.
[20] T. Konefal, P. A. Watson, A. K. Shukla, and A. Akram, "Prediction of monthly and annual availabilities on 10-50 GHz satellite-Earth and aircraft-to-aircraft links," *IEE Proceedings-Microwaves Antennas & Propagation*, vol. 147, pp. 122-7, 2000.
[21] J.P.V. Poiares Baptista and E. Salonen, "Review of rainfall rate modelling and mapping"

PROPAGATION PREDICTION FOR V-BAND SYSTEMS

P.A.Watson[1], T.Konefal[2], A.Page[1]

(1) University of Bath, Dept. of Electronic and Electrical Engineering, Claverton Down, Bath, BA2 7AY

(2) University of York, Dept. of Electronics Heslington, York, YO1 5DD

INTRODUCTION

In V-band (40/50 GHz) the propagation regime is markedly different to that experienced at lower frequencies, especially for satellite – Earth links. In particular the effects of clouds and light rain can dominate link availability for systems with modest fade margins (say 10 to 15 dB). This is in contrast to 20/30GHz and lower bands where, in most climates, heavy rain occurrences would be the dominant factor in outage calculations for the same fade margins.

Evidently at V-band we must consider the contributions of widespread and showery rains, atmospheric gases (oxygen and water vapour), clouds and scintillation from atmospheric turbulence. These effects show pronounced climatic dependencies including, in some climates, strong seasonal effects. Also the effects are not independent and one must consider methods for their combination. A review of the physical basis for relevant propagation factors is given in [1] and examples of system evaluations are given in [2] and [3].

Over the past decade several physically based approaches to propagation prediction have evolved based on mapping the meteorological parameters that determine availability [4-7]. The input data for these parameters may be found from databases of measurements, but invariably models are used to link data collected in climates with particular characteristics. One recently established technique [6,7] uses archived data from meteorological forecast models to predict (using suitable algorithms) input parameters for physically based propagation prediction. An alternative technique has been described recently [8] with some fundamental advantages, in that it permits propagation factors to be evaluated on a monthly basis. It is this technique that we will now apply to V-band predictions.

OVERALL APPROACH

Established approaches to availability prediction for satellite-Earth links use annual data for rainfall intensity, applying models for relating on-average path attenuation statistics to on-average point rainfall rate statistics. This approach includes a fundamental flaw, which detracts from the accuracy of prediction: the use of annual rain data begs the question of the influence of rain height (linked to the 0°C isotherm height) which varies considerably throughout the year. Thus if the dominant rainfalls occur in summer, then the summer rain height may be right for prediction. However in some climates the most severe rains occur in autumn (for example in the Mediterranean region) or in others, rain occurs with almost equal probability throughout the year (parts of the UK for example).

One approach to the problem [4] is to take a seasonally weighted rain height for each location. This generally does improve the quality of prediction but, of course, cannot give a full statistical description of availability, which can only come via a finer scale breakdown of the statistics of the many factors contributing to attenuation, as they vary throughout a typical year. As we move up in frequency we must, of course, consider a wider range of factors, especially including the effects of clouds and the variability of gaseous attenuation in addition to rain. The simple approach to prediction of annual attenuation from annual meteorological statistics is thus likely to be less precise.

In this paper we describe the application of a new method [8] which is the first of its type permitting prediction of attenuation on a monthly basis. Annual attenuation statistics are derived from the monthly values. A detailed description of the technique is given in [8] including comparisons with annual measured values taken from Italsat, illustrating the validity of the approach. Here we apply the technique in particular to V-band, giving some relevant predictions and also discussing the relative importance of the various physical components contributing to attenuation.

RAIN INTENSITY CUMULATIVE DISTRIBUTIONS RELEVANT TO V-BAND PREDICTION

If we consider now the fact that the occurrences of light rainfalls are likely to be of fundamental importance in predicting availability at V-band, we see a number problems with the use of existing rain intensity databases, viz.:

- rain intensities occurring for equal to or greater than 0.1% of time are poorly archived
- many raingauges used for heavy rains are inaccurate at low rain rates (< 5 mm/hr)
- occurrences of showery and widespread rains in most climates show pronounced seasonality

On the other hand, requirements on archived data record lengths for adequate sampling of a distribution should be shorter for low availabilities. Also the process of prediction from conventional meteorological databases, where the interest lies in longer duration rainfalls, should be more readily achievable. An example of the latter approach is that given in [9] however we have found by making comparisons between predicted and measured annual 1-minute rain intensity distributions [8], that the model by Tattelman and Schaar [10] gives more accurate predictions. In addition the Tattelman and Schaar model gives monthly rain intensity predictions.

PREDICTION OF CUMULATIVE DISTRIBUTIONS OF MONTHLY RAIN INTENSITIES

In the Tattelman and Scharr model [10] rainfall rates are predicted from monthly precipitation, number of rainy days and mean temperature, for six exceedance levels, namely 0.01, 0.05, 0.1, 0.5, 1.0 and 2.0%. The rain rate (in mm/min) at exceedance level p is predicted by an equation of the form:

$$R_p = A_p + B_p T + C_p I + D_p f(L,T) \qquad (1)$$

where T is the temperature (^{0}F or $1.8 \times {}^0$C+32), I is the precipitation index (precipitation/number of rainy days in mm/day) and $f(L,T)$ is a function of temperature (^{0}F) and latitude (degrees) given by:

$$f(L,T) = \begin{cases} 0 & L \le 23.5° \\ (L-23.5)T & 23.5° < L \le 40° \\ (40-23.5)T & L > 40° \end{cases} \qquad (2)$$

Coefficients A to D are regression coefficients which depend on the exceedance level p considered (see [8]). For exceedances between 2% and 100% we used a linear rain intensity interpolation against a log probability scale, in preference to ignoring very light rain contributions.

Data on monthly precipitation, monthly number of rainy days and monthly mean surface temperature were obtained from the Potsdam Institute for Climate Impact Research (PIK), based on 30 years of observation from 1931-1960. The original 62,000 land-based grid data were first passed through a sieve to produce a 1.5^0 (in both latitude and longitude) land based global grid of 6960 data points. These data were then smoothed and extrapolated into ocean regions to produce global grids of 1.5° resolution in both latitude and longitude (see [8] for further detail).

RAIN ATTENUATION PREDICTION MODEL

Rainfall rates are converted into attenuations using the method of Leitao and Watson [11]. Monthly corrections to the freezing height are included in the model, using the relationship described in Table 5 in Watson et al [4]. The section of link path below the melting layer defines L_s, the path through rain. Two sets of coefficients are defined in [11] for showery and widespread rain respectively. At high availabilities (~99.99%) showery rain dominates outages, whereas at low availabilities widespread rain is more significant. In the new model, the choice of using showery or widespread coefficients to calculate rain attenuation for each of the exceedance levels considered in the Tattelman and Scharr model depends on the exceedance considered. The transition between the two rain types is discussed in [5].

The melting layer of precipitation was included using a method which gave very similar results over the 10-50 GHz range to those predicted by Russchenberg and Ligthart [12] when using the same values of melted mass fraction of snowflakes. It is particularly important to model the melting layer separately from rain in the 10-25 GHz range, though it is noted that at 40-50GHz little would appear to be lost by modelling it as rain. Nevertheless there is still considerable uncertainty in connection with the morphology of the region and in turn, with the forward scattering properties.

MONTHLY CLOUD ATTENUATION MODEL

The approach to cloud attenuation prediction of Salonen [6,13] has been given a rigorous physically based test recently at 93 GHz by Davies et al [14] and shown to be remarkably accurate. The method predicts cloud occurrence at various heights based on upper-air data and then applies the model of Liebe [15] for attenuation prediction.

For monthly predictions there are two approaches: (a) to use mean monthly profiles (with height) of pressure, temperature and relative humidity and to develop monthly weighting factors which can be applied to annual upper-air data or, (b), to gather monthly upper-air data from meteorological databases and apply these directly to prediction using the Salonen method. In [8] and this paper we take approach (a) though more recently, databases have been collated in the framework of COST 255 (see [16]) making approach (b) possible. The two approaches have been cross-checked, with encouraging agreement, and leading to refinements in approach (a). In this paper we report predictions using approach (a) but as a result of the recent refinements expect to see very little difference to using approach (b).

MONTHLY WATER VAPOUR AND OXYGEN ATTENUATION MODELS

Our water vapour prediction model also uses annual statistical databases from radiosonde ascents weighted to give monthly values [8]. Again, as with cloud predictions, these can now be obtained from monthly collated databases [16], but once again we noted good agreement between values applying monthly weightings on annual data and those collated on a monthly basis. For oxygen attenuation predictions the Liebe/ITU approach was applied (see [1]), using numerical integration along the link path. Oxygen attenuation is assumed to be the same in both rain and non-raining conditions.

COMBINATION OF ATTENUATING COMPONENTS

Several approaches are possible to the combination of attenuating components, but in the absence of full statistical descriptions (i.e. joint density functions) we have to make approximations. At this juncture we have chosen to take a conservative approach and to add attenuations for equal exceedances for a particular month of the year. The monthly distributions are then inverted to add exceedances for fixed thresholds for the calculation of annual availabilities. The breakdown into monthly exceedances thus makes the process of combination of effects fundamentally more rigorous.

It is to be noted that scintillation effects (which are antenna size-dependent) have been excluded but could be added in, given a suitable model to cover this frequency range and a full range of elevation angles. Here the correlation between scintillation intensity and the occurrence of cloud should be observed.

EXAMPLE MONTHLY ATTENUATION PREDICTIONS

Figures 1 and 2 illustrate 40 GHz attenuation predictions for stations in two European climates and it is interesting to compare the monthly attenuations for these stations with the monthly rain distributions given in [4]. The importance of the seasonal variation of rain height is clearly seen, but the Mediterranean climates still show worst months in September and October.

COMPARISON WITH EXPERIMENTAL RESULTS FOR SATELLITE-EARTH LINKS

No monthly attenuation data are available over any extended period for comparison purposes, so we confine ourselves to comparisons using annual data. A few years of annual statistics of attenuation in the 40-50 GHz range from Italsat stations have, nevertheless, now been published for a few locations [17] allowing us to make some comparisons between predictions and measurements. Table 1 shows some example results. It can be seen that the model has provided very satisfactory estimates of attenuation statistics over the full range of availabilities.

Table 1 Comparisons between predicted and measured attenuations for Spino d'Adda
Measurements are for two years with Italsat (at 13.2° E)

Fade Margin (dB)	Link Availabilities (% time) at 39.6 GHz		Link Availabilities (% time) at 49.5 GHz	
	Predicted	Measured	Predicted	Measured
10	99.72	99.6	99.30	99.1
15	99.84	99.8	99.69	99.6
20	99.90	99.9	99.80	99.8

ACKOWLEDGEMENTS

The authors wish to thank Dr C. Riva (Politecnico di Milano, Italy) for providing experimental data with which to compare our model. Particular thanks are due to P. Baptista (ESA) and W. Cramer (Potsdam Institute for Climate Impact Research) for providing meteorological databases. Also we are most grateful to Dr A Martellucci (FUB, Italy) for checking our monthly cloud prediction models against monthly radiosonde data and enabling improvements to be made.

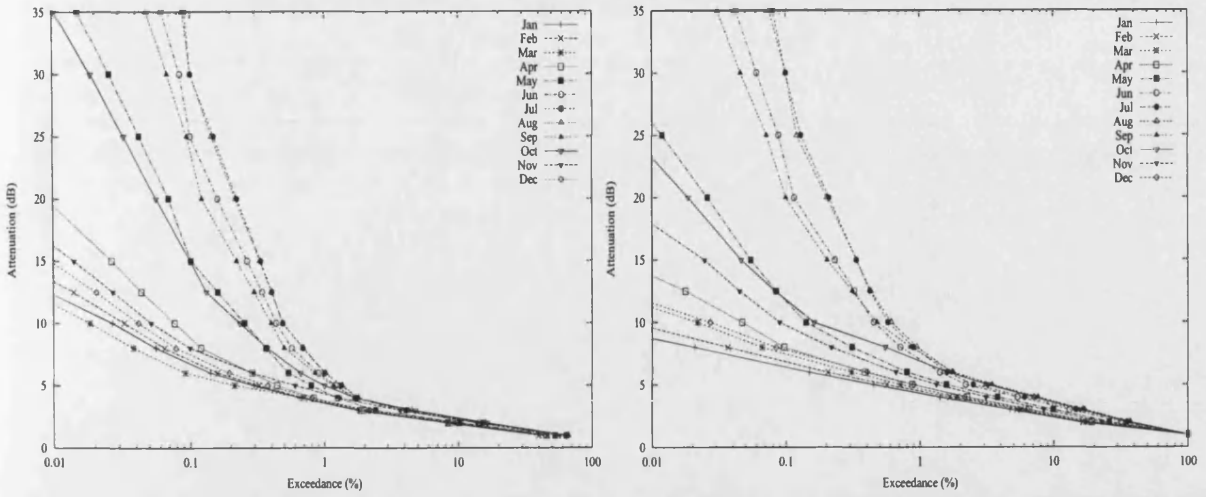

Figs. 1 and 2: Predicted monthly attenuation statistics at 39.6 GHz: for Italsat, the left-hand figure for a continental location (Darmstadt, Germany) and the right-hand figure for a mid-latitude maritime location (Lerwick, UK).

References

[1] G. Brussaard and P.A. Watson, *Atmospheric modelling and millimetre wave propagation,* Chapman and Hall, London, UK, 1995

[2] A.K. Akram, A.K. Shukla, T. Konefal and P.A. Watson, "MIDAS: A monthly link budget and signal coverage tool for frequencies between 10 and 50 GHz" *IEE ICAP*, Conf. Pub. 461, April 1999, pp 152-155.

[3] A. Page and P.A. Watson "Use of V-band in multi-media messaging services using geostationary satellites" *this conference.*

[4] P.A. Watson, M.J. Leitao, V. Sathiaseelan, M. Gunes,, J.P.V.P. Baptista, B.A. Potter, N. Sengupta, O. Turney, and G. Brussaard, "Prediction of attenuation on satellite-earth links in the European region", *IEE Proceedings*, Vol. 134, Pt. F, No. 6, October 1987, pp583-596.

[5] P.A. Watson and Y.F. Hu "Prediction of attenuation on satellite-earth links for systems operating with low fade margins", *IEE Proceedings*, Vol. 141, Pt.F, No 6, December 1994, pp467-472

[6] E. Salonen, S. Karhu, S. Uppala and R. Hyvonen, "Study of improved propagation predictions", Final report for ESA, *ESTEC contract* 9455/91/NL/LC(SC), December 1994.

[7] J.P.V. P. Baptista, E. Salonen, "Review of rainfall rate modelling and mapping", *URSI Climpara'98 Open Symposium on "Climatic Parameters in Radiowave Propagation Prediction"*, Ottawa, Canada, April 1998, pp35-44

[8] T. Konefal, P.A. Watson,, A.K. Shukla and A. Akram, "Prediction of monthly and annual availabilities on 10-50GHz satellite-Earth and aircraft-to-aircraft links" *IEE Proc. Microwaves, Antennas and Propagation*, in press.

[9] P.L. Rice and N.R. Holmberg, "Cumulative time statistics of surface point rainfall rates", *IEEE Transactions, Antennas and Propagation*, Vol. 21, No. 10, October 1973, pp1131-1136.

[10] P. Tattelman and K.G. Scharr, "A model for estimating one minute rainfall rates", *Journal of Climate and Applied Meteorology*, Vol. 22, September 1983, pp1575-1580.

[11] M.J. Leitao, and P.A. Watson, "Method for prediction of attenuation on earth-space links based on radar measurements of the physical structure of rainfall", *IEE Proceedings*, Vol. 133, Pt. F, No. 4, July 1986, pp429-440.

[12] H.J.W. Russchenberg and L.P. Ligthart, "Backscattering by and propagation through the melting layer of precipitation: A new polarimetric model", *IEEE Trans. on Geosci. and Remote sensing*, Vol. 34, No. 1, 1996, pp3-14.

[13] E. Salonen and S. Uppala, "New prediction method of cloud attenuation", *Electronics Letters*, Vol. 27, No. 12, June 1991, pp1106-1108.

[14] O.T. Davies, R.G. Howell and P.A. Watson, "Measurement and modelling of cloud attenuation at millimetre wavelengths", *Electronics Letts.*, Vol. 34, No.25, 1998, pp2433-2434

[15] H.J. Liebe, T.Manabe and G.A. Hufford, "Millimeter-Wave attenuation and delay rates due to fog and cloud conditions" *IEEE Trans. on Antennas and Propagation*, Vol. 37, No. 12, Dec. 1989, pp 1617-1623

[16] A.Martell;ucci, F.Barbelisca and M. Boumis, "Modelling and mapping of clear air atmospheric propagation", *this conference.*

[17] A. Polonio and C. Riva, "ITALSAT propagation experiment at 18.7, 39.6 and 49.5GHz at Spino D'Adda: Three years of CPA statistics", *IEEE Trans. Antennas and Propagation*, Vol. 46, No. 5, May 1998, pp631-635.